Development of a High-Effectiveness Cryogenic Stacked Slotted Plate Heat Exchanger

By

Evan P. Sheehan

A dissertation submitted in partial fulfillment of

the requirements for the degree of

Doctor of Philosophy

(Mechanical Engineering)

at the

UNIVERSITY OF WISCONSIN - MADISON

2019

Date of final oral examination: 4/24/2019

The dissertation is approved by the following members of the Final Oral Committee:

John M. Pfotenhauer, Professor, Mechanical Engineering
Franklin K. Miller, Professor, Mechanical Engineering
Gregory F. Nellis, Professor, Mechanical Engineering
Douglas Reindl, Professor, Engineering Professional Development
Frank Pfefferkorn, Associate Professor, Mechanical Engineering

Abstract

High-effectiveness heat exchangers are a ubiquitous component of cryogenic systems, but their performance typically falls short of model-based expectations [1]. The following thesis details modeling efforts of a heat exchanger designed to achieve an effectiveness in excess of 99% within a prescribed volume, weight, pressure drop, and operating conditions for SHI Cryogenics of America. With such a high effectiveness requirement, simulation efforts focused on making minimal assumptions and detailed models.

Axial conduction and parallel flow passage imbalance are major contributing factors to heat exchanger inefficiency. Consequently, a staggered stacked slotted plate geometry was chosen as the most promising design to achieve the desired effectiveness. The large number of design parameters initially spurred the development of model interfacing with the University of Wisconsin Center for High Throughput Computing, but licensing issues limited its usability. Instead, the number of parameters was thoughtfully reduced based on manufacturing limitations and scaling considerations. Manufacturing options for machining the slots and bonding the plates were investigated.

A MATLAB model which included axial conduction, parasitic heat loads, and material property variation accounted for losses in order to avoid inflating the efficiency estimate. Fluent was used to develop accurate Nusselt number and Darcy friction factor correlations, which were used as inputs to the MATLAB model. The MATLAB model was validated by comparing its results to an analytic, constant property effectiveness-NTU solution as well as experimental data from a similar heat exchanger. The Fluent correlations were compared to other correlations typically used for slotted plate heat exchangers.

Acknowledgments

First and foremost, I would like to thank my parents, Patrick and Lynda. Your love has been the foundation of my life. At each step along the way you've supported me and encouraged me to challenge myself. I can never repay you for all that you've done for me, but I try to make you proud of what I accomplish as the best way I can say thank you.

I would also like to thank my advisors. John Pfotenhauer, I owe my enthusiasm for cryogenics to you. You introduced me to the field, inspired my fascination with it, and it has now become part of my very identity. Many times, you had more confidence in my abilities than I did. You trusted me, and with your assurance I often surprised myself with what I was able to accomplish. Franklin Miller, your encyclopedic knowledge of seemingly all things technical is astonishing. On many occasions I've been struggling with a tough problem, and you've managed to solve it in a few minutes with nothing but your memory and the calculator on your phone. You and John are brilliant cryogenicists, and I feel honored to have had the two of you as my advisors.

I would like to thank a few people who I worked with during the four or so years of developing the pulsed HTS SMES. Owen Christianson, I can't convey how much I learned while working with you. I've realized that I have adopted the same processes of thought that you employ while working in the lab. Playing devil's advocate to consider every explanation for a phenomenon without prejudice, quick mental order-of-magnitude calculations, and knowing when to be quick and cut a few corners and when to slow down and be careful, to name a few. Lab work is a skill in its own right, and I learned most of what I know today from you. I'd also like to thank Gabe Bernhardt. I could always count on you for advice, a helping hand, and a friend to talk to. You were always there when something exploded or someone needed a ride to the hospital. Speaking

of, I'd also like to thank Cooper Hennick. As an undergraduate you were already doing PhD quality work. I anticipate that you'll find great success wherever your career takes you.

Finally, I'd like to acknowledge some friends of mine. First, I'd like to give a special thanks to a special girl, Michelle Marks. You've been my constant companion, and always understanding of the challenges of the graduate school experience. My good buddies from Layafette, Cameron Roche and Kevin Schmid, I'll be heading to Maryland soon and see you there! And of course, my graduate school friends. Avi Friedman, Chris Hummel, Mason Mok, Cass Wright, Becky Sondelski, Tyler Hanzlik, Brian Fehring, Joe Shinners, Kelsey McCusker, Amir Jahromi, Brian Leyde, and Diego Fonseca. I've had so many amazing, fun times with you all that have made this experience truly wonderful. We are all going or have already gone our separate ways, but I hope to see you all again before too long.

Table of Contents

List of Figures

List of Tables

Nomenclature

General

A_c	Cross-sectional area (m^2)
A_s	Surface area (m^2)
AR	Fin aspect ratio
b	Metal width surrounding each heat exchanger fluid side (m)
c_p	Specific heat capacity (J/kg-K)
$\dot{C}$	Heat capacitance rate (W/K)
D_h	Hydraulic diameter (m)
f	Darcy friction factor
$f_{Fanning}$	Fanning friction factor
h	Fluid specific enthalpy (J/kg)
$\bar{h}$	Average convective heat transfer coefficient (W/m^2-K)
H_{fin}	Fin height, perpendicular to flow direction (m)
H_{gap}	Gap height between fins on a given slotted plate (m)
H_{total}	Total heat exchanger size in height direction (m)
k	Thermal conductivity (W/m-K)
K_c	Contraction loss coefficient
K_e	Expansion loss coefficient
L	Total heat exchanger size in length or stacking direction (m)
L_{domain}	Length of the heat exchanger unit cell (m)
$L_{fd,t,laminar}$	Thermal boundary layer duct flow entrance length (m)
L_{micro}	Shared dimension for th_{plate}, th_{spacer}, H_{fin}, and H_{gap} (m)
$\dot{m}$	Mass flow rate (kg/s)
$\dot{m}''$	Mass flux (kg/m^2-s)

mL	Fin parameter
n_{fins}	Number of fins on one fluid side of each slotted plate
n_{plates}	Number of slotted plates in heat exchanger
NTU	Heat exchanger number of transfer units
$\overline{Nu}$	Average Nusselt number
p	Slotted plate porosity
P	Pressure (Pa)
Per	Perimeter (m)
Pr	Prandtl number
$\overline{\dot{q}''}$	Area-weighted average heat flux through fin surface area (W/m^2)
$\dot{Q}$	Heat transfer rate (W)
R^2	Correlation coefficient of determination
Re	Reynolds number
$\bar{S}_L$	Dimensionless longitudinal fin pitch
$\bar{S}_T$	Dimensionless transverse fin pitch
th_{plate}	Slotted plate thickness (m)
th_{spacer}	Spacer thickness (m)
T	Temperature (K)
UA	Overall heat exchanger conductance (W/K)
$\bar{V}_{gap}$	Average fluid velocity in slots (m/s)
$\bar{V}_{in}$	Average fluid velocity in Fluent domain inlet (spacers) (m/s)
V_{total}	Total heat exchanger volume (m^3)
$W_{channel}$	Width of flow channel. Also the fin size in axial direction (m)
α	Thermal diffusivity (m^2/s)
ΔT_{LM}	Log-mean temperature difference (K)

ε	Heat exchanger effectiveness
η	Fin efficiency
λ	Overall heat exchanger axial conduction parameter
μ	Dynamic viscosity (kg/m-s)
ρ	Density (kg/m^3)
σ	Electrical conductivity (S/m)
σ_{ff}	Ratio of plate to spacer free frontal area
$\tau_{thermal}$	Characteristic time scale for thermal diffusion (s)
τ_{mass}	Characteristic time scale for mass diffusion (s)
ξ	Coefficient of hydraulic resistance for plate-spacer matrix
ξ'	Coefficient of hydraulic resistance of a single slotted plate

Subscripts

2D	Two-dimensional Fluent model with 1 (m) unit length depth
3D	Three-dimensional geometry of physical heat exchanger
Fluent	Pertaining to the Fluent-derived correlations
max	Maximum value
min	Minimum value
Mikulin	Pertaining to the correlations developed by Mikulin

ENTU Solutions

$n_{tu,f}$	Number of convective heat transfer units
$n_{tu,p}$	Dimensionless plate conductance
$n_{tu,po}$	Overall dimensionless plate conductance
NTU_{eff}	Effective NTU with axial conduction included
NTU_o	Effective NTU with axial conduction ignored
R	Thermal resistance (K/W)

α	Intermediate parameter
ε_p	Effectiveness of single plate
λ_p	Dimensionless lateral conductance of separating wall
ν	Heat capacity ratio

Subscripts

1	Cold side
2	Hot side
cu	Copper plates
ss	Stainless steel spacers

MATLAB Model

A_s'	Heat transfer surface area per unit length (m^2/m)
$A'_{s,o}$	Surface area per unit length exposed to surrounding environment (m)
$\dot{q}$	Total heat transfer rate to or from heat exchanger flow stream (W)
q'	Parasitic heat load per unit length (W/m)
$R_{all\ fins}$	Parallel thermal resistance of all fins on one side of one plate (K/W)
R_{base}	Thermal resistance of half of the wall separating the two sides (K/W)
R_{cu}	Series axial conduction resistance of all copper plates (K/W)
R_{fin}	Thermal resistance of a single fin (K/W)
R_{plate}	Series thermal resistance of all fins with base for one plate (K/W)
R_{ss}	Series axial conduction resistance of all stainless steel spacers (K/W)
R_{total}	Parallel thermal resistance of all slotted plates (K/W)
T_∞	Temperature of surrounding environment (K)
U	Heat transfer conductance (W/m^2-K)
x	Axial heat exchanger position (m)
X	Dimensionless axial heat exchanger position

α_r	Dimensionless effectiveness of radiation shielding
β	Total heat exchanger NTU evaluated at node properties
ε_m	Heat exchanger metal emissivity
Θ	Dimensionless temperature
λ	Overall axial conduction parameter evaluated at node properties
μ	Dimensionless hot side heat capacitance rate
ν	Dimensionless cold side heat capacitance rate
φ	Ratio of inlet temperature to surrounding environment temperature
χ	Dimensionless parasitic heat load

Subscripts

ac	Axial conduction
c	Cold fluid side
fluid	Either the hot or cold side fluid
h	Hot fluid side
i	Spatially discretized heat exchanger element number
in	Heat exchanger inlet
m	Metal
n	Number of discrete elements

1. Introduction

Recuperative heat exchangers are used extensively in the field of cryogenics to significantly raise the overall efficiency of cryogenic systems. The effectiveness of the recuperator directly impacts the system efficiency. Maximizing the recuperator effectiveness allows for lower ultimate temperatures at the cold end and minimizes required cooling power to the flow stream. Raising the effectiveness tends to also increase the pressure drop and size of the heat exchanger. SHI Cryogenics of America (SHI) has formulated this project as a study of these tradeoffs.

Various parameters were outlined that formed the design space for the heat exchanger, including the operating conditions and size, but achieving an effectiveness of over 99% was the most important requirement. To accurately predict the performance of a heat exchanger with such a requirement necessitated computational models with minimal assumptions and simplifications. Material property variation with pressure and temperature, as well as losses due to axial conduction and parasitic heat loads, had to be included in numerical modeling. Previous workers have produced applicable correlations for friction factor and Nusselt number [2], but the correlations did not cover the full range of Reynolds numbers expected in this design study, and made assumptions that could significantly impact the accuracy of the model.

The ultimate goal was to arrive at a general manufacturable heat exchanger style that could achieve 99% or greater effectiveness, while simultaneously developing a computational modeling tool to predict the effects of each geometric facet on the tradeoffs between volume, weight, pressure drop, and effectiveness. The design could then be fine-tuned as desired by SHI.

2. Design Specifications

Table 1 outlines the heat exchanger design envelope prescribed by SHI.

Working Fluid:	Helium
Temperature Span:	300 K to 30 K
Operating Pressures:	2.6 MPa (supply side), 0.5 MPa (return side)
Pressure Drop:	< 3 bar (supply side), < 1 bar (return side)
Burst Pressure:	13.5 MPa
Flow Rate:	6 (Rating case) g/s to 12 (Design case) g/s
Materials:	316 Stainless Steel, Copper
Approximate Size:	< 0.5 m height, 0.1 m^3 volume
Effectiveness:	$\geq$ 0.99

Table 1: SHI heat exchanger design specifications.

Within this design space, all geometries, configurations, and fabrication methods were options. Several types of designs were explored and will be discussed in the forthcoming literature review. Performance, manufacturing techniques, and cost estimates were considered to determine the most promising design style to achieve high effectiveness, small size, and low cost.

3. Literature Review

3.1. The Importance of High Cryogenic Heat Exchanger Effectiveness

Recuperative heat exchangers are commonplace in cryogenic systems and used to significantly reduce heat loads on cryocoolers. Any ineffectiveness in the recuperator translates directly to extra heat that the cryocooler must remove from the system in addition to the heat leaks to the cold space. Because the refrigeration load tends to be small compared to the total stream-to-

stream heat transfer in the recuperator, a slight reduction in heat exchanger effectiveness results in an extra heat load on the cryocooler that can easily rival the cold space heat leak.

The Cryogenic Engineering Lab's high-temperature superconducting magnetic energy storage (SMES) project serves as an excellent example. A schematic of the helium gas cooling system for the superconducting electromagnet is pictured in Figure 1.

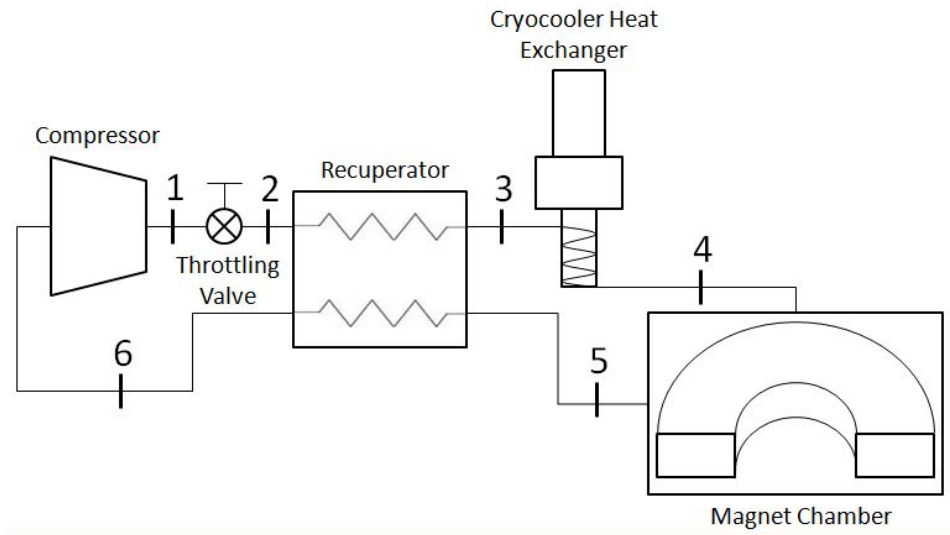

Figure 1: Helium gas cooling system for the University of Wisconsin pulsed HTS SMES device.

An energy balance applied to the helium gas in the cold section demonstrates the effect of the recuperator ineffectiveness on the cryocooler cooling load.

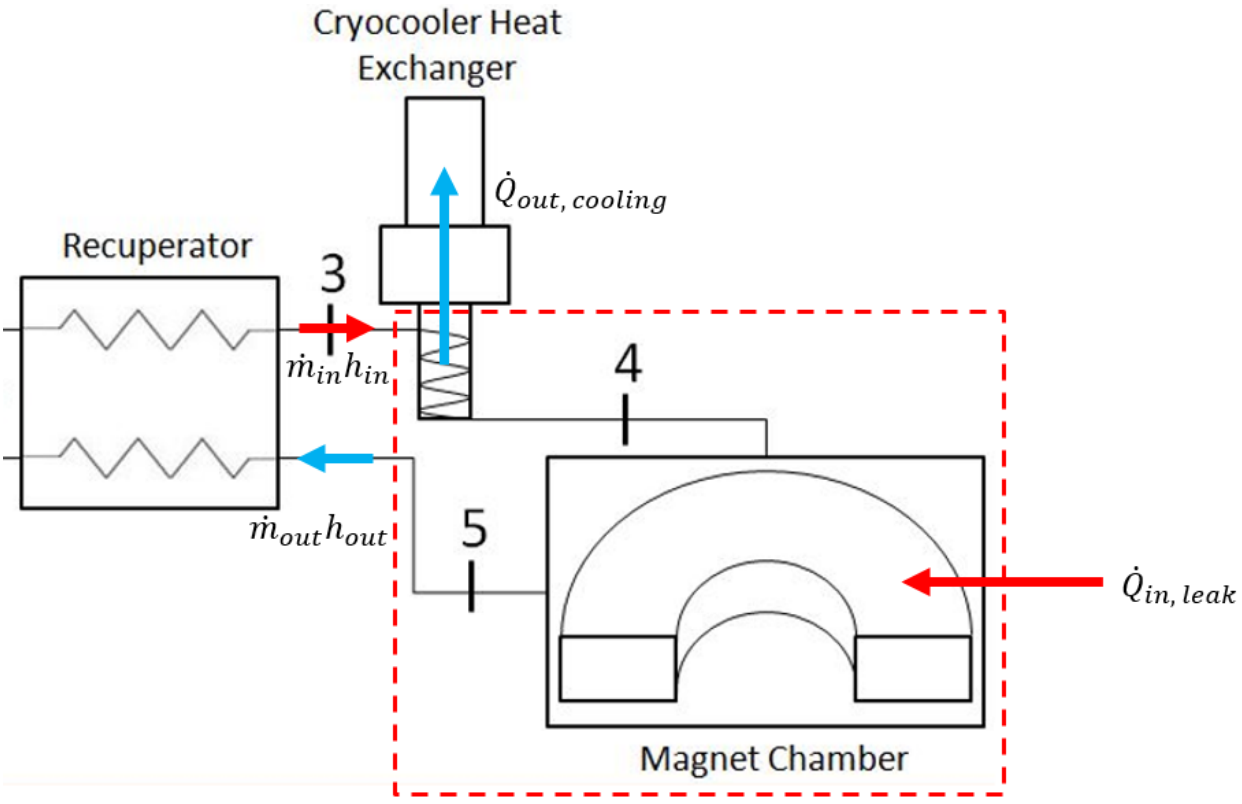

Figure 2: Energy balance control volume on the cold section of the SMES system.

The system was closed-loop, so $\dot{m}_{in} = \dot{m}_{out} = \dot{m}$. The resulting energy balance gives an expression for the cooling load on the cryocooler.

$$\dot{Q}_{out,cooling} = \dot{Q}_{in,leak} + \dot{m}(h_{in} - h_{out}) \quad (1)$$

In the case of a perfect recuperator, the difference between the incoming and outgoing gas enthalpy would be zero, and the cooling load would simply equal the rate of heat leak. In the real case, the flow enthalpy difference is equal to the maximum possible recuperator heat transfer rate, corresponding ideal operation, multiplied by its ineffectiveness.

$$\dot{m}(h_{in} - h_{out}) = \dot{Q}_{max}(1 - \varepsilon) \quad (2)$$

Which translates to an additional heat load that must be removed from the system by the cryocooler. This equation is true provided that the mass flow rate is the same on each side.

For this particular system, a Hampson-style counter-flow recuperator, depicted in Figure 3, precooled the gas from ambient to about 93 K from states (2) to (3) on Figure 1.

Figure 3: HTS SMES cooling system recuperative heat exchanger.

The cryocooler interfaced with a heat exchanger in order to cool the gas and reduced its temperature to about 42.5 K at state (4). The gas entered the magnet chamber, where it flowed through the magnet windings and removed heat from the magnet and its enclosure, including heat generated during magnet operation, residual gas conduction and radiation to the chamber, and the conductive leaks through the current leads. As a consequence, the gas exited the magnet chamber at roughly 71.5 K at state (5) before re-entering the recuperator.

By measuring the inlet and outlet gas temperatures of the recuperator, the stream-to-stream heat transfer rate while operating the system at a mass flow rate of 0.6 g/s was measured to be 627.5 W, compared to a maximum possible ideal rate of 694.8 W, and the effectiveness was determined to be about 90.3%. The heat load on the cold chamber was inferred to be about 90 W, whereas the heat load on the cryocooler was measured to be 157.4 W.

With a perfect recuperator, the cryocooler would only have needed to remove the 90 W of heat leak to the cold chamber. But the recuperator ineffectiveness of 0.097, multiplied by the maximum possible recuperator heat transfer rate of 694.8 W, increased the heat load on the cryocooler by approximately 67.4 W. Together with the 90 W heat leak, the heat load on the cryocooler nearly doubled to 157.4 W.

At $\dot{m}$ = 0.6 g/s, the heat load on the cryocooler limited the inlet temperature at the magnet chamber to about 42.5 K. Because $\dot{Q}_{max}$ scales with $\dot{m}$, raising $\dot{m}$ increased the heat load on the cryocooler and raised its temperature. It was impossible to maintain a low enough cryocooler temperature and high enough mass flow rate simultaneously. Convective cooling of the magnet was therefore limited, and as a result, the superconducting coil was unable to operate at its highest design current because the rate of joule heating in its non-superconducting joints exceeded the rate of convective cooling.

3.2. Typical Compact Heat Exchanger Designs

3.2.1. Parallel Plates: Inline Strip-Fins

In theory, parallel plate heat exchangers achieve the greatest surface area per unit volume of any recuperator geometry [1]. An example of this geometry type with rectangular inline fins for heat transfer enhancement is depicted in Figure 4.

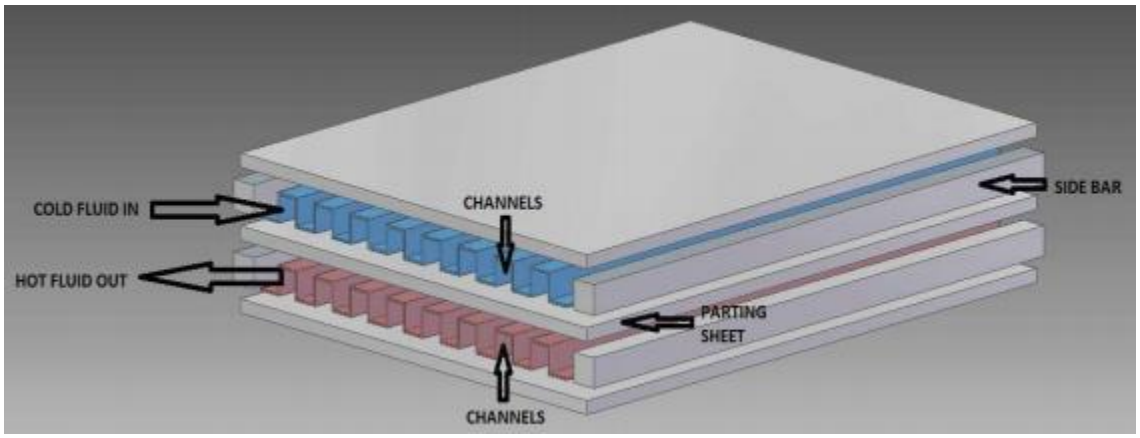

Figure 4: Parallel plate heat exchanger with rectangular inline strip-fins [3].

However, they never meet their design effectiveness due to mass flow imbalances that arise between either the parallel flow channels in a given layer, or between several layers operating in parallel. Miniscule differences in geometry create feedback loops that starve some regions of flow while others carry more than anticipated. For example, consider low temperature gas entering the cold side. If some flow paths carry gas at lower velocity, the convective heat transfer decreases, and that region remains colder than adjacent channels. The resulting higher density gas velocity decreases further. A simple argument can be used to show that the flow must be balanced between the parallel channels to within 2% to reach an effectiveness of 99% or greater. Marquardt and Radebaugh [1] use a simple example to illustrate this rule:

> "Consider two sets of identical channel pairs, each set transfers its energy only to its mated pair. If the flow is distributed 50% in each set and the heat transfer is perfect, we can have an effectiveness of 1 if longitudinal conduction is ignored. Now let the cold side of the exchanger perfectly split the flow between the two channels but let the hot side split the flow 49%/51%. With perfect heat transfer, we can only transfer 49% of the energy in one set and 50% of the energy in the other set of channels, resulting in a 99% effectiveness."

Marquardt and Radebaugh attempted to mitigate this problem by manufacturing a heat exchanger using precise photochemical etching rather than chemical milling. Even with the increased channel uniformity, their modeling predicted the design to achieve 99.5% effectiveness, but test results

reached only 97.3%. They estimated a 16% difference between the actual and target mass flow rates at the outermost channels of their heat exchanger, highlighting the difficulty of manufacturing sufficiently homogenous parallel flow passages, even with state-of-the-art manufacturing techniques.

3.2.2. Parallel Plates: Offset Strip-Fins

The offset strip-fin design is a modification of the inline strip-fin parallel plate geometry. Figure 5 shows the general form of an offset strip-fin style heat exchanger.

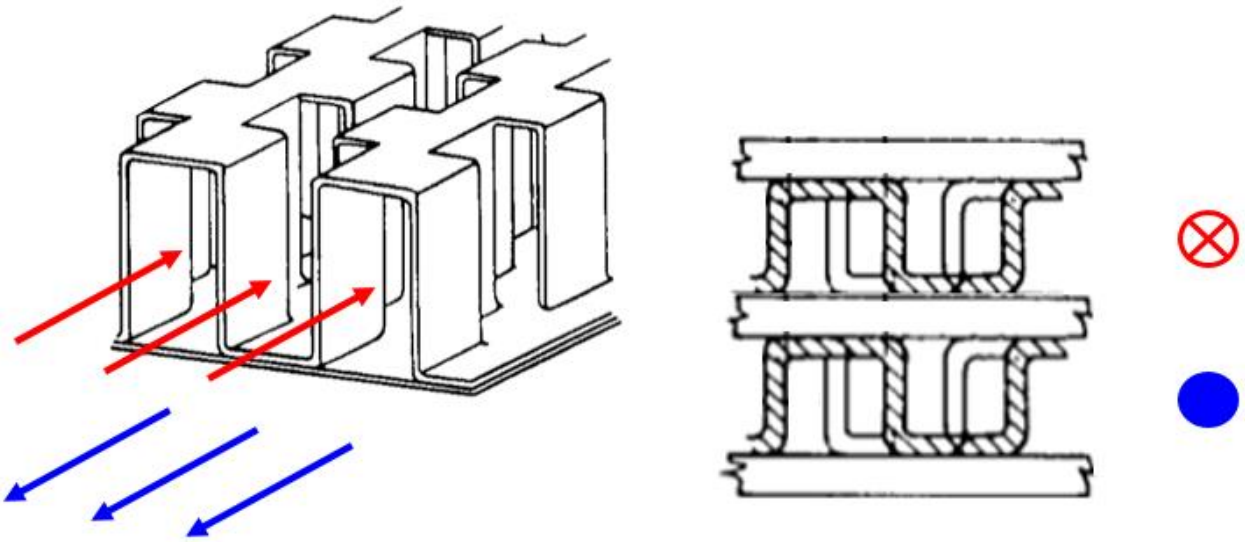

Figure 5: Offset strip-fin parallel plate geometry and flow directions [4].

A thin dividing wall separates the hot and cold streams from one another. The staggered nature of this design has two advantages over the parallel plate design. First, the flow boundary layer growth is regularly interrupted, enhancing heat transfer. Second, the flow around each strip-fin is not isolated, which may allow for sufficient redistribution of mass flow rate and prevent flow maldistribution. However, if multiple hot or cold streams are arranged in parallel to reduce the fin

length, flow imbalance is still a concern, even though it is mitigated within each individual flow stream.

Both the staggered and inline strip-fin geometries suffer from axial conduction effects. Both employ high-conductivity heat transfer surface material that is uninterrupted along the entire axial length of the heat exchanger. The material that separates the supply and return sides poses the same problem. High conductivity is desired to minimize stream-to-stream thermal resistance, but inherently also reduces axial conduction resistance.

3.2.3. Stacked Staggered Perforated Plates

Figure 6 depicts a pair of examples of stacked perforated plate heat exchanger designs.

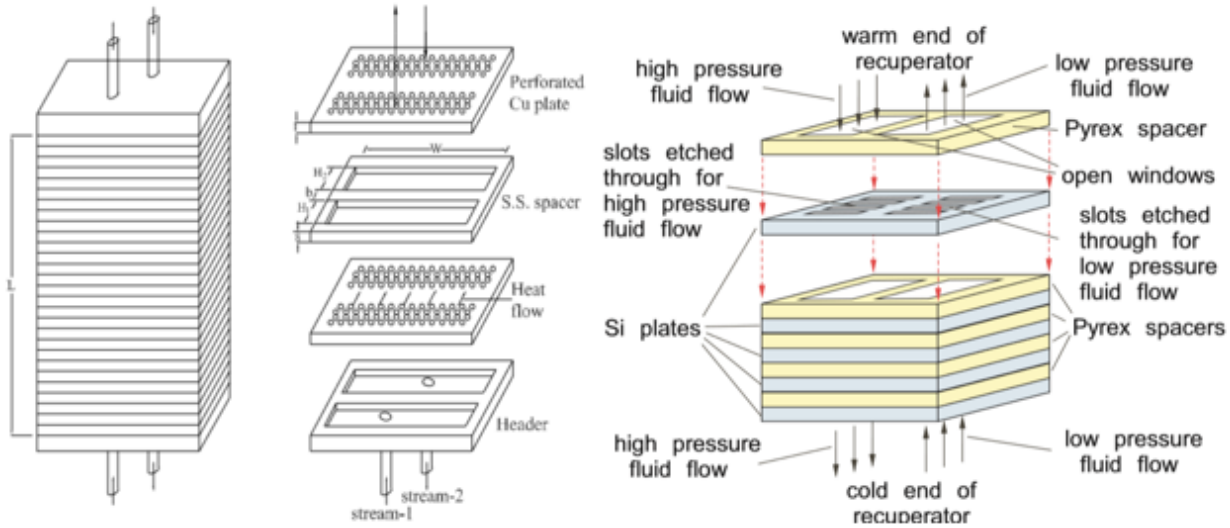

Figure 6: Stacked perforated plate heat exchangers. Copper and stainless steel with circular holes (left) [5], and silicon and Pyrex with rectangular slots (right) [6].

This type of heat exchanger is comprised of alternating layers designed to create anisotropic heat transfer. The perforated plates are constructed from relatively conductive materials, such as copper or silicon in the above examples, with some form of high surface area geometry such as circular holes or rectangular slots, which result in an array of rectangular fins. Staggering the perforations

between subsequent layers enhances heat transfer by creating flow impingement on the unperforated area of the plates at the cost of increased pressure drop. The spacer layers have a small cross-sectional area and are constructed from low conductivity materials (stainless steel and Pyrex in the above examples), and thermally insulate adjacent plates from one another. The two materials must be compatible to form some type of seal that can survive differential thermal contraction upon cooling. The result is high stream-to-stream conduction with limited axial conduction. Additionally, after the working fluid passes through the parallel channels in the perforations, it should be able to redistribute in the spacer region, preventing large-scale flow maldistribution from developing. This geometry is likely even more conducive to flow redistribution than the offset strip-fin design because the spacer regions are completely open.

The results of the experimental study of the silicon-Pyrex heat exchanger reveal a few important considerations [6]. The maximum measured effectiveness of the heat exchanger was about 78%, roughly 10% below the design effectiveness. The authors attributed the shortcoming to three factors. First, helium gas leak between the two streams. Forming a gas-tight seal around each flow channel is a nontrivial challenge, especially considering thermal contraction at the cold end. Second, parasitic heat loads. The heat exchanger will undoubtedly be contained within a vacuum chamber to virtually eliminate convection with room temperature surrounding air. However, no vacuum is perfect, and the remaining gas particles will capture heat when contacting the ambient temperature vacuum chamber wall, and deposit it upon contacting the recuperator. Additionally, some form of thermal radiation shielding, such as multilayer insulation or an actively cooled metallic shield, will be used to intercept the overwhelming majority of heat radiating from the room temperature vacuum chamber to the colder recuperator. The shields are never perfect, and some amount of radiative heat will still be transferred to the recuperator. Models should

account for residual gas conduction and radiative heat loads that are not intercepted by radiation shielding. Third, impurities in the helium gas freezing out at the cold end, obstructing parts of the flow path.

The unique combination of low axial conduction and flow redistribution zones made this heat exchanger style the most appealing option to achieve the 99% effectiveness sought by SHI. As such, this project focused solely on a stacked, staggered perforated plate design with copper used for the conducting plates and 316 stainless steel used for the spacers, in accordance with the materials listed in the aforementioned design specifications.

3.2.3.1. Arguments for Slots vs. Circular Holes

A slotted plate geometry results in fin heat transfer, which has the advantage of easily being modeled using well established fin efficiency formulas. Circular holes would require the development of a shape factor for stream-to-stream conduction resistance. They are also not conducive to a reduction into two dimensions for the computational fluid dynamics modelling that will be discussed later in this thesis. Additionally, simple calculations suggested that slots will achieve a higher density of convective heat conductance.

To roughly compare the total convective thermal resistance of the two void types, consider a long slot compared to a series of inscribed circles of the same diameter as the slot height, which fill the entire slot and touch their neighbors.

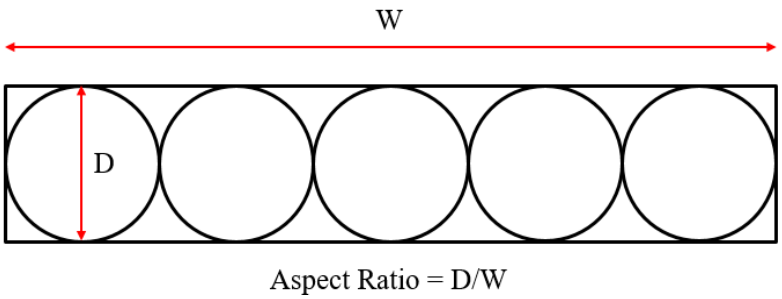

Figure 7: Visualization of the comparison between slots and circular holes, with equivalent circle diameters and slot heights, with enough tangent circles to fill the slot

The ratio of the convective heat transfer coefficient multiplied by the perforation surface area per unit length between the two cases as a function of the aspect ratio of the duct with a given slot height (or hole diameter) using fully developed flow conditions was calculated.

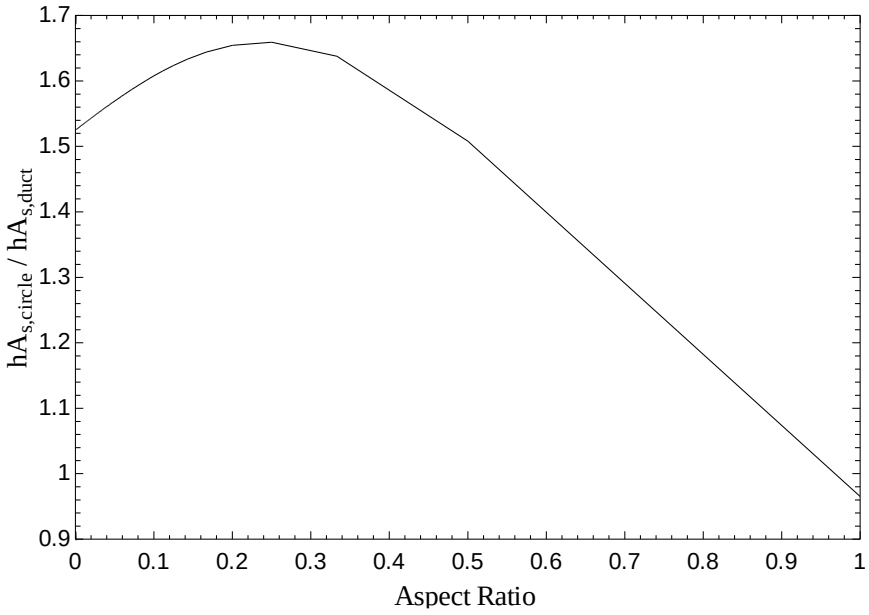

Figure 8: Ratio of circle to duct convective thermal conductance. An aspect ratio of 1 represents a square duct, while and aspect ratio of 0 represents an infinitely long duct.

For the circular case the Nusselt number, defined as $Nu = hD_h/k$, is constant at 3.66. If the duct is a square, it has an equal hydraulic diameter to a circle. However as the aspect ratio decreases, the hydraulic diameter of the duct approaches twice the value of the circle hydraulic diameter, and the

duct Nusselt number approaches 7.541 asymptotically. So, in the limit of significant aspect ratio, with roughly double the Nusselt number but also double the hydraulic diameter, the convective heat transfer coefficient is about the same for both cases. Aspect ratios were expected to be on the order of 0.1 or less.

The circle surface area is greater than the duct surface area by a factor of $\pi/2$ (ignoring the end contributions because the aspect ratio will be small, and assuming a whole number of circles). This effect is dominant and results in a greater hA value for the circular case by a factor of about $\pi/2$ for small aspect ratios, as seen in Figure 8. However, this neglects material between the circles required by the prospective manufacturing processes.

Initial conversations with fabricators suggested the material required between void features can be no less than the plate thickness. The resulting surface area of the circular geometry is reduced by a factor of 2. Accounting for this factor, the slot hA value will be between 52% and 17% larger than the circular holes of equivalent size, depending on the aspect ratio, as seen in Figure 9.

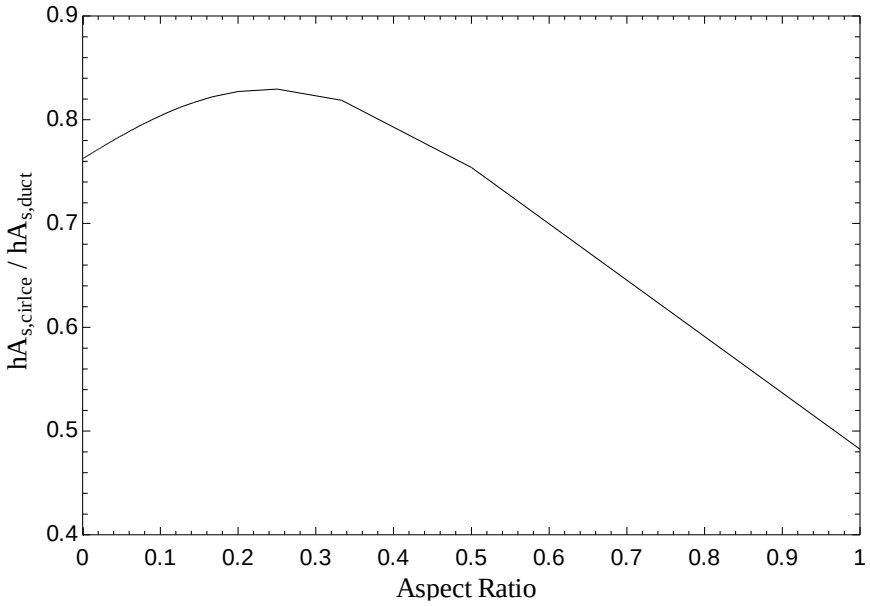

Figure 9: Ratio of circle to duct convective thermal conductance with extra material required between adjacent circular holes included, which reduces its relative conductance.

This result, combined with the ease of using well-established fin heat transfer expressions, persuaded the choice to use slots rather than circular holes.

3.2.3.2. Treatment of the Fin Efficiency

The typical equation for the efficiency of a fin with an adiabatic tip assumes that the temperature of the surrounding fluid is constant along the entire length of the fin and is defined as [7]:

$$\eta = \frac{\tanh(mL)}{mL} \tag{3}$$

where mL is the fin parameter. However, this equation does not apply to stacked plate heat exchangers. The assumption of a constant fluid temperature is only valid for the first plate. Minimal fluid mixing occurs in the fin length direction. After the first few slotted plates, a temperature gradient develops in the fluid in the stream-to-stream direction, along the fin length, which follows the temperature gradient in the fins [8].

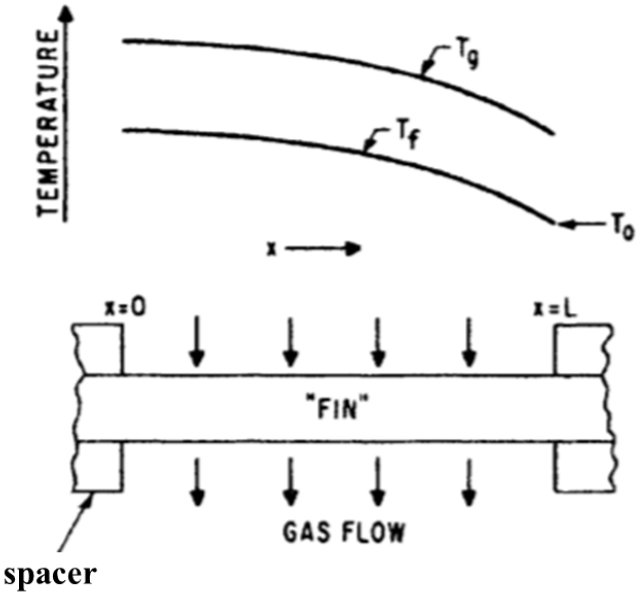

Figure 10: Temperature gradient in fin and surrounding fluid after the first few slotted plates [8].

Fleming derived the equation for the fin efficiency under the assumption of a constant temperature difference between the fin and fluid at all locations along the fin length with an adiabatic tip.

$$\eta = \frac{1}{1 + \frac{(mL)^2}{3}} \tag{4}$$

The resulting temperature gradient follows a parabolic curve, rather than a hyperbolic tangent. At all values of mL, the fin efficiency predicted by Fleming's method is lower, and therefore provides a more conservative estimation of the fin efficiency.

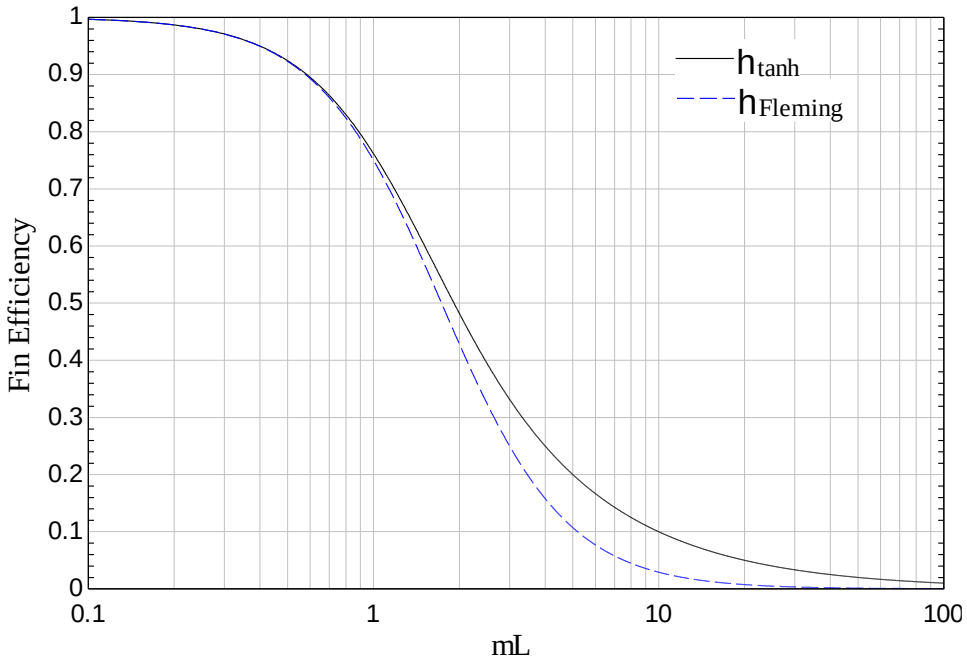

Figure 11: Comparison between the fin efficiency predicted using the conventional constant fluid temperature equation and the constant fluid-fin temperature difference modification.

The difference between the two treatments is significant at lower efficiency configurations, with the greatest difference occurring at mL values around 5, where the fin efficiency predicted using Fleming's assumption is about a factor of 2 lower than the conventional hyperbolic tangent. This behavior has been experimentally validated, and the constant fluid-fin temperature difference form of the fin efficiency has been used universally for slotted plate heat exchangers since Fleming's derivation [9].

3.3. Stacked Plate Heat Exchanger Modeling

3.3.1. Effectiveness – NTU Solutions

Analytic solutions based on the traditional effectiveness – NTU approach, modified to be applied to stacked plate heat exchangers, have been developed over the past several decades. The high-effectiveness nature of these heat exchangers necessitates inclusion of secondary effects that

reduce performance, namely axial conduction and parasitic heat loads. An initial solution proposed by Fleming in the late 1960's was to simply replace the ideal NTU with an apparent or effective NTU based on corrections presented by Kays and London [10] that account for axial conduction effects which reduce the actual effectiveness below the ideal effectiveness [8].

$$NTU = \frac{UA}{\dot{C}_{min}} \tag{5}$$

$$NTU_i = \frac{\varepsilon_i}{1 - \epsilon_i} \tag{6}$$

$$NTU_{eff} = \frac{\epsilon}{1 - \epsilon} \tag{7}$$

The NTU modifications were derived from experimental studies of periodic flow heat exchangers.

Kroeger proceeded to mathematically derive expressions for the effective NTU of both balanced and imbalanced flow heat exchangers subject to axial conduction effects [11]. In the balanced flow case:

$$NTU_{eff} = NTU_o \frac{1 + \lambda\sqrt{\frac{\lambda NTU_o}{1 + \lambda NTU_o}}}{1 + \lambda NTU_o} \tag{8}$$

where λ is the overall axial conduction parameter, and NTU_o is the effective NTU of the heat exchanger if axial conduction were not present. Kroeger's approach treated the heat exchanger as a homogenous geometry and made no distinction between plates and spacers. The unmodified NTU was simply based on the total UA of the heat exchanger, and the axial conduction parameter was an overall value for the entire heat exchanger.

Years later in the mid – 1990's, Venkatarathnam aimed to improve upon Kroeger's work by including the effects of the discrete nature of stacked plate heat exchangers in the expression for the unmodified overall NTU (prior to modification by axial conduction effects) [12]. He then

used Kroeger's technique to account for axial conduction. His approach began by defining the effectiveness of a single plate in the absence of axial conduction effects:

$$\frac{1}{\epsilon_p} = \frac{1}{1 - exp\left(-n_{tu,f,1}\right)} + \frac{\nu}{1 - exp\left(-n_{tu,f,2}\right)} + \frac{1}{n_{tu,po}} \tag{9}$$

which corresponded to the following effectiveness of a heat exchanger with n plates:

$$\epsilon = \frac{n_{plates}(1-\alpha_1)(1-\alpha_2)}{\left[n_{plates}(1-\alpha_1)(1-\alpha_2) + 1 - \alpha_1\alpha_2 + \frac{(1-\alpha_1)(1-\alpha_2)}{n_{tu,po}}\right]} \tag{10}$$

with $\alpha = \exp(-n_{tu,f})$. ν is the capacitance rate ratio $\dot{C}_1/\dot{C}_2$. 1 denotes the side with the lower capacitance rate. $n_{tu,f,1}$ and $n_{tu,f,2}$ are the fluid NTU on each side, which exclude any reductions that arise from the conduction resistance of the plates. $n_{tu,po}$ is the overall plate conductance, which accounts for the conductance of the metal separating the two flow streams (λ_p), as well as the fin efficiency's modulation of the plate conductance, $n_{tu,p}$, on each side.

$$n_{tu,po} = \frac{1}{\frac{1}{\lambda_p} + \frac{1}{3n_{tu,p,1}} + \frac{\nu}{3n_{tu,p,2}}} \tag{11}$$

He then used Kroeger's solution under the assumption of a large NTU_o and small λ to determine an expression for the $N_{tu,eff}$ of a heat exchanger with discreet plates and spacers, with the inclusion of axial conduction:

$$NTU_{eff} = \frac{n_{plates}(1-\alpha_1)(1-\alpha_2)}{\left[n_{plates}\lambda(1-\alpha_1)(1-\alpha_2) + 1 - \alpha_1\alpha_2 + \frac{(1-\alpha_1)(1-\alpha_2)}{n_{tu,po}}\right]} \tag{12}$$

which can be used in conjunction with the conventional expression of effectiveness as a function of NTU.

None of the above treatments are equipped to include material property variations with temperature and pressure. The pressure difference between the two sides of the heat exchanger this

work was concerned with was large compared to the allowable pressure drop on each side and resulted in minimal helium property variation on a given side due to the pressure drop, but the 270 K temperature change causes significant differences in the fluid and metal properties, seen in the figures below.

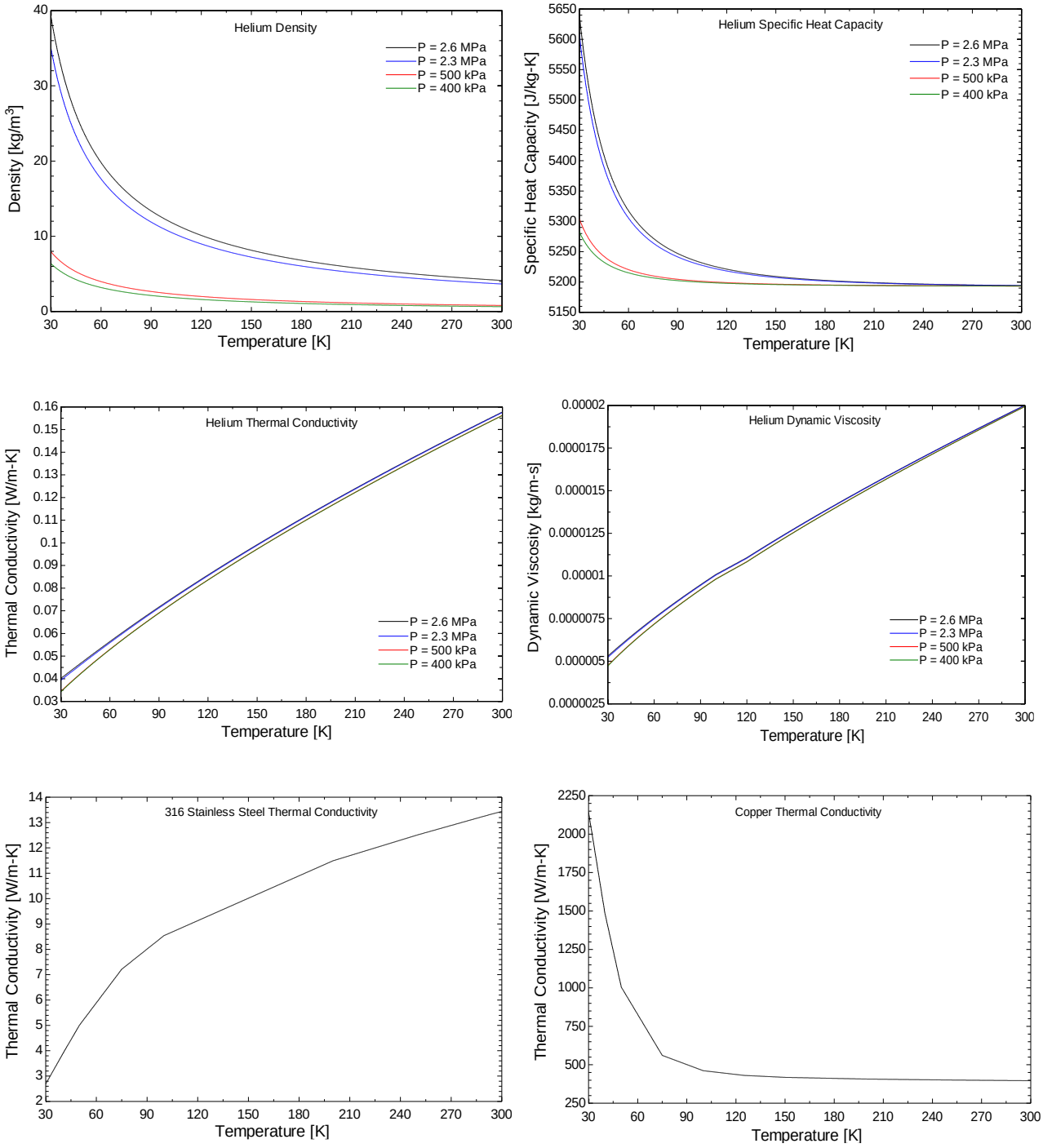

Figure 12: Variation of material properties within the ranges of temperature and pressure of the heat exchanger. Top-left: helium density. Top-right: helium specific heat capacity. Middle-left: helium thermal conductivity. Middle-right: helium viscosity. Bottom-left: 316 stainless steel thermal conductivity. Bottom-right: copper thermal conductivity

Kroeger noted in his concluding statements that neglecting material property variation in cryogenic heat exchangers can introduce errors. However, he stated that the use of average material property values usually predicts heat exchanger performance accurately. Additionally, none of the methods discussed in this section account for parasitic heat loads which may also be present. Not wanting to risk overestimating the effectiveness by assuming average material properties, this work chose to use a finite difference model to study the heat exchanger instead.

3.3.2. Finite Difference Model

To increase the likelihood that the high-effectiveness heat exchanger would meet theoretical expectations, a finite difference model was desired that explicitly included non-ideal effects, including axial conduction, parasitic heat loads, and material property variation with temperature and pressure. Nellis developed a finite difference numerical model that included all of these facets and was implemented in MATLAB [13] [14].

In its generalized form the model discretizes a heat exchanger and is set up to receive inputs that describe the specific heat exchanger. These include the number of transfer units on the supply and return sides, the axial conduction parameter, heat capacitance ratios, and parasitic heat loads. All are non-dimensionalized and can easily be configured to evaluate each element using the material properties associated with that element’s temperature. Figure 13 displays the discretization of the heat exchanger model.

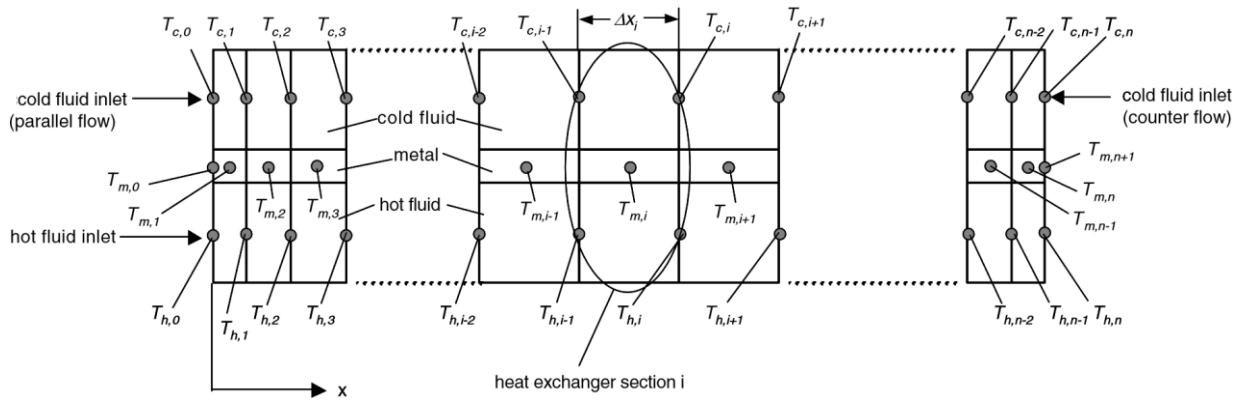

Figure 13: Discretization of the finite difference heat exchanger numerical model.

If computational efficiency is a concern, the grid can be concentrated near the ends, where the effects of axial conduction are most pronounced. For the stacked staggered slotted plate design, the model was configured to apply heat transfer and pressure drop correlations with the appropriate material properties and fluid velocities in each cell energy balance, one of which is depicted in Figure 14.

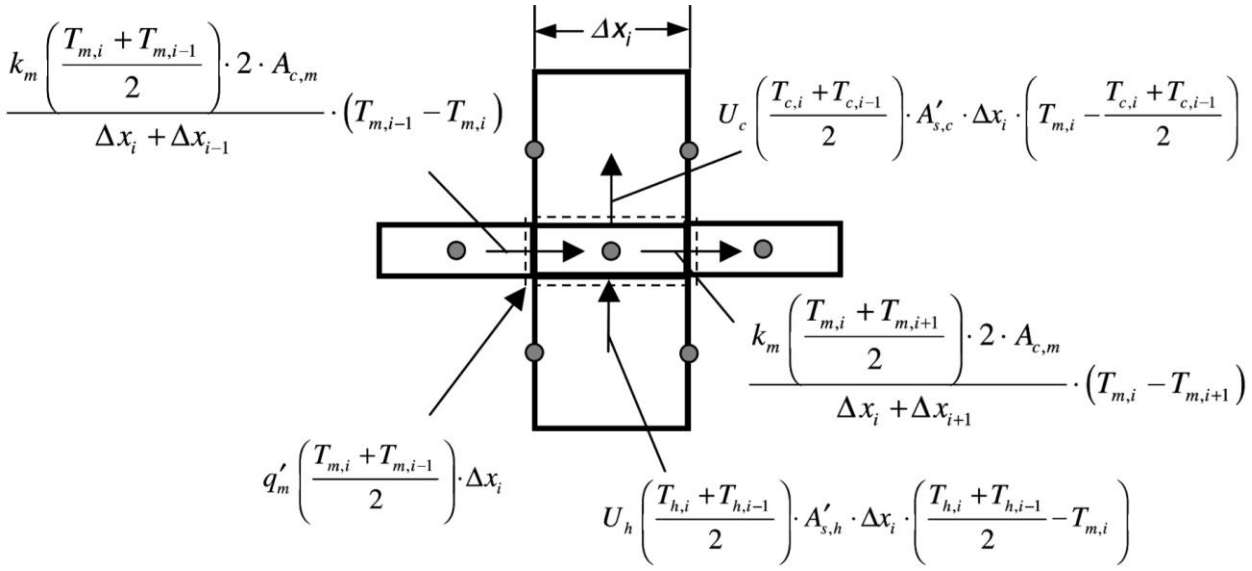

Figure 14: Energy balance terms applied to a single finite difference element.

Subscripts c and h denote the cold and hot fluid sides, and subscript m denotes the metal. U is the overall heat transfer coefficient, A_s' is the convection surface area per unit length, A_c is the axial conduction cross-sectional area, and Δx is the length of the element. In addition to the two conduction and two convection terms, there is a fifth term that handles parasitic heat loads. In this term, q_m' is the parasitic heat transferred into the metal per unit length.

The program solves for the temperature distribution using a sparse matrix decomposition and relaxation. Once the largest difference in dimensionless temperature between the previous solution and the current solution for all cells is less than the relaxation tolerance, the solution has converged. If not, the code takes a weighted average between the old and new solution to reform the sparse matrix and repeat the calculation until convergence is reached.

The numerical model has been validated by comparing its effectiveness-NTU predictions to those made by analytical solutions which consider axial conduction and parasitic heat loads individually. Figure 15 and Figure 16 display plots of the predicted ineffectiveness of a balanced, equal NTU-per-side heat exchanger with constant material properties as a function of NTU compared to the analytical solutions derived by Kroeger [11] and Chowdhury [15], respectively. Figure 15 displays the comparison of the model to Kroeger's solution for various values of the axial conduction parameter and assuming zero parasitic heat load.

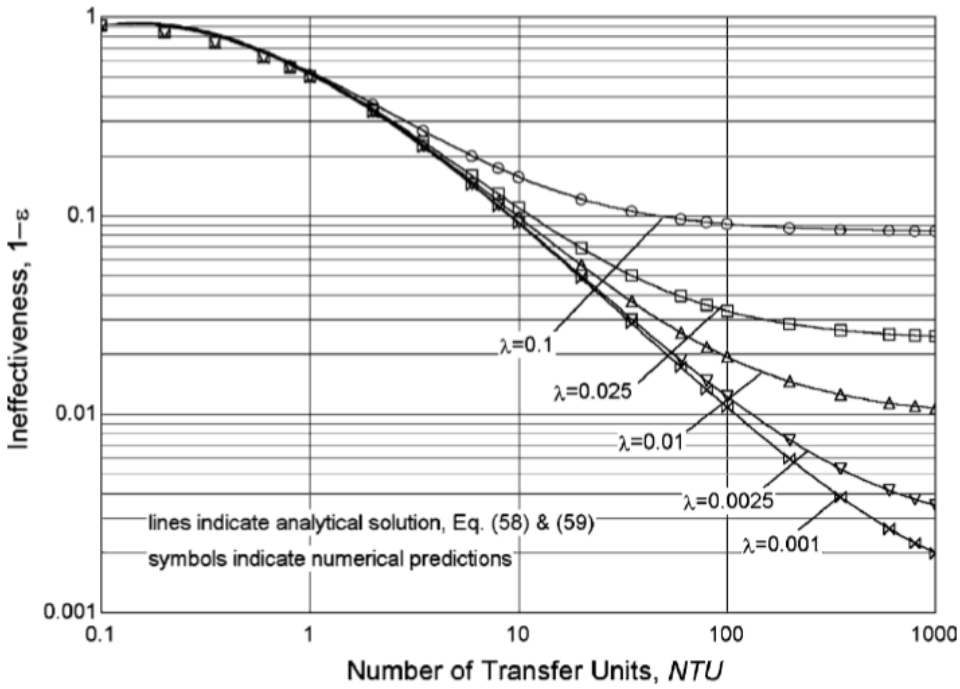

Figure 15: Validation of numerical model's ability to predict the effects of axial conduction based on comparison with Kroeger's solution.

Figure 16 displays the comparison of the model to Chowdhury's solution assuming zero axial conduction, for different values of the ratio of thermal conduction between the return fluid and the environment to the conduction between the supply and return sides.

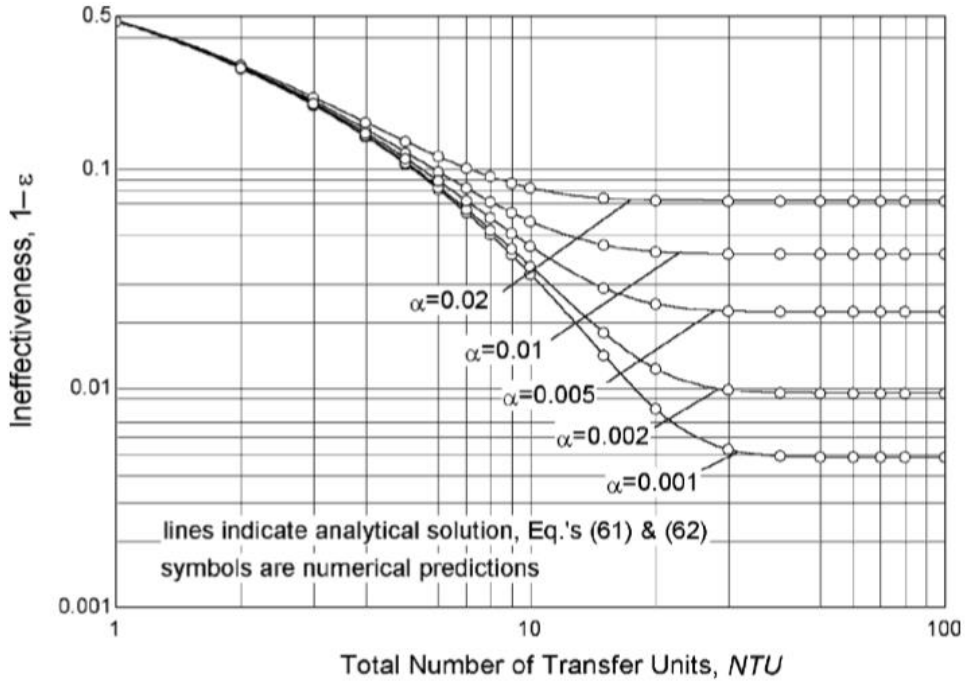

Figure 16: Validation of numerical model's ability to predict the effects of parasitic heat load based on comparison with Chowdhury's solution.

The agreement between the analytic and numerical solutions is excellent. The model in its general form can confidently be used as a tool to accurately predict the behavior of heat exchangers subject to axial conduction and parasitic heat loads.

This numerical model has a few key advantages over the effectiveness-NTU solution developed by Venkatarathnam. It allows for the inclusion of parasitic heat loads. Additionally, material property variations are included. Although Kroeger stated with confidence that average material properties will suffice, we were skeptical based on the large changes at cryogenic temperatures. For future work, the model also has the ability to adjust certain regions of the heat exchanger's geometry to maximize its performance. For example, at the cold end, the density increases by about a factor of four compared to the warm end. This reduces the velocity by a factor of 4 as well. It may be beneficial to adjust the fin geometry to be optimized for the velocity present in different regions of the heat exchanger. For the above reasons, the finite difference model was

used to model the heat exchanger, and the model was compared to the effectiveness-NTU solution of Venkatarathnam to confirm its accuracy.

4. Application of the Numerical Model to the SHI Heat Exchanger

4.1. Plate Geometry and Geometric Nomenclature

To describe the geometric attributes of the heat exchanger will require definitions of terminology. Figure 17 labels the geometric parameters for a single slotted plate and spacer with a coordinate system axis.

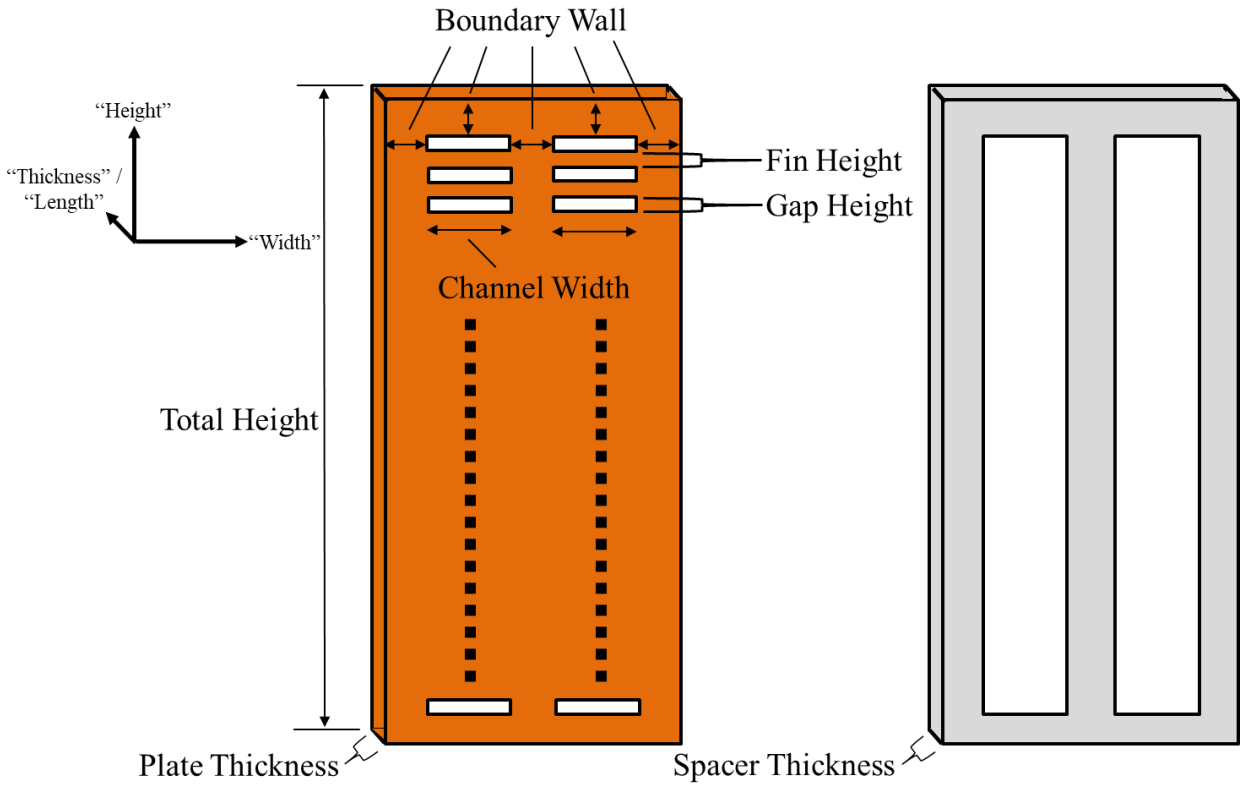

Figure 17: Geometric nomenclature used to describe the dimensions of the slotted plate geometry.

The plates and spacers will be stacked in the into-the-page direction to build up the total "length" of the heat exchanger. Helium flows in a counter-flow orientation normal to the page. The plate thickness and the fin thickness are equal. Boundary wall and channel widths for the spacer and slotted plate are also equal.

4.2. Overall Geometry and Size Constraints

The maximum allowable volume for this heat exchanger is about 0.1 m^3. The overall spatial dimension of the heat exchanger in any one direction cannot exceed 0.5 m. If all of the allowable space was utilized, the heat exchanger would be a cube with side lengths of slightly under 0.5 m. Its size will be limited in the "width" direction to prevent the fins from becoming too long, a condition that would result in a very low fin efficiency. Consequently, the heat exchanger would need to be "folded" into the width direction if the length is to exceed 0.5 m using re-headering manifolds. Figure 18 depicts the concept.

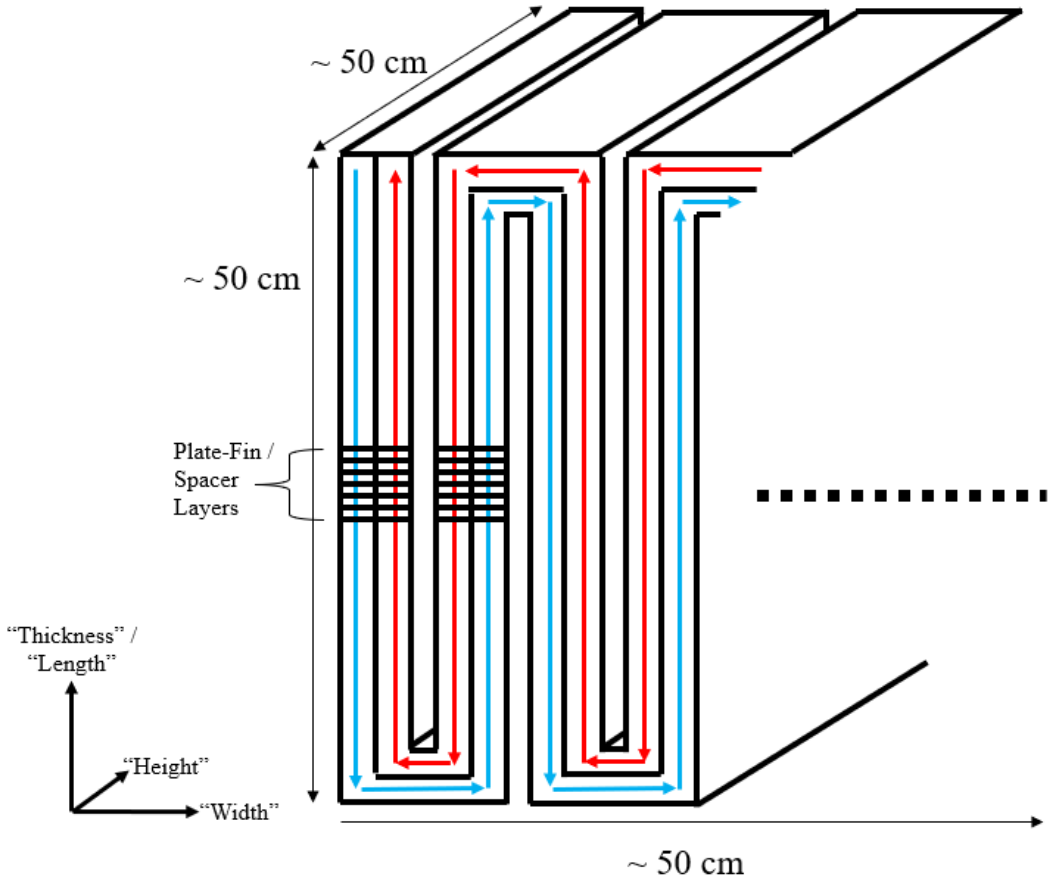

Figure 18: Heat exchanger packaging into prescribed dimension constraints.

Assuming rough estimates for the various geometric parameters, and material choices of copper for the finned plates and stainless steel for the spacers, the approximate weight of the device if the entire volume is used will exceed 600 lbs. This was far too heavy for SHI. It became apparent that this heat exchanger would be weight-limited rather than volume-limited. SHI prefers to consider designs only under 100 lbs.

4.3. Details of the Numerical Model

The MATLAB implementation of the numerical model described in the previous chapter can be found in Appendix A. Parameters that were varied in the study were read from a tab-delimited text file with each row containing a unique combination of the parameters. The

relaxation weighting factor was reduced to 0.4 to prevent convergence problems. The hot and cold side metal boundary conditions were set to adiabatic, and the inlet fluid temperatures and pressures were specified.

The code is arranged into separate functions that calculate the axial conduction parameter, the NTU for each side, and specify the parasitic heat loads, in each control volume. Calculations of the axial conduction parameter, NTU, and parasitic heat loads are performed for each control volume as though the entire heat exchanger were operating at the temperatures and material property values of that node, but they are scaled by the dimensionless length to account for the small contribution made by each individual control volume.

Temperature dependence of material properties was implemented by forming 6^{th}-order polynomials based on the values generated by EES property function calls, with 1000 temperature values evenly spaced over the 300 to 30 K temperature range [16]. For the fluid properties on the low and high pressure sides, the polynomial was generated assuming a constant pressure of 500 kPa and 2.6 MPa, respectively, because properties did not vary substantially over the allowable pressure range on a given side.

4.3.1. Non-Dimensionalization

In order to convert the energy balance to a non-dimensional form, the temperature and spatial position of the heat exchanger are scaled. The position x along the axial direction of the heat exchanger is scaled by the total stack length L of the heat exchanger core. Headers at each end are not modeled, and this position ignores any 180-degree turn seen in Figure 18 (e.g. position and L can exceed 50 cm). Subscript i denotes element number.

$$X_i = \frac{x_i}{L} \tag{13}$$

$$\Delta X_i = \frac{\Delta x_i}{L} \tag{14}$$

Computational efficiency was not a concern. Solutions with hundreds or thousands of nodes solved within seconds. Grid concentration at the ends to more efficiently capture the effects of axial conduction was therefore unnecessary, so a uniform grid was used.

Temperature T is scaled into non-dimensional temperature Θ by the amount that it exceeds the minimum temperature of the heat exchanger, $T_{c,in}$, compared to the maximum temperature difference of the heat exchanger.

$$\Theta_i = \frac{T_i - T_{c,in}}{T_{h,in} - T_{c,in}} \tag{15}$$

The hot and cold side heat capacity rates are scaled by the minimum of the two inlet heat capacity rates.

$$\mu_i = \frac{\dot{C}_{h,i}}{\min\left(\dot{C}_{h,in}, \dot{C}_{c,in}\right)} \tag{16}$$

$$\nu_i = \frac{\dot{C}_{c,i}}{\min\left(\dot{C}_{h,in}, \dot{C}_{c,in}\right)} \tag{17}$$

4.3.2. Axial Conduction Function

In general, the axial conduction parameter represents the ratio of heat conducted axially to the heat transferred between the two flow streams in the heat exchanger, which can be expressed in terms of the thermal resistance to axial conduction, R_{ac}, and the minimum fluid capacitance rate $\dot{C}_{min}$.

$$\lambda_i = \frac{1}{R_{ac,i}\dot{C}_{min}} \tag{18}$$

The overall axial conduction parameter for the heat exchanger is calculated using the total series thermal resistance of all plates and spacers.

$$R_{cu,i} = \frac{n_{plates} th_{plate}}{k_{cu,i} A_{c,cu}} \tag{19}$$

$$R_{ss,i} = \frac{(n_{plates} + 1) th_{spacer}}{k_{ss,i} A_{c,ss}} \tag{20}$$

$$\lambda_i = \frac{1}{\left(R_{cu,i} + R_{ss,i}\right) \dot{C}_{min}} \tag{21}$$

The cross-sectional areas are normal to the heat exchanger's axial direction. Copper plates are denoted by subscript cu, and 316 stainless steel spacers are denoted by subscript ss. The total copper plate metal cross-section, including the fins, was used when calculating the axial conduction contribution of the plates, rather than the smaller cross-section of the spacers, to be conservative. However, the choice makes little difference because the axial conduction parameter is dominated by the thermal resistance of the stainless steel spacers. Even though the copper thermal conductivity increases as temperature decreases by about a factor of 5, as seen in Figure 12, the overall axial conduction parameter is lower at the cold end because the stainless steel thermal conductivity decreases with temperature, also by about a factor of 5. Thermal resistance associated with the bonding interface between layers was not considered but should be miniscule, and its exclusion is conservative.

4.3.3. NTU Functions

Helium properties will be subject to temperature and pressure dependence. Attempts to include pressure dependence caused convergence problems. However, as seen in Figure 12, the properties of helium do not vary considerably on a given side between its inlet pressure and the exit pressure if the maximum allowable pressure drop on that side occurs. Therefore, the supply and return side pressures used for material properties were assumed to be constant, at 2.6 MPa and 0.5 MPa, respectively. For each side of the heat exchanger, 6^{th} order polynomials in temperature

were formed to express the material properties as a function of temperature at the appropriate pressure.

Although the difference between the metal and fluid temperatures in any given control volume was miniscule, the helium properties in each control volume were defined using the film temperature. Each control volume has a fluid inlet and outlet temperature associated with it, and a single metal temperature. So, the film temperature was defined as the average between the fluid inlet and outlet temperatures, averaged with the metal temperature.

$$T_{film,i} = \frac{\left(\frac{T_{fluid,i-1} + T_{fluid,i}}{2}\right) + T_{m,i}}{2} \tag{22}$$

Correlations for Nusselt number and Darcy friction factor were made using Fluent, the details of which will be described in the following sections. The chosen characteristic length was the hydraulic diameter of the gap between fins on a given slotted plate. In the limit of a wide duct, in which $W_{channel} >> H_{gap}$, the hydraulic diameter reduces to two times the smaller dimension.

$$D_h = \frac{4A_c}{Per} = \frac{4H_{gap}W_{channel}}{2(H_{gap} + W_{channel})} \cong 2H_{gap}$$

The Nusselt number was correlated on the Reynolds number, which was defined as:

$$Re_i = \frac{\rho_i \bar{V}_{gap,i} D_h}{\mu_i} \tag{23}$$

The chosen velocity was the average fluid velocity in the gap region between fins in a given slotted plate. The correlations for Nusselt number as a function of Reynolds number are used to convert back to an average convective heat transfer coefficient.

$$\bar{h}_i = \frac{\overline{Nu}_i k_i}{D_h} \tag{24}$$

The number of transfer units on each side was calculated using the total thermal resistance from the fluid to the center of the metal wall separating the two flow streams. When the NTU function is called by a node, a total heat exchanger UA is calculated as though the entire heat exchanger were operating under the conditions of that node. That total UA is then multiplied by the fraction of the heat exchanger length that is occupied by that control volume in the energy balance equations to get the individual contribution of each control volume, with its unique properties. The same applies to the axial conduction parameter function. The model has a separate NTU function for each side.

The fin parameter mL of the individual fins was calculated in the typical way:

$$(mL)_i = \sqrt{\frac{Per\bar{h}_i}{k_{cu,i}A_c}}W_{channel} \tag{25}$$

The individual fin efficiency η was calculated using the form associated with the assumptions made by Fleming [8].

$$\eta_i = \frac{1}{1 + \frac{((mL)_i)^2}{3}} \tag{26}$$

The fin efficiency modulates the thermal resistance of each individual fin.

$$R_{fin,i} = \frac{1}{\eta_i \bar{h}_i A_s} \tag{27}$$

The thermal resistance of all fins on one fluid side of one slotted plate is the parallel thermal resistance of the number of fins per side per slotted plate.

$$R_{all\ fins,i} = \frac{R_{fin,i}}{n_{fins}} \tag{28}$$

The thermal resistance of the metal boundary wall separating the two flow streams must also be included in the thermal resistance network. Half of the wall width is included in the hot side NTU function, and the other half in the cold side NTU function.

$$R_{base,i} = \frac{\left(\frac{b}{2}\right)}{k_{cu,i} H_{total} th_{plate}} \tag{29}$$

Where b is the stream-to-stream width dimension of the separating wall, and H_{total} is the total height of the separating wall. Arranging the thermal resistance of the fin bank in series with the base gives the total thermal resistance on one side of the slotted plate.

$$R_{plate,i} = R_{all\ fins,i} + R_{base,i} \tag{30}$$

Finally, the total thermal resistance associated with a total UA of the heat exchanger, as if the entire thing was operating with the properties associated with node i, is calculated by recognizing that the slotted plates are arranged as parallel thermal resistances.

$$R_{total,i} = \frac{R_{plate,i}}{n_{plates}} \tag{31}$$

The resulting total thermal resistance is non-dimensionalized into the number of transfer units, β.

$$\beta_i = \frac{1}{R_{total,i} \dot{C}_{min}} \tag{32}$$

Recall that this overall NTU, treating the model as though the entire heat exchanger were operating under the conditions present in node i, is scaled by the fraction of the total heat exchanger length that is occupied by node i to get the proper contribution from that node alone.

4.3.4. Parasitic Heat Load Function

Parasitic heat loads, denoted by χ, can be applied either to the hot side fluid, cold side fluid, or the metal, but the non-dimensionalization is the same for each case.

$$\chi_i = \frac{q_i' L}{\dot{C}_{min}\left(T_{h,in} - T_{c,in}\right)} \tag{33}$$

q_i' is the heat load per unit length of heat exchanger that is acting on either the hot fluid, cold fluid, or metal of a given control volume. The heat load can easily be defined as a function of temperature, for example to model radiation loads. It can also be applied only to certain control volumes, for example in locations where structural supports may result in localized conduction parasitic heat loads.

4.3.5. Non-Dimensional Boundary Conditions and Energy Balances

The problem is defined by the following dimensionless boundary conditions and energy balances. They describe adiabatic metal end conditions for a counter-flow heat exchanger.

Hot side fluid specified inlet temperature:

$$\Theta_{h,i=0} = 1 \tag{34}$$

Cold side fluid specified inlet temperature:

$$\Theta_{c,i=n} = 0 \tag{35}$$

Warm end adiabatic metal:

$$\Theta_{m,i=0} = \Theta_{m,i=1} \tag{36}$$

Cold end adiabatic metal:

$$\Theta_{m,i=n} = \Theta_{m,i=n+1} \tag{37}$$

And the energy balances are:

Metal:

$$\chi_m \Delta X_i + \frac{\beta_{h,i-1} + \beta_{h,i}}{2} \Delta X_i \left(\frac{\Theta_{h,i-1} + \Theta_{h,i}}{2} - \Theta_{m,i}\right) + \frac{[\lambda_i + \lambda_{i-1}]}{[\Delta X_i + \Delta X_{i-1}]}\left(\Theta_{m,i-1} - \Theta_{m,i}\right)$$
$$= \frac{\beta_{c,i-1} + \beta_{c,i}}{2} \Delta X_i \left(\Theta_{m,i} + \frac{\Theta_{c,i-1} + \Theta_{c,i}}{2}\right) + \frac{[\lambda_i + \lambda_{i+1}]}{[\Delta X_i + \Delta X_{i+1}]}\left(\Theta_{m,i} - \Theta_{m,i+1}\right) \tag{38}$$

Hot fluid:

$$\frac{\mu_{i-1}+\mu_i}{2}\Theta_{h,i-1}+\frac{\chi_{h,i}+\chi_{h,i-1}}{2}\Delta X_i = \frac{\mu_{i-1}+\mu_i}{2}\Theta_{h,i}+\frac{\beta_{h,i}+\beta_{h,i-1}}{2}\Delta X_i\left(\frac{\Theta_{h,i}+\Theta_{h,i-1}}{2}-\Theta_{m,i}\right) \quad (39)$$

Cold fluid:

$$\frac{\nu_i+\nu_{i-1}}{2}\Theta_{c,i}+\frac{\chi_{c,i}+\chi_{c,i-1}}{2}\Delta X_i+\frac{\beta_{c,i}+\beta_{c,i-1}}{2}\Delta X_i\left(\Theta_{m,i}-\frac{\Theta_{c,i}+\Theta_{c,i-1}}{2}\right) = \frac{\nu_i+\nu_{i-1}}{2}\Theta_{c,i-1} \quad (40)$$

where i = 1:n for all equations. The result is a set of 3n + 4 equations and unknown dimensionless temperatures which are solved for using sparse matrix decomposition and relaxation. Once the temperature profile has been determined, the effectiveness of the heat exchanger is calculated by integrating the heat transfer in each flow stream:

$$\dot{q}_h = \int_{T_{h,in}}^{T_{h,n}} \dot{C}_{h,i}\,dT_i \quad (41)$$

$$\dot{q}_c = \int_{T_{c,in}}^{T_{c,0}} \dot{C}_{c,i}\,dT_i \quad (42)$$

and comparing it to the maximum possible heat transfer that the heat exchanger would achieve if it operated perfectly:

$$\dot{q}_{max} = min\left[\int_{T_{c,in}}^{T_{h,in}} \dot{C}_{h,i}\,dT_i\,,\int_{T_{c,in}}^{T_{h,in}} \dot{C}_{c,i}\,dT_i\right] \quad (43)$$

to determine the effectiveness of the heat exchanger:

$$\varepsilon_h = \frac{\dot{q}_h}{\dot{q}_{max}} \quad (44)$$

$$\varepsilon_c = \frac{\dot{q}_c}{\dot{q}_{max}} \quad (45)$$

Note that the effectiveness of each side may not be equivalent in the presence of a parasitic heat load.

4.3.6. Pressure Drop

Like the convective heat transfer coefficient, the pressure drop calculations are also fluid property dependent. Correlations for Darcy friction factor as a function of Reynolds number were produced using Ansys Fluent, as will be described in the next section. Converting the friction factor back into a pressure drop for each control volume is accomplished using the Darcy-Weisbach equation.

$$\Delta P_i = \frac{f_i \Delta x_i \rho_i \bar{V}_{gap,i}^2}{2D_h} \tag{46}$$

where the velocity and hydraulic diameter are defined in the same manner as in the Reynolds number. The total pressure drop on each side is simply the sum of the pressure drops that occur within each control volume.

$$\Delta P_{total} = \sum_{i=1}^{n} \Delta P_i \tag{47}$$

5. Fluent Model

The friction factor and Nusselt number correlations used in the MATLAB model were generated from a parametric study performed in Ansys Fluent. The design study was specified in a table of design points in Ansys Workbench 19.2. Each row contained a unique combination of geometric values, mass flow rate, temperature, pressure, and the appertaining helium gas properties, which were the parametric inputs to the model. Each case was solved in series. The order in which the cases were solved was optimized automatically in Workbench, such that cases that shared a geometry were solved sequentially so the geometry did not need to be re-meshed as

often. The configuration of the Fluent model is best explained by describing each of the Ansys Workbench component systems: DesignModeler geometry, Ansys meshing, Fluent setup/solution methods, and CFD-Post post-processing.

5.1. Geometry

A small 3-D simulacrum of the staggered stacked slotted plate geometry with square cross-section fins modeled in Fluent is depicted in Figure 19.

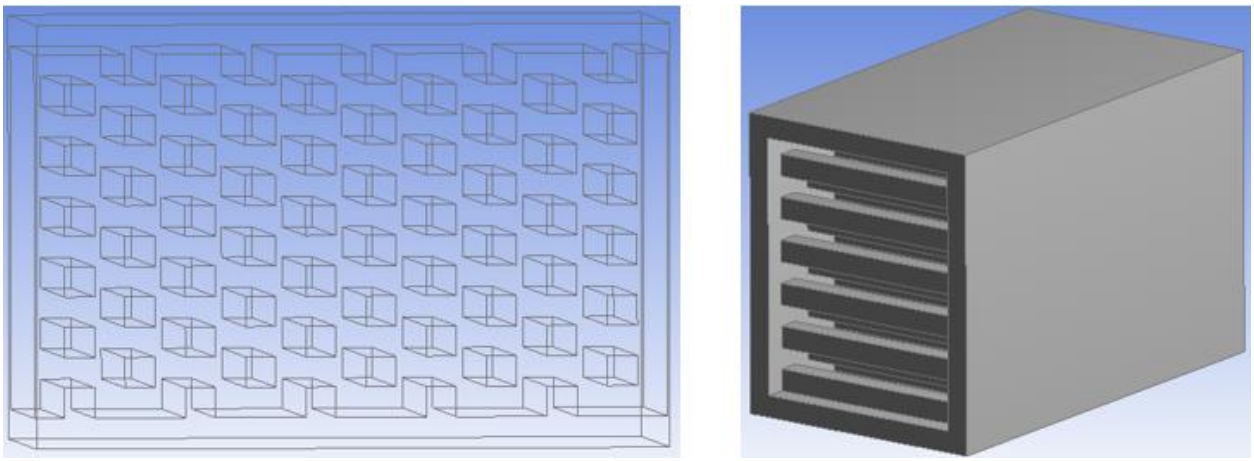

Figure 19: Example of the geometry in 3-dimensions represented in Ansys.

The length of the fins can be assumed to be long relative to the other dimensions. Therefore, the model was reduced to 2 dimensions and end effects were ignored. The fin geometry was entirely parameterized. The four geometric parameters are the fin height, gap height, fin thickness, and spacer thickness, shown in Figure 20.

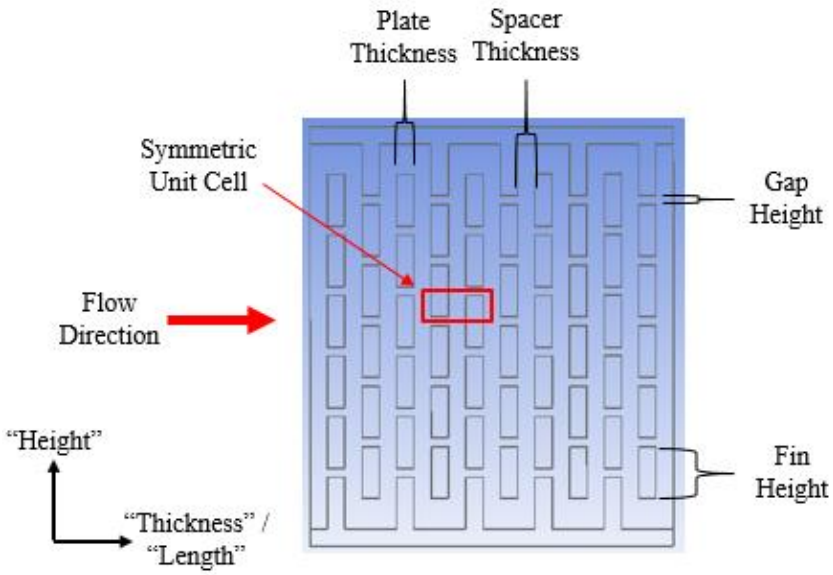

Figure 20: Example of the Ansys model in 2 dimensions, with geometric nomenclature labeled.

The size of the model was further reduced by modeling just one unit cell and applying the appropriate symmetry boundary conditions.

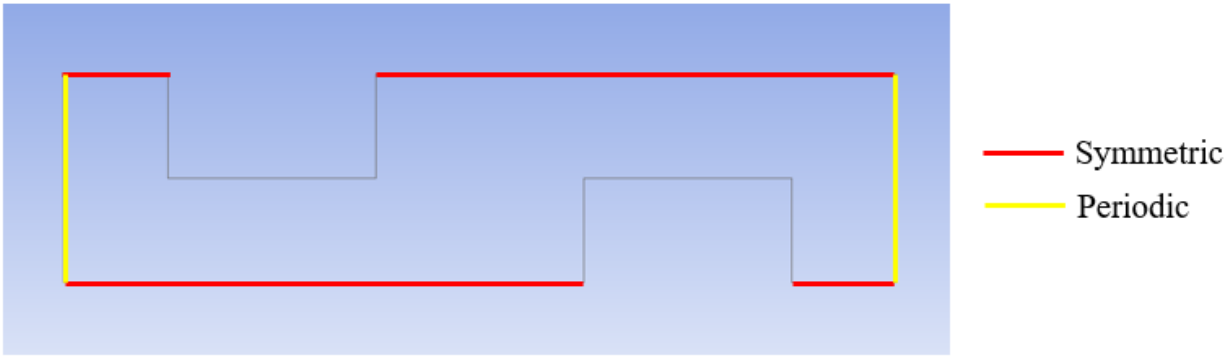

Figure 21: Example a single unit cell modeled in Ansys using symmetric and periodically symmetric boundary conditions.

Together with a specified mass flow rate, the periodic boundary condition constrained the inlet and outlet velocity profiles to be identical, simulating the flow conditions as if the geometry repeated infinitely in the periodic direction.

5.2. Meshing

A quadrilateral-dominated mesh was used to discretize the model, shown in Figure 22.

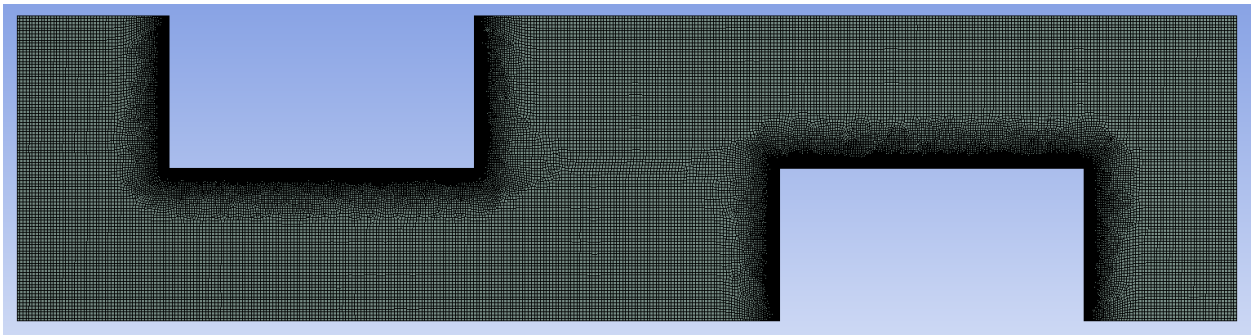

Figure 22: Typical meshing of the geometry.

Generally, quadrilaterals give superior accuracy compared to triangles by virtue of its extra face and vertex. The rectangular nature of the geometry allowed for a relatively structured mesh. To better capture the effects of the fluid interaction with the fin walls, element edge sizing was applied to the fin surfaces. The element size at the fin surface is $1/5^{th}$ of the bulk element size, and transitions with a growth rate of 1.05. Figure 23 provides a closer view of the mesh transition to the edge size.

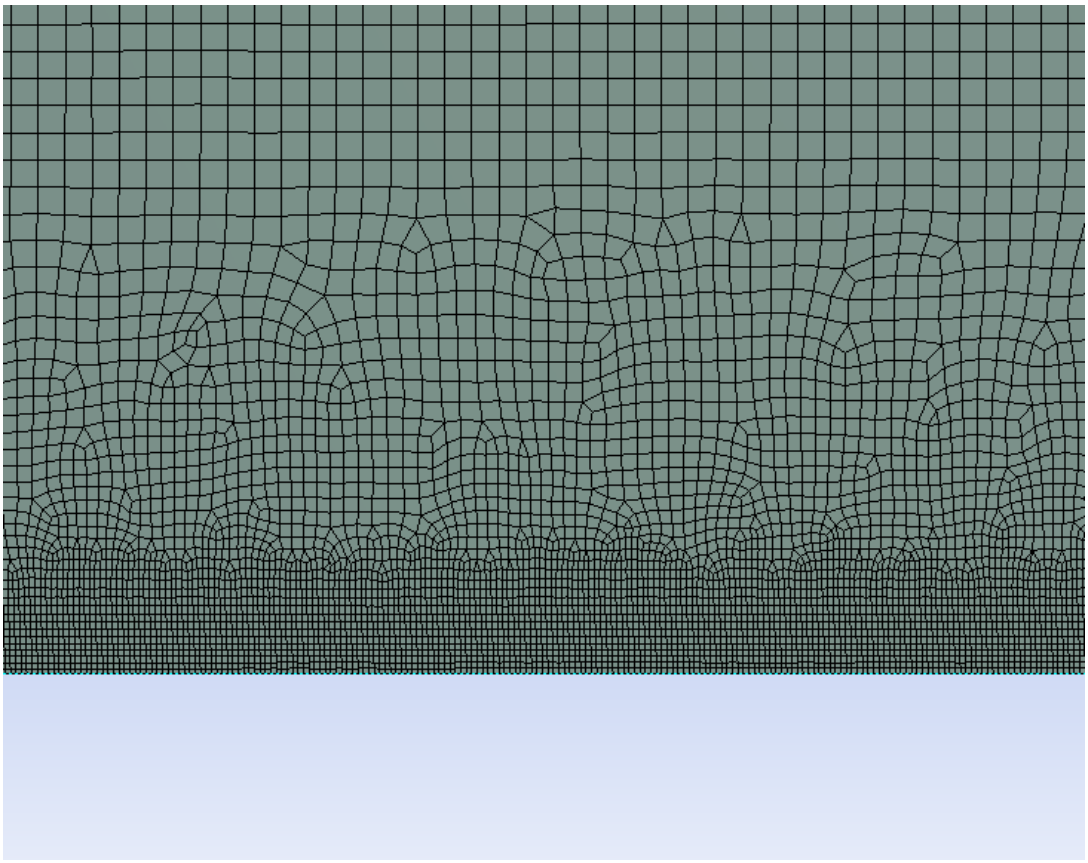

Figure 23: Transition to a refined mesh at the fin surface. Elements at the fin surface are smaller than in the bulk mesh by a factor of 5.

The size of the elements relative to the geometry was chosen based on a mesh sensitivity analysis which will be described in a subsequent section. However, the relative size of the elements compared to the geometry is the same for all geometries and results in about 44,000 elements in all cases.

5.3. Fluent Setup / Solution Methods

Figure 24 displays the boundary conditions for the single unit cell.

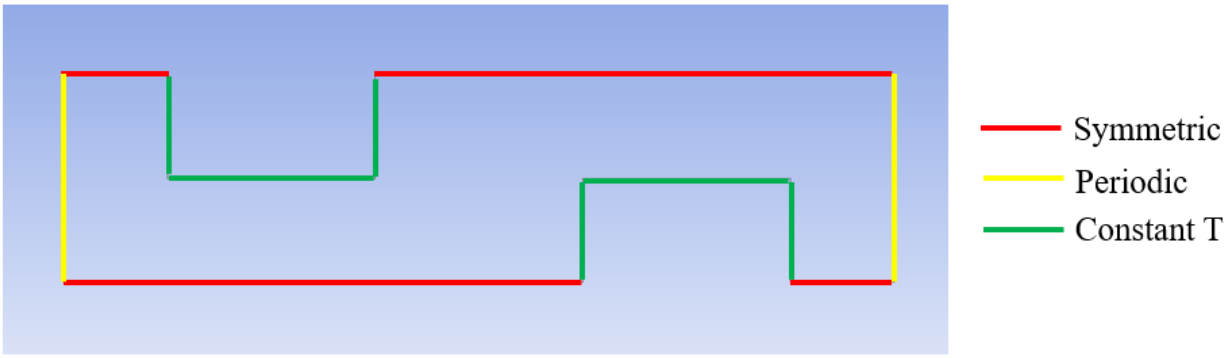

Figure 24: Fluent model boundary conditions.

The periodic boundary condition constrains the inlet and outlet velocity profiles to be identical, as if the domain were infinitely repeated in the periodic direction. It requires a specified mass flow rate through the unit cell, which is defined by a Fluent scheme procedure, typed directly into the text user interface (TUI). Scheme procedures are saved permanently into the Fluent file configuration, are executed for each design point, and provide a way to update certain variables that cannot be parameterized using the GUI. The following scheme procedure set the mass flow rate:

(lambda (value) (ti-menu-load-string (format #f "/define/periodic-conditions/massflow-rate-specification ~g" value)))

The mass flow rate variable was configured for use in scheme procedure 1, where “value” was the numerical value of the mass flow rate variable, defined in the row of the table of design points being solved.

The periodic boundary condition also takes the bulk upstream temperature as the mass flow weighted average temperature at the inlet, and calculates identical profiles for the inlet and outlet,

but the bulk outlet temperature is shifted by an amount corresponding to the heat transferred to the fluid from the fins. It too was set by a scheme procedure:

(lambda (value) (ti-menu-load-string (format #f "/define/periodic-conditions/massflow-rate-specification , , , ~g" value)))

“value” was replaced by the bulk upstream flow temperature variable value, which was configured for use in scheme procedure 2. The commas simply indicate to advance through 3 of the sequential settings to arrive at the bulk upstream flow temperature setting under the “/define/periodic-conditions/massflow-rate-specification” parent path.

The temperature difference between the fins and the inlet gas temperature was arbitrary to determine the convective heat transfer coefficient and was set to 1 K. EES was used to calculate the fluid properties for each case based on the inlet temperature and pressure. The miniscule pressure drop and temperature change across a single unit cell allowed the material properties to be set as constants.

The flow exhibited turbulent behavior, and as such a turbulence model is required. The Spalart-Allmaras model was chosen for a few reasons [17]. It was originally developed for solving wall-bounded flows, which matches the description of the flow conditions in stacked plate heat exchangers. It is a one-equation model that solves for a turbulent viscosity $\tilde{\upsilon}$ to close the Reynolds-averaged Navier-Stokes equations. The model is known for being highly stable due to its simple, one-equation formulation, which is desirable in this case because models with periodic boundary conditions are susceptible to convergence problems. It is also known to accurately solve in situations with large adverse pressure gradients. The staggered fins will have stagnation points on the front face, resulting in local adverse pressure gradients. Finally, the large number of

permutations that must be solved imposes a practical limitation on how fine the mesh can be. The version of the Spalart-Allmaras turbulence model in Fluent is a modified version of the original formulation that automatically opts to using wall functions if the mesh is too coarse near the wall to fully resolve the viscous sublayer. This trait makes the model particularly attractive for cases with limitations on the degree of fineness of the mesh such as this. The tuning constants of the model were kept at their default values.

The solution techniques were chosen based on a combination of recommended settings for the type of problem (steady state, incompressible, single phase flow) detailed in the Ansys Fluent 19.2 theory guide [17], and trial and error to see what produced the best solution behavior. For these types of flows, a coupled pressure-velocity solver is known to be more robust than the segregated options, and indeed produced the best convergence. Gradients were calculated using a least-squares cell based technique. The least-squares cell based and Green-Gauss node based gradient evaluations are similar in accuracy to one another, and both are superior to the Green-Gauss cell based option, but the least-squares technique is more computationally efficient. Pressure was calculated to second order for improved accuracy. The momentum and energy equations were solved using a 2^{nd} order upwind scheme.

Use of a pseudo-transient implicit under-relaxation method was recommended to expedite convergence while using a coupled solver. Trial and error of solution attempts resulted in the decision to reduce the pseudo-transient under relaxation factors. By default, the pressure, momentum, and energy factors are 0.5, 0.5, and 0.75, respectively, but were reduced to 0.3, 0.3, and 0.5. Fluent's advanced hybrid initialization technique was used to calculate a first guess for the velocity field, and proved to be much more stable and effective compared to the standard initialization technique. The average value between the bulk upstream and fin wall temperatures

was patched into the initial solution, superimposed upon the initial velocity profile, using the following scheme procedure:

(lambda (value) (ti-menu-load-string (format #f "/solve/patch () temperature ~g" value)))

“value” was replaced by the patch temperature variable value, which was configured for use in scheme procedure 3.

Figure 25 shows a characteristic convergence plot. In addition to the typical scaling of the residual, the residuals were normalized by dividing them by their maximum value within the first five iterations at the fifth iteration. This allowed for a simple definition of a convergence criterion. Depending on the specific geometry and flow conditions, the un-normalized residuals will have different values at their first few iterations. Solutions are typically considered converged once every equation’s residual has decreased by at least three orders of magnitude. By normalizing all residuals based on their values at an early iteration, a simple convergence criterion of scaled, normalized residuals under $1x10^{-3}$ is applicable to all cases, because all normalized residuals will start at order of magnitude 1.

The 2-D, single unit cell model was small and allowed large numbers of permutations to be solved quickly. Convergence was typically achieved in under 1000 iterations. The example shown in Figure 25 displays typical convergence behavior and reached the convergence criterion in 128 iterations over 73 seconds. Solution times vary from about 1 minute to up to 5 minutes.

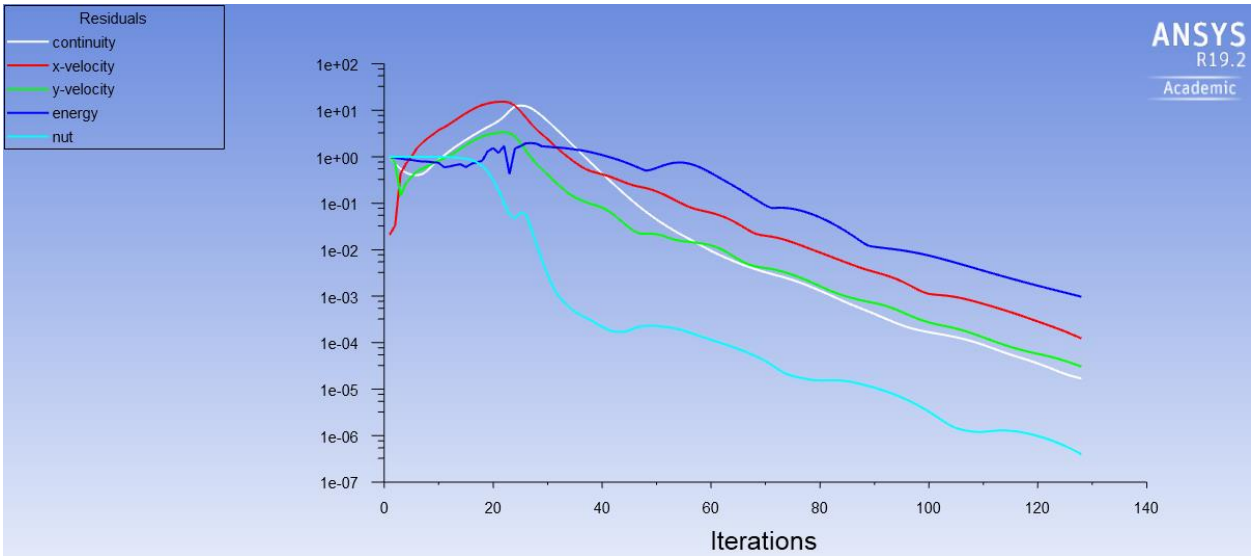

Figure 25: Typical convergence plot produced by the Fluent model.

5.4. CFD-Post Flow Visualization and Derived Quantities

The illustrations in this section were produced in CFD-Post with a bulk upstream helium temperature of 30 K, fin temperature of 31 K, nominal pressure of 2.6 MPa, and a mass flow rate that corresponds to the 10.5 g/s case for the entire heat exchanger, with 0.7625 mm plate thickness, spacer thickness, fin height, and gap height. Figure 26 show the velocity, temperature, and the periodic component of the pressure, respectively, with flow from left to right.

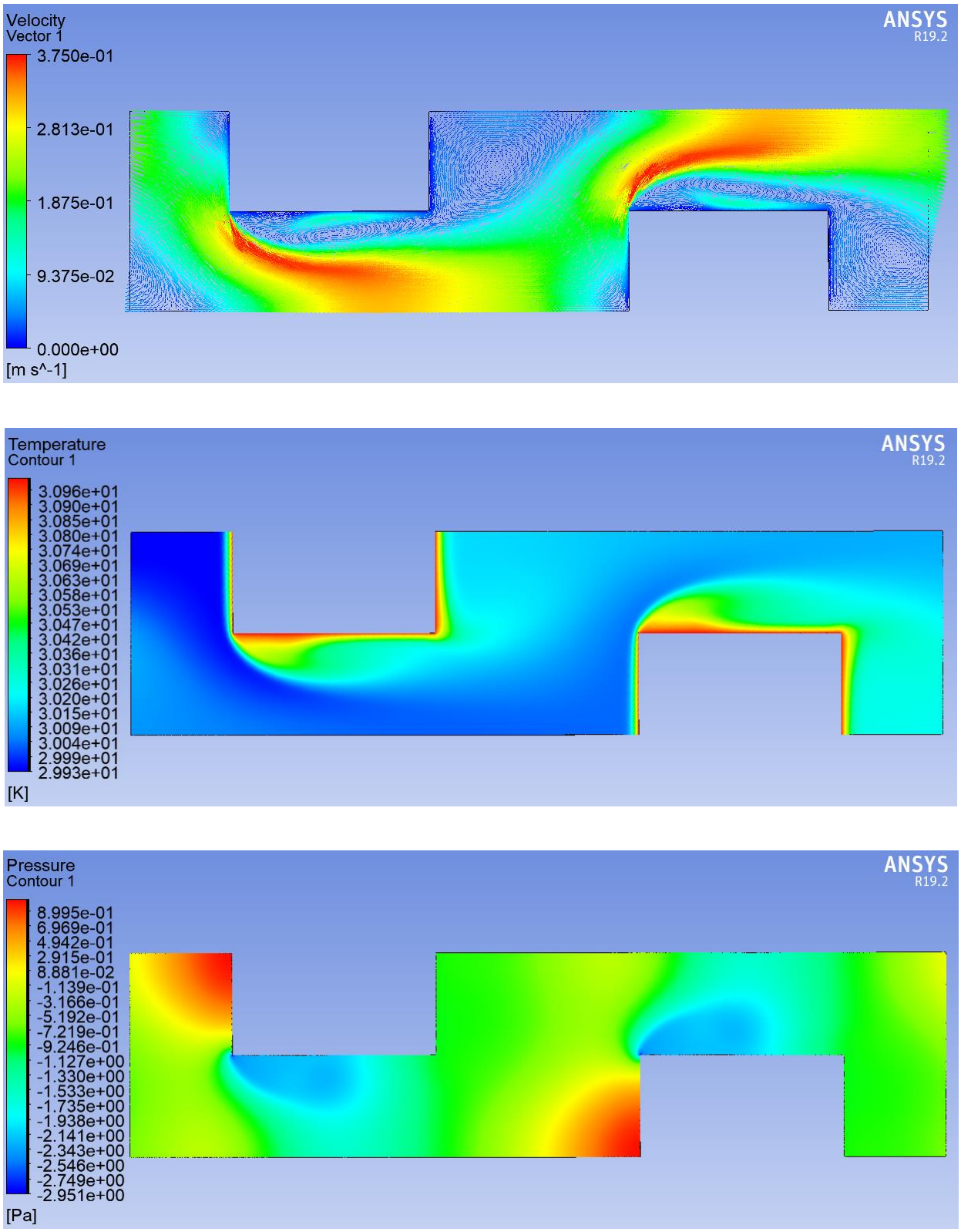

Figure 26: Velocity (top), temperature (middle), and periodic pressure component (bottom) for the H_{gap} = 0.7625 mm, T_{in} = 30 K, P = 2.6 MPa, $\dot{m}$ = 10.5 g/s, resulting in Re = 2105.

The behavior of the flow will be discussed in greater detail in a later section. The convective heat transfer coefficient was calculated by dividing the area-weighted average heat flux at the fin boundaries by the log mean temperature difference through the domain.

$$\bar{h} = \frac{\overline{\dot{q}''}}{\Delta T_{LM}} \tag{48}$$

When using a periodic boundary condition, Fluent decomposes the pressure gradient into a cyclically varying component and a constant pressure gradient in the periodic direction. Looking at just the periodic component, the average pressure at the inlet and outlet are identical. The linearly varying component represents the actual pressure gradient through the single unit cell domain, and is a direct output value of the solution.

5.5. Mesh Sensitivity Analysis

A mesh sensitivity analysis is imperative to ensure that the solution is not significantly dependent on element size. The design study covered a range of geometric sizes as well as combinations of temperature, pressure, and mass flow rate, which result in many different flow velocities. Higher Reynolds number cases demand a smaller element size to resolve the attributes of the flow. Ideally, the turbulent high Reynolds number cases capture the effects of the viscous sublayer, which is much thinner than the boundary layers of the laminar cases, but the modified version of the model in Fluent does not require it [17]. For these reasons, the mesh sensitivity analysis was performed on the highest Reynolds number case, and should be valid for all lower Reynolds number cases, provided that the relative size of the elements compared to the bulk geometry remains constant. The convective heat transfer coefficient and the pressure gradient are the quantities of interest that should not significantly vary with element size. The results for each quantity are displayed in Figure 27.

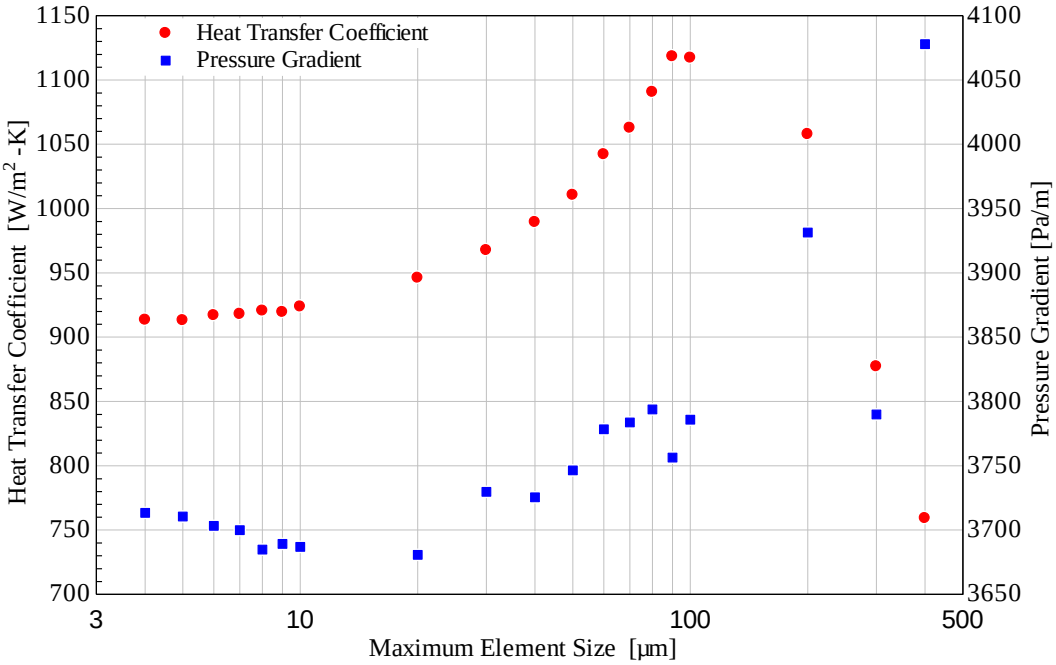

Figure 27: Convective heat transfer coefficient and pressure gradient for the highest Reynolds number case spanning over two orders of magnitude in maximum element size.

The variation of solution values of heat transfer coefficient and pressure gradient change by less than about 1% once the mesh size is about two orders of magnitude less than the geometric feature size. The geometric feature size was 1 mm at the highest Reynolds number case. It was desirable to use the coarsest mesh possible that still produced consistent results; the correlation development requires large numbers of permutations that take significant time to compute, and finer meshes exponentially increase solution time. For all geometries, the maximum element size was set to $1/100^{th}$ of the geometric feature dimension. For example, the maximum element size for all 1 mm cases was $1x10^{-5}$ m, with edge sizing to $2x10^{-6}$ m at the fin surfaces, whereas the 0.05 mm case was $1x10^{-7}$ m, with edge sizing to $2x10^{-8}$ m at the fin surface.

6. Correlation Development

6.1. Ideal Detailed Correlation Form

The four relevant geometric parameters are the slotted plate thickness, spacer thickness, fin height, and gap height.

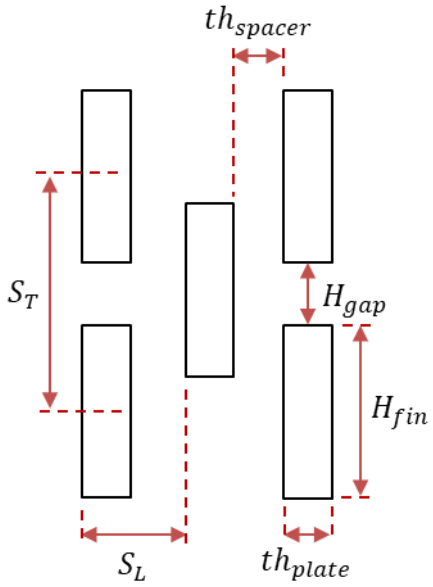

Figure 28: Correlation geometric parameters, including the dimensional longitudinal and transverse fin pitches.

These can be related to one another either explicitly or implicitly using three ratios. The ratio between the thickness of the spacer and slotted plate is similar to a dimensionless longitudinal fin pitch. The two differ only by a constant addition of 1, which has no impact on correlation.

$$\bar{S}_L = \frac{S_L}{th_{plate}} = \frac{th_{plate} + th_{spacer}}{th_{plate}} = 1 + \frac{th_{spacer}}{th_{plate}} \rightarrow \frac{th_{spacer}}{th_{plate}} \tag{49}$$

Likewise the ratio between the height of the gap between fins on a slotted plate and the height of the fins themselves is analogous to a dimensionless transverse fin pitch.

$$\bar{S}_T = \frac{S_T}{H_{fin}} = \frac{H_{fin} + H_{gap}}{H_{fin}} = 1 + \frac{H_{gap}}{H_{fin}} \rightarrow \frac{H_{gap}}{H_{fin}} \tag{50}$$

One more relationship is required to fully relate all four parameters, so the aspect ratio of the fin was chosen.

$$AR = \frac{H_{fin}}{th_{plate}} \tag{51}$$

Any other relationship between the four parameters can be expressed using two of these ratios.

The characteristic length and velocity used by most who have studied slotted plate heat exchangers are the hydraulic diameter of the gap between fins in a given slotted plate, and the average fluid velocity in the gap [9]. The gap is the minimum cross-sectional area, and the most applicable option for internal flow. The following definitions for dimensionless numbers result:

$$Re = \frac{\rho \bar{V}_{gap} D_h}{\mu} \tag{52}$$

$$f = 2\frac{D_h}{\rho \bar{V}_{gap}^2}\frac{dP}{dx} \tag{53}$$

$$\overline{Nu} = \frac{\bar{h} D_h}{k} \tag{54}$$

where $D_h = 2H_{gap}$.

Correlations could be developed using the following functional form:

$$\overline{Nu}(Re, \bar{S}_L, \bar{S}_T, AR) = a_0 Re^{a_1} \bar{S}_L^{a_2} \bar{S}_T^{a_3} AR^{a_4} \tag{55}$$

$$f(Re, \bar{S}_L, \bar{S}_T, AR) = b_0 Re^{b_1} \bar{S}_L^{b_2} \bar{S}_T^{b_3} AR^{b_4} \tag{56}$$

The equations can be linearized by taking the natural logarithm so the linear regression tool in EES could be used to solve for the best fit values of the correlation coefficients.

$$\ln\left(\overline{Nu}(Re, \bar{S}_L, \bar{S}_T, AR)\right) = a_0 + a_1 \ln(Re) + a_2 \ln(\bar{S}_L) + a_3 \ln(\bar{S}_T) + a_4 \ln(AR) \tag{57}$$

$$\ln\left(f(Re, \bar{S}_L, \bar{S}_T, AR)\right) = b_0 + b_1 \ln(Re) + b_2 \ln(\bar{S}_L) + b_3 \ln(\bar{S}_T) + b_4 \ln(AR) \tag{58}$$

The polynomial order for each term can be increased up to 6 to improve the fit between the correlation and data.

In total, correlations of this form consist of seven parameters: temperature, pressure, mass flow rate (which all impact the Reynolds number), plate thickness, spacer thickness, fin height, and gap height. With increasing numbers of parameters, the number of unique combinations of the parameters becomes exceedingly large, even with a small number of chosen values for each parameter, because the number of permutations scales like the number of values considered raised to the number of parameters power.

$$n_{permutations} = (n_{values})^{n_{parameters}} \tag{59}$$

Table 2 displays the number of permutations that result for different numbers of parameters and values considered.

		# Values Per Parameter						
		1	2	3	4	5	6	7
# Parameters	1	1	2	3	4	5	6	7
	2	1	4	9	16	25	36	49
	3	1	8	27	64	125	216	343
	4	1	16	81	256	625	1296	2401
	5	1	32	243	1024	3125	7776	16807
	6	1	64	729	4096	15625	46656	117649
	7	1	128	2187	16384	78125	279936	823543

Table 2: Resulting number of permutations for different numbers of parameters and numbers of values of each parameter.

To create detailed correlations that include the effects of each geometric parameter individually, use of the University of Wisconsin's Center for High Throughput Computing (CHTC) would be

required due to reduce computations times from months or years to days or weeks. It remains a promising option but is hampered by Ansys licensing issues at the time of this writing.

6.2. High Throughput Computing

The ideal design space for the Fluent model includes 7 design parameters (4 geometric, plus temperature, pressure, and mass flow rate). Solutions typically take on the order of 3 minutes to update. If each parameter takes on 5 values, the result is 78125 unique permutations, which would take over 5 months to solve. With 7 values, it would take nearly 5 years!

The University of Wisconsin Center for High Throughput Computing can drastically reduce the time required for large parametric studies by sending many iterations to a distributed campus-wide computing network known as HTCondor. As of June 2014, the CHTC allowed for about 960,000 hours per week of effective computational time. In practice, the effective number of computation hours per week that can be used to run Ansys in parallel is limited by the number of available licenses. Currently, there are 50 research licenses (with no element number limit) and 500 teaching licenses (limited to 512,000 elements). The models used in this study have about 44,000 elements, and can therefore use the teaching licenses. To ensure that some licenses are still available for other users, the CHTC administrators limit the number of teaching licenses a single CHTC user can occupy to 250. This effectively allows for 42,000 computation hours per week. Running 250 simulations in parallel, the time required to solve 78125 permutations would be reduced from about 5 months to less than 1 day.

Unfortunately, at this time the CHTC is not configured correctly to access the teaching licenses. Until the problem is solved by the CHTC administrators, the CHTC is not worth using and the number of design parameters must be reduced instead. It is still worthwhile to discuss the usage of the CHTC for future reference and use when the teaching licenses become available.

Figure 29 displays the general flow path of data from a single local computer to the HTC cluster. Each unsolved Fluent file on the local computer is known as a job. A submission file tells HTCondor about the jobs that need to be executed and what program will be needed to run the jobs. HTCondor then assigns computers on the campus cluster to handle and solve jobs remotely before sending the return data back through HTCondor to the local computer.

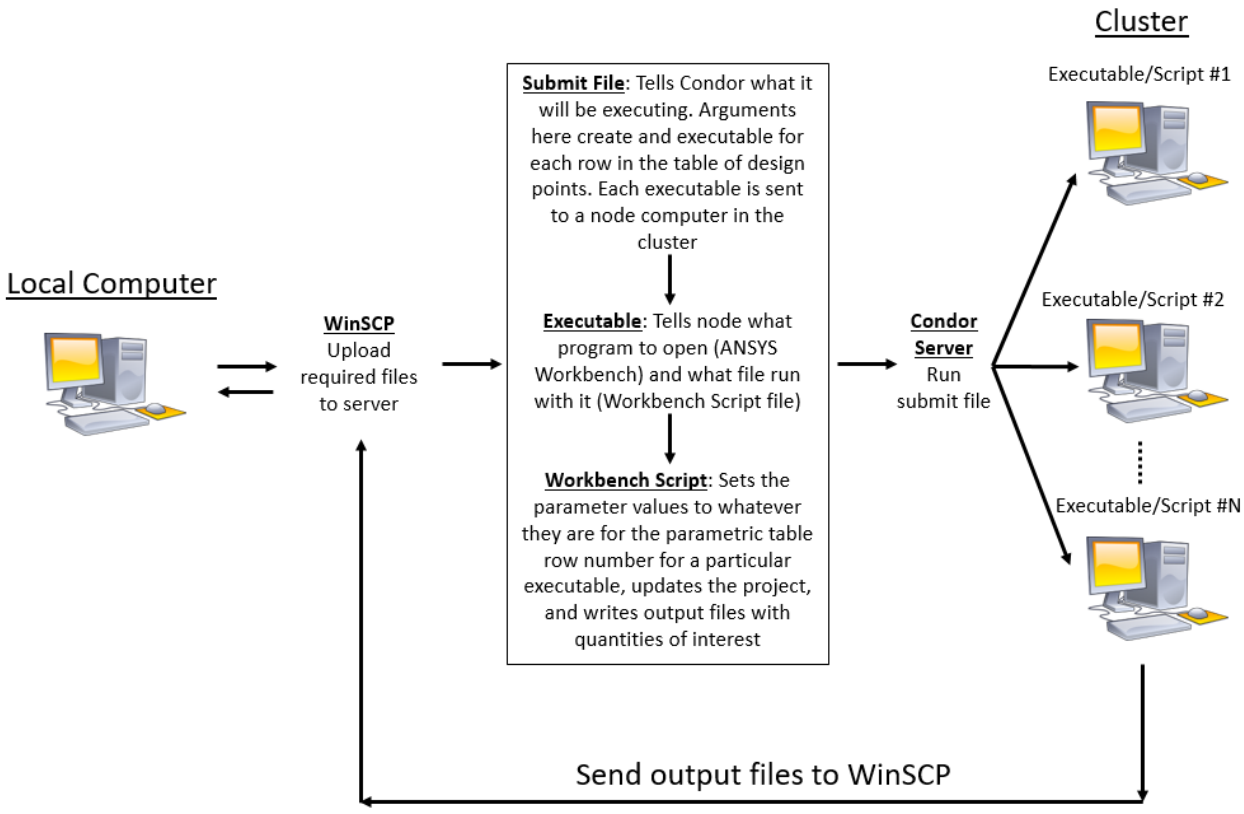

Figure 29: Components of the interface between a local computer and the University of Wisconsin high throughput computing cluster.

The submission, executable, and workbench python script files can all be found in the appendix, as well as the python script used to process the individual text-based output files into a single amalgamated file. These codes are all fully functional and ready for use as soon as the teaching

licenses are made available. More information on how to use the CHTC can be found on the University of Wisconsin CHTC website [18].

6.3. Practical Limited Correlations

It was necessary to reduce the number of parameters so that the correlations could be developed by running cases in series on a single computer, rather than thousands in parallel on the CHTC. As will be discussed in a later section, photochemical etching is likely the best manufacturing option to produce the plates, which places further constraints on the relative dimensions of certain geometric features. Fotofab, a manufacturing company based in Chicago, Illinois, with experience fabricating slotted plate heat exchangers, lays out the limitations of the process in their design guide [19], which are essentially universal throughout the industry.

The minimum manufacturable slot width (gap height) is between 90% - 120% of the base material thickness. The minimum dimension for the material separating slots, known as the “bar width” (or, for the slotted plate geometry, the fin height), is 90% of the base metal thickness. For a given plate thickness, the surface area per unit volume is maximized by etching the most slots into the plate as possible. In other words, it is optimal to use the thinnest possible slot width and bar widths. Consequently, the plate thickness, slot width, and bar width are all about the same value, which reduces the number of parameters that need to be varied by 2. For the sake of simplicity, the spacer thickness was also set to the same value to remove another parameter. This singular value for the dimensions of the heat exchanger’s miniature features will hereafter be referred to as $L_{micro.}$

The maximum allowable pressure drop prescribed by SHI are 300 kPa and 100 kPa for the supply and return sides, respectively. They are small relative to the operating pressures of 2.6 MPa and 500 kPa, and result in minimal property variation on a given heat exchanger side, as seen prior

in Figure 12. To further reduce the number of permutations, rather than producing a single correlation with many pressure values that span from 400 kPa to 2.6 MPa, a pair of correlations were made, with one using properties for a constant pressure of 500 kPa, and the other for 2.6 MPa.

The result of these constraints reduced the total number of parameters from 7 down to 3: characteristic length, mass flow rate, and temperature, plus two values for pressure which doubles the $(n_{values})^3$ permutations. The effects of all of these parameters, including the effects of pressure and temperature on fluid properties and velocity, were accounted for in the definition of the Reynolds number. The correlation form was the same, but now with the Reynolds number as the only independent variable. Accuracy was improved by increasing the polynomial order to 6.

$$\ln\left(\overline{Nu}(Re)\right) = a_0 + a_1 \ln(Re) + a_2 \ln(Re)^2 + a_3 \ln(Re)^3 + a_4 \ln(Re)^4 + a_5 \ln(Re)^5 + a_6 \ln(Re)^6 \quad (60)$$

$$\ln\left(f(Re)\right) = b_0 + b_1 \ln(Re) + b_2 \ln(Re)^2 + b_3 \ln(Re)^3 + b_4 \ln(Re)^4 + b_5 \ln(Re)^5 + b_6 \ln(Re)^6 \quad (61)$$

The Fotofab etching design guide lists the minimum possible slot dimension as 0.102 mm [19]. Creare constructed a prototype heat exchanger with fins and etched slots dimensions of 0.064 mm [20]. Some leeway was added into the correlations by setting the minimum slot size to 0.05 mm. Based on the discussions in this section, this means that the minimum plate thickness, bar width (fin height), and spacer thickness will all also be 0.05 mm.

Choosing the maximum value of L_{micro} was a trial and error process. Correlations were first made using broad ranges. The results of the MATLAB model heat exchanger performance using the broad correlations provided an idea of the viable range of values for L_{micro}. A subsequent set of correlations were then made with a tighter range of L_{micro} that produced performance more

within the desired range. Designs with L_{micro} greater than about 1 mm performed poorly, so the maximum value of L_{micro} was set to 1 mm to create the final correlations.

It is important to note that Fluent assumes a unit length of 1 meter for the depth of 2-D models. While arbitrary, it must be considered when choosing or evaluating certain properties, such as the mass flow rate. The mass flux in the Fluent model inlet with an assumed 1 meter depth must match the mass flux that would occur in the physical heat exchanger with a given channel width to result in matching velocities between the model and the physical 3-D geometry. To determine the required inlet mass flow rate for the Fluent model under a given set of geometric conditions, the physical mass flow rate must be scaled by the ratio of the model to physical cross-sectional areas.

$$\frac{\dot{m}_{2D}}{A_{c,2D}} = \frac{\dot{m}_{3D}}{A_{c,3D}} \tag{62}$$

$$\frac{\dot{m}_{2D}}{\left(\frac{H_{gap}}{2} + \frac{H_{fin}}{2}\right)(1\ [meter])} = \frac{\dot{m}_{3D}}{H_{total} W_{channel}} \tag{63}$$

$$\dot{m}_{2D} = \dot{m}_{3D} \frac{\left[\left(\frac{H_{gap}}{2} + \frac{H_{fin}}{2}\right)(1\ [meter])\right]}{H_{total} W_{channel}} \tag{64}$$

Although the 2-D Fluent model does not explicitly account for the channel width into the excluded third dimension, a range of good values for the channel width also needed to be determined in the same trial-and-error manner as L_{micro} because it is explicitly modeled in the MATLAB simulation, and has a bearing on the fluid velocity associated with each mass flow rate and the overall range of velocities expected. Trial and error revealed that a good range for $W_{channel}$ was between 5 to 50 mm. The actual range of mass flow rate ($\dot{m}_{3D}$) is set by SHI's design specifications. As will be discussed later, an overall heat exchanger size in the height direction of

H_{total} = 0.5 m will always produce the best performance. So the range of 2-D Fluent model mass fluxes that will result in the same range of 3-D MATLAB model mass fluxes (and, crucially, equal velocities for each case), is bounded by:

$$\dot{m}''_{2D,min} = \frac{\dot{m}_{3D,min}}{H_{total} W_{channel,max}} \tag{65}$$

$$\dot{m}''_{2D,max} = \frac{\dot{m}_{3D,max}}{H_{total} W_{channel,min}} \tag{66}$$

5 values were chosen for each parameter, with the exception of pressure, which was set to the two nominal pressures. Table 3 summarizes the values chosen for all parameters. The result was 2 x 125 = 250 unique combinations of inputs to the Fluent model.

		Values				
Parameter	L_{micro} [mm]	0.05	0.2875	0.525	0.7625	1
	$\dot{m}_{2D}$'' [kg/m^{2}s]	0.24	1.38	2.52	3.66	4.80
	T [K]	30	97.5	165	232.5	300
	P [MPa]	0.5			2.6	

Table 3: Numerical values chosen for each component of the parametric study.

Figure 30 displays the Reynolds number as a function of dimensionless axial position in the heat exchanger for the highest and lowest Reynolds number configurations. Position 0 corresponds to the warm end, and 1 corresponds to the cold end.

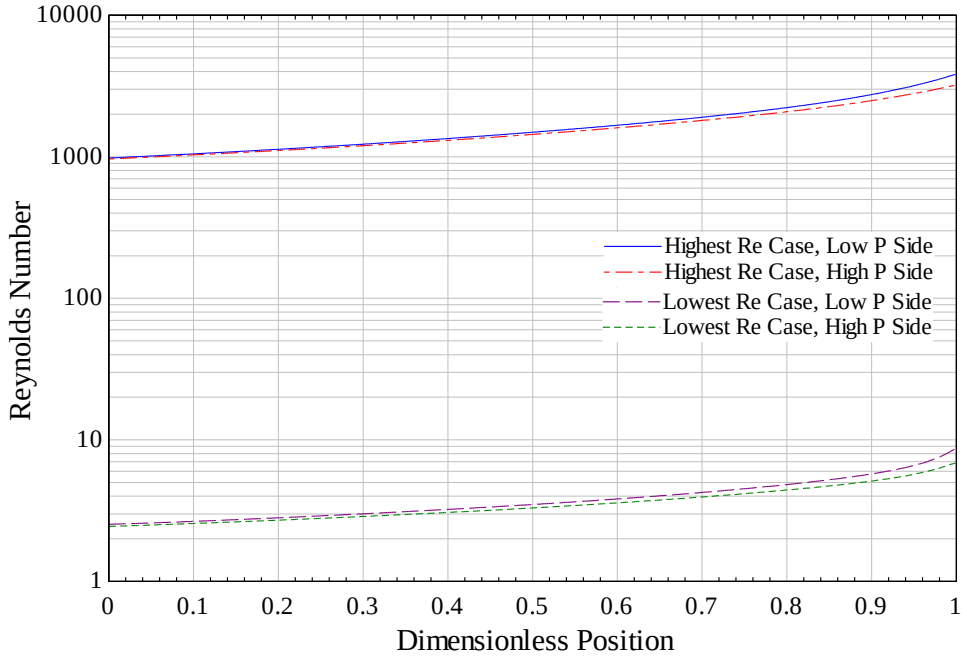

Figure 30: Reynolds number variation with axial position in the heat exchanger for the minimum and maximum Reynolds number configurations.

All other cases followed nearly parallel lines between these two extremes. The Reynolds number on each side was about the same despite the large difference in pressure between the two sides. The density difference that resulted from the pressure difference was offset by an accompanying change in fluid velocity. Consequently, the correlation on each side was nearly the same. The Reynolds number at the cold end was greater than at the warm end by nearly a factor of 4 for all cases.

After solving all Fluent permutations, the EES linear regression tool was used to determine the best fit coefficients for each correlation. The coefficients are displayed Table 4.

	Correlation Coefficient Order						
	0	1	2	3	4	5	6
Nu, P=0.5 MPa	1.40182	-0.57310	0.68494	-0.23773	0.04147	-0.00359	0.00012
f, P=0.5 MPa	9.87192	-12.58010	9.03582	-3.34372	0.63226	-0.05830	0.00208
Nu, P=2.6 MPa	1.61900	-1.00786	0.98924	-3.41092	0.05990	-0.00525	0.00018
f, P=2.6 MPa	9.80181	-12.46452	8.97123	-3.32701	0.63012	-0.05816	0.00208

Table 4: Coefficients for the 6th order polynomial correlations of Nusselt number and friction factor at the nominal helium pressure of each side of the heat exchanger.

Figure 31 through Figure 34 show the degree of agreement between the data generated by the Fluent models and the predictive correlations. Because the correlation is linearized, a perfect agreement between the predictions and the data would fall on a straight line with a slope of 1.

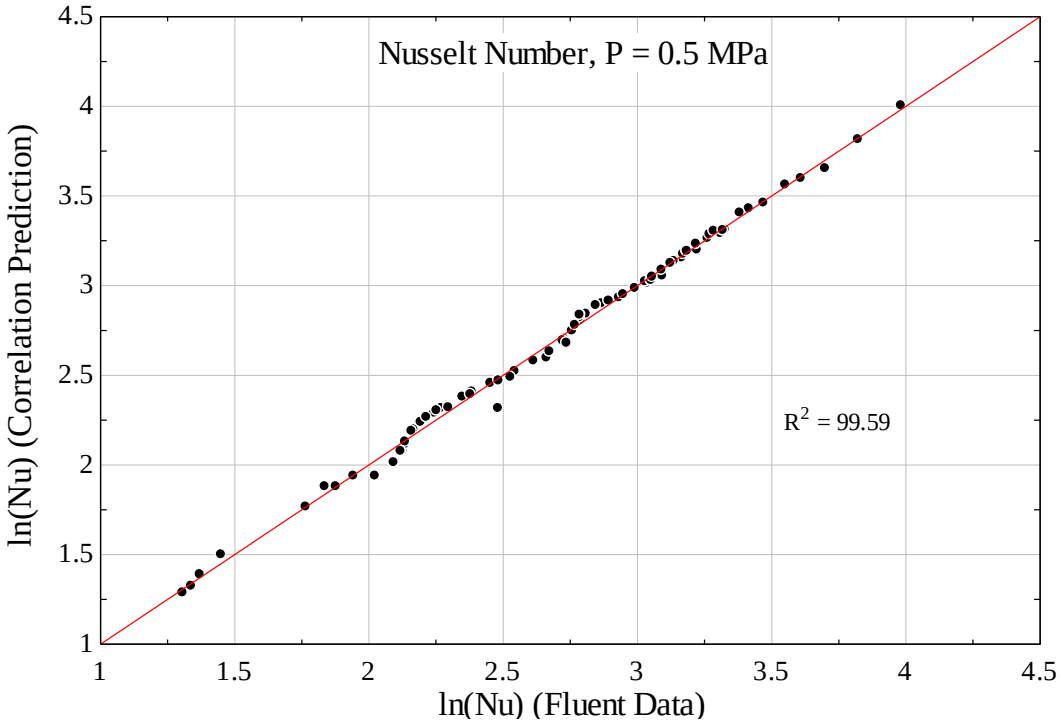

Figure 31: Predicted vs. Fluent-calculated Nusselt number for the P = 0.5 MPa side.

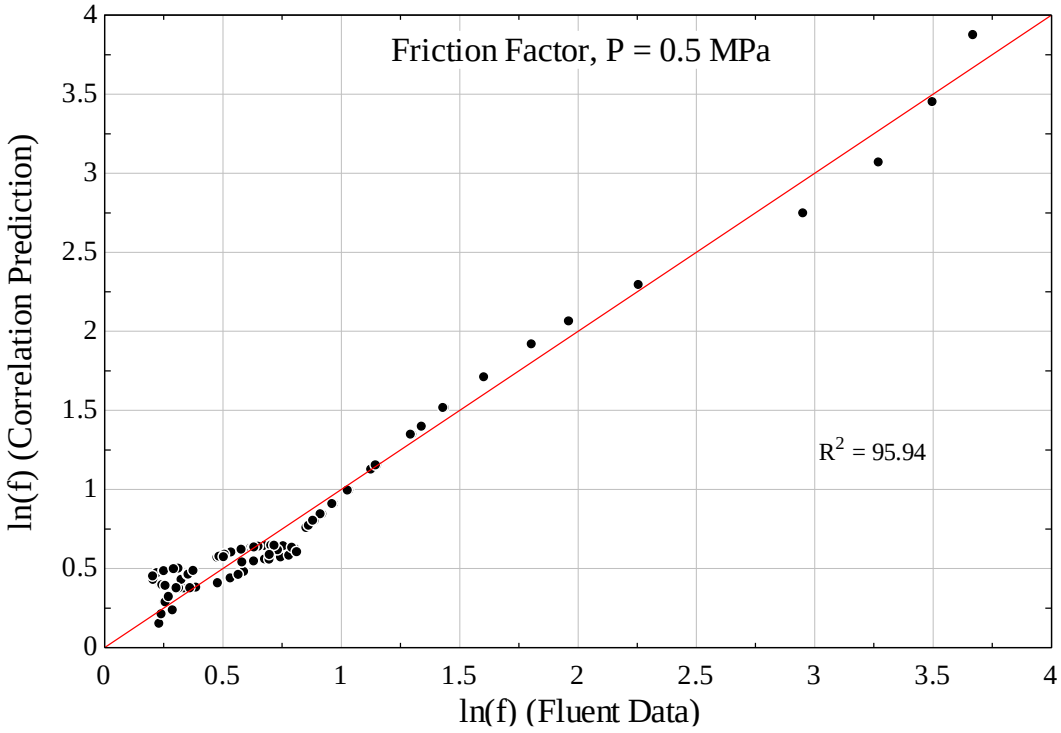

Figure 32: Predicted vs. Fluent-calculated friction factor for the P = 0.5 MPa side.

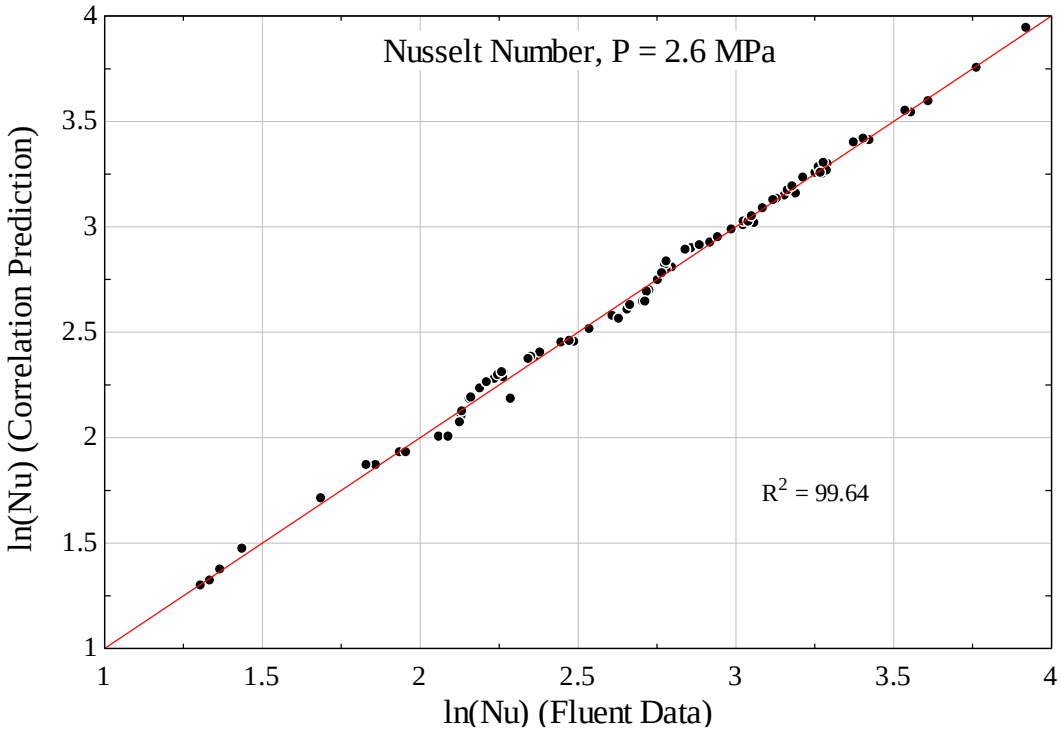

Figure 33: Predicted vs. Fluent-calculated Nusselt number for the P = 2.6 MPa side.

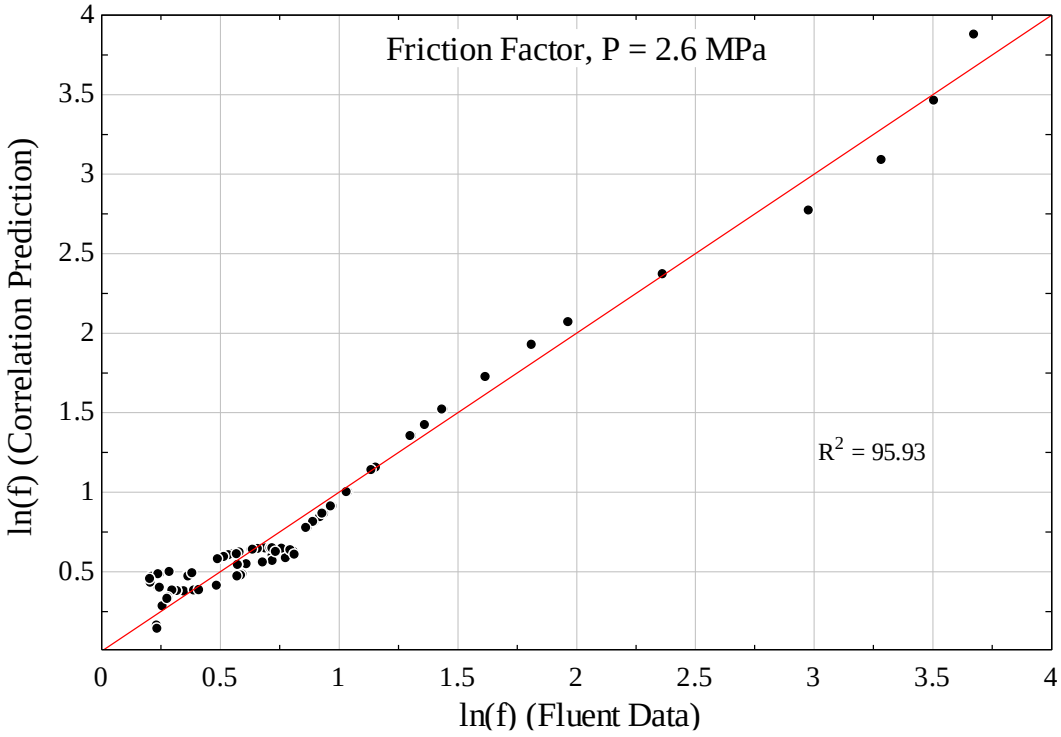

Figure 34: Predicted vs. Fluent-calculated friction factor for the P = 2.6 MPa side.

The differing pressure between the two sides did not result in substantial differences between their respective correlations. Generally, the agreement is good, especially for the Nusselt number, which has coefficients of determination around 99.6. The friction factor is not predicted as accurately by the correlations, with coefficients of determination just under 96. The most egregious data point has a calculated friction factor of about 1.22 (corresponding to ln(f) = 0.2, roughly), but the correlation predicts a friction factor under those conditions of about 1.57 (corresponding to ln(f) = 0.45). However, the majority of points achieve better agreement.

6.4. Comparison to Other Slotted Plate Correlations

The Fluent correlations can be compared to others that are in some ways suitable to stacked slotted plate heat exchangers. As a rough first estimate, the Fluent correlations can be compared to the developing duct flow correlations found in EES under the non-dimensional duct flow

function [16]. They will be most accurate in the gaps between fins, but in no way account for the effects of the plate staggering or spacers. More applicable experimental correlations were developed by Mikulin et al. [2] for stacked, staggered plates with rectangular slots. The Reynolds number and characteristic length used by Mikulin are identical to the Fluent model choice, with the exception of the exclusion of the factor of 2 in the hydraulic diameter. This discrepancy is adjusted for in the comparison. In the following equations, $D_{h,Mikulin}$ will refer to the hydraulic diameter defined as simply H_{gap} rather than $2H_{gap}$. The Reynolds number in the heat exchanger is expected to range from as low as 2.4 to as high as 4,000, depending on the geometry, pressure, temperature, and mass flow rate (with the factor of 2 retained in the definition of hydraulic diameter).

6.4.1. Darcy Friction Factor

Mikulin characterized flow friction using a "coefficient of hydraulic resistance", ξ, rather than the typical Darcy friction factor. The coefficient was experimentally determined using the relationship:

$$\xi = \frac{\Delta P}{n_{plates}\rho \bar{V}_{gap}^2} \tag{67}$$

The correlation for the coefficient of hydraulic resistance was created by amending the coefficient of hydraulic resistance of a singular slotted plate, ξ', found in the Handbook of Hydraulic Resistance [21], section 8-4 diagram 8-1.

$$\xi = \xi' \left[1 + 0.18\left(\frac{th_{spacer}}{H_{gap}}\right)^{-1.58}\right], \qquad \xi' = [0.707(1-p)^{0.5} + (1-p)]^2 \tag{68}$$

In the above expression, p is the porosity of the plate. Interestingly, it is an expression independent of the Reynolds number and only dependent on the relative size of the flow passage in the spacers

to the gap between fins. The coefficient of hydraulic resistance is related to the Fanning friction factor [9]:

$$\xi = 2f_{Fanning}\frac{(th_{plate} + th_{spacer})}{D_{h,Mikulin}} \tag{69}$$

The length used is the sum of the plate and spacer thicknesses, because there is one spacer for each slotted plate, and the hydraulic resistance is on a per-plate basis. As noted, Mikulin dropped the factor of 2 in his definition of the hydraulic diameter. The Reynolds number used in the Fluent and duct flow correlations is therefore twice the Reynolds number used in Mikulin's correlation.

$$Re_{Fluent} = \frac{\rho\bar{V}_{gap}D_{h,Fluent}}{\mu} = \frac{\rho\bar{V}_{gap}(2D_{h,Mikulin})}{\mu} = 2Re_{Mikulin} \tag{70}$$

The Darcy friction factor is 4 times the Fanning friction factor.

$$f = 4f_{Fanning} \tag{71}$$

As a check, these equations can be rearranged into the more familiar Darcy-Weisbach equation.

$$\xi = \frac{\Delta P}{n_{plates}\rho\bar{V}_{gap}{}^{2}} = 2f_{Fanning}\frac{(th_{plate} + th_{spacer})}{D_{h,Mikulin}}$$

$$\frac{\Delta P}{n_{plates}(th_{plate} + th_{spacer})} = 2f_{Fanning}\frac{\rho\bar{V}_{gap}{}^{2}}{D_{h,Mikulin}}$$

$$\frac{\Delta P}{n_{plates}(th_{plate} + th_{spacer})} = f\frac{\rho\bar{V}_{gap}{}^{2}}{2D_{h,Mikulin}} \tag{72}$$

The correlation is considered valid for shifted slots with Re > 200 (using the Fluent correlation hydraulic diameter definition), and $0.075 < th_{spacer} / H_{gap} < 1.1$.

Figure 35 displays the comparison of Darcy friction factor predictions between the Fluent, Mikulin, and developing duct flow correlations.

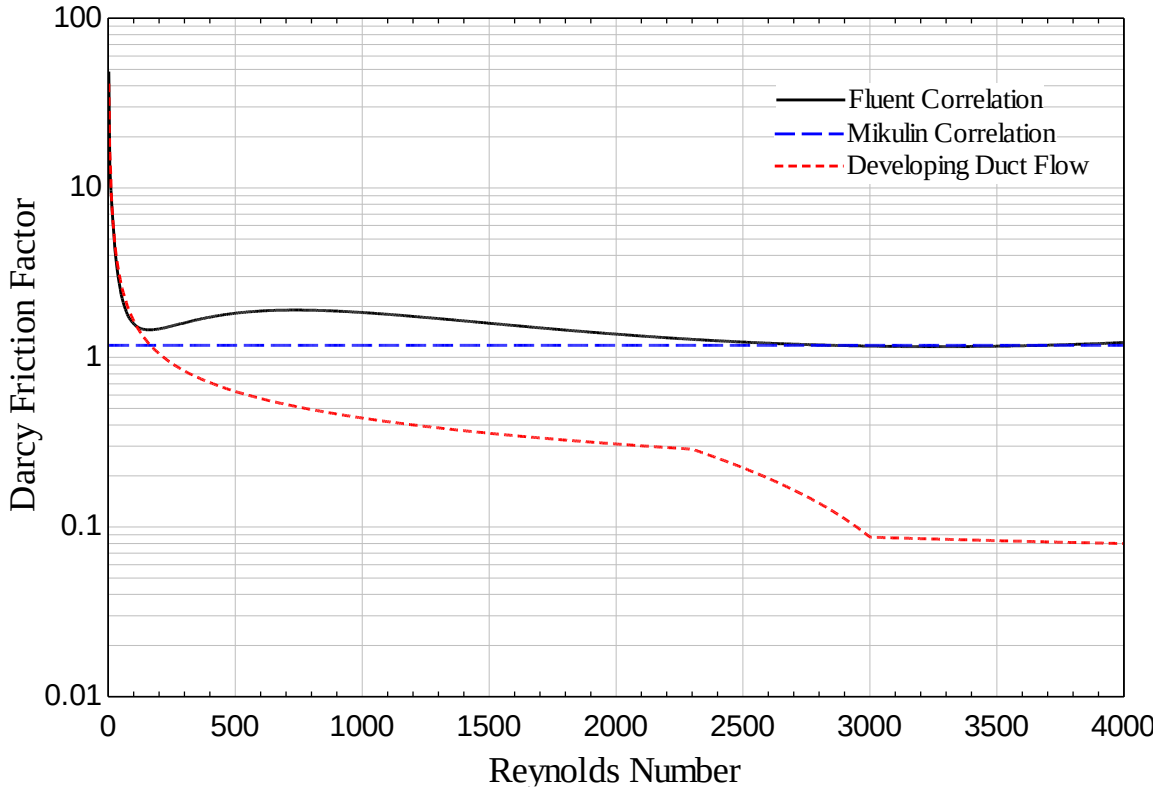

Figure 35: Comparison of the friction factor dependence on Reynold number for the Fluent correlations compared to those produced by Mikulin and developing duct flow correlations.

From the lowest Reynolds number studied of 2.4 up to about 150, the Fluent and developing duct correlations collapse to the same values, likely due to highly laminar, viscous-dominated flow, depicted in Figure 36. Much like a typical laminar duct flow, the friction factor decreases with increasing Reynolds number in this range. Flow direction in the proceeding plots is from left to right.

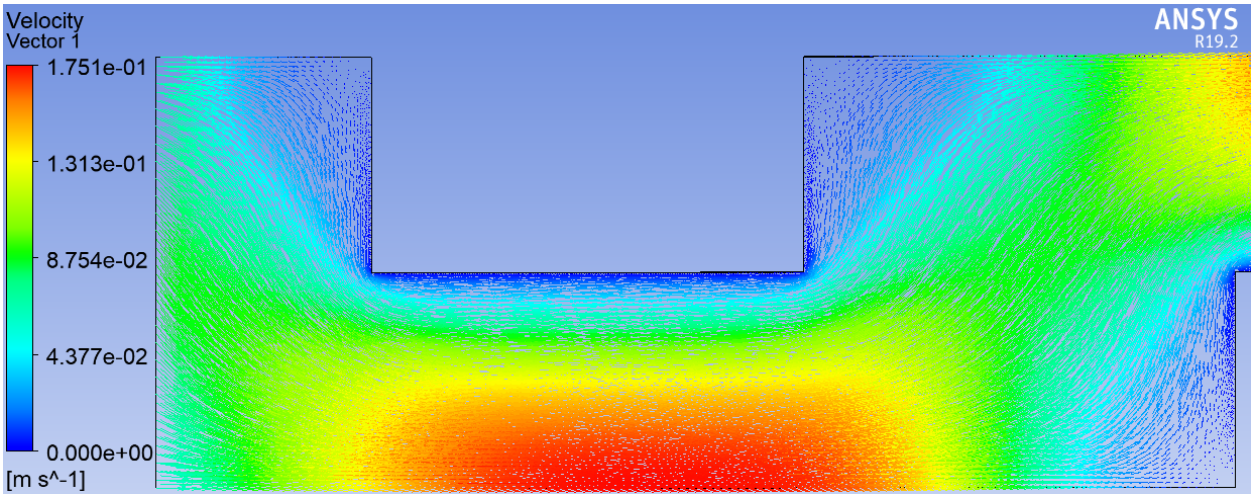

Figure 36: H_{gap} = 0.05 mm, T_{in} = 300 K, P = 2.6 MPa, $\dot{m}$ = 6 g/s, resulting in Re = 2.4, the lowest Reynolds number condition for the heat exchanger.

Around Re = 150, the boundary layer in the gap exhibits waviness associated with the onset of turbulence, and recirculation begins in the wake on the leeward face of the fins. The duct flow correlation is no longer an acceptable approximation of the flow.

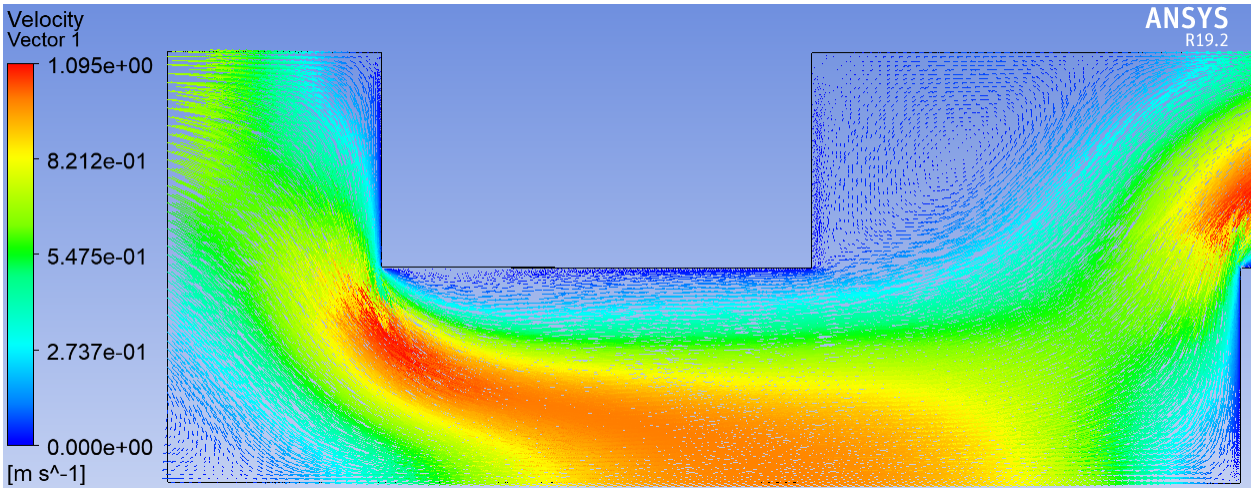

Figure 37: H_{gap} = 0.525 mm, T_{in} = 300 K, P = 2.6 MPa, $\dot{m}$ = 7.5 g/s, resulting in Re = 145.

Between about 150 < Re < 750, a second recirculation zone appears and begins to grow in the fin gap region boundary layer. The velocity and size of the recirculation region increases until about Re = 750, raising the friction factor.

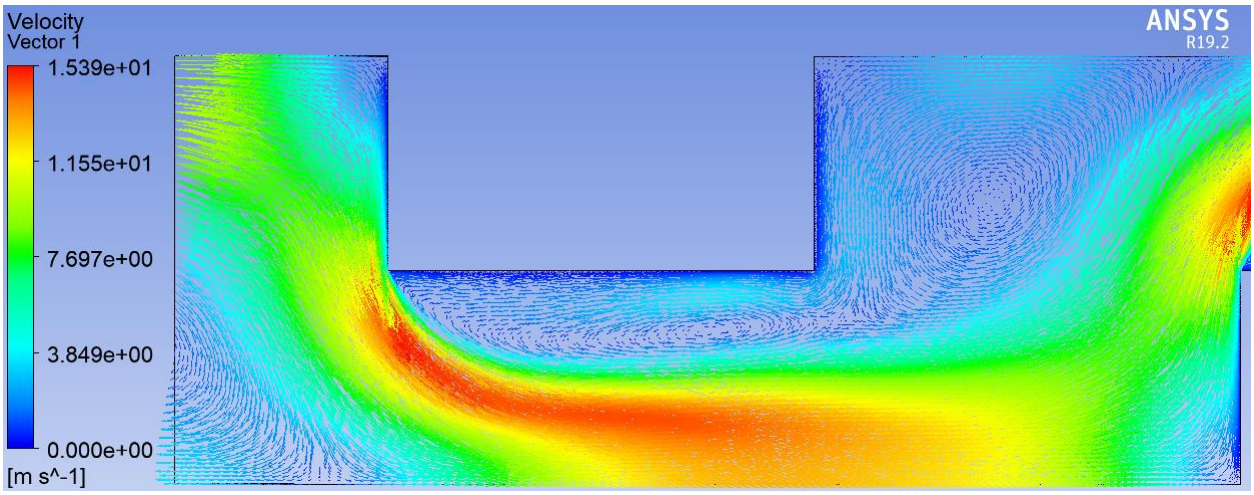

Figure 38: H_{gap} = 0.525 mm, T_{in} = 165 K, P = 500 kPa, $\dot{m}$ = 12 g/s, resulting in Re = 755.

Between 750 < Re < 3000, the recirculation region moves closer to the leading edge of the fin, the size of the turbulent eddy decreases, and the friction factor decreases.

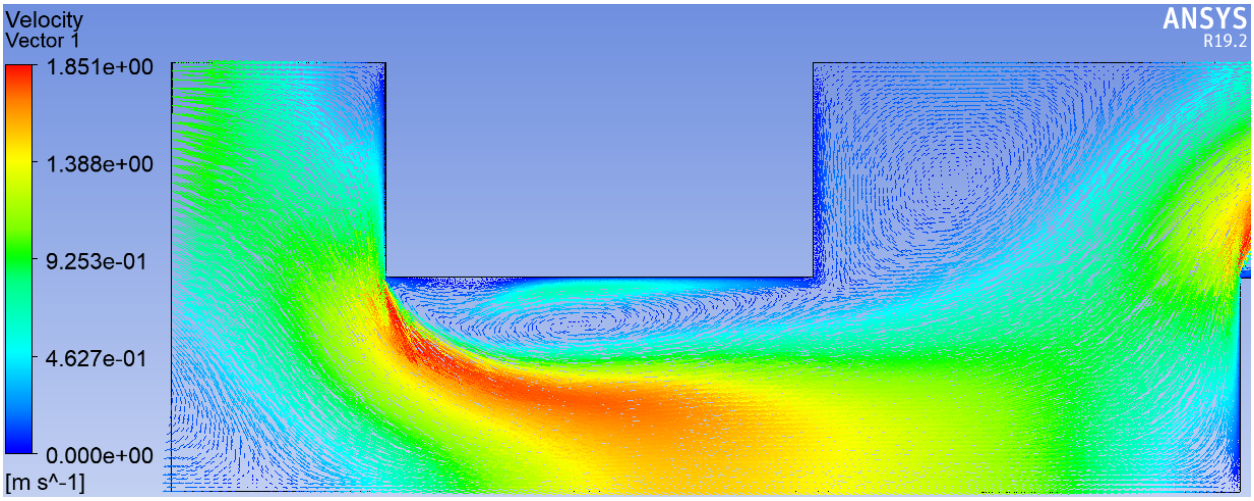

Figure 39: H_{gap} = 1 mm, T_{in} = 30 K, P = 500 kPa, $\dot{m}$ = 10.5 g/s, resulting in Re = 3085.

Beyond about Re = 3000, the eddy size remains constant, as does the friction factor.

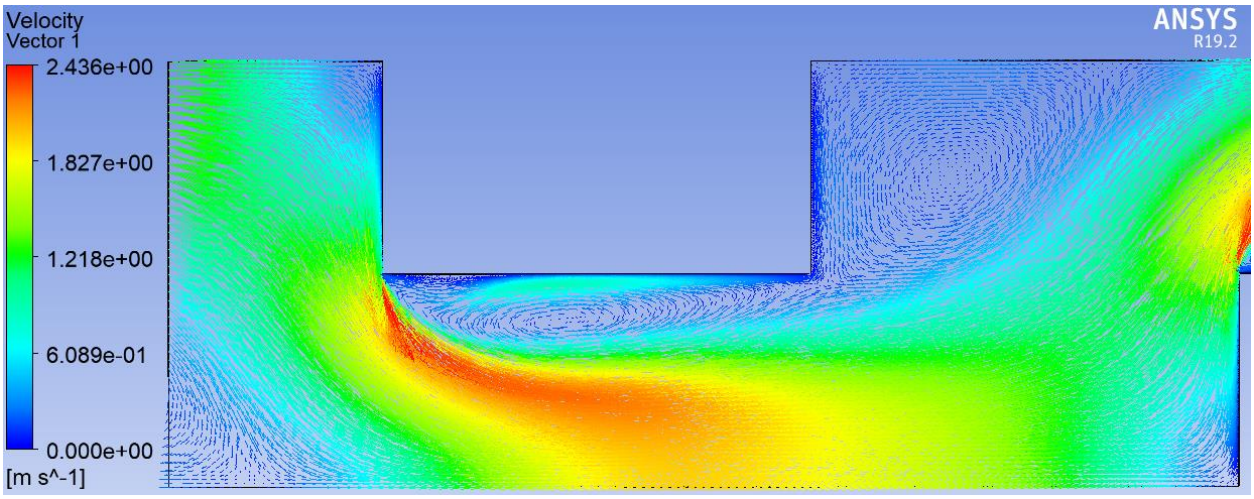

Figure 40: H_{gap} = 1 mm, T_{in} = 30 K, P = 500 kPa, $\dot{m}$ = 12 g/s, resulting in Re = 4046, the highest Reynolds number condition for the heat exchanger.

Mikulin's correlation assumed a constant friction factor, based on the independence of flow resistance on Reynolds number presented in the Handbook of Hydraulic Resistance, which only considered Reynolds numbers exceeding 100,000. The assumption appears to be valid at very high Reynolds numbers, but at lower Reynolds numbers, the changing shape of the velocity profile can result in a difference up to a factor of 2. Mikulin's correlation is not claimed to be valid below Re = 200, and in that range, it deviates substantially from the developing duct and Fluent correlations. The Fluent correlation is superior to the developing duct flow correlation and Mikulin's correlation, because it accounts for the behavior of the flow through the entire range of expected Reynolds numbers in the heat exchanger, whereas the developing duct and Mikulin correlations are only accurate in regions of very low or very high Reynolds number, respectively.

6.4.2. Nusselt Number

It is important to note that in addition to the Fluent Reynolds number being twice the equivalent Mikulin Reynolds number due to the differing definitions of the hydraulic diameter, the

Mikulin Nusselt number itself is a factor of 2 different from the equivalent Fluent Nusselt number due to the hydraulic diameter discrepancy.

$$\overline{Nu}_{Fluent} = \frac{\bar{h}D_{h,Fluent}}{k} = \frac{\bar{h}(2D_{h,Mikulin})}{k} = 2\overline{Nu}_{Mikulin} \tag{73}$$

Mikulin's Nusselt number correlation is valid for shifted slots with 60 < Re < 3200 (using the Fluent correlation hydraulic diameter definition). It is based solely on Reynolds number and is therefore independent of all geometric parameters except the gap height and channel width, which effect the Reynolds number.

$$\overline{Nu}_{Mikulin} = 0.22{Re_{Mikulin}}^{0.69} \tag{74}$$

Taking into account the conversions, Figure 41 displays the dependence of the Nusselt number on the Fluent-definition Reynolds number for the 3 correlations. Recall that this is the Nusselt number for a constant temperature wall condition.

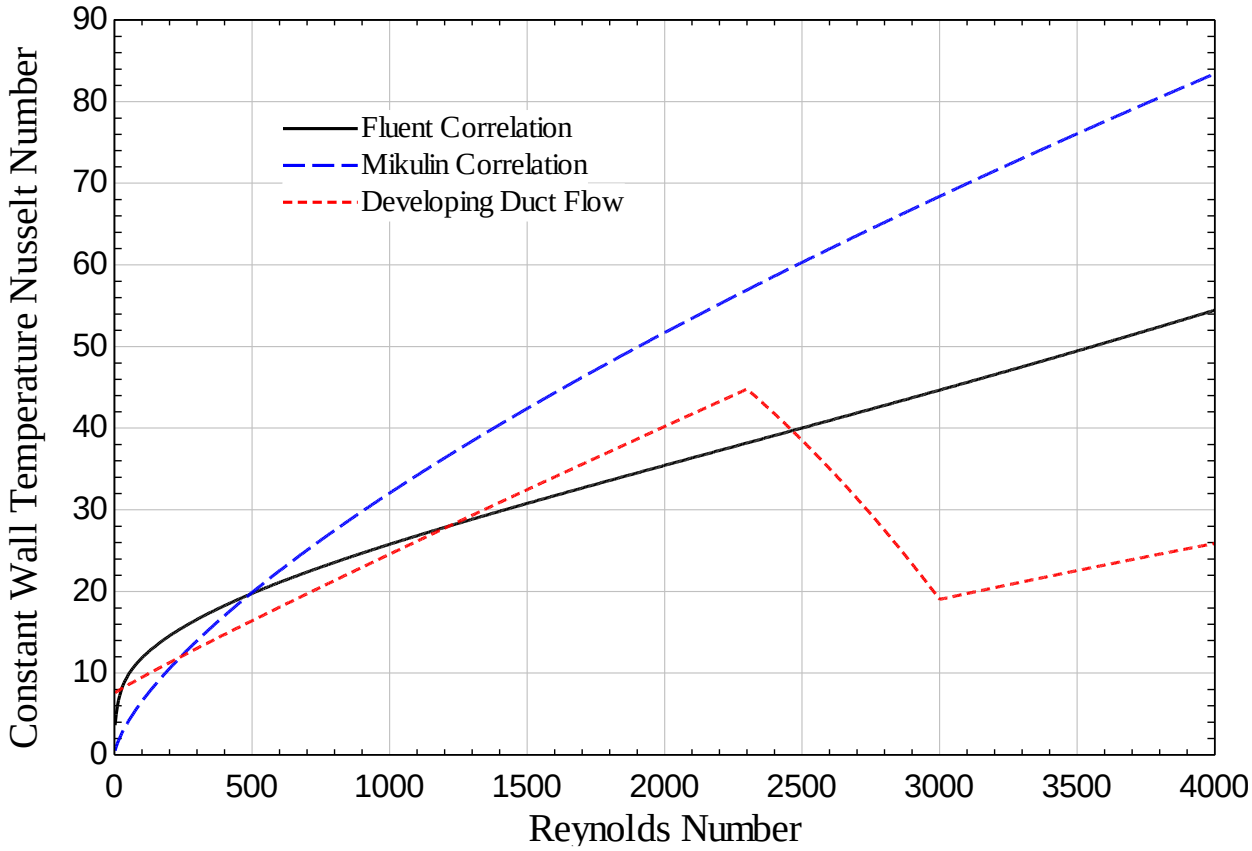

Figure 41: Comparison of the Nusselt number dependence on Reynold number for the Fluent correlations compared to those produced by Mikulin and developing duct flow correlations with a constant temperature wall condition.

Directly comparing the Nusselt number correlations for this geometry to a developing duct is in some ways meaningless because the duct flow ignores the front and wake faces of the fins, while the correlations produce an average Nusselt number based all surfaces. For example, consider the lowest Reynolds number case. The thermal boundary layer entrance length of a laminar duct flow can be approximated by:

$$L_{fd,t,laminar} = 0.05 Re D_h Pr \tag{75}$$

The lowest Reynolds number case occurs at the smallest gap height studied of 0.05 mm, and the Prandtl number is 0.659. Consequently, the estimated hydrodynamic entrance length is 0.008 mm, which is only 16% of the plate thickness. The flow is predominantly fully developed, and the

predicted Nusselt number at this Reynolds number should approximately equal 7.54, the value for a fully developed infinitely wide duct with a constant surface temperature. The duct flow correlation returns 7.6, which makes sense considering the small developing region raising the Nusselt number slightly. The Fluent correlation returns 3.626, which also makes sense. At the smallest Reynolds numbers, the velocity and temperature profile is gradual on the front and wake faces of the fin compared to the duct-like gap. It could be assumed that they contribute essentially nothing to the convective heat transfer coefficient and reduce the area-averaged convective heat transfer coefficient and therefore the Nusselt number of the geometry by a factor of 2. The Mikulin correlation returns 0.499 for the Nusselt number at Re = 2.4, which is inaccurate. The Mikulin correlation is not considered valid below Reynolds numbers of 60 (using the Fluent and duct flow definition of Reynolds number).

By about Re = 25, the convective heat transfer coefficient on the front face is about double that of the two gap faces, making up for the near-zero convection from the rear face and resulting in an equivalent area-average convective heat transfer coefficient and Nusselt number as the duct flow correlation. Within Reynolds numbers of about 25 to 150, in the laminar regime, the Fluent correlation Nusselt number begins to exceed the duct flow correlation due to further increase of convection on the front face. Beyond about Re = 150, the turbulent behavior gives rise to complex flow conditions and no meaningful conclusion can be drawn from comparing the duct flow and Fluent correlations.

Below about Re = 500, the Fluent correlation predicts greater convective heat transfer compared to the Mikulin correlation. Above Re = 500, the Fluent correlation will be more conservative. The difference between the two correlations increases with increasing Reynolds number.

At the lowest Reynolds numbers, the fluid nearly becomes isothermal by the time it reaches the outlet of the domain. To illustrate this very roughly, a sort of characteristic pseudo time scale of thermal diffusion through the gas as though it were stagnant can be compared to a characteristic time required for mass to traverse the domain.

$$\tau_{thermal} \approx \frac{{H_{gap}}^2}{4\alpha} \tag{76}$$

$$\tau_{mass} \approx \frac{L_{domain}}{\bar{V}_{gap}} \tag{77}$$

Using the conditions of the lowest Reynolds number case as an example, assuming the gap height of 0.05 mm as a characteristic length for thermal diffusion, and the average gap velocity of 0.15 m/s, the pseudo time constants for thermal and mass propagation are 8.5×10^{-5} and 1.3×10^{-3} seconds, respectively, indicating that the flow will become nearly isothermal before reaching the end of the domain. This can make it difficult for the model to reconcile the requirements of the periodic boundary condition, as seen in the nonphysical slightly lower temperature near the outlet in Figure 43. Flow direction is from left to right.

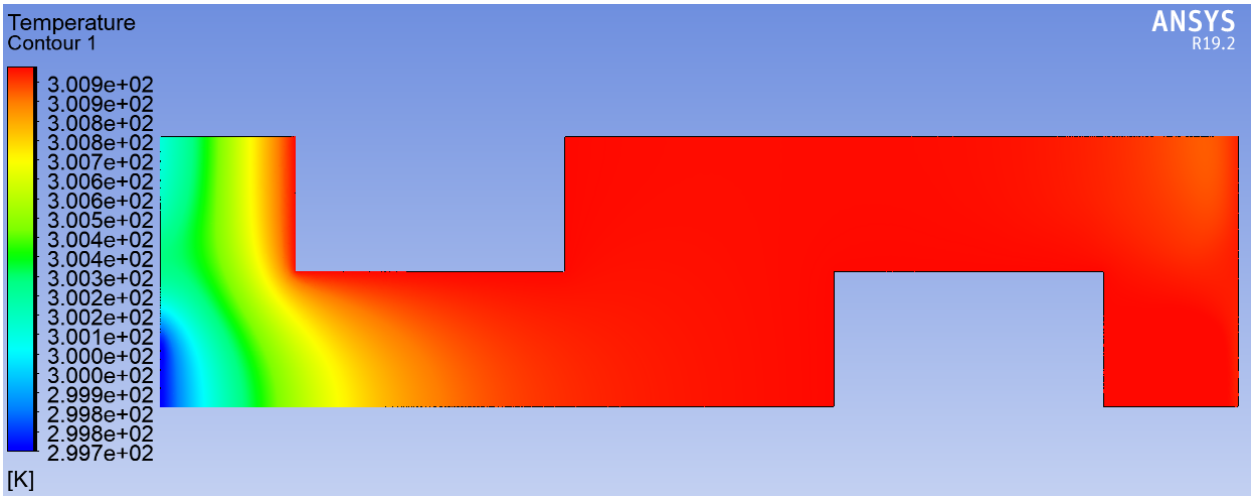

Figure 42: H_{gap} = 0.05 mm, T_{in} = 300 K, P = 2.6 MPa, $\dot{m}$ = 6 g/s, resulting in Re = 2.4, the lowest Reynolds number condition for the heat exchanger.

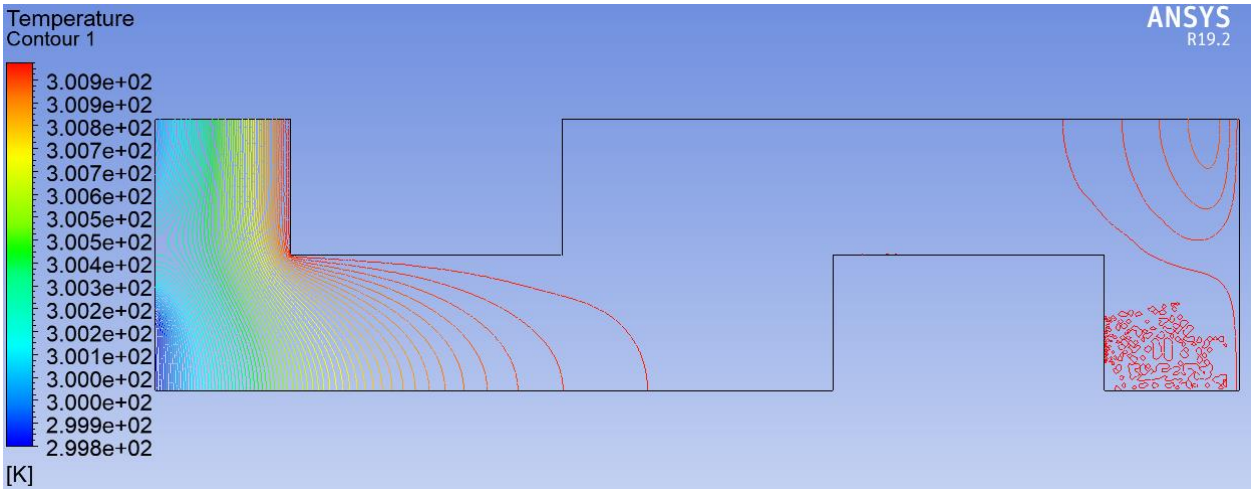

Figure 43: Duplicate of Figure 42 with unfilled contours to highlight the slightly lower nonphysical temperature near the domain exit.

This impacts only the instances with very low Reynolds numbers, and prevents them from achieving a full 3 order of magnitude reduction in energy equation residual. Nevertheless, the impact on the predicted Nusselt number in these cases appears minimal, and the energy residual does still decrease by about 2 orders of magnitude.

Figure 45 corresponds to Re = 28, and displays a highly laminar, duct-like temperature profile. By this Reynolds number, the nonphysical region near the outlet is no longer present.

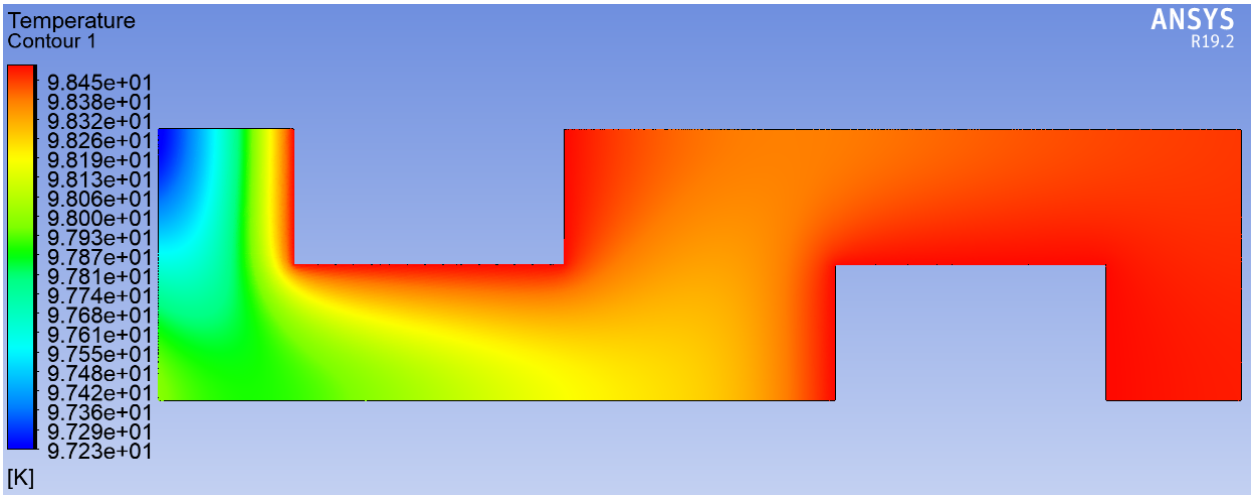

Figure 44: H_{gap} = 0.2875 mm, T_{in} = 97.5 K, P = 2.6 MPa, $\dot{m}$ = 6 g/s, resulting in Re = 28.

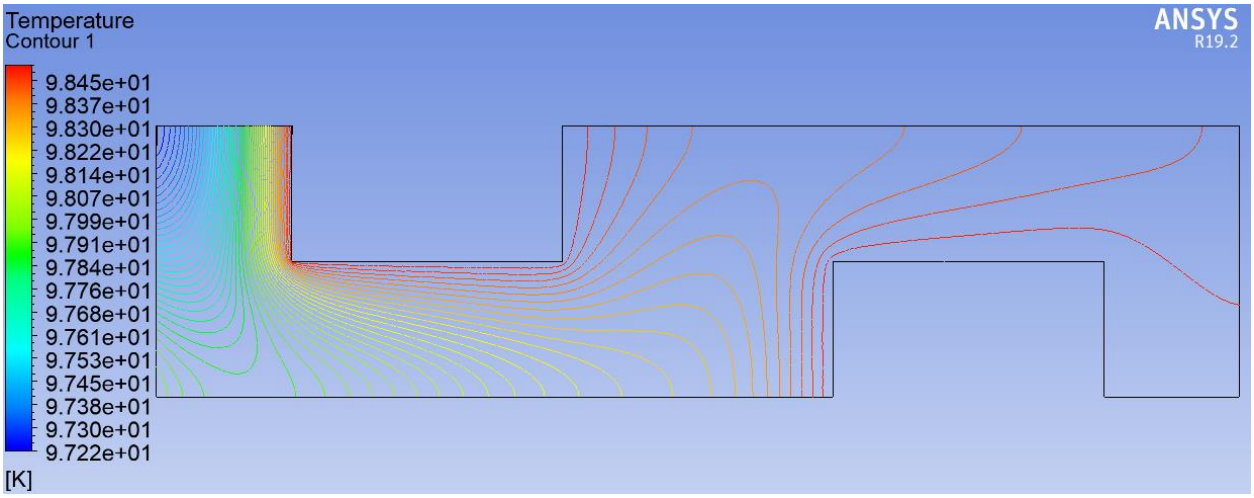

Figure 45: Duplicate of Figure 44 with unfilled contours to highlight the slightly lower nonphysical temperature near the domain exit.

The temperature profile continues to look highly laminar until about Re = 150, beyond which point the turbulent eddies appear.

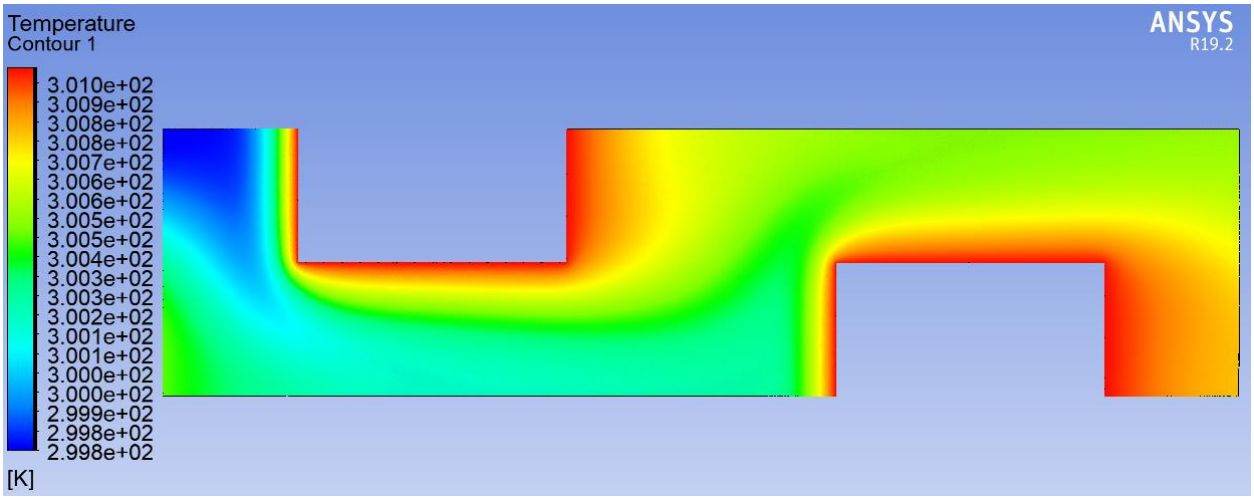

Figure 46: H_{gap} = 0.525 mm, T_{in} = 300 K, P = 2.6 MPa, $\dot{m}$ = 7.5 g/s, resulting in Re = 145

As the Reynolds number increases further, the temperature profile is shaped based on the size, location, and intensity of the turbulent eddies.

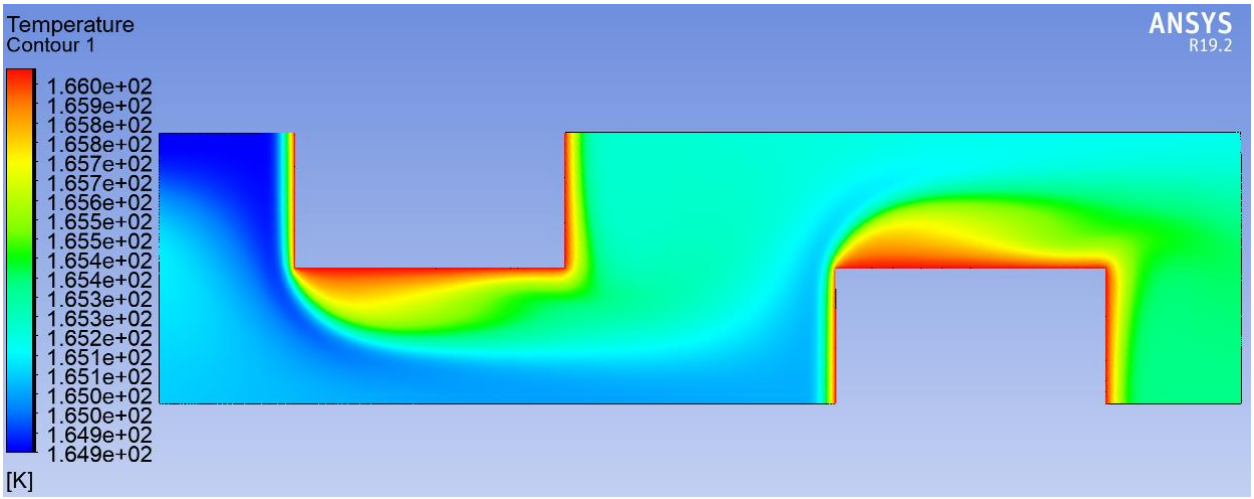

Figure 47: H_{gap} = 0.525 mm, T_{in} = 165 K, P = 500 kPa, $\dot{m}$ = 12 g/s, resulting in Re = 755.

Once the turbulent eddy in the fin gap has formed, it moves toward the leading edge of the fin, and the velocity of both the gap eddy and the leeward face eddy increase, as the Reynolds number increases. The temperature gradient on the front fin face becomes increasingly steep.

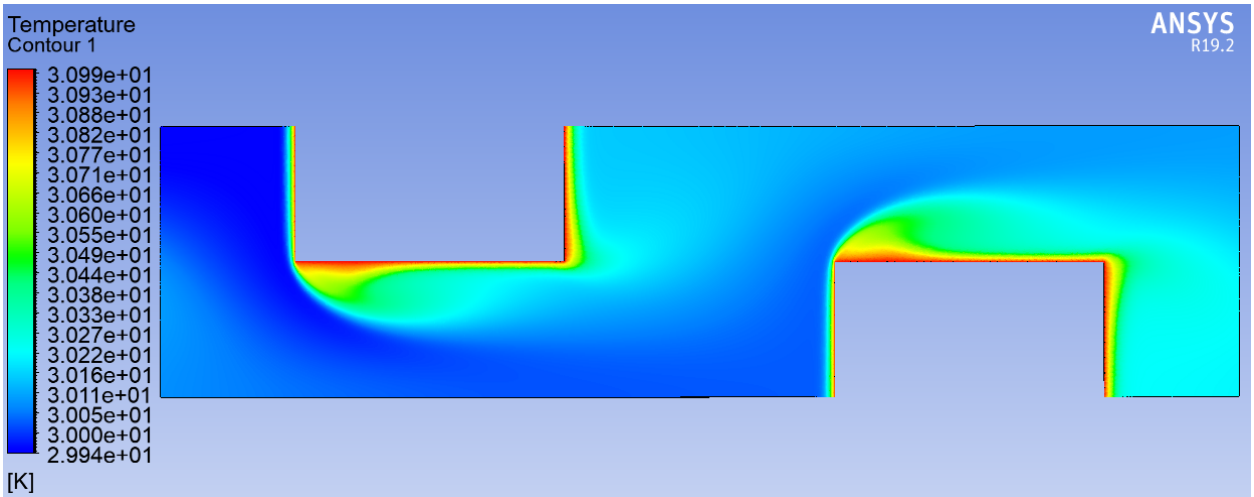

Figure 48: H_{gap} = 1 mm, T_{in} = 30 K, P = 500 kPa, $\dot{m}$ = 10.5 g/s, resulting in Re = 3085.

Like the velocity profile shape, the evolution of the temperature profile shape ceases beyond about Re = 3000.

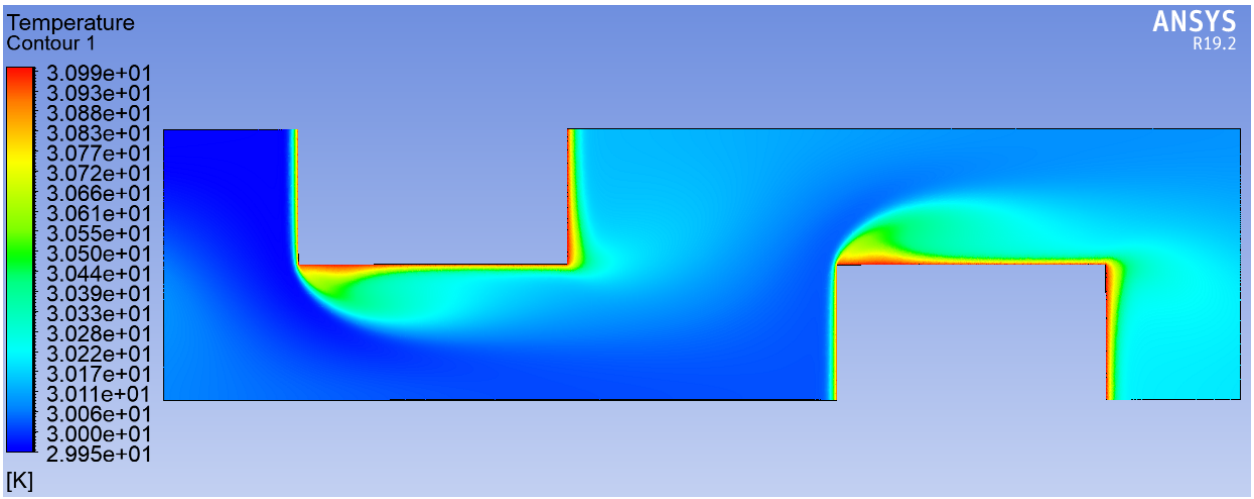

Figure 49: H_{gap} = 1 mm, T_{in} = 30 K, P = 500 kPa, $\dot{m}$ = 12 g/s, resulting in Re = 4046, the highest Reynolds number condition for the heat exchanger.

7. MATLAB Model Validation

To confirm the accuracy of the MATLAB model, its results were compared to simpler closed-form approximations and experimental data. The solutions produced for the entire range of

parameter combinations used in the design study were compared to the solutions produced using the effectiveness-NTU solution described in section 3.3.1. This analytical solution assumes constant material properties, evaluated at T = 165 K, the average temperature in the heat exchanger, and that the number of transfer units is large relative to the axial conduction parameter. Despite these assumptions it should produce comparable results. Additionally, the MATLAB model was modified to represent the geometry of a similar physical heat exchanger for which experimental data of effectiveness and pressure loss exists. The model and the experimental data were compared.

7.1. Comparison with Effectiveness – NTU Solution

The effectiveness-NTU solution requires a description of the fluid NTU, fin NTU, separating wall conductance for a single plate, and the axial conduction parameter. The effectiveness-NTU solution separates stream-to-stream heat conduction into two parts: the NTU of conduction through the fins ($n_{tu,p}$), and the lateral conductance of the wall at the base of the fins that separates the two flow streams (λ_p).

The fluid NTU is simply the product of the summed surface area of the individual fins and the average convective heat transfer coefficient, averaged through the entire heat exchanger on a given side. It is non-dimensionalized by the fluid capacitance rate on each side evaluated at the average temperature.

$$n_{tu,f,1} = \frac{\overline{\bar{h}_c} A_{s,fin} n_{fins}}{\overline{\dot{C}_c}} \tag{78}$$

$$n_{tu,f,2} = \frac{\overline{\bar{h}_h} A_{s,fin} n_{fins}}{\overline{\dot{C}_h}} \tag{79}$$

(Note that the fin efficiency's modulation of the fluid NTU is incorporated into the equation for the overall plate conductance, $n_{tu,po}$, in section 3.3.1). The NTU associated with the fin conductance

portion of the plates is based on the total cross-sectional area of the n fins, non-dimensionalized by the capacitance rate.

$$n_{tu,p,1} = \frac{\overline{k_{cu}} A_{c,fin} n_{fins}}{W_{channel} \overline{\dot{C}_c}} \tag{80}$$

$$n_{tu,p,2} = \frac{\overline{k_{cu}} A_{c,fin} n_{fins}}{W_{channel} \overline{\dot{C}_h}} \tag{81}$$

The conductance of the separating wall (λ_p) is defined in the same way as the plate NTU, except the cross-sectional area used is the area perpendicular to the stream-to-stream direction, the overall channel height multiplied by the plate thickness. The conduction path length through the separating wall is the thickness of the material separating the two flow streams, b. Again, the plate thermal conductivity and capacitance rates are average values. The cold side has the lower capacitance rate, and therefore is used to non-dimensionalize the equation.

$$\lambda_p = \frac{\overline{k_{cu}} H_{total} th_{plate}}{b \overline{\dot{C}_{min}}} \tag{82}$$

The axial conduction parameter is based on the series thermal resistance associated with the full stack of n plates and (n + 1) spacers, with average material properties.

$$\overline{R_{cu}} = \frac{n_{plates} th_{plate}}{\overline{k_{cu}} A_{c,cu}} \tag{83}$$

$$\overline{R_{ss}} = \frac{(n_{plates} + 1) th_{spacer}}{\overline{k_{ss}} A_{c,ss}} \tag{84}$$

$$\bar{\lambda} = \frac{1}{(\overline{R_{cu}} + \overline{R_{ss}}) \overline{\dot{C}_{min}}} \tag{85}$$

These equations describe the geometry, flow conditions, and average properties of the heat exchanger, and serve as inputs to the effectiveness-NTU solution for heat exchangers comprised of many plates presented in 3.3.1. This form of the E-NTU solution accounts for the fin resistance using Fleming's definition, in the expression for the overall plate NTU, $n_{tu,po}$. An effective NTU

is calculated by modulating the ideal NTU based on axial conduction effects, which is used to predict the actual effectiveness.

The parametric study spanned a range of values for the small-scale feature size L_{micro}, channel width (or fin length), mass flow rate, and allowable weight. The parameter values chosen are discussed in detail later in section 8.4. Initially, 11 values were chosen for each parameter, resulting in 14,641 unique combinations, but to investigate the degree to which the MATLAB finite difference model and E-NTU solutions differ, it was only necessary to observe cases comprised of the parameters at their extrema, which should capture the case with the largest discrepancy between the two models. The extrema were: $W_{channel}$ = 0.4 and 2 cm, L_{micro} = 0.064 and 1 mm, weight = 50 and 100 lbs, and $\dot{m}$ = 6 and 12 g/s. Considering just the minimum and maximum values of the 4 parameters, the result was 16 combinations. Their effectiveness produced by the numerical model and E-NTU solution are compared in Figure 50.

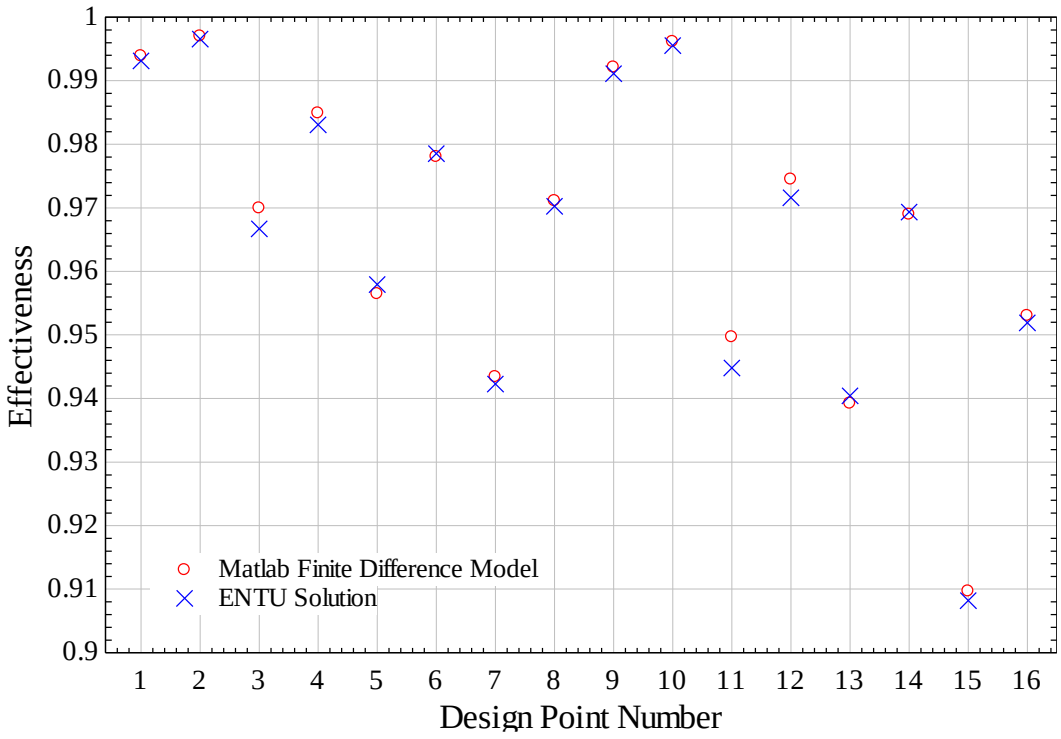

Figure 50: Heat exchanger effectiveness predicted by the MATLAB finite difference model and effectiveness-NTU solution for stacked plate heat exchangers at parameter combinations comprised of the most extreme values.

The design point number is arbitrary. The agreement between the two solutions was surprisingly good considering the E-NTU solution's property averaging over the 270 K temperature range. The worst agreement occurred at design point # 11, which differed in effectiveness by less than 0.005, and corresponded to the design point with the smalles L_{micro}, largest channel width (or fin length), highest mass flow rate, and lightest allowable weight. The difference caused by assuming constant material properties may be greater in the case of a heat exchanger operating under conditions with non-ideal gas behavior, which will not have as linear of a temperature profile and therefore introduce more error from evaluating material properties at the average temperature.

7.2. Comparison with Sub-Scale Hybrid Cryocooler Recuperator Data

In the mid-2000's, interest in a hybrid cryocooler with a pulse-tube 1st stage and reverse-Brayton 2nd stage, with a recuperative heat exchanger between the two stages, spurred the development of a high-effectiveness recuperator design by the University of Wisconsin by Hoch et al. [22]. The general design was very similar to the concept explored in this thesis. It consisted of a brazed stack of alternating slotted copper plates and stainless steel spacers, with helium gas as the working fluid. A small scale prototype, depicted in Figure 51, was designed and built, and its performance was experimentally studied [23].

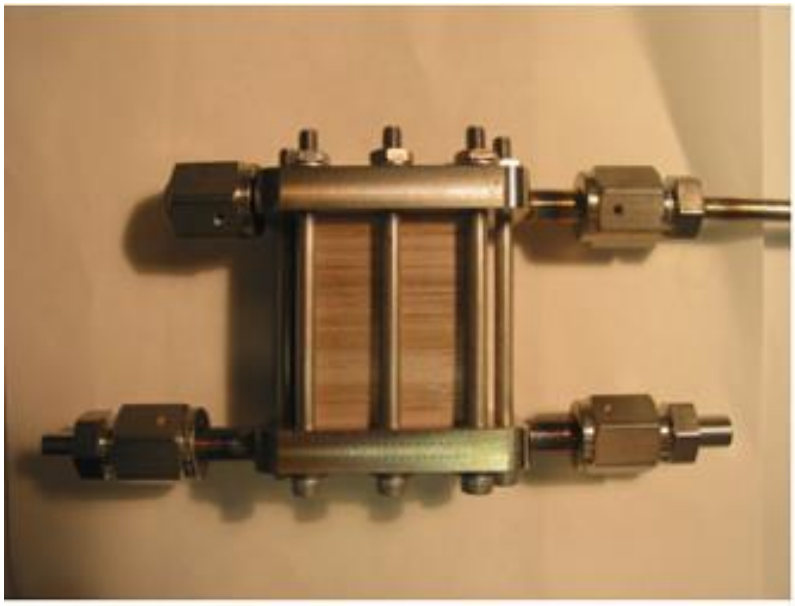

Figure 51: Complete small-scale hybrid cryocooler stacked plate heat exchanger [23].

The fins were arranged in columns and oriented perpendicular to the stream-to-stream direction, with each column separated by a conducting web to transport heat in the stream-to-stream direction, and the fin arrangement in adjacent plates was inline rather than staggered. A schematic of one slotted plate is shown in Figure 52, with all dimensions in inches.

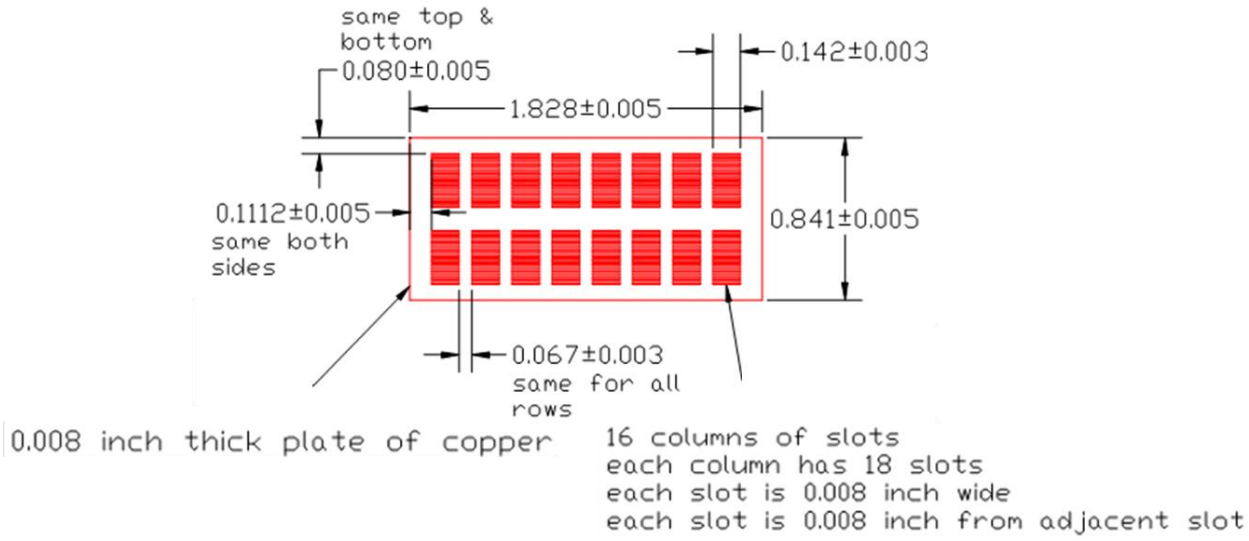

Figure 52: Geometric dimensions of a single slotted plate for the sub-scale hybrid cryocooler heat exchanger, in inches [23].

Each plate was separated from its neighbors by a stainless steel spacer with the dimensions shown in Figure 53.

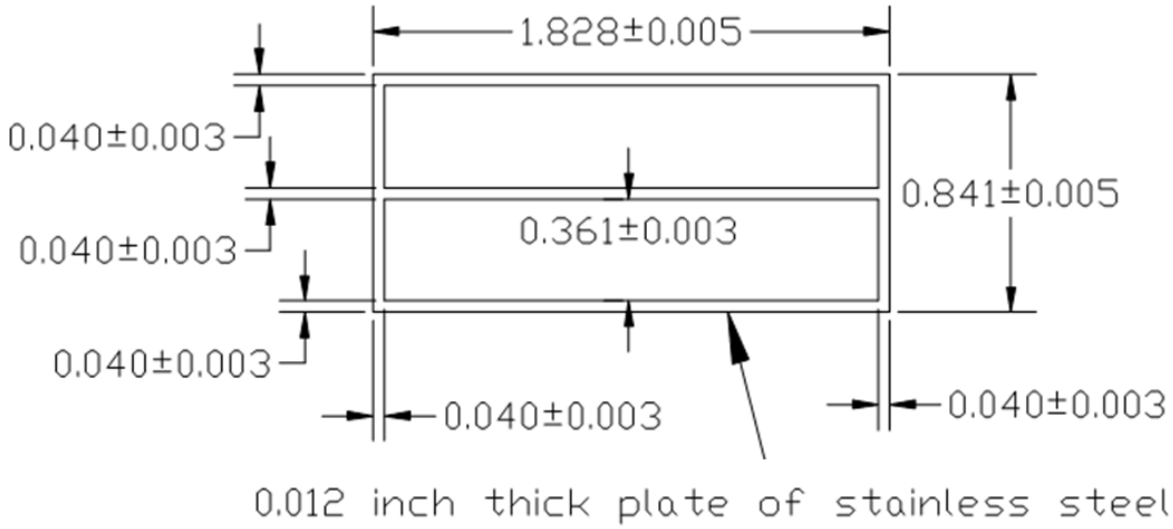

Figure 53: Geometric dimensions of a single spacer for the sub-scale hybrid cryocooler heat exchanger, in inches [23].

The sub-scale module consisted of a stack of 100 plates and spacers, resulting in a total core length of 2 inches.

The experiments measured the mass flow rate using a rotameter. The temperature at each inlet and outlet location was measured with a platinum resistance thermometer. The cold side included redundant thermocouples. The temperature difference was produced by exchanging heat between the helium gas and a liquid nitrogen bath, resulting in a nominal hot side inlet temperature of 295 K and a cold side inlet temperature of 77 K. Pressure transducers at each inlet and outlet recorded the pressure. A schematic of the test setup is shown in Figure 54.

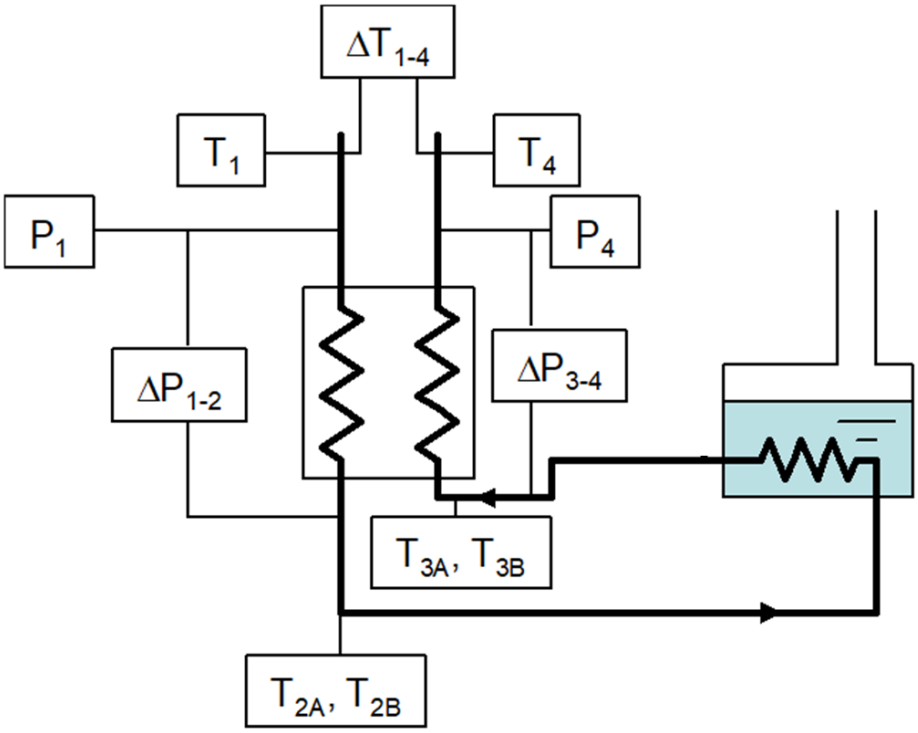

Figure 54: Schematic of the test setup used to measure the performance of the sub-scale hybrid cryocooler recuperator [23].

The MATLAB model was modified to match the geometry and flow conditions of the sub-scale hybrid cryocooler heat exchanger. Additionally, the correlations for the staggered plate heat

exchanger friction factor and Nusselt number were no longer applicable due to the inline fin orientation and had to be reproduced using the geometry and flow conditions of the hybrid cryocooler recuperator. The Fluent model settings were unchanged. The new unit cell consisted of a single slotted plate and spacer. The largest Reynolds number for the conditions of this heat exchanger was 503. A strong jetting effect resulted in very little evidence of turbulent behavior, even at the highest Reynolds number, with the exception of gentle flow recirculation in the stagnant regions. Figure 55 and Figure 56 display typical velocity vectors and temperature profiles for the modified Fluent model.

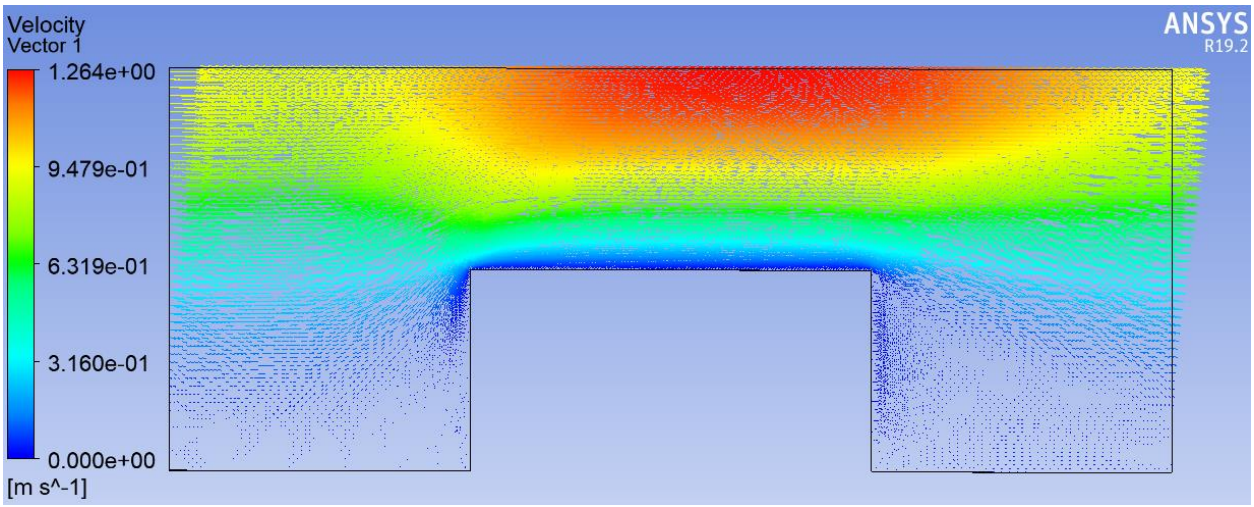

Figure 55: Sub-scale hybrid cryocooler Fluent model velocity vector plot. T_{in} = 77 K, $\dot{m}$ = 0.07 g/s, resulting in Re = 33.3.

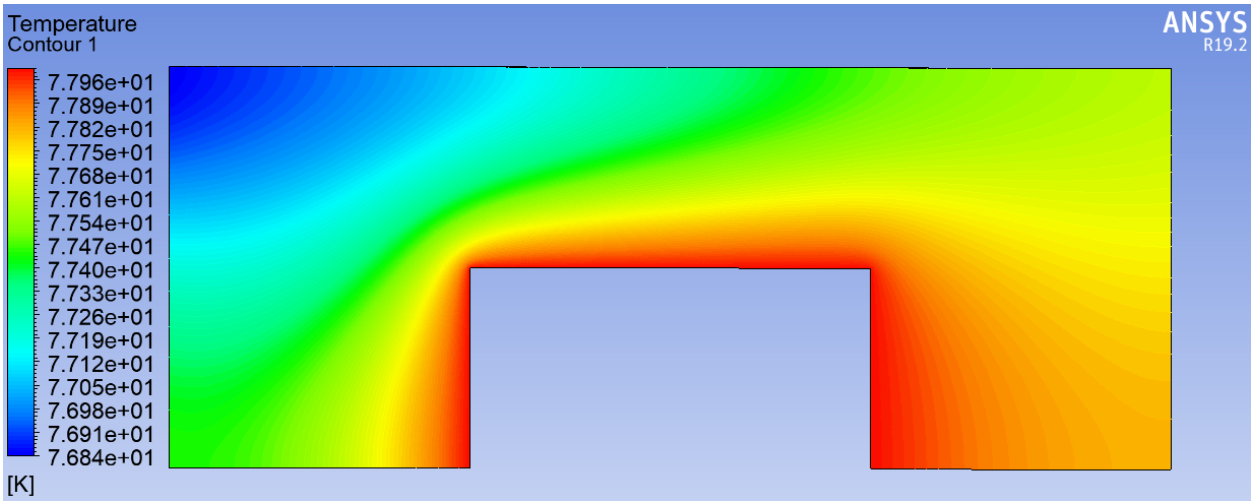

Figure 56: Sub-scale hybrid cryocooler Fluent model temperature profile. T_{in} = 77 K, $\dot{m}$ = 0.07 g/s, resulting in Re = 33.3

Correlations for friction factor and Nusselt number were formed in the same way as described in Section 6.3 by varying the temperature and mass flow rates. The heat exchanger did not vary in pressure significantly enough to warrant its inclusion in the correlation development. Depending on the mass flow rate, the inlet pressure varied from 111 kPa to 151 kPa, and the outlet pressure varied from 111 kPa to 128 kPa. The material properties were all evaluated based on the average pressure of 131 kPa, and only the temperature was varied from 77 K to 295 K. The correlations were used in the MATLAB model, which was also modified to match the geometry and flow conditions of the hybrid cryocooler sub-scale heat exchanger.

7.2.1. Effectiveness Comparison

Figure 57 displays a plot showing the ineffectiveness as a function of mass flow rate based on experimental data compared to the MATLAB model as well as the models originally used to develop the heat exchanger.

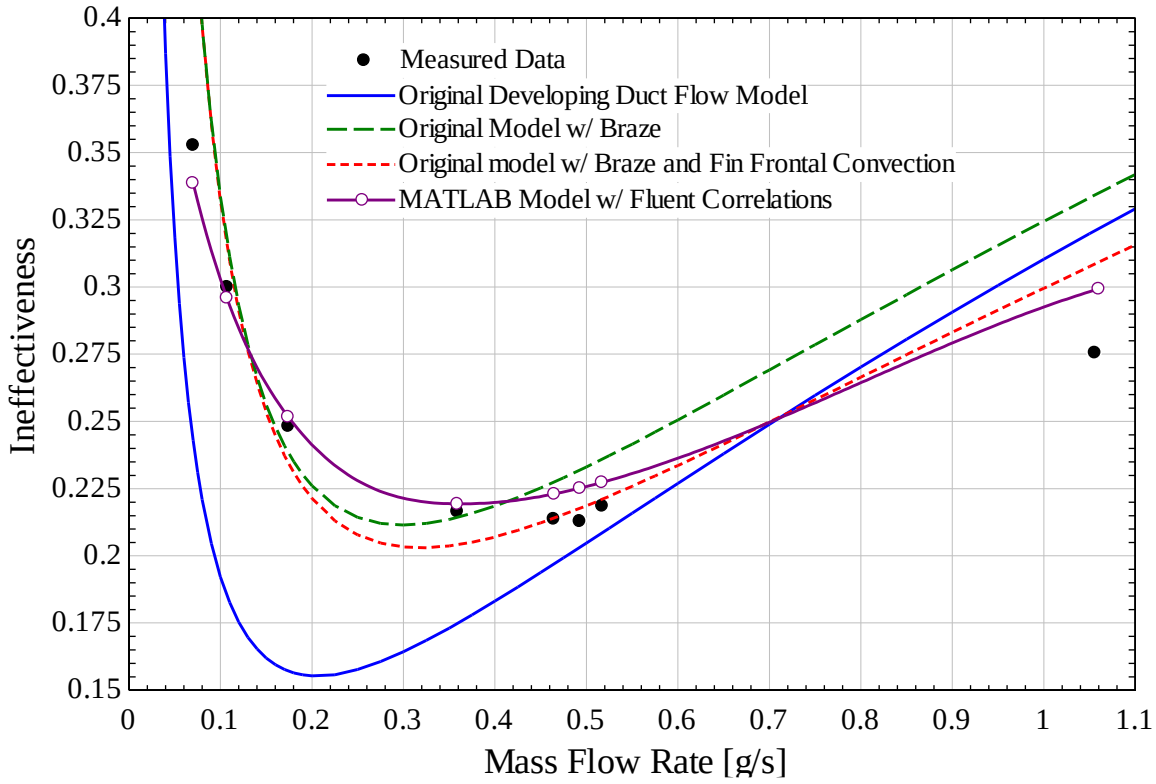

Figure 57: Data points showing the effectiveness of the sub-scale hybrid cryocooler recuperator compared to the original models used to predict its performance and the MATLAB finite difference model with an applicable Nusselt number correlation.

Generally, the MATLAB model accurately predicted the performance of the recuperator over the range of mass flow rates for which data was collected. This included the axial conduction dominated region at low mass flow rates, where the ineffectiveness increased, as well as the convectively dominated region at high mass flow rate. At the highest mass flow rate, the MATLAB model achieved better agreement with the data than the original models, likely because the CFD correlations more accurately predicted convection than the simple developing duct flow approximation used by the original authors, even after they modified their model to include convection in the nearly stagnant gas regions between fins of adjacent plates.

All of the models were highly inaccurate, especially at low mass flow rates, if the effects of excess braze material that leaked into the spacer regions during construction was not included

in the axial conduction calculations. Figure 58 shows a cross-section of part of the stack in the location of the separating wall between the two flow streams.

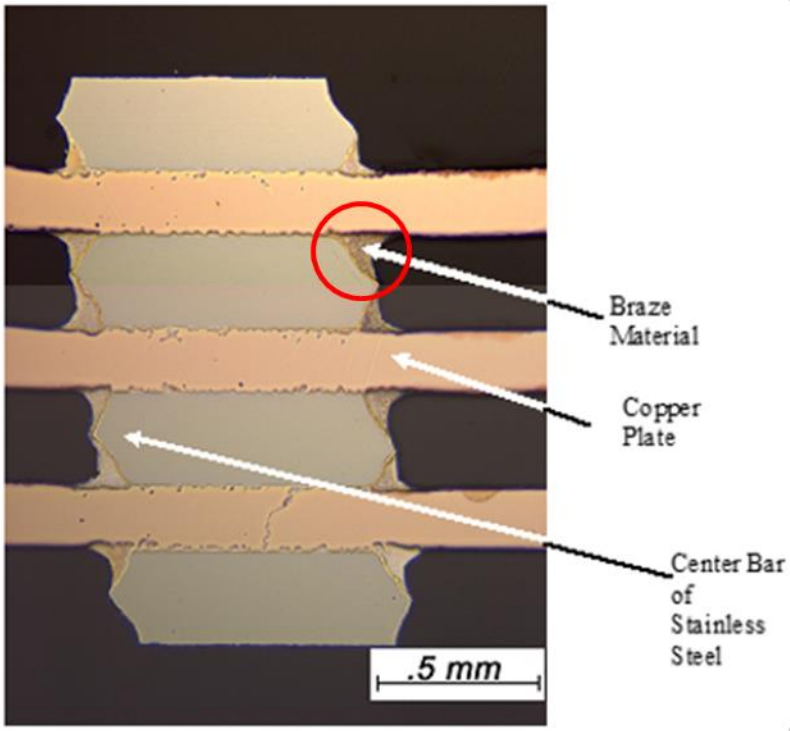

Figure 58: Cross-sectional view of the alternating copper plates and stainless steel spacers between the two flow streams. Excess braze material is clearly visible in parallel with the stainless steel spacers [23].

The braze material was Lucas-Milhaupt alloy 721, which is approximately 72% silver and 28% copper [24]. Although the cross-sectional area was small compared to the stainless steel spacers, the alloy has a very high thermal conductivity. Lucas Milhaupt has not published the thermal conductivity of this braze material, but it could be estimated from its known room-temperature electrical conductivity using the Wiedemann-Franz law. Lucas-Milhaupt lists the room-temperature electrical conductivity at 87% International Annealed Copper Standard (IACS), which corresponds to an electrical conductivity of about $5.05 \times 10^7\ \Omega^{-1}m^{-1}$. The ratio of the thermal to

electrical conductivity of metals is proportional to temperature, with the Lorentz number L = 2.44×10^{-8} W-Ω/K^2 as the constant of proportionality.

$$\frac{k}{\sigma} = LT \tag{86}$$

At room temperature, the estimated thermal conductivity is 364 W/m-K. The resulting thermal conduction path across the insulating spacers significantly reduced the effectiveness. Temperature dependence was not considered because the cross-sectional area was so poorly known. The performance was highly sensitive to the value chosen for the cross-sectional area, and it was therefore a sort of tuning parameter for the models. Brazing stacked plate heat exchangers is a manufacturing option, but this observation highlights the importance of managing excess braze material if it is chosen as the bonding mechanism, perhaps with extra slots that serve as reservoirs for the excess braze. Alternatively, a relatively insulating nickel-based braze alloy could be used instead.

7.2.2. Pressure Drop Comparison

The pressure transducers were located in the tubing near each inlet and outlet, meaning that pressure measurements included a short length of tubing as well as the headers. To infer the pressure loss in the heat exchanger core alone, the two headers were removed and bolted directly to one another. The recorded pressure drop across the headers alone was subtracted from the total pressure drop across the headers with the core in between. The pressure loss experiments were performed at room temperature, and the range of mass flow rates was lower than those used in the effectiveness experiments. Figure 59 displays the measured pressure loss across the core as a function of mass flow rate compared to a few predictive solutions.

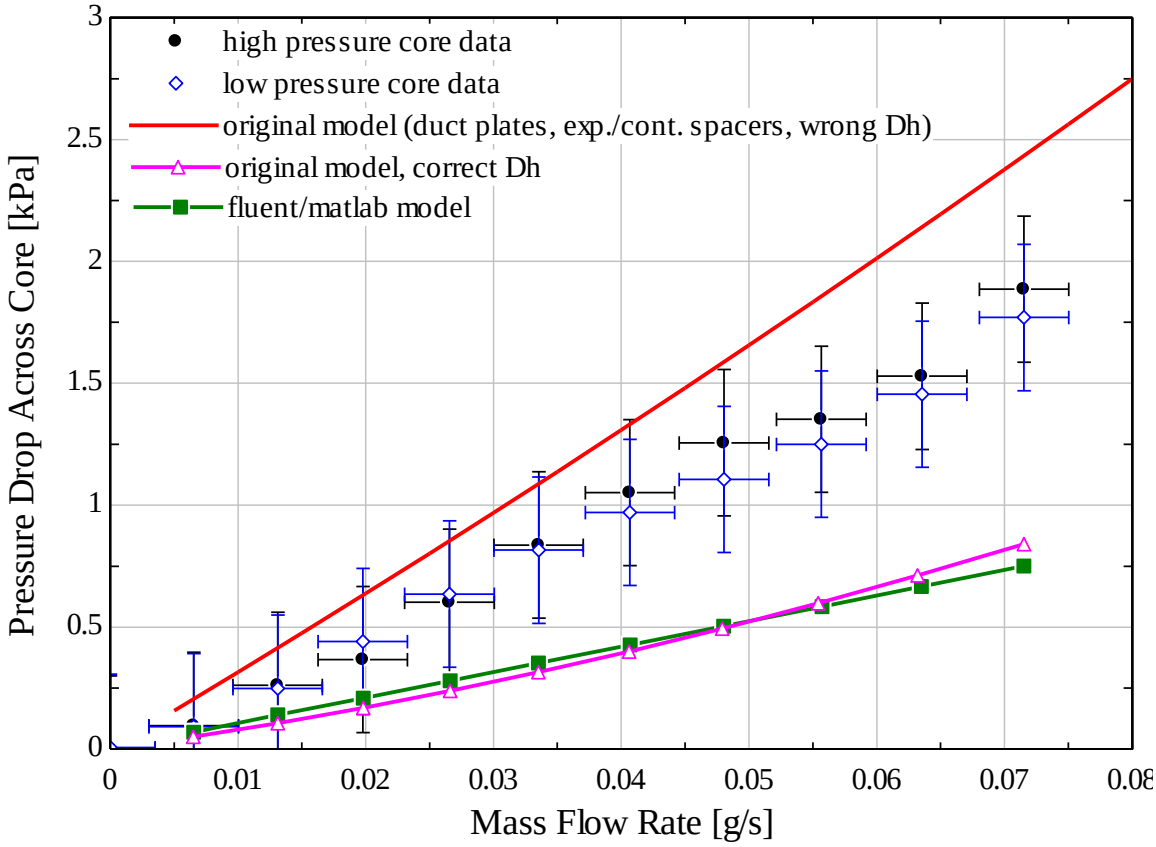

Figure 59: Inferred pressure loss in the heat exchanger core based on experimental data compared to the predictions of various models.

The original model used by the authors treated the slots as regions of developing duct flow with additional terms for gas expansion and contraction in the spacers. They used the duct flow correlations found in EES [16]. The expressions for the contraction and expansion loss coefficients can be found in the appendix of Thomas Fraser's master's thesis, "Design of a Cryogenic Turbine for a Hybrid Cryocooler" [25]

$$K_c = 0.79352 + 0.060341\sigma_{ff} - 0.44822{\sigma_{ff}}^2 \quad (87)$$

$$K_e = 1 - 2.35386\sigma_{ff} + 0.96156{\sigma_{ff}}^2 \quad (88)$$

where σ_{ff} is the free frontal area ratio of the plates to the spacers. The coefficients multiply the dynamic pressure of the fluid to determine pressure loss associated with fluid contraction and

expansion. These expressions each contributed to the total pressure per unit cell in addition to the losses associated with the duct-like plates. The total pressure drop through the heat exchanger was found by multiplying the total loss per plate-spacer pair by the number of plates.

$$\Delta P_{total} = n_{plates}\left[\Delta P_{duct} + \frac{1}{2}\rho \bar{V}_{gap}{}^{2}(K_c + K_e)\right] \tag{89}$$

The duct flow correlations are designed to use $D_h = 4A_c/Per$ as the hydraulic diameter. However, the original model erroneously excluded the factor of 4, which resulted in a large overestimation of the friction factor and pressure drop. The contribution of the contraction and expansion losses was small relative to the duct flow losses. For example, at the highest mass flow rate considered of 0.0715 g/s, where the relative contribution of contraction and expansion to total pressure drop were largest, the duct flow losses still comprised 0.6543 kPa of the 0.8405 kPa total loss.

The pressure drops estimated by the Fluent CFD model agreed very closely to the analytical solution approximations. Both severely under predict the pressure drop. It may be that the pressure losses were much higher in the first few plates. In the most extreme case, the first plate encountered in the header should see a nearly uniform inlet velocity because the profile will require some number of plates to develop. Modifying the highest mass flow rate case from a pair of periodic boundary conditions to a uniform velocity inlet, the worst-case scenario was modeled and is shown in Figure 60.

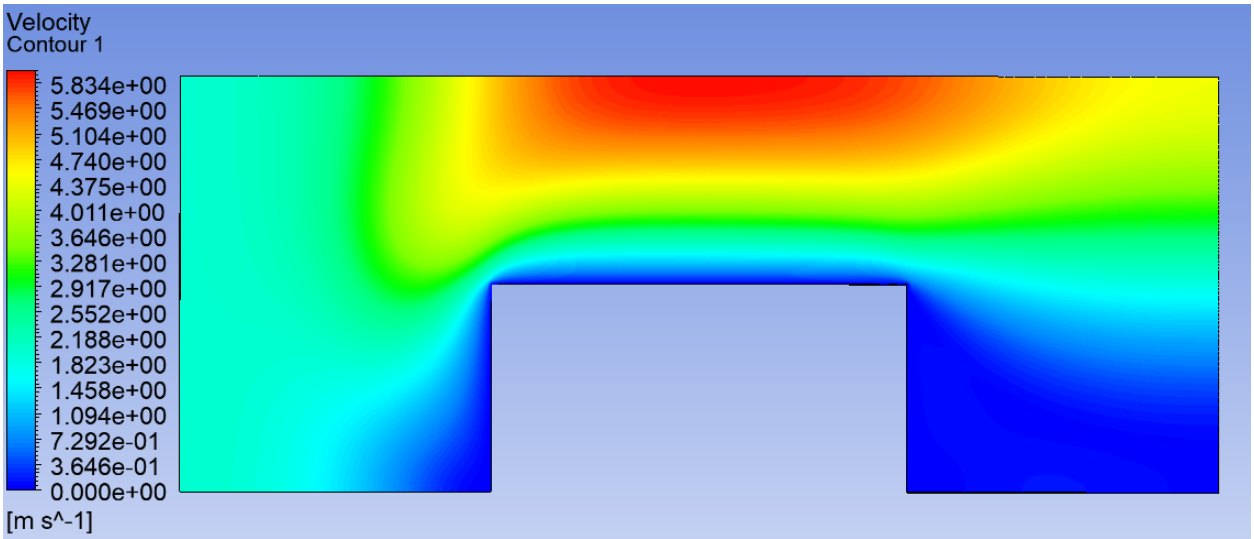

Figure 60: Velocity profile of the highest mass flow rate case (0.0715 g/s) with the periodic boundary condition replaced with a uniform velocity inlet, simulating the first plate in the stack.

Taking the area-averaged pressure at the inlet and outlet to calculate the pressure drop (because there is no longer a linear component pressure gradient associated with the periodic boundary condition), the Fluent model predicted a pressure loss per plate of 10.6 Pa. Even if all 100 plates were subjected to the entrance flow condition associated with the first plate, the predicted total pressure loss would only equal 1.06 kPa. This still agreed better with the predictive models (which predicted $\Delta P \approx 0.8$ kPa), than the experimental data (which predicted $\Delta P \approx 1.8$ kPa), at the highest mass flow rate. Because the analytical and CFD models agreed closely, and it appeared that the entrance effects could not account for the discrepancy between the models and data, it was concluded that the method used to infer the pressure loss through the core was not accurate. The headers must have interacted with the plate stack in a more complex way that introduced a greater pressure loss between the headers and the stack compared to the losses of the two headers simply bolted to one another with no transition to a stack of slotted plates.

7.3. MATLAB Model Results with Mikulin vs. Fluent Correlations

Section 6.4 demonstrated that the Fluent-based correlations captured effects that were not accounted for in Mikulin's correlations. The results produced by the MATLAB model using Mikulin's correlations were compared to those produced with the Fluent correlations as a percent difference in effectiveness and pressure drop.

$$\% \, Diff = \frac{(Fluent - Mikulin)}{\frac{1}{2}(Fluent + Mikulin)} \cdot 100 \, \% \tag{90}$$

The result for each case was plotted as a function of a representative nominal Reynolds number, evaluated with properties corresponding to the average temperature in the heat exchanger, because the actual Reynolds number for a given case varied by about a factor of 4 through the heat exchanger's length. 5 values of L_{micro}, $\dot{m}$, $W_{channel}$, and weight were chosen over the broad parameter ranges described in section 8.4.1, which spanned the majority of the Reynolds number range of the correlations.

Figure 61 displays the percent difference in effectiveness between the MATLAB model predictions using the two correlations for Nusselt number.

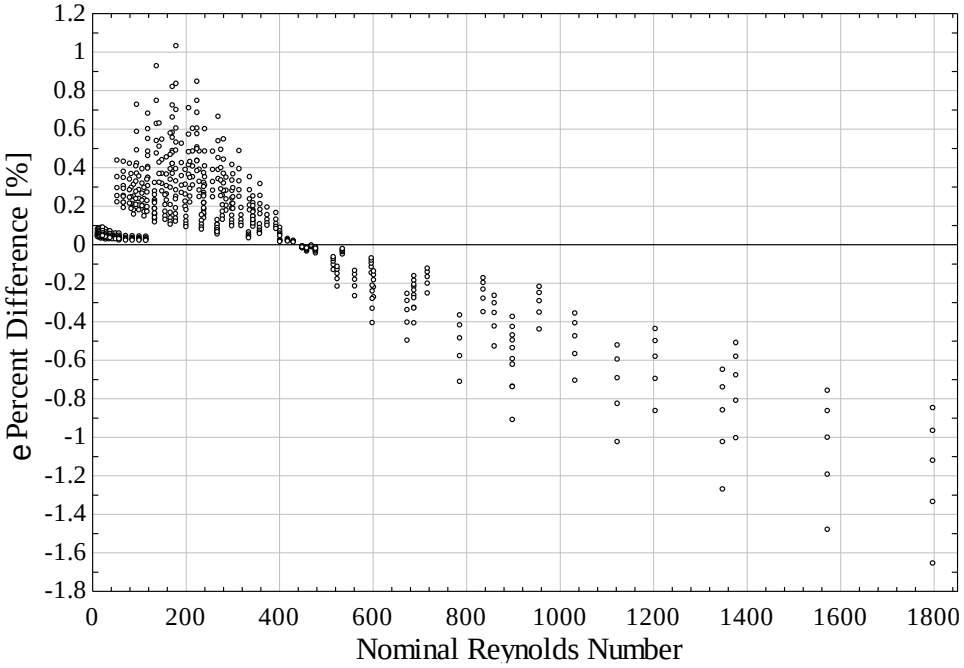

Figure 61: Percent difference in effectiveness predicted by the MATLAB model using the Fluent-derived Nusselt number correlations compared to those developed by Mikulin.

With effectiveness near 1, these percent differences correspond approximately to differences in effectiveness itself. The percent difference was nearly zero at a nominal Reynolds number of 440, which roughly coincided with the convergence of the two Nusselt number correlations at Re = 500 in Figure 41. The two only differ slightly due to the nominal average Reynolds number used to compare cases. At Reynolds numbers below the crossing point of the two correlations, the MATLAB model predicted a higher effectiveness by up to 1.03% when using Fluent correlations for Nusselt number compared to the Mikulin correlation. Above the crossing point, the Mikulin correlations produced higher effectiveness, by up to 1.66%. In general, use of the Mikulin correlations can result in a significant difference in predicted effectiveness, but the difference depends on the specific combination of parameters.

Figure 62 shows the percent difference in pressure drop on each side.

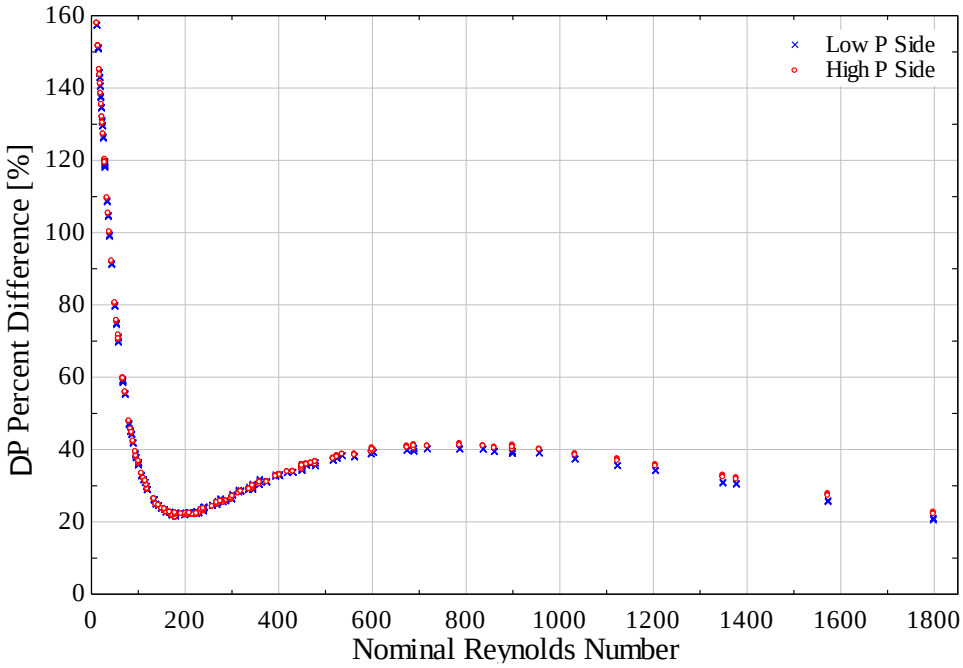

Figure 62: Percent difference in pressure drop predicted by the MATLAB model using the Fluent-derived Darcy friction factor correlations compared to those developed by Mikulin.

The pressure drop was a linear function of the friction factor in the MATLAB model, and also varied linearly with heat exchanger length. The Mikulin friction factor was constant, derived from high Reynolds number behavior. Consequently, the percent difference in pressure drop was identical to the percent difference in Darcy friction factor seen in Figure 35. The MATLAB model predicted a greater pressure drop at all Reynolds numbers using the Fluent correlations. The percent difference became large in the laminar range, approaching 160%. At the local minimum near Re = 200, the difference was about 20%.

From Figure 35, the difference should approach zero beyond approximately Re = 3,000. The highest nominal Reynolds number in Figure 62 of about 1,800 corresponded to a design that would operate with a Reynolds number of about 4,000 at the cold end and about 1,000 at the warm end. This meant that no design considered in this study would produce the same pressure drop using the Mikulin correlation for friction factor as it would using the Fluent correlations.

8. MATLAB Model Parametric Study Results and Discussion

8.1. Set of Parameters

The set of parameters that were varied in the final MATLAB parametric study were deduced via a combination of logical reasoning and manufacturing constraints. All of the parameter reductions discussed in prior sections continue to apply. The heat exchanger size will be limited by weight rather than volume, as discussed in section 4.2. The manufacturing processes constrain the relative sizes of the plate thickness, gap height, and fin height to be roughly equal to maximize the convective heat transfer area density (see section 6.3). The width of the flow channel boarder (labeled b in Figure 63) must be as thin as possible to minimize axial conduction, without being so thin that bonding is unreliable. From Kumar's work that will be discussed in section 9.2.2, the width of the flow channel boarder was set to a constant 2 mm [26].

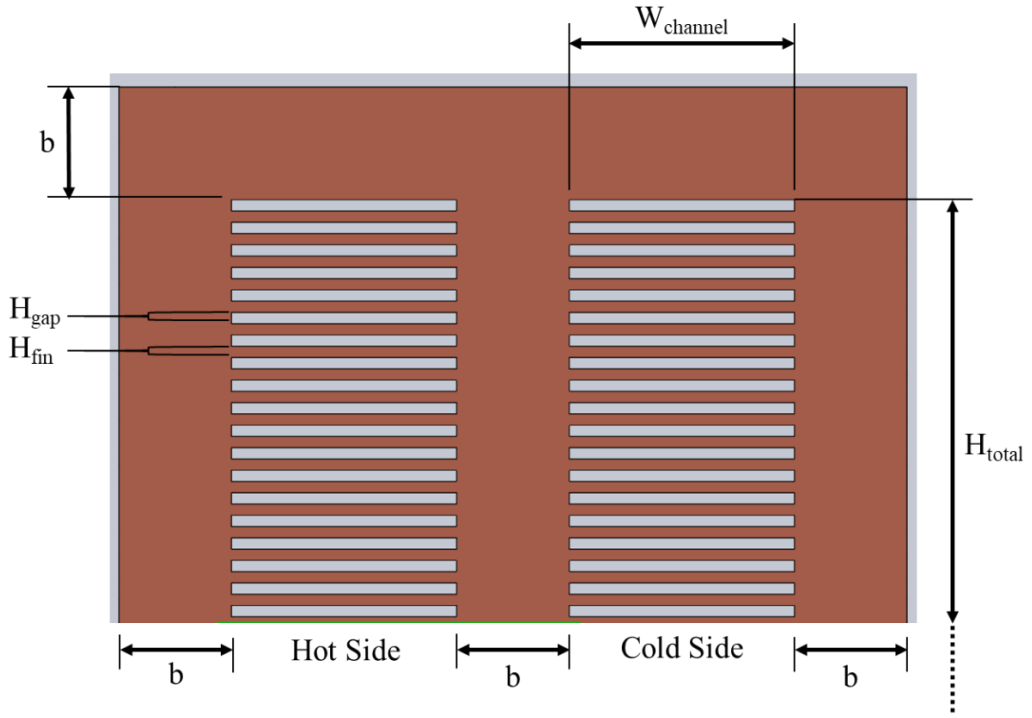

Figure 63: Geometric facets of the slotted plates.

Increasing the channel width or the total height had the same effect on the pressure drop. The open cross-sectional area increased. The fluid velocity and pressure drop were reduced, which is desirable. However, there were two counteracting effects on heat transfer. The lower fluid velocity reduced the convective heat transfer coefficient. Conversely the surface area per plate increased, which increased the total heat transfer area per plate. The increase in surface area and open flow area scaled in the same manner whether $W_{channel}$ or H_{total} was varied. For example, if $W_{channel}$ was doubled, the surface area of each fin doubled and the total surface area per plate doubled. If H_{total} was doubled, the surface area per fin was the same, but the number of fins doubled, so the total surface area also doubled. The same was true for the open flow area cross-section.

In this regard, whether $W_{channel}$ or H_{total} was varied was arbitrary because the effects were the same. However, the fin efficiency decreased with increasing $W_{channel}$ but not with increasing H_{total}. It was concluded that H_{total} should not be varied, and should instead be set to the maximum value allowed in the design specifications of 0.5 m. This ensured the highest surface area per plate for a given fin efficiency. $W_{channel}$ was then varied. The viable designs would have a large enough value of $W_{channel}$ to achieve a high heat transfer area per plate and a low pressure drop, without being so large that the heat transfer would be crippled by low fin efficiency.

The allowable weight was the final parameter chosen to constrain the design space. SHI had not provided a specific target value but were generally interested in designs under 100 lbs. Heavier designs achieved higher effectiveness, but also suffered higher pressure drops. Below a certain weight, no combination of the other parameters resulted in a design that met the

effectiveness requirement set by SHI. The number of plates was linked to the weight. For a given set of parameters, the number of plates that resulted in the specified weight was calculated.

The end result of this process of parameter reduction was 4 total parameters: L_{micro}, the singular length dimension used for the plate thickness, spacer thickness, fin height and gap height; $W_{channel}$, which was also the fin axial length; allowable weight, which was achieved under a given set of parameters by choosing the appropriate number of plates and spacers; and the mass flow rate, which varied from 6 to 12 g/s for the rating and design cases, respectively.

8.2. Discretization Sensitivity

A sensitivity analysis was performed to determine the required number of elements for the MATLAB results to be sufficiently independent of the number of elements that discretize the heat exchanger. The study was performed on the case with the highest weight, smallest L_{micro}, smallest $W_{channel}$, and highest mass flow rate. This case was chosen because it resulted in the longest design in the discretization direction. It was therefore the coarsest case and applying the same number of elements to any other case will result in spatial discretization that is as fine or finer. It was also the case with the largest pressure drop. Figure 64 and Figure 65 display the results for effectiveness and pressure drop, respectively, as a function of the number of elements.

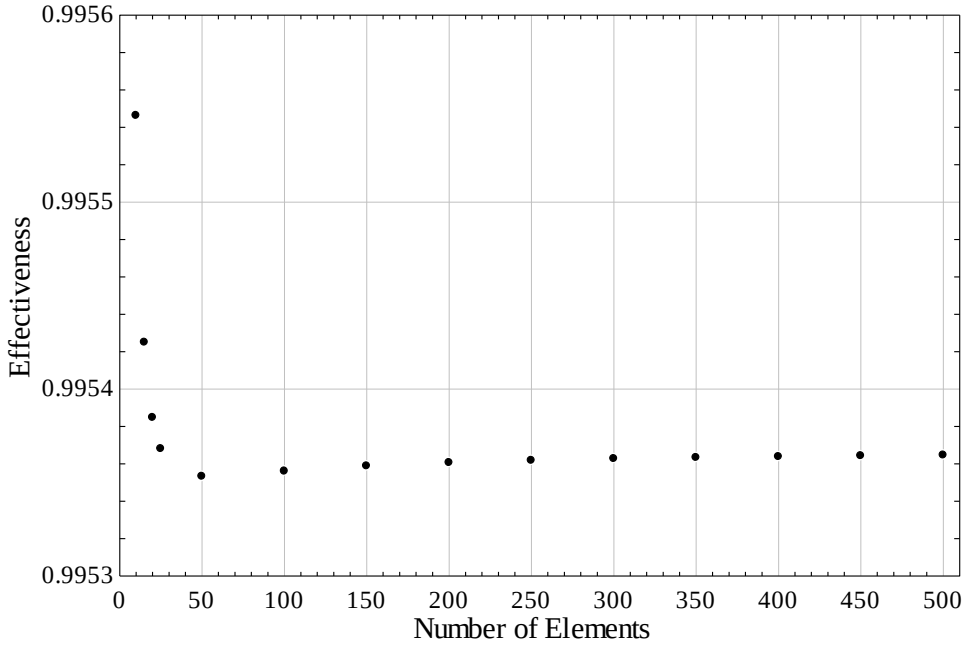

Figure 64: Effect of the number of MATLAB model elements on predicted effectiveness. L_{micro} = 0.064 mm, $W_{channel}$ = 0.5 cm, $\dot{m}$ = 12 g/s, weight = 100 lbs (n_{plates} = 9521).

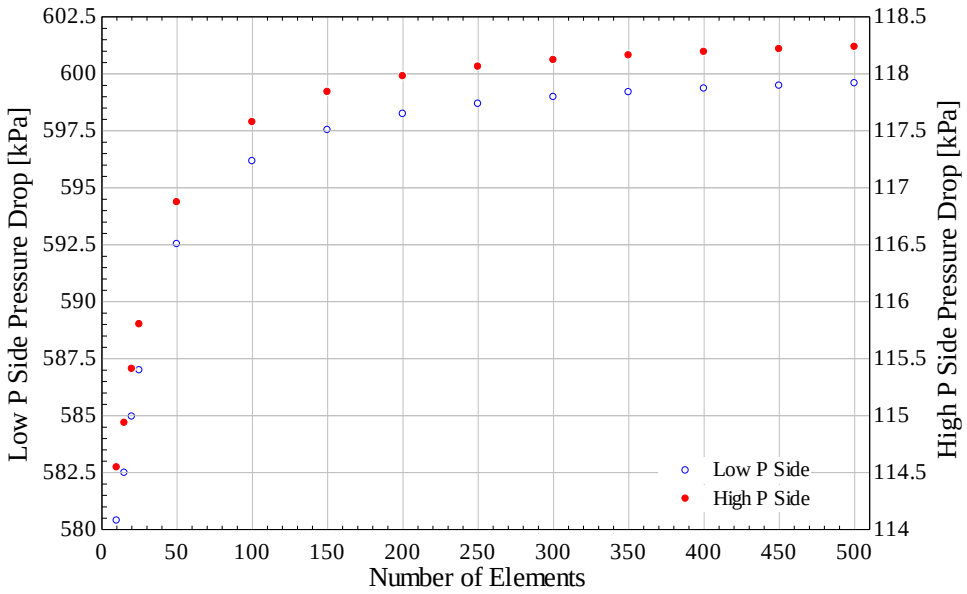

Figure 65: Effect of the number of MATLAB model elements on predicted pressure drop on each side. L_{micro} = 0.064 mm, $W_{channel}$ = 0.5 cm, $\dot{m}$ = 12 g/s, weight = 100 lbs (n_{plates} = 9521).

With just a few hundred elements, the solution appeared to become relatively independent of the number of elements. To establish a point of reference to a solution with an extremely large

number of elements, the model was also solved with n = 10,000 elements, and resulted in ΔP_{low} = 600,453 Pa, ΔP_{high} = 118,405 Pa, and ε = 0.995368 with the chosen set of parameters. Each point plotted in Figure 64 and Figure 65 was compared to the values produced with this very fine discretization as a percent error. By n = 400 elements, the percent error of the low pressure side pressure drop, high pressure side pressure drop, and effectiveness had decreased to 0.1825 %, 0.178 %, and 0.0004 %, respectively. The solution was therefore deemed to be sufficiently independent of the number of elements. 400 elements were used for all subsequent solutions.

It should be noted that the number of elements can be lower than the number of plates and spacers, and it is not necessary to match each element location to a plate or spacer. The correlations for friction factor and heat transfer coefficient were made based on a unit cell, rather than only applying to either the plate regions or spacer regions. Likewise, the stream-to-stream thermal resistance was based on the total heat exchanger UA, and the UA of an arbitrarily sized element was simply the total UA calculated using the temperature, pressure, and gas velocity in that element, multiplied by the fraction of the total heat exchanger length occupied by that element. The axial conduction parameter was treated similarly, with a total axial conduction parameter for the entire heat exchanger calculated using the material properties present in each element, but that axial conduction parameter was only applied to the energy balance of that particular element. Errors associated with a continuous rather than a stepwise temperature profile are small provided the number of plates is large [12].

8.3. Data Reduction

Some observations were used to further reduce the amount of data. The initial range of parameters chosen was broad, with 0.064 mm $\leq L_{micro} \leq$ 1 mm, 50 lbs $\leq$ Weight $\leq$ 100 lbs, 0.4 cm $\leq W_{channel} \leq$ 2 cm, and 6 g/s $\leq \dot{m} \leq$ 12 g/s. The capacitance rates on each side were almost equal

because the mass flow rate was identical, and the specific heat capacity was almost the same despite the different operating pressure on each side. The heat exchanger was therefore balanced, and the effectiveness on each side was the same. Figure 66 displays the nearly identical effectiveness of the low and high pressure sides for the 81 unique combinations that result from assigning the highest, lowest, and central intermediate values to each of the 4 parameters. The number of design points was limited for the sake of plot clarity.

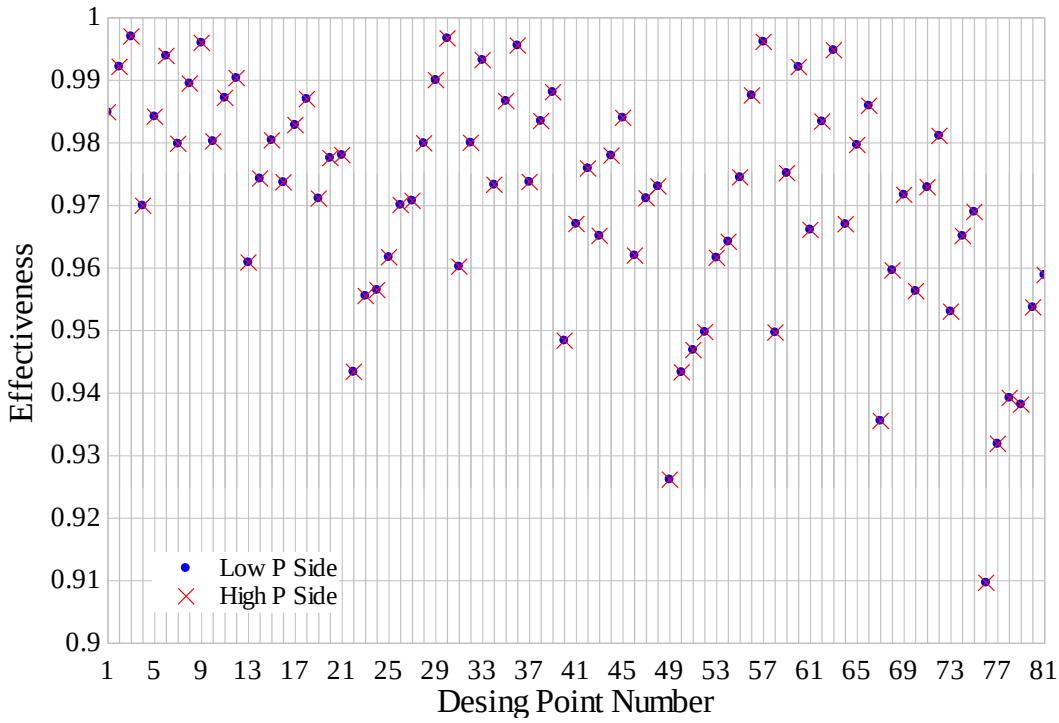

Figure 66: High and low pressure side effectiveness for 81 combinations of parameters. L_{micro} = 0.064, 0.532, and 1 mm; Weight = 50, 75, and 100 lbs; $W_{channel}$ = 0.4, 1.2, and 2 cm; $\dot{m}$ = 6, 9, and 12 g/s.

However, the lower pressure on the return side resulted in a lower helium density and higher velocity, which translated to a higher pressure drop for every given parameter combination, seen in Figure 67.

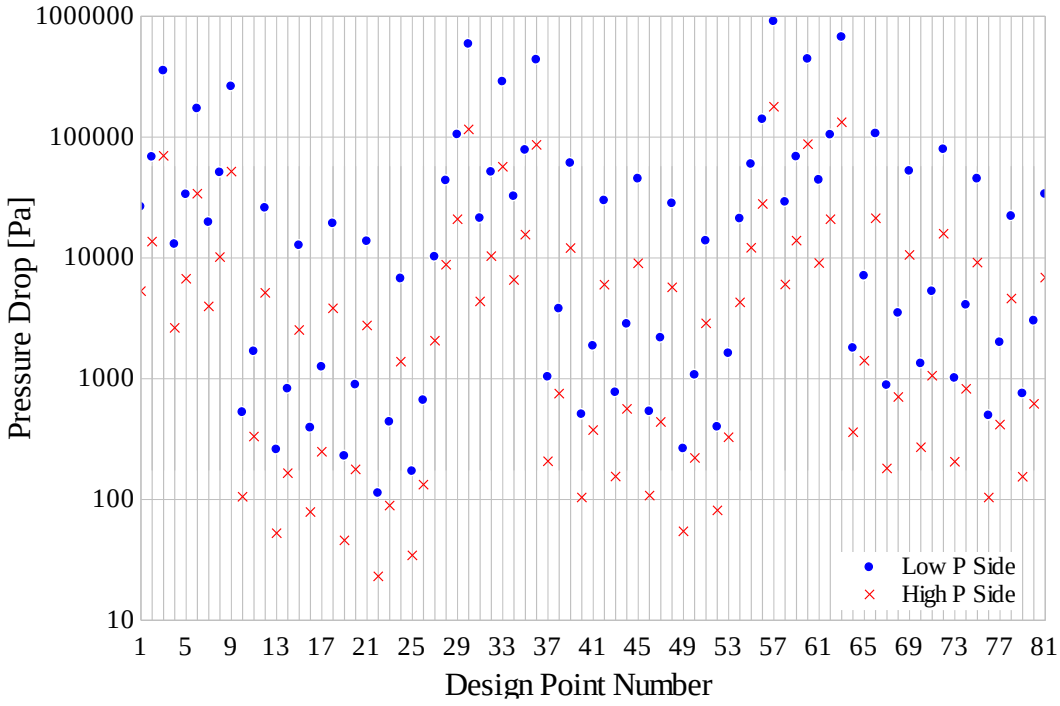

Figure 67: Comparison of pressure drop on each side for 81 combinations of parameters. L_{micro} = 0.064, 0.532, and 1 mm; Weight = 50, 75, and 100 lbs; $W_{channel}$ = 0.4, 1.2, and 2 cm; $\dot{m}$ = 6, 9, and 12 g/s.

Additionally, the specifications provided by SHI stated that the maximum allowable pressure drop on the low pressure side was only 100 kPa, as opposed to 300 kPa on the high pressure side. For a given set of parameters, the low pressure side always had a higher pressure drop than the high pressure side, but was restricted to a lower maximum allowable pressure drop. Only the low pressure side needed to be considered when analyzing the viability of each design. As long as a design met the effectiveness and pressure drop requirements on the low pressure side, the high pressure side was guaranteed to have an equal effectiveness and operate within its pressure limitations.

Within the range of values for each parameter that were considered, for any given combination of weight, $W_{channel}$, and L_{micro}, the effectiveness was observed to monotonically decrease with increasing mass flow rate while the pressure drop monotonically increased. Figure

68 and Figure 69 show the effectiveness and pressure drop on the low pressure side for 27 designs, color coded by geometric parameter. Figure 70 shows the same data points, color coded by mass flow rate, with designs that share the same geometry circled. The weight was set to 100 lbs for all points for the sake of plot clarity, and each point is a unique combination of $W_{channel}$, L_{micro}, and $\dot{m}$.

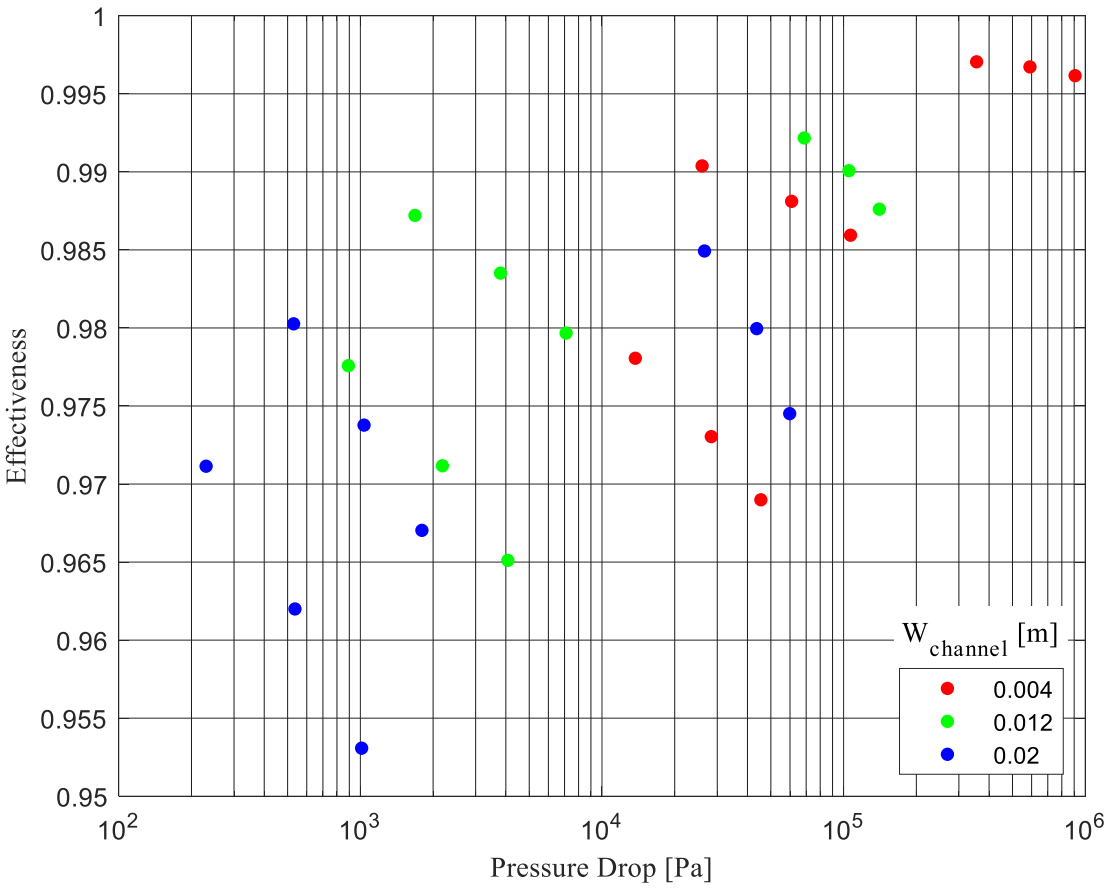

Figure 68: 100 lb. design permutations with 3 values for $W_{channel}$, L_{micro}, and $\dot{m}$, color-coded by channel width.

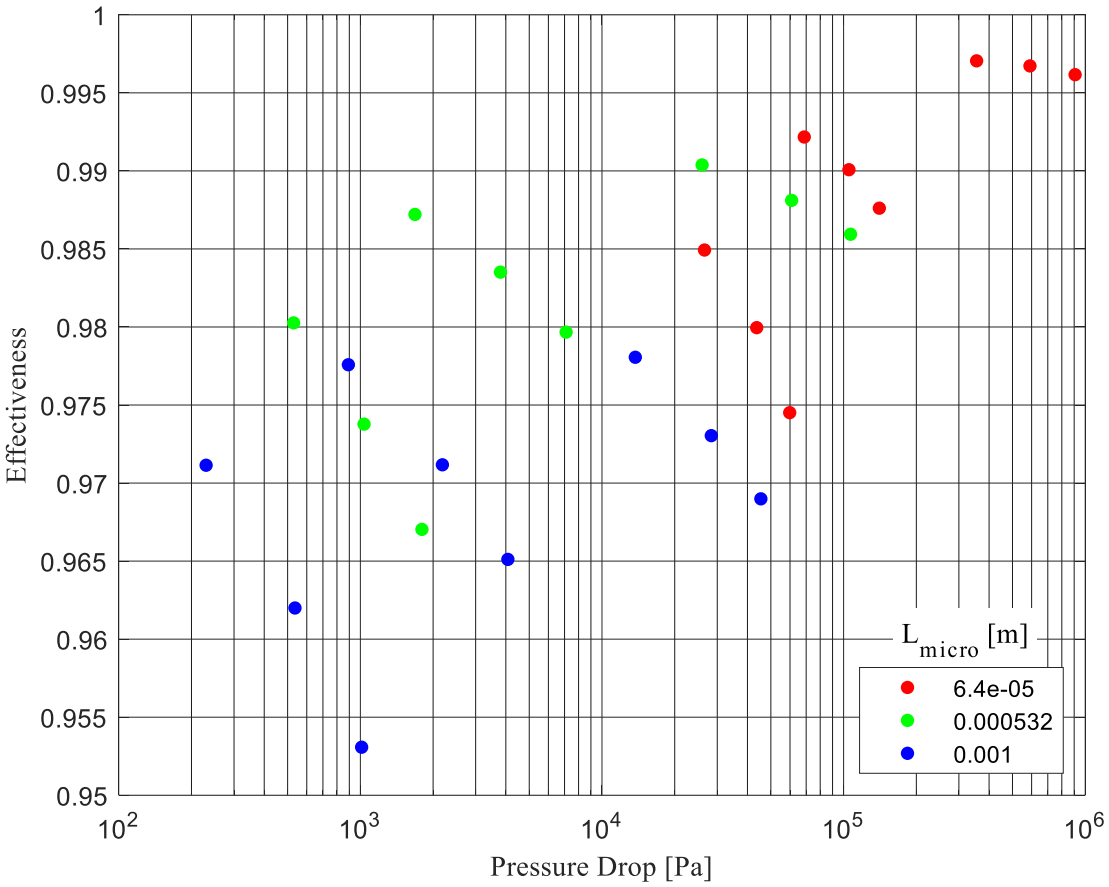

Figure 69: 100 lb. design permutations with 3 values for $W_{channel}$, L_{micro}, and $\dot{m}$, color-coded by L_{micro}.

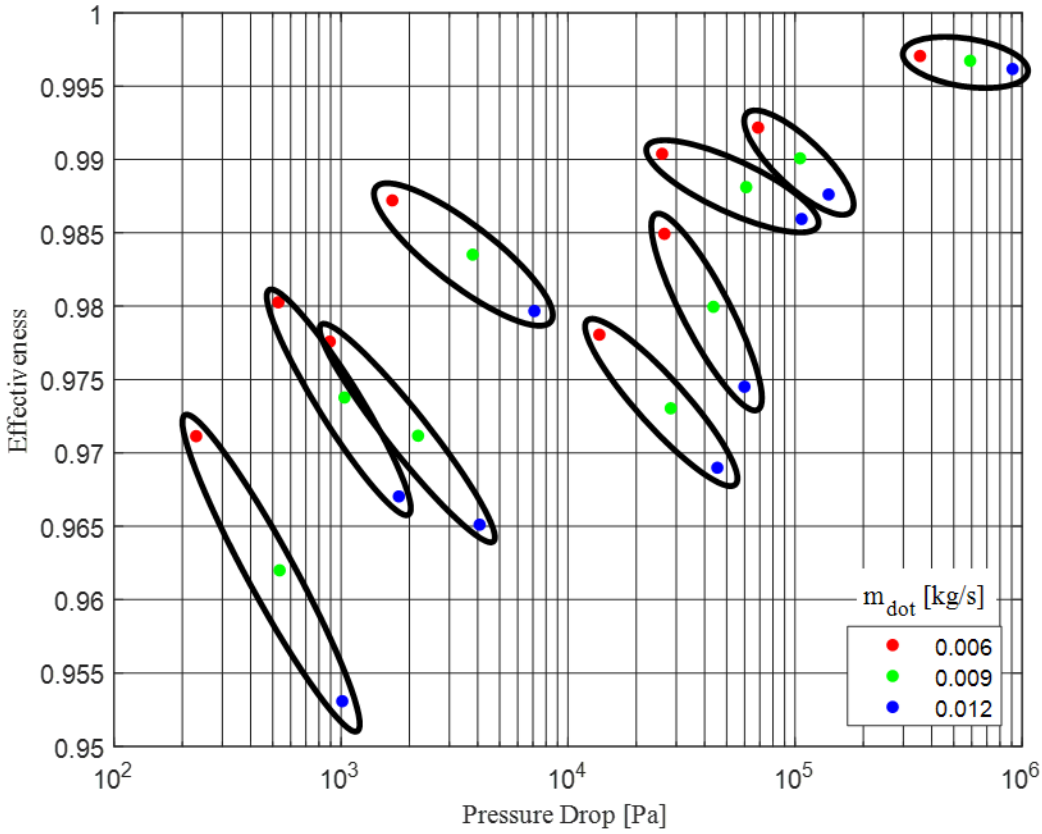

Figure 70: 100 lb. design permutations with 3 values for $W_{channel}$, L_{micro}, and $\dot{m}$, color-coded by $\dot{m}$. The circled groups denote configurations that share the same $W_{channel}$ and L_{micro}.

To be considered viable by SHI's metrics, a design must achieve an effectiveness in excess of 99% while the low pressure side pressure drop remains below 100 kPa. The design must meet these criteria throughout the entire range of mass flow rates, from the rating case (6 g/s) to the design case (12 g/s). Because the highest mass flow rate case of each design always had both the lowest effectiveness and the highest pressure drop, only the 12 g/s case needed to be considered in assessing the viability of designs. As long as a design met the effectiveness and pressure drop requirements at the highest mass flow rate, lesser mass flow rates were guaranteed to have a higher effectiveness and lower pressure drop.

To conclude this section, when evaluating the ability of a design to meet the pressure drop and effectiveness requirements, 1) Only the effectiveness of one side of the heat exchanger needed to be considered because it was the same on both sides, 2) Only the low pressure side needed to be considered because it experienced a higher pressure drop than the high pressure side while restricted to a lower allowable pressure drop, and 3) Only the highest mass flow rate had to be considered because, for a given geometry, it resulted in the lowest effectiveness and highest pressure drop.

8.4. Results and Analysis

8.4.1. Initial Broad Parameter Range

Initially, a broad range of values were chosen for weight, $W_{channel}$, and $L_{micro.}$ The parameter ranges were 0.4 cm $\leq W_{channel} \leq$ 2 cm, 0.064 mm $\leq$ Lmicro $\leq$ 1 mm, and 50 lbs $\leq$ weight $\leq$ 100 lbs, with 11 evenly spaced values for each parameter. The result was 1,331 unique geometries. All were evaluated at the 12 g/s case. Figure 71, Figure 72, and Figure 73 display the low pressure side pressure drop and effectiveness that resulted from every combination, color-coded by each parameter. The minimum effectiveness and maximum pressure drop for viable designs are marked by the horizontal line at 0.99 and vertical line at 10^5 Pa.

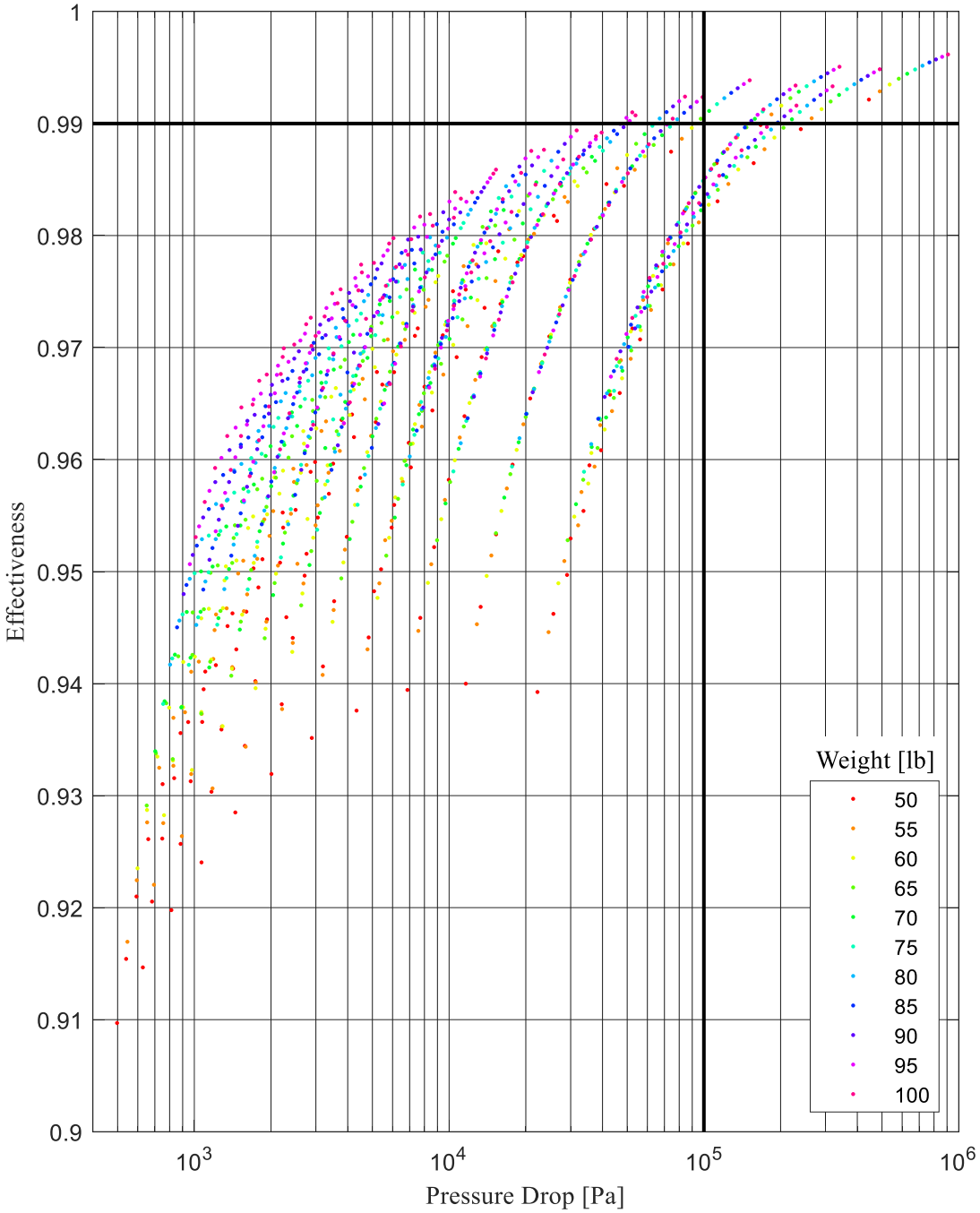

Figure 71: Effectiveness and low pressure side pressure drop of design permutations with $\dot{m}$ = 12 g/s, 0.4 cm ≤ $W_{channel}$ ≤ 2 cm and 0.064 mm ≤ Lmicro ≤ 1 mm, with 11 evenly spaced values for each parameter, and allowed weight ranging from 50 to 100 lbs.

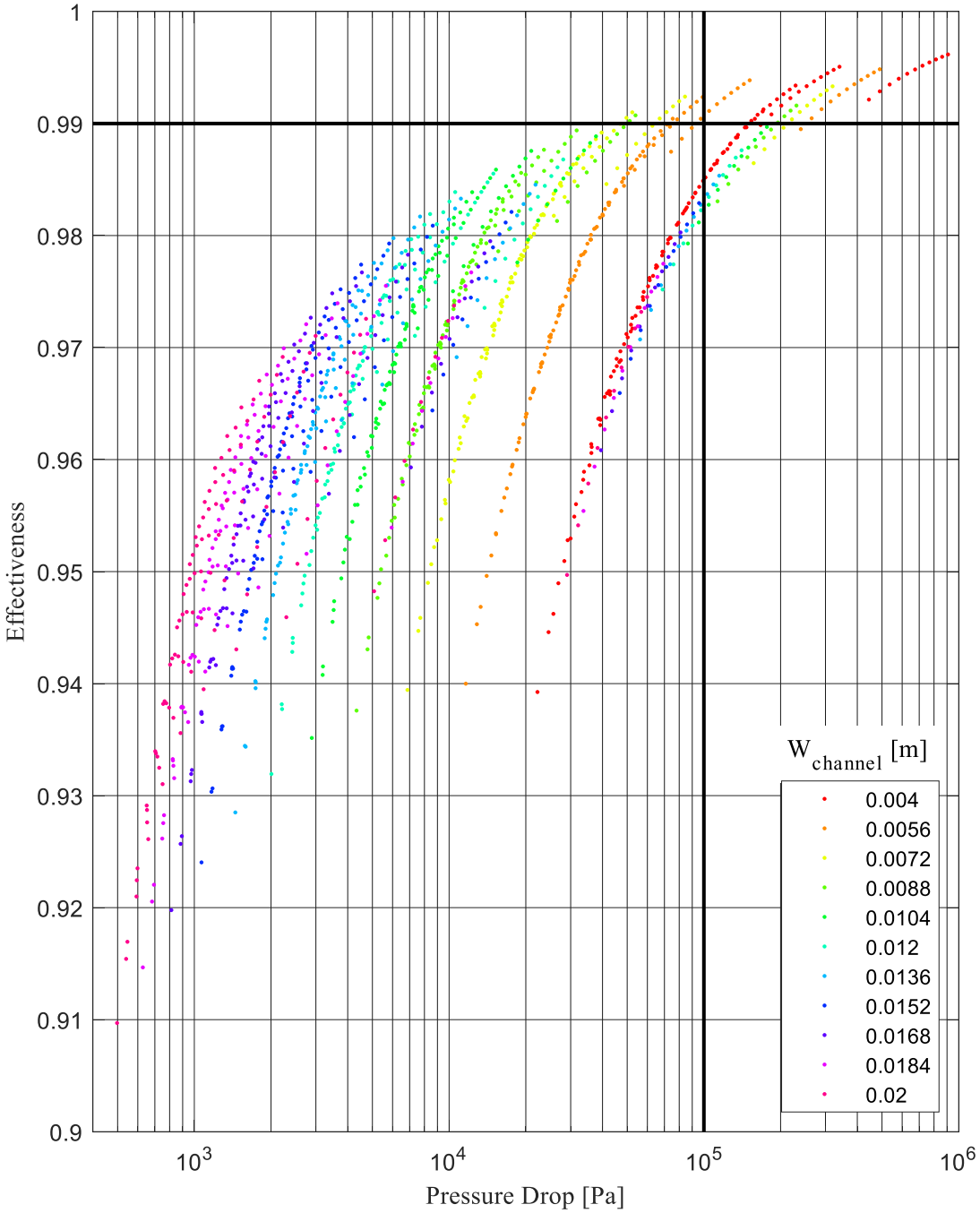

Figure 72: A duplicate of Figure 71, color-coded by $W_{channel}$.

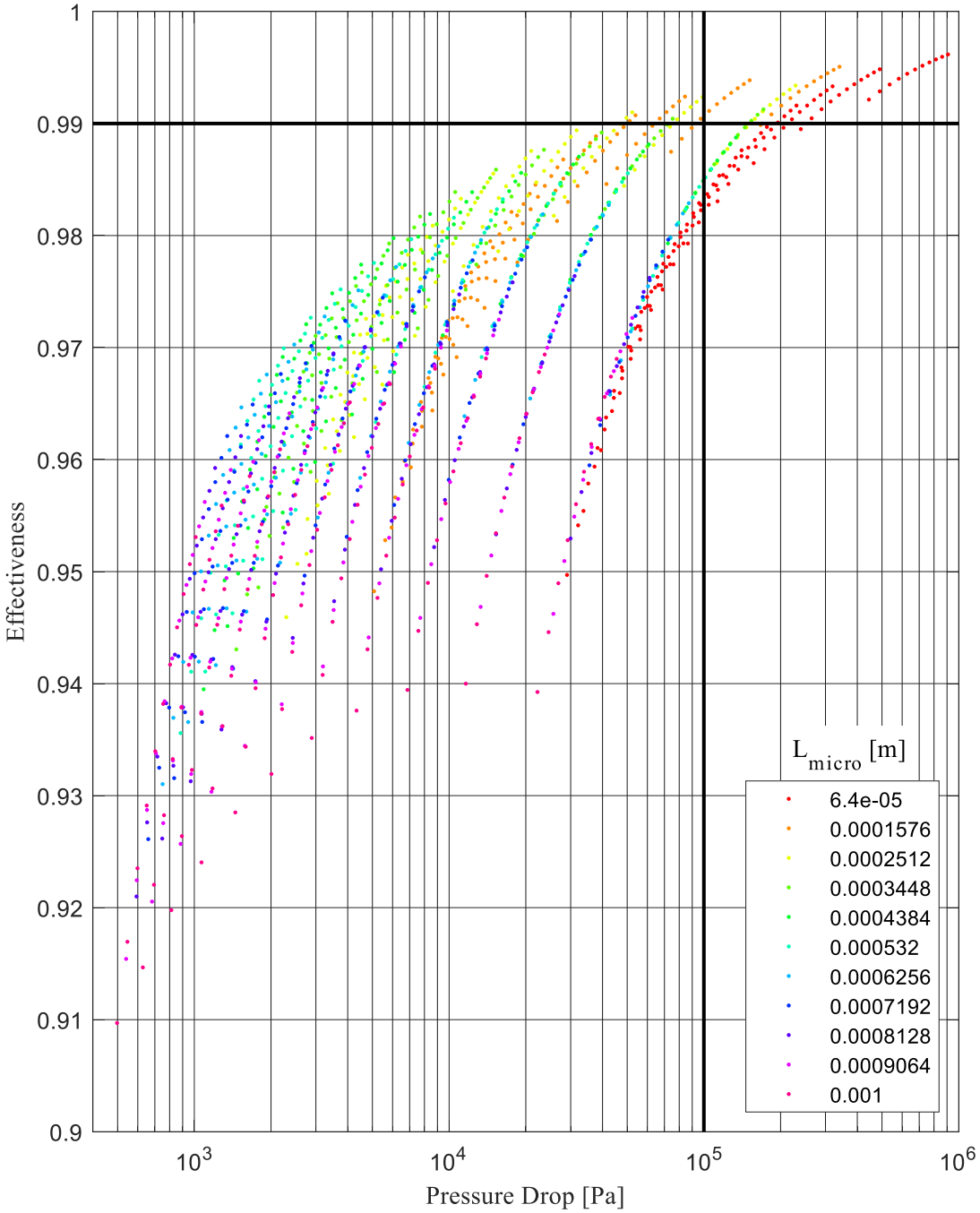

Figure 73: A duplicate of Figure 71, color-coded by L_{micro}.

The plots reveal that some designs weigh under 100 lbs while achieving the desired effectiveness and pressure drop. The initial range of values chosen was excessivly broad. Some of the larger values of $W_{channel}$ and L_{micro} were not capable of attaining the required effectiveness, even with the large number of plates assocaited with the 100 lb designs. Likewise, it was impossible to achieve a high enough effectiveness with the lightest designs. The smallest values of L_{micro} did achieve a high enough effectiveness, but only in conjunction with excessive pressure drop, seen as the red markers in Figure 73.

8.4.2. Refined Parameter Range Near Viable Designs

Through a process of trial and error, the range was modified such that the maximum and minimum value of each parameter was just beyond the point where, no matter what combination of other parameters were paired with it, a viable design would never result. The range of each parameter was refined to more appropriate values, which increased the population of viable designs. The new parameter ranges were 0.4 cm $\leq W_{channel} \leq$ 1 cm, 0.064 mm $\leq$ Lmicro $\leq$ 0.5 mm, and 55 lbs $\leq$ weight $\leq$ 100 lbs. Figure 74, Figure 75, and Figure 76 display the pressure drop and effectiveness for designs within the refined range of parameters color-coded by weight, $W_{channel}$ and L_{micro}, respectively.

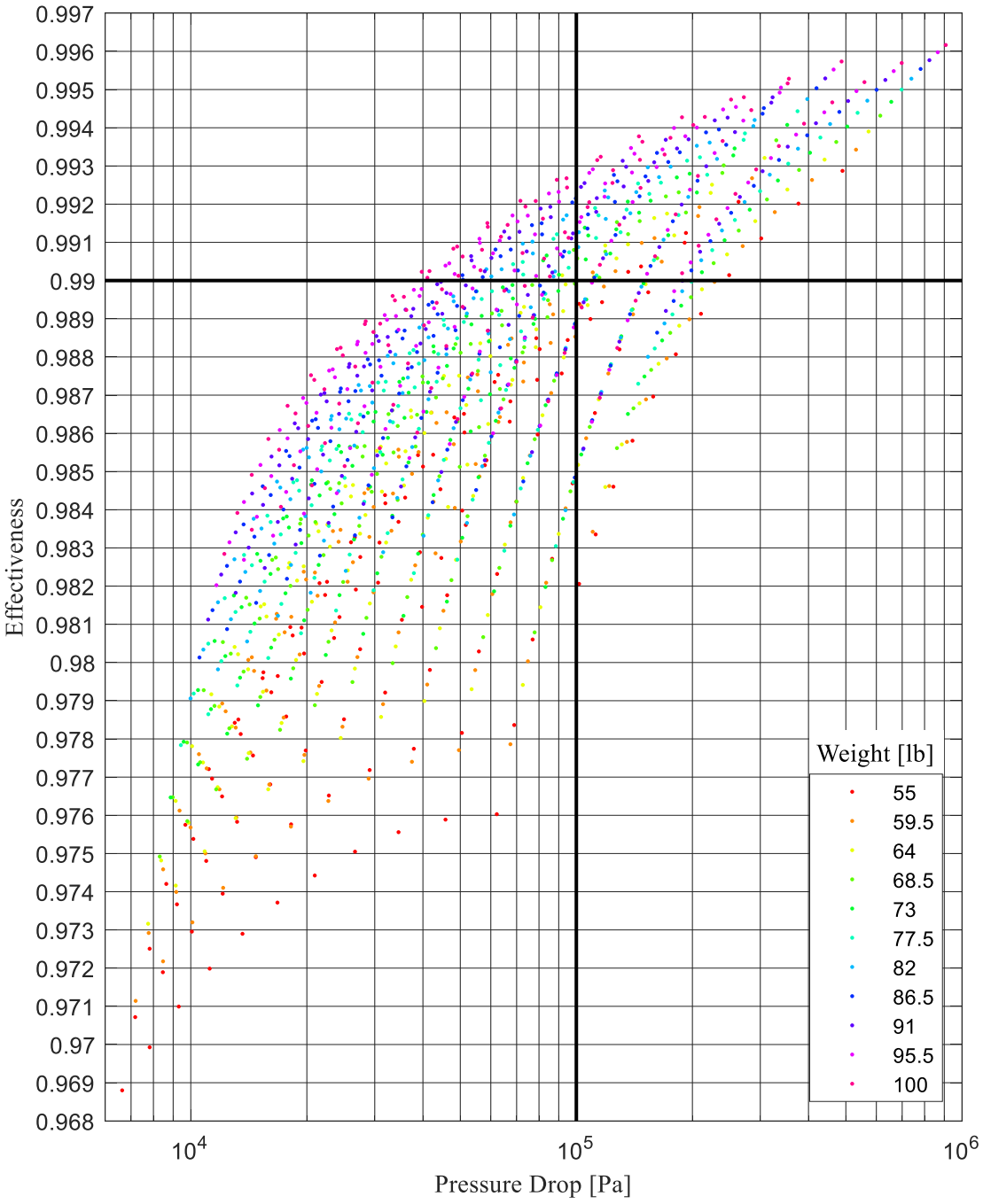

Figure 74: Effectiveness and low pressure side pressure drop of design permutations with $\dot{m}$ = 12 g/s, 0.4 cm ≤ $W_{channel}$ ≤ 1 cm and 0.064 mm ≤ Lmicro ≤ 0.5 mm, with 11 evenly spaced values for each parameter, and allowed weight ranging from 55 to 100 lbs.

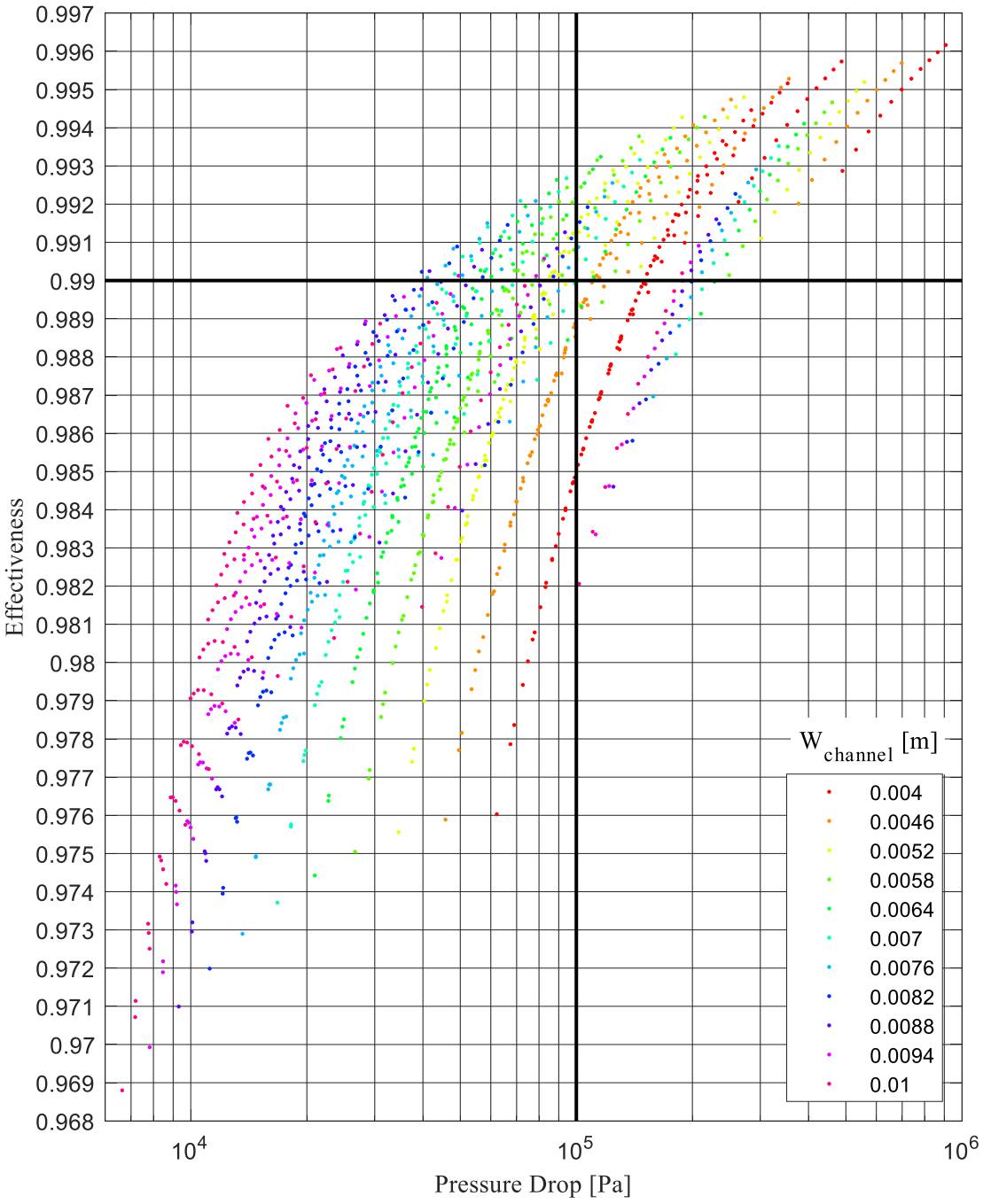

Figure 75: A duplicate of Figure 74, color-coded by $W_{channel}$.

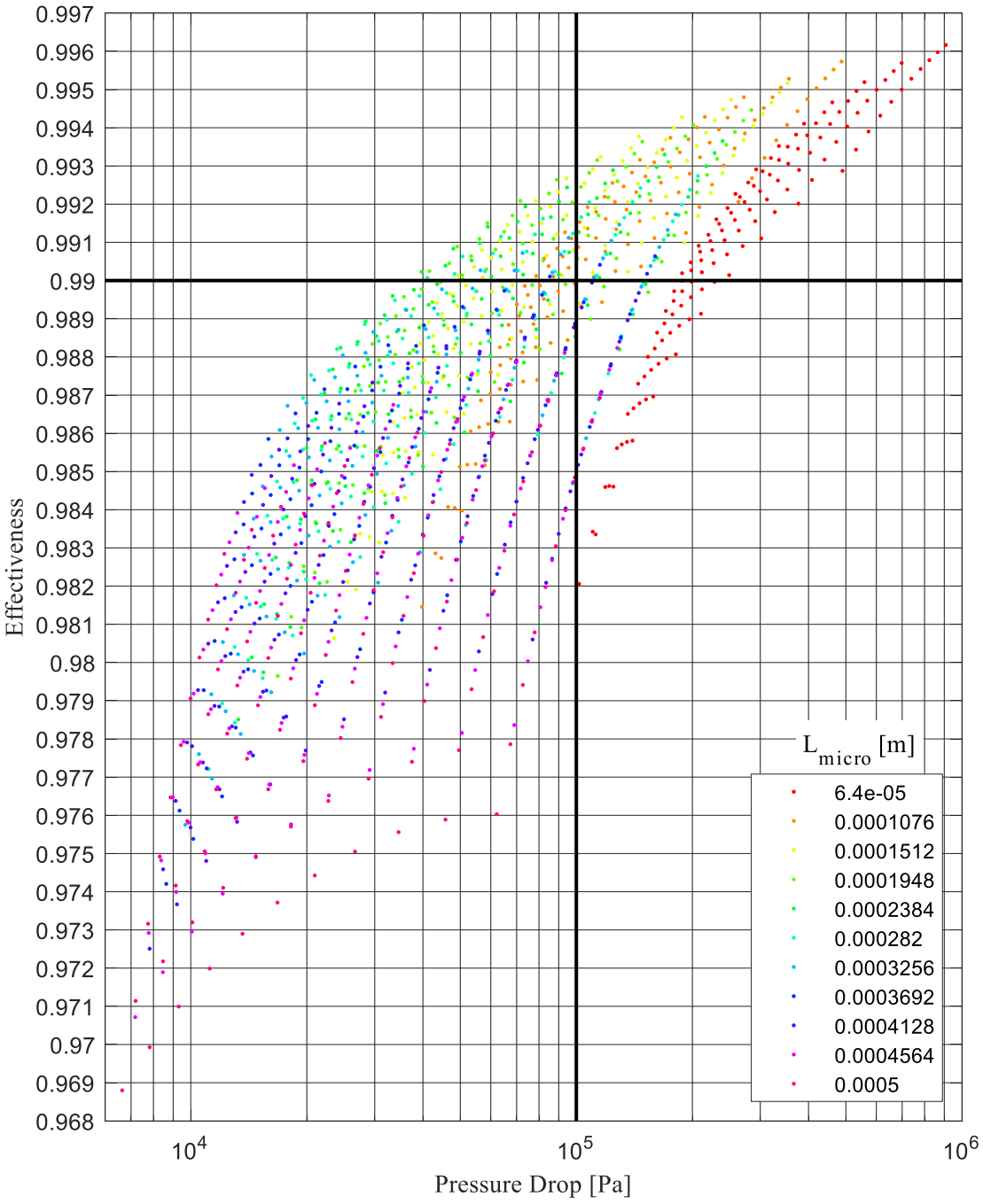

Figure 76: A duplicate of Figure 74, color-coded by L_{micro}.

Generally, the higher the allowed weight, the larger the plate number, higher the effectiveness, and higher the pressure drop. The highest effectiveness was 0.9927 and occurred very close to the limit of allowable pressure drop, with $W_{channel}$ = 0.7 cm and L_{micro} = 0.1512 mm. The design with the lowest pressure drop that still barely achieved 0.99 effectiveness exhibited 40 kPa of pressure loss, with $W_{channel}$ = 0.82 cm and L_{micro} = 0.2384 mm. Both coincided with the largest allowable weight of 100 lbs.

8.4.3. Determination of the Lightest Viable Design

To determine the lightest possible design, the parameter ranges were reduced further to refine the increments of the parameter values and increase the density of points in the vicinity of the lightest designs. L_{micro} was limited to 0.1 to 0.2 mm. The range for $W_{channel}$ was adjusted to 0.45 to 0.7 cm. The weight range was also refined once it became evident that the lightest design would be between 60 to 65 lbs. Figure 77, Figure 78, and Figure 79 display the pressure drop and effectiveness of designs with paramter value ranges that produced the lightest viable designs, color-coded by L_{micro}, $W_{channel}$ and weight, respectively.

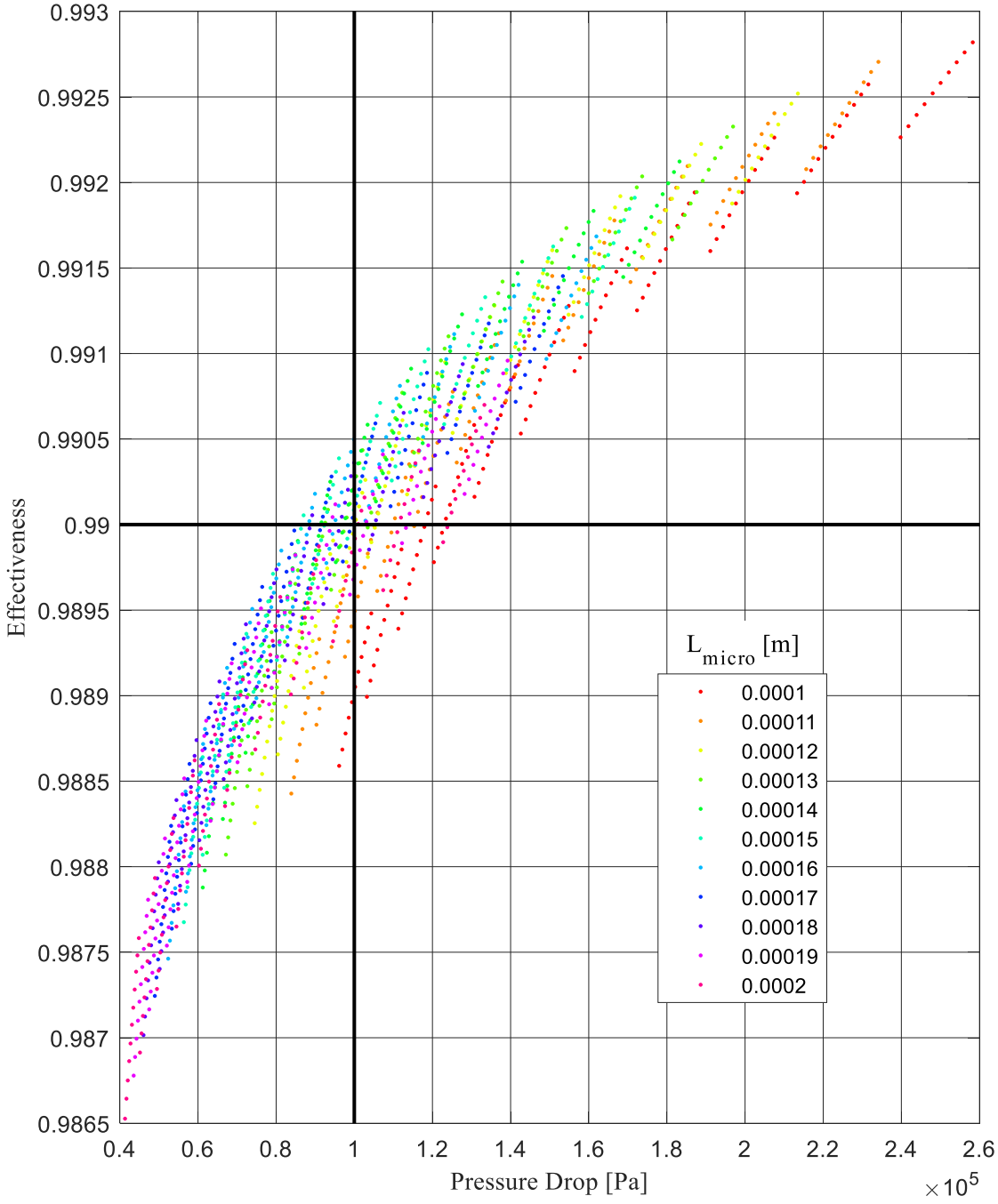

Figure 77: Effectiveness and low pressure side pressure drop of design permutations with $\dot{m}$ = 12 g/s, 0.44 cm ≤ $W_{channel}$ ≤ 0.7 cm and 0.1 mm ≤ Lmicro ≤ 0.2 mm, with 11 evenly spaced values for each parameter, and allowed weight ranging from 60 to 65 lbs.

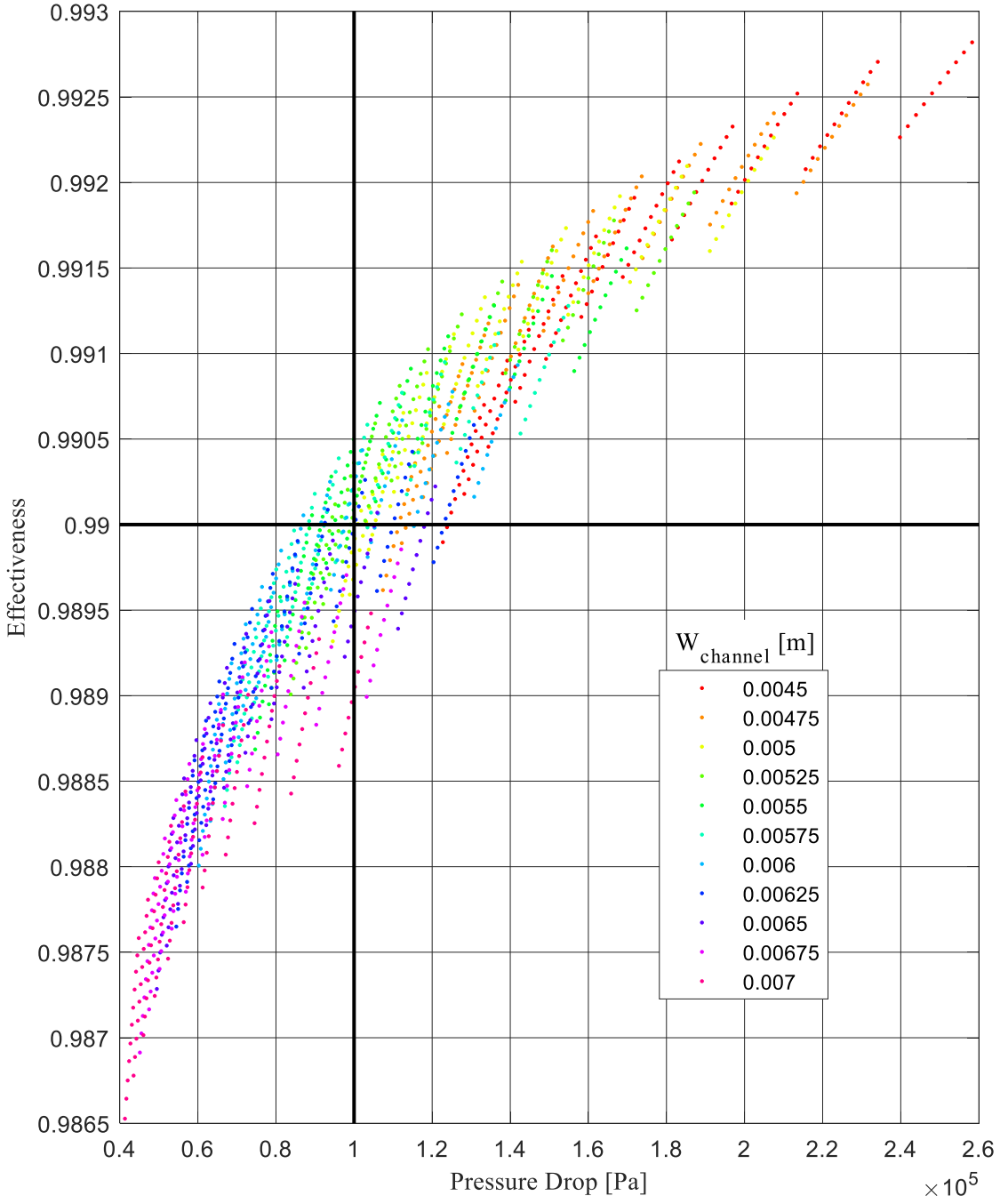

Figure 78: A duplicate of Figure 77, color-coded by $W_{channel}$.

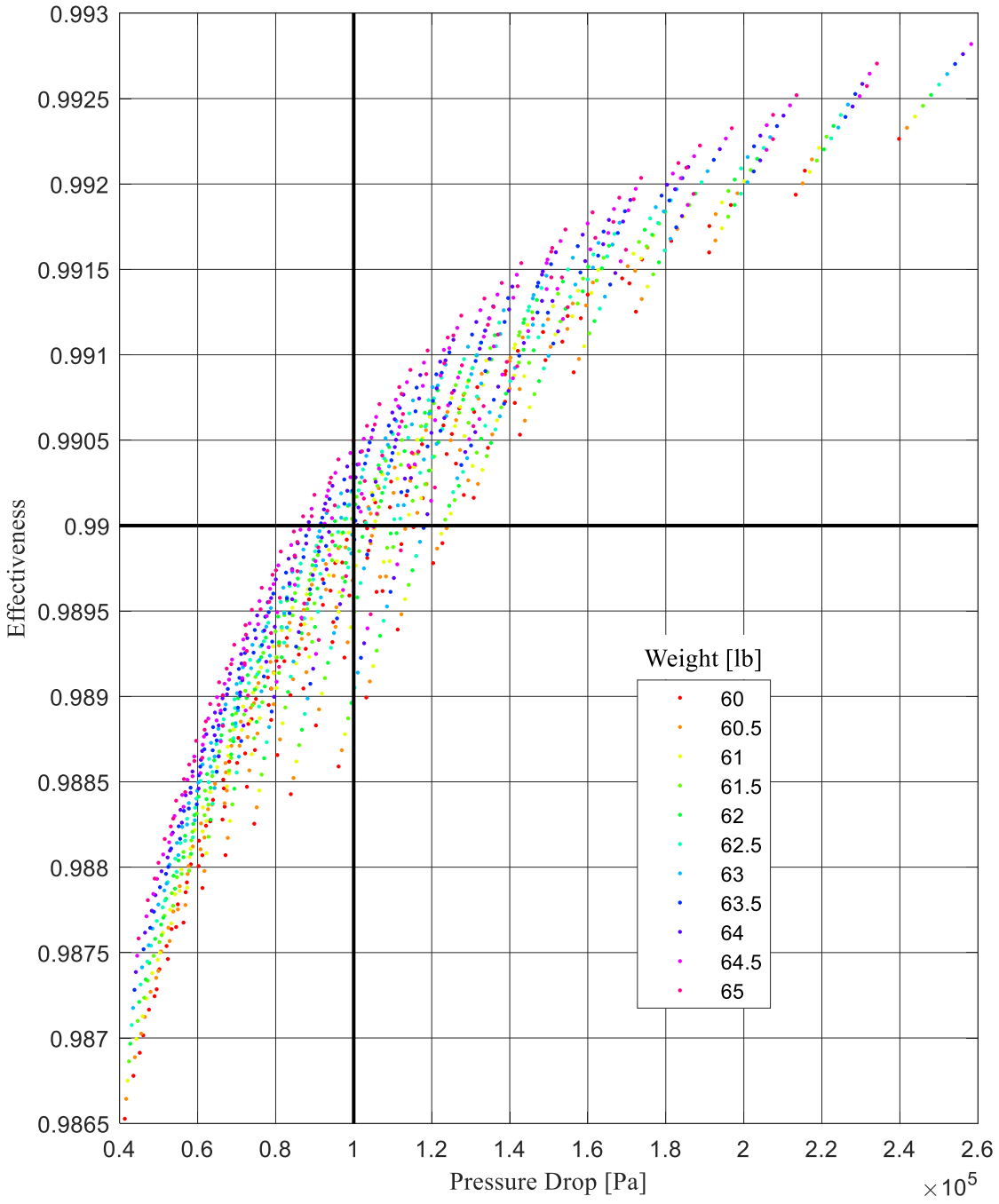

Figure 79: A duplicate of Figure 77, color-coded by weight.

The lightest possible design that can achieve 99% effectiveness and remain under 100 kPa of pressure drop weighed 61 lbs, with $W_{channel}$ = 0.55 cm and L_{micro} = 0.15 mm. The corresponding number of plates was 2403, and the total length was 0.721 m. The total volume was only 0.00618 m^3, well under the maximum allowable 0.1 m^3. Figure 81, Figure 80, and Figure 82 display the lightest viable design points, color-coded by number of plates, total length, and total volume, respectively.

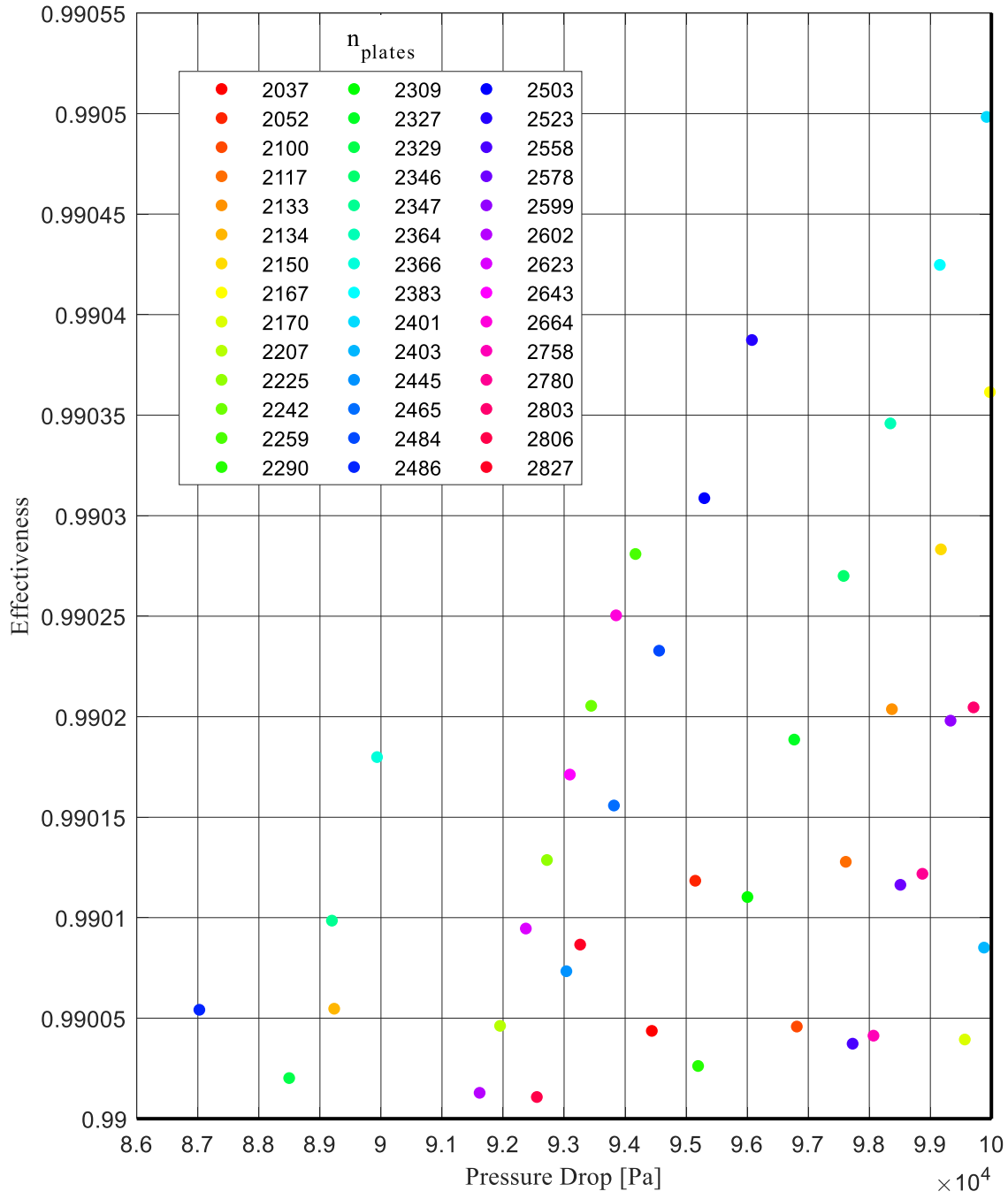

Figure 80: Effectiveness and low pressure side pressure drop of design permutations with $\dot{m}$ = 12 g/s, 0.44 cm ≤ $W_{channel}$ ≤ 0.7 cm and 0.1 mm ≤ Lmicro ≤ 0.2 mm, with 11 evenly spaced values for each parameter, and allowed weight ranging from 60 to 65 lbs. Points are color-coded by n_{plates}.

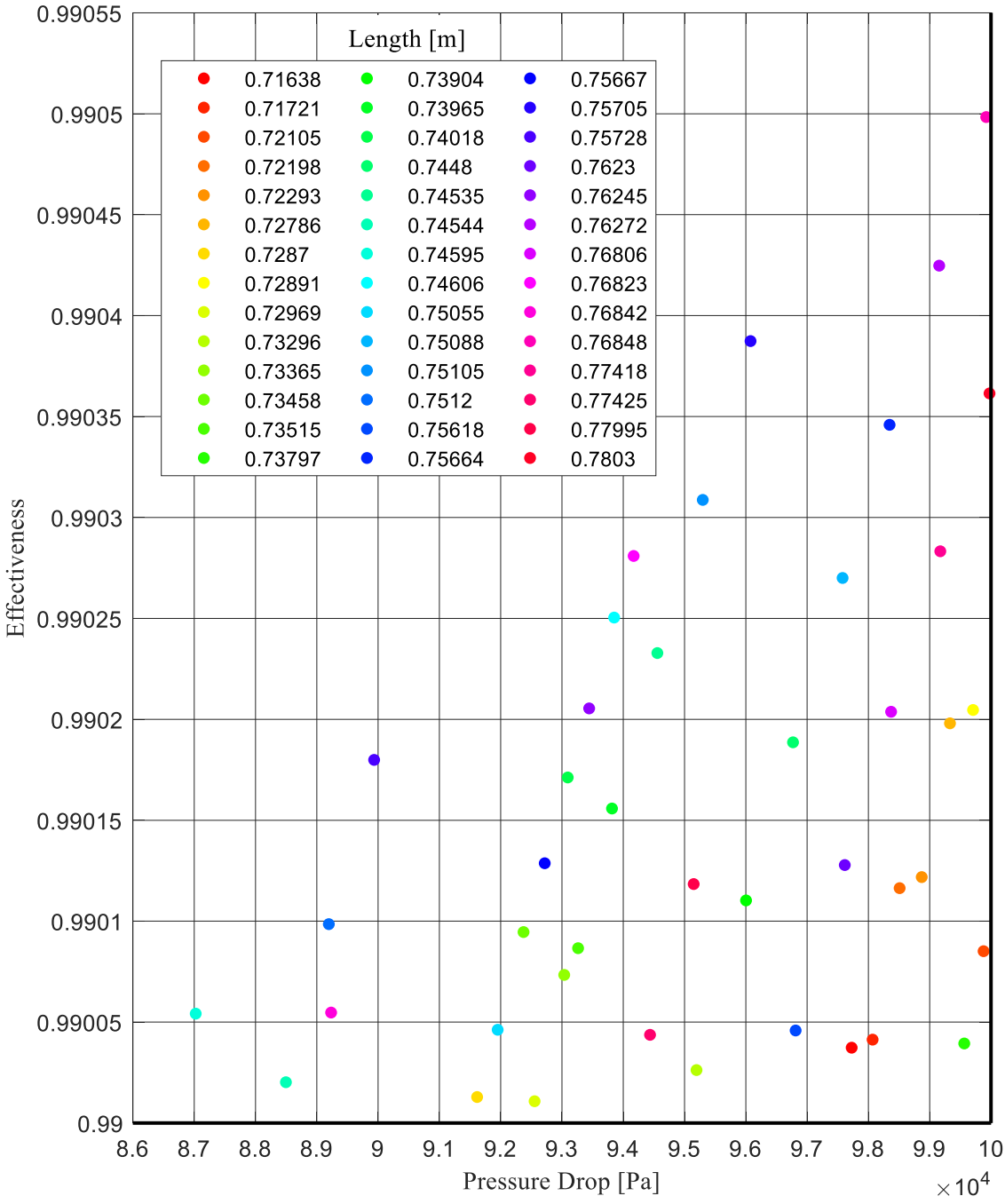

Figure 81: Duplicate of Figure 80, color-coded by total heat exchanger length.

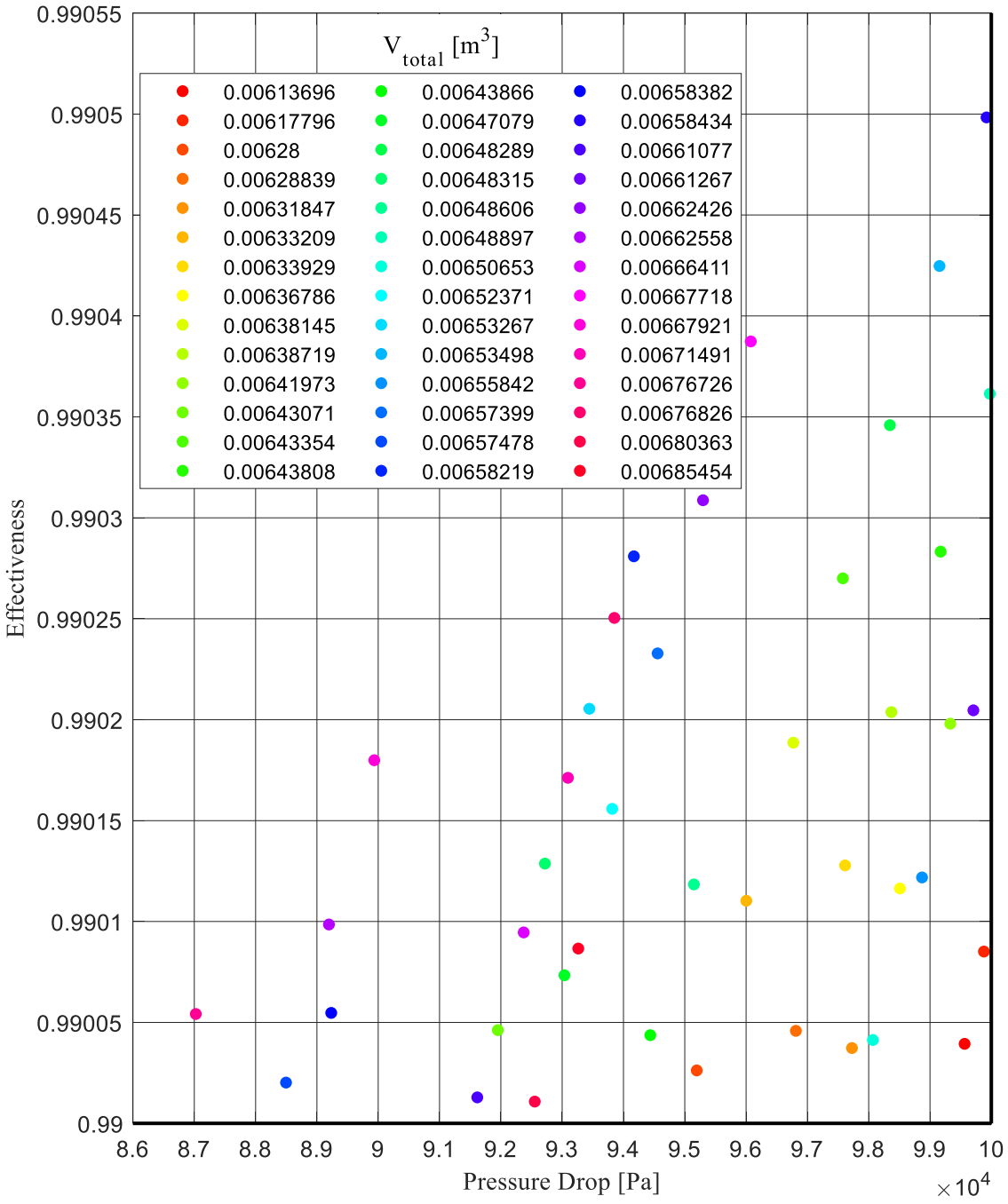

Figure 82: Duplicate of Figure 80, color-coded by total volume.

As shown before, all designs that met the effectiveness and pressure drop requirements at the highest mass flow rate also would do so at reduced mass flow rates within the parameter ranges studied. Figure 83 shows the dependence of effectiveness and pressure drop on mass flow rate for the lightest viable design.

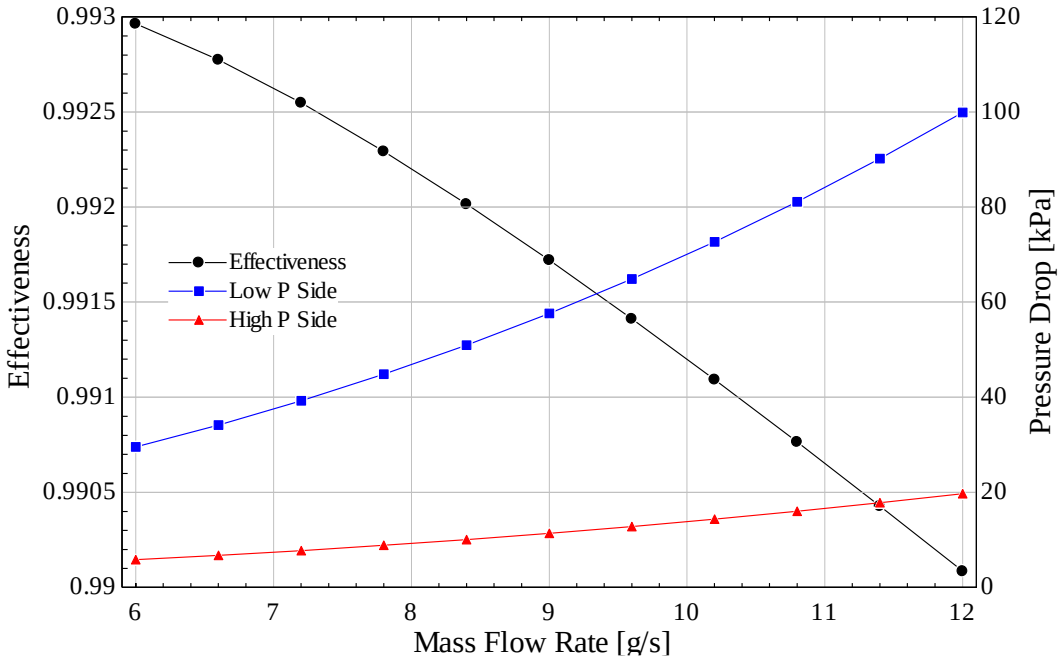

Figure 83: Effectiveness and pressure drops for the lightest possible design that meets the effectiveness and pressure drop criteria as a function of the mass flow rate.

The pressure drop and effectiveness were just barely within the allowable limits at the 12 g/s case, and the margins increased as the mass flow rate decreased.

The temperature profile is depicted in Figure 84.

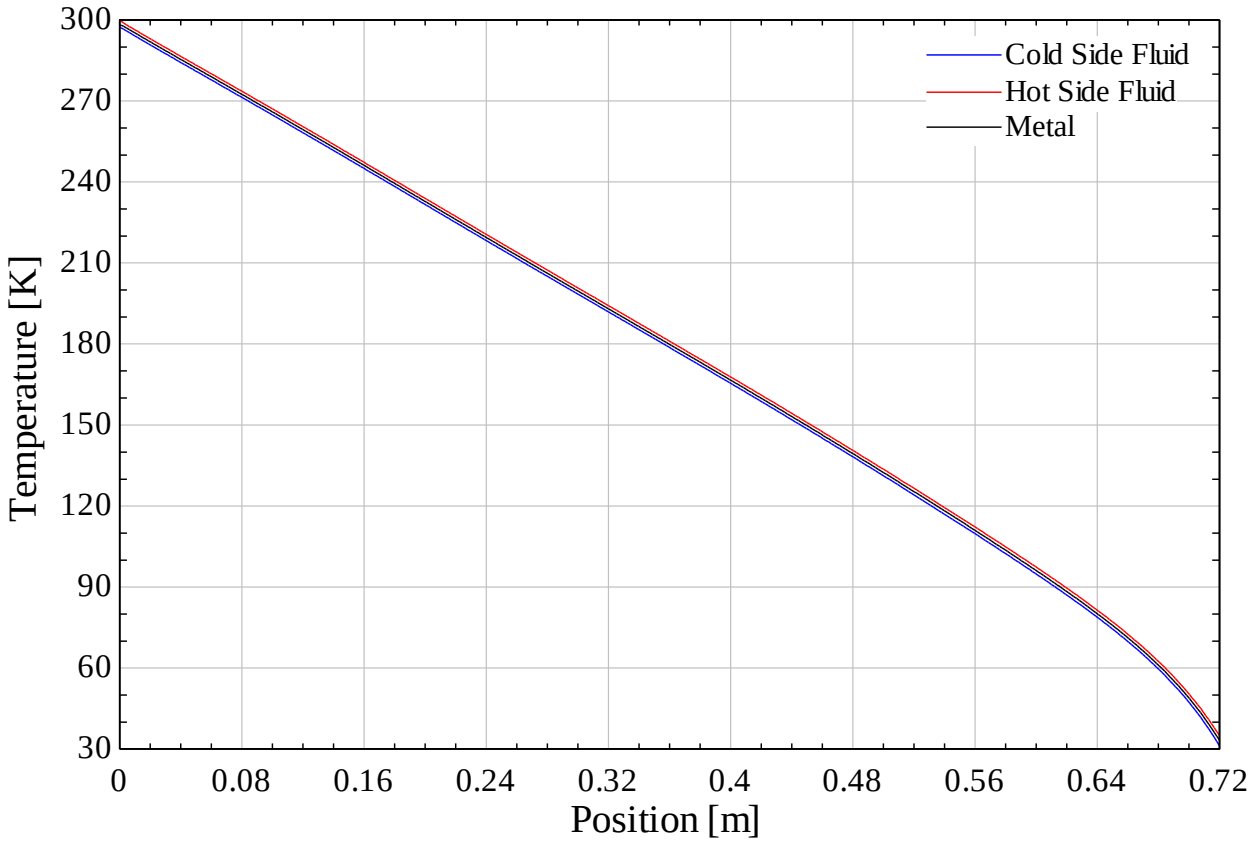

Figure 84: Temperature profile of the lightest viable heat exchanger operating at $\dot{m}$ = 12 g/s.

The high effectiveness coincides with a very small temperature difference between the two flow streams. Below about 70 K the temperature profile becomes nonlinear, indicating the onset of non-ideal gas behavior.

8.4.4. Effects of Individual Parameter Variation

Using the parameters of the lightest design and 12 g/s mass flow rate, each individual parameter was varied while holding the others constant to observe the effects of each parameter on effectiveness and low pressure side pressure drop. As suspected, as H_{total} increases, so does the effectiveness, while the pressure drop decreases, confirming that H_{total} should be maximized within spatial limitations.

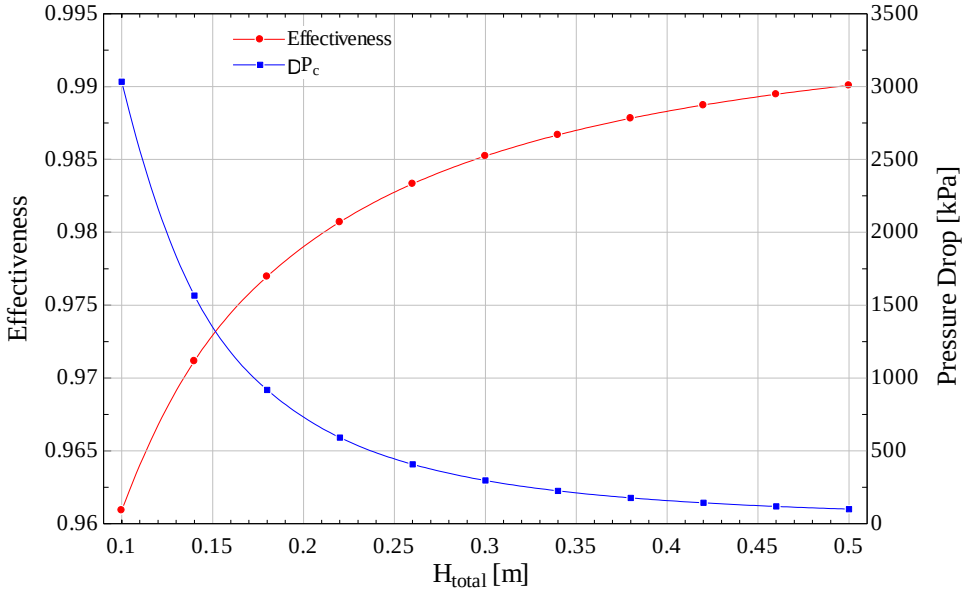

Figure 85: Dependence of effectiveness and low-pressure side pressure drop with varying H_{total} with the other parameters corresponding to the lightest design case.

Changing the number of plates or length of the heat exchanger results in a linear variation in pressure drop and asymptotic effectiveness.

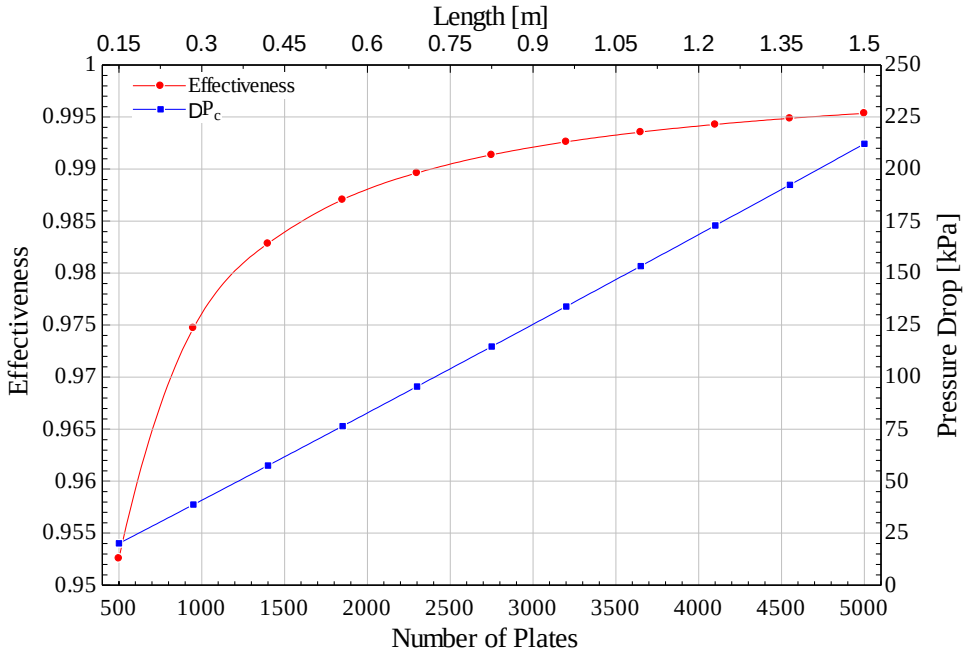

Figure 86: Dependence of effectiveness and low-pressure side pressure drop with varying number of plates (or overall heat exchanger length) with the other parameters corresponding to the lightest design case.

Varying the characteristic small-scale dimension L_{micro} reveals a steep reduction in effectiveness at low values corresponding to poor fin efficiency. The pressure drop follows a similar shape as the Darcy friction factor correlations used in the model, seen in Figure 35, because Reynolds number depends on L_{micro}. It is interesting to note that the lightest viable design, which requires L_{micro} = 0.15 mm, coincides with the local minimum of pressure drop and is not that value that results in the greatest effectiveness.

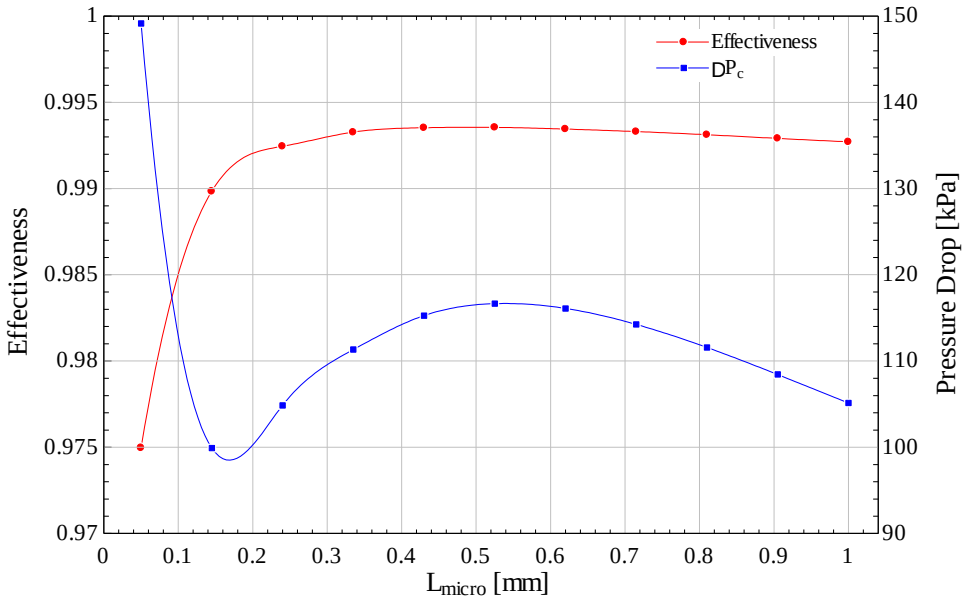

Figure 87: Dependence of effectiveness and low-pressure side pressure drop with varying L_{micro} with the other parameters corresponding to the lightest design case.

Likewise, the channel width of the lightest design also does not correspond with the value that results in maximum effectiveness.

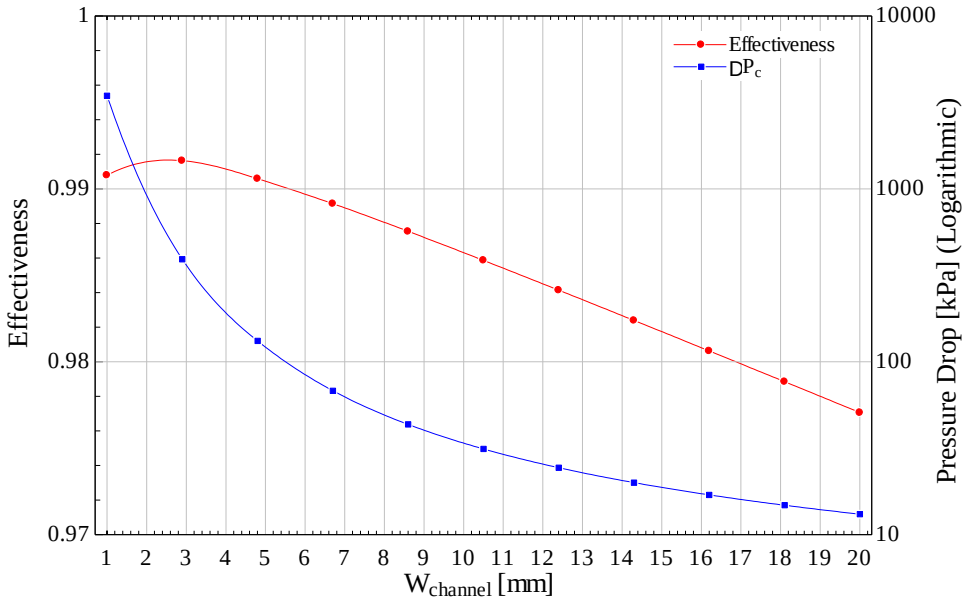

Figure 88: Dependence of effectiveness and low-pressure side pressure drop with varying $W_{channel}$ with the other parameters corresponding to the lightest design case.

Finally, variation in flow boarder size results in a linear variation in effectiveness due to its linear contribution to axial conduction.

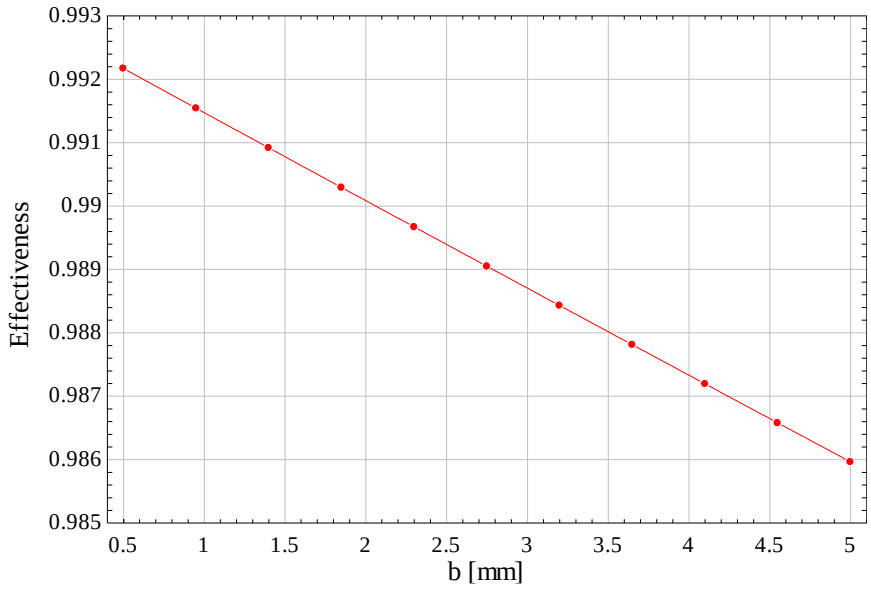

Figure 89: Dependence of effectiveness with varying flow boarder size b with the other parameters corresponding to the lightest design case.

8.5. Lightest Design Geometry

Figure 90 displays a dimensioned drawing of the lightest design. All viable designs are similar in appearance to this lightest design.

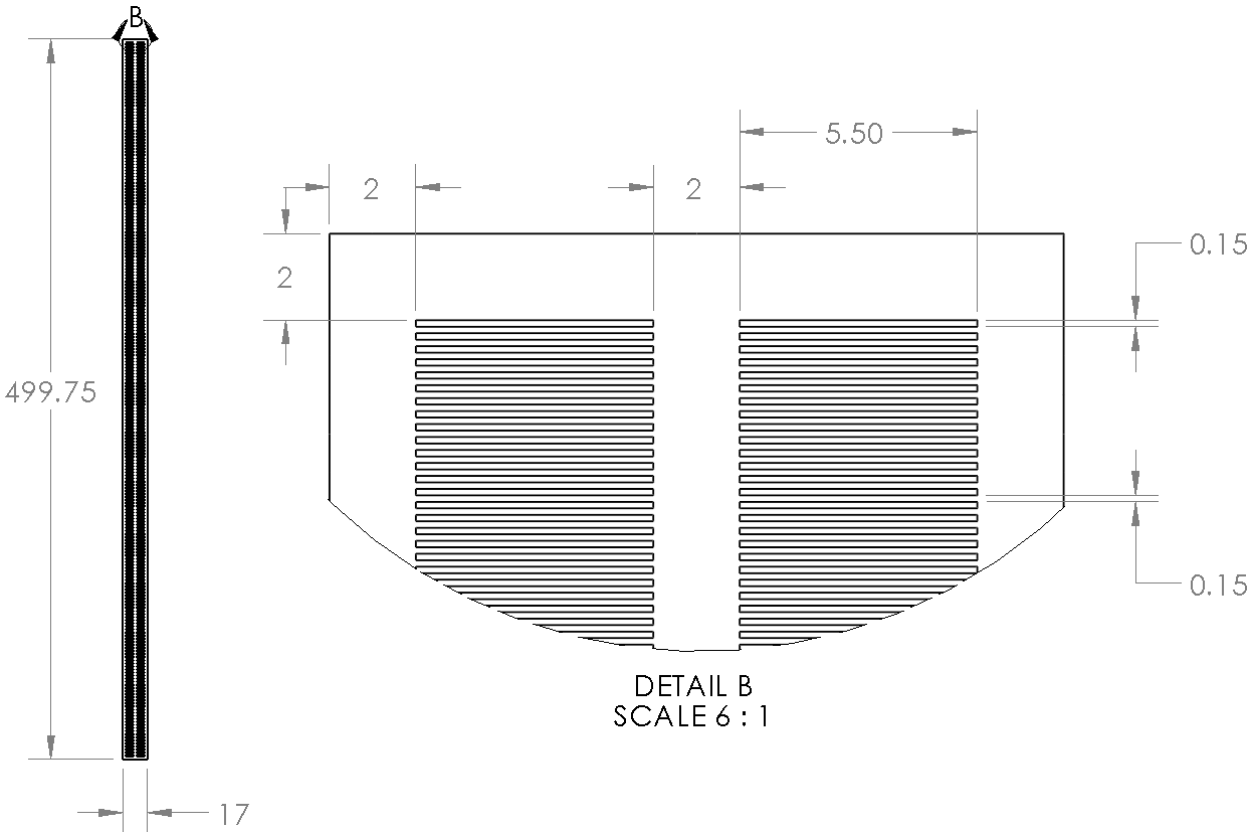

Figure 90: Drawing of a single plate of the lightest design. All dimensions are in [mm]. The design has 1653 slots per side.

The required small slot size to maximize the area density for heat transfer necessitated that the fin length be reasonably small to avoid significant losses due to the fin efficiency. The overall aspect ratio becomes large with the imposed logical constraint of H_{total} = 0.5 m discussed in section 8.1. The viable designs range from 0.721 to 1.204 m in total length. The design specifications provided by SHI forbid the heat exchanger from exceeding 0.5 m in any one direction in space, so designs

between about 0.721 and 1 m will need to be re-headered and double-back on themselves once, as in Figure 91, and designs that exceed 1 m will need to be re-headered twice.

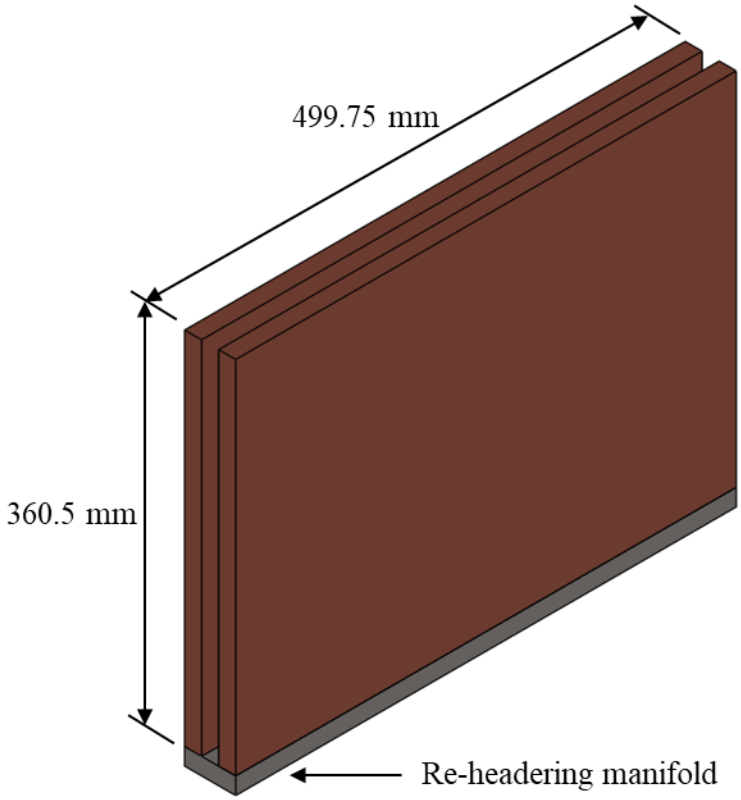

Figure 91: Rough appearance of the bulk dimensions of the lightest design with re-headering manifold.

8.6. Effects of Parasitic Heat Load Inclusion

One of the advantages of the numerical model over the effectiveness-NTU solution is its ability to include parasitic heat loads that reduce effectiveness. To demonstrate, a parasitic radiation heat load was added to the model, and applied to the lightest design operating at 12 g/s. The dimensionless parasitic heat load due to radiation is expressed as

$$\chi = \alpha_r \frac{\left[1 - \left(\varphi_{c,in} + \Theta\left(\varphi_{h,in} - \varphi_{c,in}\right)\right)^4\right]}{\varphi_{h,in} - \varphi_{c,in}} \tag{91}$$

Θ is either the dimensionless hot or cold side temperature. φ are the ratios of inlet temperature to the environment temperature, T_∞.

$$\varphi_{c,in} = \frac{T_{c,in}}{T_\infty} \tag{92}$$

$$\varphi_{h,in} = \frac{T_{h,in}}{T_\infty} \tag{93}$$

The parameter α_r is a dimensionless representation of the effectiveness of radiation shielding.

$$\alpha_r = \frac{L\sigma\varepsilon_m A'_{s,o} T_\infty^3}{\dot{C}_{min}} \tag{94}$$

σ is the Stefan-Boltzmann constant, $A'_{s,o}$ is the external surface area per unit length of the heat exchanger exposed to the surroundings, and ε_m is the emissivity of the heat exchanger metal.

The parasitic heat load was applied to both fluid sides of the lightest design operating at 12 g/s. Figure 92 displays the resulting effectiveness of each side, as well as the average effectiveness between the two sides.

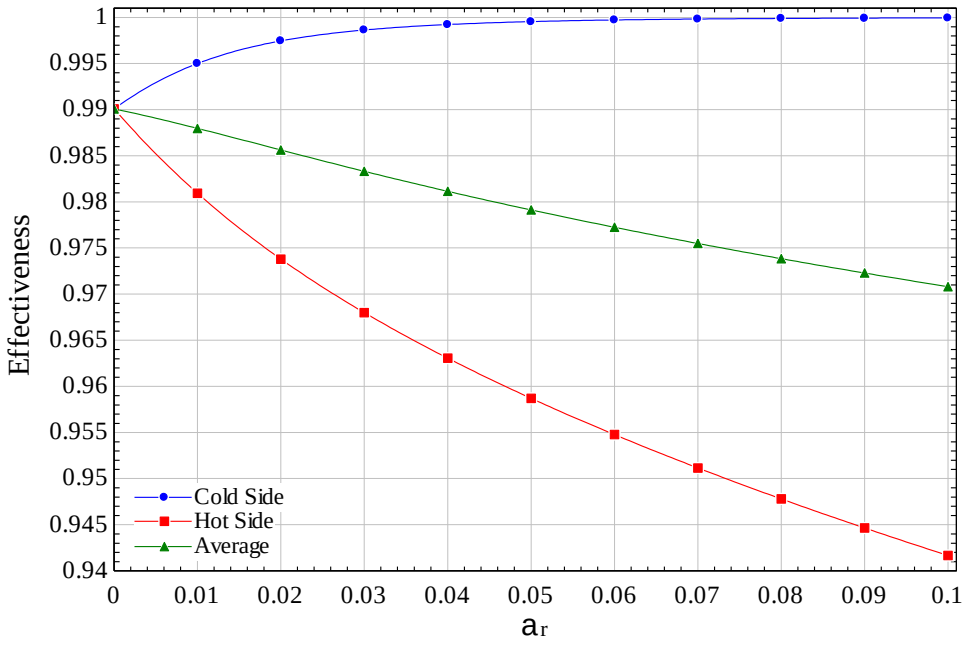

Figure 92: Effectiveness of lightest viable design when subject to varying values of α_r for parasitic heat loads applied to the cold and hot fluid sides.

The cold side benefits from the extra heat input, but not enough to outweigh the performance reduction on the hot fluid side. This behavior cannot be predicted using the effectiveness-NTU method discussed in section 3.3.1, which does not account for parasitic loads. The method developed by Chowdhury [15] does account for parasitic loads, but does not simultaneously include axial conduction.

As α_r increases, the temperature profile transitions from nearly linear to highly skewed toward warmer temperatures, as seen in Figure 93.

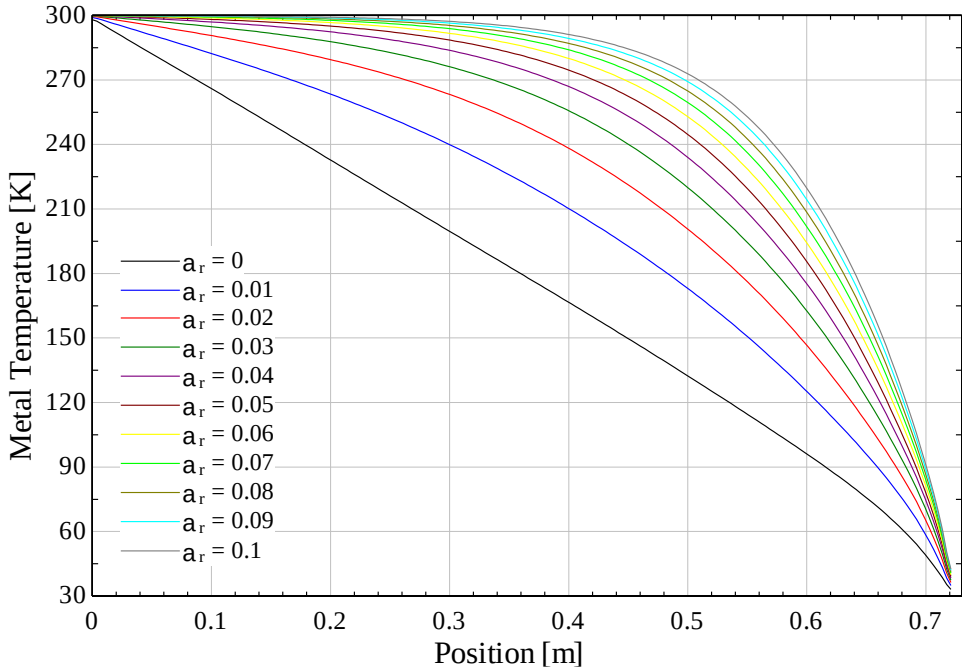

Figure 93: Temperature profile of the lightest heat exchanger operating at 12 g/s with increasingly large radiation heat load applied to both fluid sides.

In reality the worst-case scenario would occur if the exchanger was operating with no radiative insulation such as MLI or actively cooled metallic shield. In this case the radiative heat exchange is dictated by the emissivity of the heat exchanger metal surface. Assuming emissivities of 0.37 for the nickel-plated copper plates (the nickel plating will be discussed in the diffusion bonding

section) and 0.28 for the 316 stainless steel spacers based on the data found on Omega's table of emissivity of various surfaces [27], the resulting value of α_r is only 0.006 using the average emissivity. The resulting reduction in effectiveness is small, and can be virtually eliminated with appropriate radiation shielding.

9. Manufacturing Considerations

The manufacturing of a stacked slotted plate heat exchanger can be broken up into two parts: machining the plates and spacers, and bonding the stack of plates and spacers together. A few manufacturing options were explored for each, and their advantages and disadvantages were compared. Companies capable of providing the desired services were identified. Cost was a vital consideration when comparing manufacturing options, but in many cases obtaining even rough estimates proved difficult without committing to a protracted prototype development process, which SHI is not interested in pursuing at the time of this writing.

9.1. Plate and Spacer Machining

9.1.1. Fineblanking / Gripflow®

Fineblanking and the closely related GRIPflow® processes were initially a very attractive option for manufacturing the plates. Once a die has been created, many plates can be punched in rapid succession economically. GRIPflow® tooling typically costs 30 – 50% less to produce than the equivalent fineblank tooling [28]. Both processes improve upon conventional stamping by applying counter pressure during the punching process to limit the size of burrs and maintain superior flatness. The two processes have similar limitations and achieve similar tolerances.

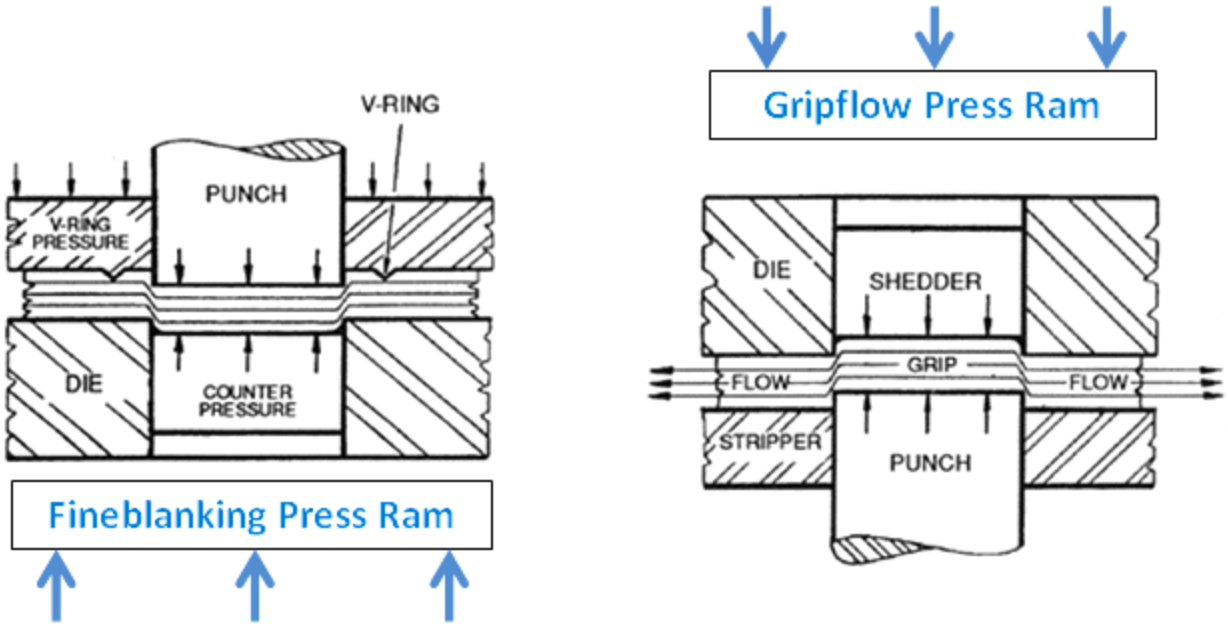

Figure 94: Fineblanking (left) and GRIPflow® (right) punching processes [28].

However, even with this counter-pressure, plate flatness was a concern. Bowed plates may be difficult to bond. The large 0.5 m dimension of the plates is not conducive to flatness. EBway's GRIPflow® design guide [29] specifies that, for parts over 5 inches in length, the flatness tolerance is 0.004 to 0.006 inches, plus 0.0012 inches per each additional inch. For the 0.5 m plates, this corresponds to about 0.6 mm. As discussed in section 8.4, viable heat exchanger designs require plate thicknesses less than 0.5 mm, with the lightest design having a plate thickness of 0.15 mm. With the potential for the plates to bow by an amount equal to or even greater than the plate thickness, it was concluded that fineblanking and GRIPflow® would not maintain adequate plate flatness. The processes were therefore abandoned in favor of other options that did not rely on mechanical force.

9.1.2. Laser Cutting

Initially, laser cutting was considered as a manufacturing option. The minimum slot size that can be cut is equal to the laser diameter, known as the kerf width. Depending on the machine,

kerf widths can be as small as 0.1 mm [30] [31]. Using the kerf width to cut each slot is advantageous if possible, because each slot cut is a line rather than a rectangle that roughly doubles the time to produce each slot. It should also be noted that not every laser cutter can machine copper. Laser cutters either use CO2 gas or glass fiber to amplify the beam. CO2 laser cutters cannot machine copper because it reflects the beam back into the cutter and damages it.

Based on the listed capabilities of Wisconsin Metal Parts Inc of Waukesha, WI, copper can be machined at up to 787 in/min [31]. As a rough estimate, if a slot width of 0.1 mm is assumed and the full 0.5 m overall height is assumed, and the slot length is assumed to be 1 cm, the resulting 5000 slots on one plate would only take about 150 seconds to cut. In the ideal case, with on the order of 1000 plates, cutting all of them would take a few days. R&D Laser of Janesville, Wisconsin, expressed concern over the density of cuts that needed to be made in the slotted plates. With such thin material and so many cuts so close together, thermal expansion may warp the plane of the plate, and the total deposited thermal energy may even melt the fins between cuts unless the process speed is limited.

Fotofab of Chicago, Illinois, have to capacity to both laser cut and photochemical etch parts. They firmly believed that etching would be more economical than laser cutting. Etching allows for many plates to be manufactured in parallel. Cost roughly varies linearly with time spent on machine (which also means cost will vary almost linearly with the number of plates of a design). To estimate the cost, a quote was received from R&D laser for 500 1 mm thick plates with 500 1 mm slots. The price reported was $26.65 per plate, or $13,325 in total. This was far too expensive, especially considering the additional costs of manufacturing the spacers, headers, and bonding. The concerns and cost associated with laser cutting led us to reject it as a manufacturing option.

9.1.3. Photochemical Etching

Multiple plates can be etched simultaneously, and from both sides to reduce time on machine and cost. Etches are not perfectly straight, and will result in a bevel in the slots. Etching from both sides reduces the bevel size roughly by half. Typical double-sided etch bevels range from 5 to 20% of the plate thickness [32] [33].

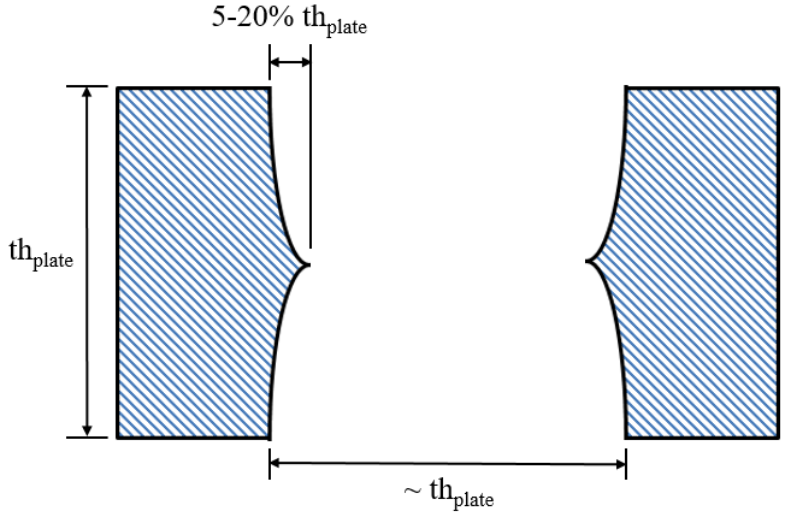

Figure 95: Relative size of slots to plate thickness, with bevel of material in the slot

The effect of the bevel on flow friction and heat transfer coefficient would be an interesting topic for future investigation. In general, slot sizes cannot exceed 120% of the thickness of the plate, and the material between slots cannot be less than 90% of the plate thickness [19]. However, there are absolute limits to how small the feature sizes can be reliably etched. Fotofab lists the minimum practical slot width as 0.102 mm, and the minimum practical bar width of material separating slots of 0.076 mm. Creare used a trial-and-error process with an unknown manufacturer to determine the minimum manufacturable slot width while designing a similar heat exchanger, and concluded that 0.064 mm was the absolute thinnest slot size without incomplete etching. Fotofab estimates a delivery time of 7 to 10 days. As with laser cutting, cost will vary linearly with time required on

machine, implying that cost will also vary linearly with the required number of plates for a design. Photochemical etching has been the manufacturing option of choice used by most workers [9].

9.2. Plate-Spacer Stack Bonding

9.2.1. Vacuum Brazing

Vacuum brazing has been used to manufacture stacked plate heat exchangers, but generally has been surpassed in favor of diffusion bonding for a few reasons. As discussed in section 7.2.1, excess braze material leaking into the flow channels can diminish effectiveness by creating thermally conductive paths across the insulating spacers. Braze may also obstruct the flow passages.

The thermal short problem can be mitigated with a careful choice of braze alloy. In discussions with Lucas-Milhaupt, they recommended a nickel-based alloy such as their 82Ni/18Au alloy which is known to have a thermal conductivity of about 30 W/m-K, or their Hi Temp® 820 alloy, which is 82% nickel, 7% chromium, 2.75% boron, 4.5% silicon, 3% iron, and the remainder other elements, which should have an even lower thermal conductivity [24]. These alloys are about an order of magnitude lower in thermal conductivity compared to the silver-based alloy used in the sub-scale hybrid cryocooler recuperator discussed previously.

Nilles et al. built and tested several copper-stainless steel stacked plate heat exchangers using both brazing and diffusion bonding [34]. They found that brazing had other disadvantages in addition to those aforementioned. Laying up the stack for brazing was more complicated due to the braze material required between each layer. They also found that the brazed heat exchangers actually had a lower bond strength than the diffusion bonded equivalents. They also note that analysis is easier for the diffusion bonded heat exchangers because they do not need to estimate the thermal and geometric effects of the braze material.

Information about the manufacturing cost can be gleaned from the documentation of the sub-scale hybrid cryocooler recuperator. The process of fabricating a holding frame for the stack during brazing, plating the spacers with braze, and brazing 3 modules took 8 weeks. Another 8 modules were built over 14 weeks, meaning that each one required about 2 weeks. The frame design and fabrication was a one-time cost of $1,800. The cost of plating and brazing the first 3 heat exchangers was $6,342, and the next 8 costed $16,712. Each one required one braze oven cycle. Braze oven operating cost is the driving expense, and it scales linearly with the number of required braze cycles, with each cycle costing about $2,100. With the heat exchanger design discussed in this thesis, only one braze cycle should be required per heat exchanger, so if brazing is chosen as the bonding mechanism, it should be affordable.

9.2.2. Diffusion Bonding

In initial discussions with Fotofab and Vac-Met, both companies were not confident that they could achieve a hermetically sealed stack via diffusion bonding. However, a literature review revealed a number of instances of successfully diffusion bonded stacked copper-stainless steel plate heat exchangers [9]. In fact, diffusion bonding is the recommended bonding mechanism, but great care must be taken to ensure a complete seal.

Kumar et al. [26] performed extensive experimental studies on the success rate and strength of diffusion bonds between copper and stainless steel. They machined standard ASTM E8-04 tensile strength test sections, with half copper and half 304 L stainless steel, and bonded the two halves together. They arrived at a number of conclusions to improve bond quality. They found that the bond strength could be improved by electroless nickel plating the copper to create a nickel interlayer between the copper and stainless steel. The nickel prevented the copper from oxidizing, and had a similar coefficient of thermal contraction to copper and stainless steel. Copper, 316

stainless steel, and nickel have linear coefficients of thermal expansion of 16.6, 15.4, and 13.4 (1/K) respectively, based on EES property functions [16]. It also conforms to the topography of the joint better and more readily disperses into the neighboring metals, as seen in the comparison of Figure 96 with Figure 97.

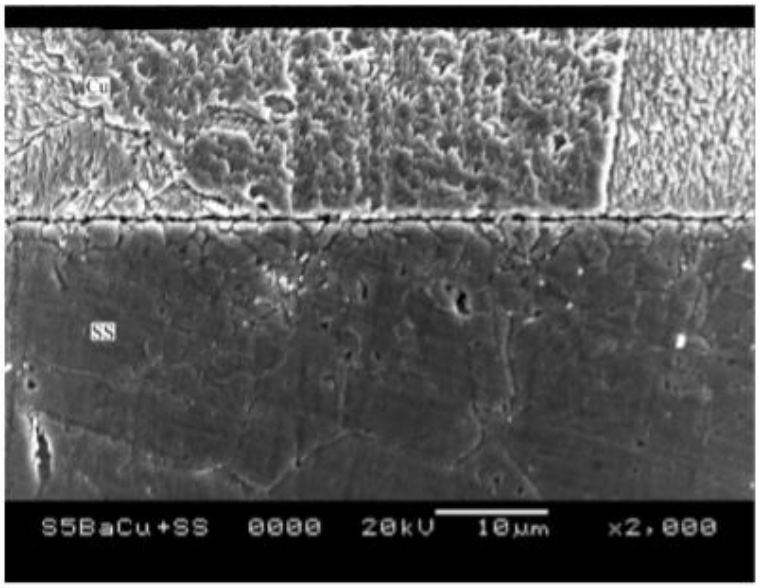

Figure 96: Copper-stainless steel interface without a nickel interlayer.

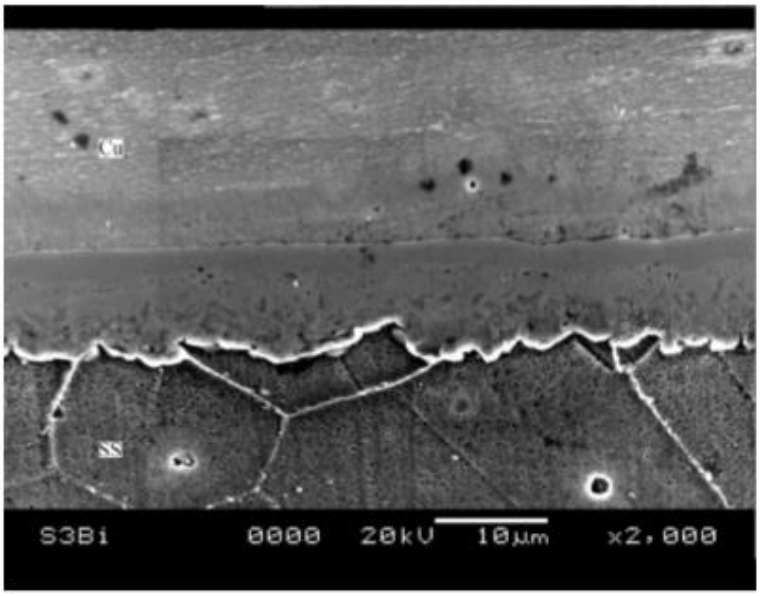

Figure 97: Copper-stainless steel interface with a 20-22 micron interlayer.

Nickel disperses readily into the copper and stainless layers, and prevents an abrupt transition from one to the other. Kumar used an electron probe micro-analyzer to discern the weight percentages of the different elements at the interface. From Figure 98 it is clear that the breadth of the transition region is enhanced significantly by the ~20 micron nickel layer.

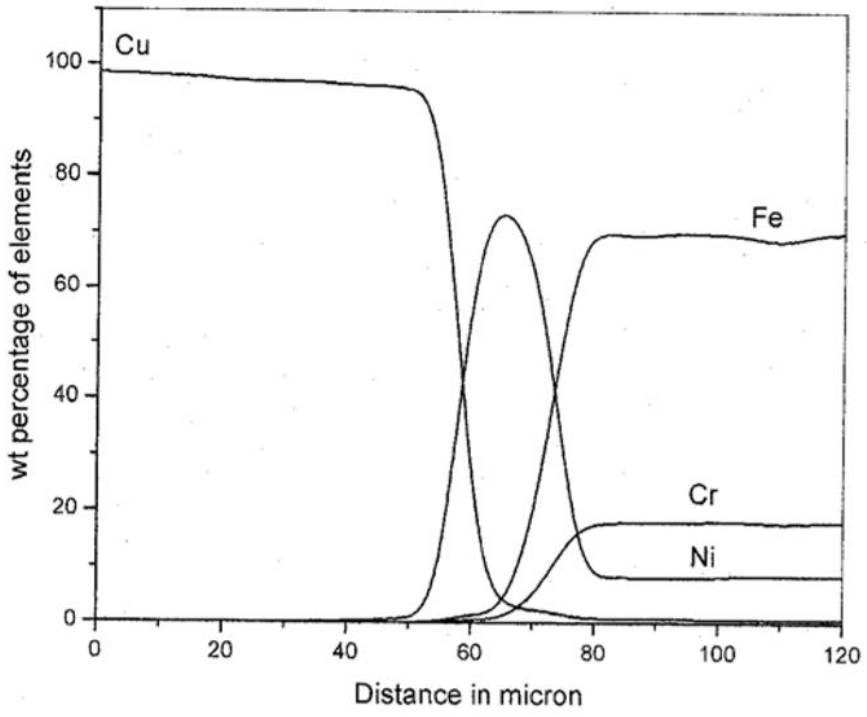

Figure 98: Weight percentage of copper, nickel, iron, and chromium near the interface, determined using an electron probe micro-analyzer.

The effect of varying copper grade and interlayer thickness, as well as bonding temperature, pressure, and duration were studied. They concluded that oxygen-free high conductivity (OFHC) copper should be used. A nickel interface layer of 20 to 30 micron was sufficiently thick. Bonding was performed at 850º C for 1 hour. All testing was done at 10 MPa of pressure applied to the stack. The choice of applied pressure was based on their own literature

review. These conditions produced the test section with the strongest diffusion bond, which achieved 190 MPa ultimate tensile strength.

Under these conditions, they were able to create a hermetic seal between 100 plates with a leak rate of 2.7×10^{-7} mbar-L/s at 15 bar of pressure, that was unaffected by 10 thermal cycles of immersion in liquid nitrogen. With the small-scale heat exchanger only tested to 15 bar, whether or not a stack of plates and spacers can achieve a similar ultimate tensile strength to that observed for the ASTM E8-04 test rod was not investigated.

The bonding area is a critical design parameter, and is set by the width of the spacer where it bounds the gas channels. A larger bonding area results in a superior seal, but also increases axial conduction through the heat exchanger. It is therefore desirable to minimize the spacer cross-sectional area while retaining enough area to create an acceptable bond. With this tradeoff in mind, Kumar chose a spacer width of 2 mm (but did not elaborate). Based on this choice and the resulting excellent ultimate tensile strength, the design process presented in this thesis assumed a spacer width of 2 mm as well to eliminate a design parameter.

SHI prescribed that the heat exchanger must be able to withstand a burst pressure of 13.5 MPa. For the geometries considered in this thesis, with a singular characteristic small-scale dimension L_{micro}, in the transverse (stream-to-stream direction), the ratio of area that is acted upon by the gas pressure relative to area occupied by metal fin cross-section is 6 units to 2 (see Figure 24). Consequently, the tensile stress in the copper fins is amplified by a factor of 6/2 compared to the gas pressure. At the burst pressure, this means the fins will experience 40.5 MPa of stress, which is below the nominal yield and ultimate tensile strength of copper at room temperature of 70 and 220 MPa, respectively [16].

Similar logic can be applied in the axial direction. View Figure 17 to recall the spacer cross-section. Consider the worst-case scenario, with both sides of the heat exchanger holding 13.5 MPa of pressure, and the largest $W_{channel}$ used of 2 cm, which results in the largest area for the gas to exert pressure on. With H_{total} = 0.5 m and b = 2 mm, the total area acted upon by gas pressure is 0.02 m^2, compared to 0.0032 m^2 of spacer metal cross-sectional area. The axial pressure in the spacers (and crucially, the diffusion bonds) is therefore 84.4 MPa, a factor of 0.02/0.0032 greater than the burst pressure. This is lower than the 190 MPa that Kumar measured for the ultimate tensile strength of his ASTM E8-04 test rods, but it is unknown if an actual heat exchanger with many bonded layers can reach the same strength.

Kumar used a process to meticulously prepare the surfaces for bonding, ensuring they were smooth and free of oxides. First, the edges of the plates were sanded with 2000 grade emery paper. They were then rinsed in a hot water and potassium hydroxide solution. Subsequently they were placed in an ultrasonic cleaner. The stainless steel spacers were pickled in 8 – 20% Nitric acid for 3 minutes. The nickel coated copper plates were pickled in 5 – 7% hydrochloric acid for 3 minutes. The acid was rinsed with demineralized water and hot air blow dried. Finally, each plate was inspected for blemishes under a magnifying glass. Defected plates were picked again. Kumar was able bond the heat exchanger with the vacuum hot press furnace at the India Institute of Technology – Kharagpur for an unspecified but low cost. However, the process is labor-intensive, which could have cost implications if done by a company rather than graduate student labor.

The stack was aligned using tungsten rods, chosen because the material retains mechanical strength in the high temperatures of the vacuum brazing oven. Graphite plates were placed between the hydraulic rams and the plate stack to avoid accidentally bonding the ram to the headers. The vacuum furnace, bonding layup, and completed 100-plate heat exchanger are shown in Figure 99.

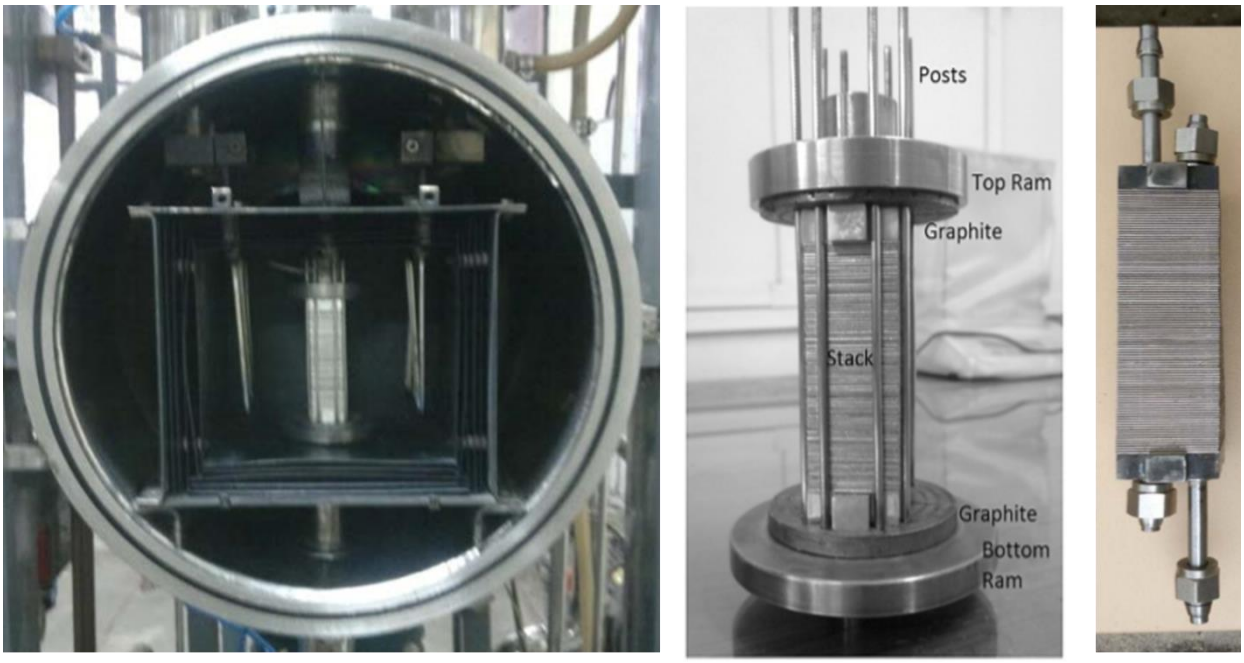

Figure 99: Stack placed in vacuum hot press (left). Stack layup before diffusion bonding (center). Completed 100-plate heat exchanger (right).

Based on Kumar's work and other literature, diffusion bonding seems to be the best option for manufacturing copper-stainless steel stacked slotted plate heat exchangers, provided that steps are taken to ensure the success of the bonding process. Vacuum Process Engineering of Sacramento, CA have experience in diffusion bonding microchannel heat exchangers, and are currently doing research and development work for a similar project at the University of Wisconsin [35]. Fotofab also does diffusion bonding (outsourced through Refrac). They are a particularly appealing company to work with, because they also can photochemical etch the plates, making them a convenient singular company to coordinate with to determine the details of the manufacturing process and design. However, they did not agree to provide a cost estimate without first establishing a non-disclosure agreement, which SHI is not interested in pursuing at this time.

10. Summary of Work

SHI Cryogenics of America was interested in exploring high-effectiveness recuperative heat exchanger designs. The goals of this project were threefold. First, determine which style of heat exchanger is likely to achieve the greatest effectiveness, and how best to construct it. Second, develop a tool that can be used to model and analyze the performance of high-effectiveness heat exchangers. Third, apply the model with varying geometric parameters to determine whether the design can meet the desired performance specifications, and study the tradeoffs between weight, effectiveness, and pressure drop.

10.1. Prospective Design

Because the refrigeration loads of cryogenic systems tend to be so small compared to the heat transferred in the recuperators, secondary effects that are often neglected must be considered and mitigated. Namely, axial conduction and flow imbalance. Stacked parallel plate heat exchangers achieve very high area densities, while mitigating axial conduction with low cross-sectional area, low thermal conductivity spacers between conduction plates. The spacers also allow flow to redistribute after each slotted plate, preventing large-scale flow imbalances from developing.

Slots were chosen over circular holes for ease of modeling and because simple calculations of convective conductance in conjunction with manufacturing limitations suggested that fins can achieve more spatially compact heat transfer. Heat transfer was further enhanced by choosing to stagger the fins with each subsequent slotted plate.

Research into manufacturing techniques revealed that photochemical etching is likely the best option for machining the plates and has been used by most workers [9]. It has the capacity to produce sufficiently small slots without bowing the plates or creating burrs. To bond the stack,

some workers have had success with vacuum brazing, but excess material squeezed into the spacer regions risks creating thermal shorts and obstructing the flow path [23]. Diffusion bonding is a superior option, but great care must be taken to ensure a successful bond, including the removal of oxides and blemishes from the surfaces, and electroless nickel plating to create a malleable interstitial layer that copper and iron readily diffuse through [26]. A bonded tensile strength test section prepared by Kumar exhibited an ultimate tensile strength of 190 MPa, which can handle the burst pressure prescribed by SHI, but whether or not a stack of plates and spacers can achieve a similar strength is unknown.

10.2. Heat Exchanger Modeling

10.2.1. MATLAB Model

A finite difference MATLAB model was used to predict the performance of heat exchanger designs [13]. Property variations with temperature at each of the two flow stream nominal pressures were included. Axial conduction effects were modeled, and parasitic heat loads can be added. Ansys Fluent-derived correlations for Nusselt number and Darcy friction factor were used in calculations of NTU and pressure drop. Due to the development of a temperature gradient in the stream-to-stream direction, the fin efficiency was calculated assuming a constant temperature difference between the fluid and fin at each location along the fin [8], rather than a constant fluid temperature, resulting in a reduced efficiency compared to a constant fluid temperature assumption, for all values of fin parameter.

The ability of the model to predict performance was validated in two ways. First, thermal results were compared to those produced using an effectiveness-NTU solution with axial conduction, modified for discrete plate heat exchangers [12]. One of the key assumptions of the E-NTU solution was constant material properties, which were an average value for the heat

exchanger. The large temperature difference resulted in significant variation in metal conductivity and helium gas properties, especially density, which in turn effected velocity and therefore convective heat transfer coefficient. These effects were anticipated to significantly alter effectiveness predictions, but in actuality, the simple E-NTU solution produced nearly identical predictions and likely could have been used to model this particular heat exchanger. The highly linear temperature profile is conducive to minimizing the effects of averaging the material properties. The E-NTU solution is expected to deviate from the MATLAB model for heat exchangers with nonlinear temperature profiles, perhaps in the case of operating conditions which result in non-ideal gas behavior, or in the presence of substantial parasitic heat load. The MATLAB model has additional advantages. It allows for parasitic heat loads to be included. It also allows the geometry to be altered on a given flow side at different axial locations in the heat exchanger. For example, it may be advantageous to alter the size of the slots as the density changes with temperature to locally optimize the geometry for the local flow conditions.

The MATLAB model was also compared to experimental data of effectiveness and pressure drop taken from a small heat exchanger with a similar geometry, as well as the original models that were used to develop the heat exchanger [23]. The original model used a simple constant property E-NTU solution with axial conduction, with developing duct flow correlations to determine the convective heat transfer coefficient. Pressure drop was determined using developing duct flow correlations, in conjunction with expansion and contraction losses associated with the spacer-to-plate transition. Effectiveness agreement between experimental data and all models was good, but the predictions were sensitive to an estimated cross-sectional area of high thermal conductivity braze that leaked into the insulating spacers. In its correlation for friction factor, the original model used the incorrect definition of the hydraulic diameter. With the correct

definition, agreement in pressure drop predictions between the original model and MATLAB model was excellent, but both under predicted pressure drop by more than a factor of 2. The discrepancy was attributed to the method used to experimentally infer the pressure drop in the core, with headers excluded.

10.2.2. Fluent Model and Correlations

Ansys Fluent was used to generate correlations for Nusselt number and Darcy friction factor. The 3-dimensional geometry was reduced to a single, 2-dimensional unit cell using symmetry and periodic boundary conditions, and assuming the channel was wide relative to its height so end effects could be neglected. A Spalart-Allmeras turbulence model was required to capture the turbulent behavior of the flow at higher Reynolds numbers.

Initially, comprehensive correlations based on longitudinal and transverse fin pitch, fin aspect ratio, and Reynolds numbers were planned, and the University of Wisconsin Center for High Throughput Computing was to be employed to vastly expedite the solution process. Fluent licensing problems prevented effective use of the CHTC. Instead, the number of design parameters was reduced based on limitations of the manufacturing processes, which reduced the number of permutations such that they could be solved on a single computer in reasonable time. The result were 6^{th} order polynomial correlations based solely on Reynolds number, which was dependent on the single characteristic small-scale dimension, mass flow rate, and material properties effected by temperature and pressure.

The Fluent-based correlations were compared to simple developing duct flow correlations [16] as well as experimentally derived correlations generated by Mikulin et al [2]. The agreement in Darcy friction factor between the developing duct flow and Fluent correlations was good at low Reynolds numbers, where the flow was laminar and the effect of impingement on the front faces

of the fins was minimal. In this range, the Mikulin correlation was highly inaccurate. The Mikulin correlation assumed Reynolds numbers high enough such that the friction factor is independent of Reynolds number. At the higher Reynolds numbers studied, the agreement between the Mikulin correlation and Fluent correlation became good. The Fluent correlation became independent of Reynolds number. As expected, the duct flow correlations were not accurate at high Reynolds numbers, where drag due to flow impingement became dominant. For Reynolds numbers in the transition range from laminar to turbulent, the Fluent correlation did not agree with either the duct flow or Mikulin correlations, and captured behavior not described by either. With large spans in temperature, these cryogenic heat exchangers are likely to operate with a large range of Reynolds numbers, and correlations that describe the full range of laminar to turbulent flow should be used.

Similar to the friction factor, the Nusselt number predicted by the developing duct flow and Fluent correlations matched in the laminar range (with the Fluent Nusselt number adjusted for convective heat transfer coefficient area averaging), but the Mikulin correlation did not. The Mikulin correlations were not claimed to be accurate at low Reynolds numbers, and the duct flow correlations were not accurate at high Reynolds number, which reiterated that correlations should be used that span a large range of Reynolds numbers for these types of heat exchangers.

10.3. Design Viability and Performance Study

Certain conclusions were drawn that simplified the design process.

1. The heat exchanger will be weight limited rather than volume limited. Full use of the 0.1 m^3 allowable volume results in weights in excess of 600 lbs. SHI only wish to consider designs under 100 lbs.

2. Manufacturing constraints dictate that the fin height, slot gap height, and plate thickness will be roughly equal [19] to maximize heat transfer area density. The spacer thickness was set to the same value for simplicity
3. The flow channel boarder should be as small as possible to minimize axial conduction, while still providing enough surface area for successful diffusion bonding and mechanical strength. 2 mm was used for these designs based on the work of others [26].
4. The overall plate height should be large and was maximized in this study. Fin length (or channel width) should then be tuned to maximize the overall plate conductance. The effects are multifaceted. Varying the channel width effects fin efficiency, fin surface area, and total flow cross-sectional area. As a consequence, velocity and therefore convective heat transfer coefficient and pressure drop are influenced.
5. The prescribed allowable pressure drop on the low pressure side is lower than the high pressure side. The low-pressure side exhibits higher fluid velocity and therefore higher pressure drop. Therefore, for the design process of this specific heat exchanger, any design that met the pressure drop requirements on the low-pressure side would also do so on its high-pressure side.
6. For the ranges of parameters studied in this design process, pressure drop monotonically increased and effectiveness monotonically decreases with increasing mass flow rate. Any design that meets the performance requirements at the highest mass flow rate would also do so at the lowest mass flow rate.

The effectiveness reached by the highest effectiveness design that remained within pressure drop limitations was 0.9927. The minimum possible low-pressure side pressure drop while still reaching an effectiveness of 0.99 was 40 kPa. Both occur at the highest weight considered of 100

lbs. The lightest possible design weighed 61 lbs, with $W_{channel}$ = 0.55 cm, L_{micro} = 0.15 mm, n_{plates} = 2403, V_{total} = 0.00618 m^3, and L = 0.721 m. Its Reynolds number range was in the vicinity of the local minimum of friction factor near Re = 200.

11. Future Work

A number of topics and outstanding questions could be pursued in future work.

1. The degree to which the flow manages to redistribute in the spacer regions is a concern. It may be possible to investigate this by modeling a larger section of the heat exchanger in 2 dimensions and observe whether large-scale flow imbalances develop.
2. Correlations for Nusselt number and friction factor with each of the 4 small-scale dimensions varied independently of one another is desired. This will require the high-throughput computing Fluent license issues to be resolved to compute the resulting large number of permutations. In particular, the spacer thickness is not limited to be approximately the same size as the plate thickness and slot size by manufacturing constraints. The spacers are mostly void space, so varying the spacer thickness will effect volume more than weight. Larger spacers will further reduce axial conduction and may achieve superior flow uniformity.
3. A detailed investigation into the optimal flow channel boarder size is warranted. The value chosen in this work was 2 mm based on the work of Kumar [26], but the details on how he arrived at that value are unknown. This work was not thorough in investigating the heat exchanger's ability to withstand the prescribed burst pressure of 13.5 MPa set by SHI. Simple calculations suggest it may succeed when compared to the experimental data of

Kumar, but the data was taken from simple tensile test sections rather than a stack of many plates and spacers.

4. The MATLAB model can be adjusted such that different regions of the heat exchanger have different geometric feature sizes. With a factor of 4 increase in Reynolds number between the cold and hot ends of the heat exchanger, it will be possible to increase performance by varying the geometry in the axial direction to be more suitable for the local Reynolds number.
5. Further discussions with manufacturers to gain a better understanding of costs, and potentially identify unforeseen manufacturing details that may impact the design.
6. Photochemical etching is the most promising option for making the slots. As discussed in section 9.1.3, the slot walls will not be perfectly straight, but rather will exhibit a slight bevel. This detail can be added to the Fluent model, and its effect on convective heat transfer coefficient and pressure drop can be compared to the idealized geometry.
7. The lightest possible design weighed 61 lbs, which is too heavy for SHI to be interested in pursuing at this time. It may be possible to construct an all-aluminum heat exchanger that meets the design requirements while weighing far less. The thermal conductivity is lower from a stream-to-stream standpoint, yet higher from an axial conduction standpoint. The thermal performance per unit volume will be worse, but it may still be able to achieve the desired effectiveness and pressure drop by utilizing more volume and still weigh less than the copper-stainless steel design.
8. A small-scale version of this type of heat exchanger could be constructed to develop manufacturing techniques, and experimentally compare the performance to the predictions of the MATLAB model.

To conclude, the results of this study suggest that a copper-stainless steel stacked plate heat exchanger with offset rectangular slots can achieve the effectiveness and pressure drop requirements prescribed by SHI, but the lightest viable design weighs 61 lbs, excluding headers. The numerical modelling tool that has been developed is validated and can be applied to heat exchangers of varying geometries and flow conditions provided that they fall within the bounds of the Nusselt number and Darcy friction factor correlations developed using Fluent. Other geometries can also be simulated using this finite difference model, provided that its geometry and correlations are altered appropriately.

References

[1] E. D. Marquardt and R. Radebaugh, "Compact high effectiveness parallel plate heat exchangers," in *Cryocoolers 12*, R. G. Ross, Ed., Boston, MA: Springer, 2003.

[2] E. Mikulin, Y. Shevich, V. Potapov, M. Solntsev and G. Yusova, "Study of matrix-type heat exchangers made of perforated plates," *Chem. Pet. Eng.*, vol. 16, no. 9, pp. 154-159, 1980.

[3] G. Jain, S. Chaudhary, P. K. Gupta and P. Kush, "Flow mal-distribution study in cryogenic counter-flow plate fin heat exchangers," *IOP Conf. Ser.: Mater. Sci. Eng.*, vol. 171, p. 012014, 2017.

[4] H. Joshi and R. Webb, "Heat transfer and friction in the offset stripfin heat exchanger," *Int. J. Heat Mass Transfer*, vol. 30, no. 1, pp. 69-84, 1987.

[5] K. A. Bhanumurthy, S. S. Murthy and G. Venkatarathnam, "Optimum design of complete matrix heat exchanger geometry," in *2010 3rd Int. Conf. Thermal Issues in Emerging Technol. Theory and Appl. (thETA 3)*, Cairo, Dec. 2010, pp. 163-170.

[6] W. Zhu, M. J. White, G. F. Nellis, S. A. Klein and Y. B. Gianchandani, "A perforated plate stacked Si/glass heat exchanger with in-situ temperature sensing for Joule-Thomson coolers," in *Proc. IEEE Int. Conf. Micro Electro Mech. Syst.*, 2008.

[7] G. Nellis and S. Klein, Heat Transfer, New York: Cambridge University Press, 2009.

[8] R. Fleming, "A compact perforated-plate heat exchanger," in *Advances in Cryogenic Engineering*, vol. 14, K. D. Timmerhaus, Ed., Boston, MA: Springer, 1969, pp. 197-204.

[9] G. Venkatarathnam and S. Sarangi, "Matrix heat exchangers and their application in cryogenic systems," *Cryogenics*, vol. 30, no. 11, pp. 907 - 918, 1990.

[10] W. M. Kays and A. L. London, in *Compact Heat Exchangers*, 2nd ed., McGraw-Hill Book Co., 1964, p. 30.

[11] P. Kroeger, "Performance deterioration in high effectiveness heat exchangers due to axial heat conduction effects," in *Advances in Cryogenic Engineering*, vol. 12, K. D. Timmerhaus, Ed., Boston, MA: Springer, 1967, pp. 363-372.

[12] G. Venkatarathnam, "Effectiveness-Ntu relationship in perforated plate matrix heat exchangers," *Cryogenics,* vol. 36, pp. 235 - 241, 1996.

[13] G. Nellis, "A heat exchanger model that includes axial conduction, parasitic heat loads, and property variations," *Cryogenics*, vol. 43, no. 9, pp. 523-538, 2003.

[14] MATLAB Release R2018a, Available: www.mathworks.com.

[15] K. Chowdhury and S. Sarangi, "Performance of cryogenic heat exchangers with heat leak from the surroundings," in *Advances in Cryogenic Engineering*, vol. 29, R. W. Fast, Ed., Boston, MA: Springer, 1984, pp. 273-280.

[16] S. Klein, *Engineering Equation Solver*, (V.10.372) [software]: F-Chart, 2018.

[17] "Fluent 19.2 User's Guide," Ansys Inc., [Online]. Available: https://ansyshelp.ansys.com. [Accessed 2019].

[18] "Center for High Throughput Computing," University of Wisconsin - Madison, [Online]. Available: http://chtc.cs.wisc.edu. [Accessed 2018].

[19] "Fotofab Design Guide to Photochemical Machining," Fotofab LLC, 2017. [Online]. Available: https://www.fotofab.com. [Accessed 2018].

[20] A. Niblick, J. Cox and M. Zagarola, "A Lightweight, High-Effectiveness Recuperator for Next-Generation Airborne Cryocoolers," in *ICC20*, Burlington, Vermont, 2018.

[21] I. Idel'chik, Handbook of Hydraulic Resistance: Coefficients of Local Resistance and of Friction, D. Grunaer, Ed., Jerusalem: Israel Program for Scientific Translations, 1966.

[22] D. W. Hoch, G. F. Nellis, N. L. Meagher, J. R. Maddocks and S. Stephens, "Development and Testing of a Multi-Plate Recuperative Heat Exchanger for Use in a Hybrid Cryocooler," *Cryocoolers*, vol. 14, pp. 515-524, 2007.

[23] D. Hoch and G. Nellis, "Sub-Scale Module Fabrication and Test," Univ. of Wisc., Madison, 2004.

[24] Lucas Milhaupt, "Filler Metals," [Online]. Available: https://www.lucasmilhaupt.com/EN/Products/Filler-Metals.htm. [Accessed 2018].

[25] T. L. Fraser, "Design of a Cryogenic Turbine for a Hybrid Cryocooler," M.S. thesis, Dept. Mech. Eng., Univ. of Wisc., Madison, WI, 2006.

[26] S. S. Kumar, "Perforated Plate Heat Exchangers - Modelling, Fabrication and Performance Evaluation," Ph.D. dissertation, Indian Inst. of Technol., Kharagpur, India, 2014.

[27] OMEGA, "Emissivity of Common Materials," [Online]. Available: https://www.omega.com/literature/transactions/volume1/emissivitya.html. [Accessed 2019].

[28] EBway, "About GRIPflow," 2005-2019. [Online]. Available: http://www.ebway.com/about-gripflow.php. [Accessed 2018].

[29] EBway, "Basic Design Guide for GRIPflow," [Online]. Available: http://www.ebway.com/literature/grip-flow-metal-stampings-design-guide.pdf. [Accessed 2018].

[30] R. Todd, D. K. Allen and L. Alting, in *Manufacturing Processes Reference Guide*, Industrial Press Inc., 1994, p. 185.

[31] Wisconsin Metal Parts Inc., "Fiber Laser Cutting Capabilities," 2018. [Online]. Available: https://www.wisconsinmetalparts.com/services-capabilities/fiber-laser-cutting-services. [Accessed 2018].

[32] Elcon Precision LLC, "PCM Design Guidelines," [Online]. Available: https://www.elconprecision.com/photochemical-machining-design-guidelines. [Accessed 2018].

[33] Advanced Metal Etching, "Chemical Etching Technical Guidelines," [Online]. Available: https://metaletching.com/technical-guidelines. [Accessed 2018].

[34] M. J. Nilles, M. E. Calkins, M. L. Dingus and J. B. Hendricks, "Heat Transfer and Flow Friction in Perforated Plate Heat Exchangers," *Exp. Therm. Fluid Sci.,* vol. 10, no. 2, pp. 238-247, 1995.

[35] S. Aakre, I. W. Jentz and M. H. Anderson, "Nuclear code case development of printed-circuit heat exchangers with thermal and mechanical performance testing," in *The 6th Int. Supercritical CO2 Power Cycles Symp.*, Pittsburgh, 2018.

Appendices

Appendix A: MATLAB Model

Main Code

```
clear;
clear global;
clc;

global Cmin Thin Tcin mdot L Acm_ss Acm_cu th_plate th_spacer n_plates
W_channel n_fins As_fin Per_fin Ac_fin D_H Ac_total_open_oneside b H_overall
H_fin H_gap alpha_r phi_c_in phi_h_in

delete('*.mat'); %Delete old matlab data files

%Read text file specifying tab-delimited text file parameter list
dp_list=tdfread('MatlabPermutationsENTUComparison.txt','');
n_dp=length(dp_list.Lmicro); %Determine number of design points

tic;%Start timing calculation
for loopcount = 1:(n_dp) %Loop through each design point
fprintf('Design point # %f',loopcount);

wt=0.4;          %relaxation weighting parameter
cf=1;
mhot='a';        %hot side METAL adiabatic boundary condition
mcold='a';       %cold side METAL adiabatic boundary condition
% mhot=1;        %hot side METAL non-dim temp boundary condition
% mcold=0;       %cold side METAL non-dim temp boundary condition
g=0;             %grid concentration factor
tol1=0.00001;    %absolute tolerance
tol2=0.00001;    %absolute tolerance
n=400;           % # of discrete elements

%Inlet temperatures
Thin=300;
Tcin=30;

%mass flow rate (kg/s). Design case is 0.012, rating case is 0.006 kg/s
mdot=dp_list.mdot(loopcount)./1000;

%capacitance rate of helium @ P=2.6 MPa, 30 K <= T <= 300 K
Ch_in=mdot.*(6762.2-57.8438*Thin+0.893344*Thin^2-
0.00718172*Thin^3+0.0000313679*Thin^4-7.04555E-08*Thin^5+6.36825E-11*Thin^6);
%capacitance rate of helium @ P=500 kPa, 30 K <= T <= 300 K
Cc_in=mdot.*(5574.4-14.4836*Tcin+0.227804*Tcin^2-
0.00185276*Tcin^3+0.00000815612*Tcin^4-1.84217E-08*Tcin^5+1.67193E-
11*Tcin^6);
Cmin=min(Ch_in,Cc_in);

%Geometry
```

```
H_total=0.5;%Total height of flow channel (All H_gap + H_fin) [m]
% H_total=dp_list.Htotal(loopcount);
W_channel=dp_list.Wchannel(loopcount)./1000;%Width of flow channel [m]
th_plate=dp_list.Lmicro(loopcount)./1000;
th_spacer=th_plate;
H_fin=th_plate;%Height of fins (perpendicular to flow) [m]
H_gap=th_plate;%Height of gaps between fins (perpendicular to flow) [m]
D_H=H_gap.*2; %Hydraulic diameter

%Boarders
b=2./1000;%Width of separating wall of spacer [m]
% b=dp_list.b(loopcount)./1000;
b_w=b;%Width of outer walls of spacer along channel width [m]
b_h=b;%Width of outer walls of spacer along channel height [m]

%Fin geometry
Per_fin=2.*H_fin+2.*th_plate;
Ac_fin=H_fin.*th_plate;
As_fin=Per_fin.*W_channel;

%Fin numbers
n_fins=round(H_total./(H_fin+H_gap));%number of fins
n_gaps=n_fins+1;%number of gaps on each side

%Cross sectional areas
H_overall=H_total+2.*b_h;
Ac_total=H_overall.*(2.*W_channel+2.*b_w+b);%Total cross sectional area
Ac_total_open_oneside=W_channel.*H_total;%Open area per side
Acm_ss=Ac_total-2.*Ac_total_open_oneside;
Acm_cu=Ac_total-2.*Ac_total_open_oneside+2.*n_fins.*(H_fin.*W_channel);

%Weight and number of plates
rho_cu=8957;%kg/m^3
rho_ss=8024;%kg/m^3
Weight_approx_lbs=dp_list.Weightapprox(loopcount);
Weight_approx_kg=Weight_approx_lbs./2.205;
n_plates_approx=(Weight_approx_kg-
Acm_ss.*th_spacer.*rho_ss)./(Acm_cu.*th_plate.*rho_cu+Acm_ss.*th_spacer.*rho_
ss);
n_plates=round(n_plates_approx);%closest whole # plates
%
Weight_kg=n_plates.*(Acm_cu.*th_plate.*rho_cu)+(n_plates+1).*(Acm_ss.*th_spac
er.*rho_ss);
% Weight=Weight_kg.*2.205;
Weight=Weight_approx_lbs;

%Total length and volume
L=(n_plates+1).*th_spacer+n_plates.*th_plate; %Total length
V_total=L.*Ac_total; %Total volume

%Radiation parasitics
sigma=5.67*10^(-8); %Stefan-Boltzmann constant [W/m^2*K^4]
E_316ss=0.28; %Room temp 316 stainless steel emissivity (from Omega.com)
E_cu_ni=0.37; %100-500 deg. F Nickel-plated copper emissivity (Omega.com)
E_m=(E_cu_ni+E_316ss)/2; %Average metal emissivity
```

```
T_inf=300; %Driving temperature [K]
As_o_prime=2*H_overall+2*(2*W_channel+2*b_w+b); %Surface area/length [m]
phi_c_in=Tcin/T_inf; %Cold end temp to driving temp ratio
phi_h_in=Thin/T_inf; %Hot end temp to driving temp ratio
% alpha_r=L*sigma*E_m*As_o_prime*T_inf^3/Cmin; %non-dim rad shield par
alpha_r=0;

%function call to determine non-dimensionalized solution
[Qm,Qh,Qc,X,Qdh,Qdc,Qdhm,Qdmc,Qpdh,Qpdc,Qpdm,Qdmhot,Qdmcold,effh,effc,eff_avg
,UBtotal,layer,betac,betah,lambda,mu,nu,DeltaPh,DeltaPc,DeltaPh_total,DeltaPc
_total,DeltaP_total,h_c,h_h,kss,kcu,Re_c,Re_h]=HXCryogenics_II(n,wt,cf,mhot,m
cold,g,tol1,tol2);

%Temperature Profile
Tm_finished=Qm.*(Thin-Tcin)+Tcin; %metal
Th_finished=Qh.*(Thin-Tcin)+Tcin; %hot side
Tc_finished=Qc.*(Thin-Tcin)+Tcin; %cold side
```

E-NTU Comparison Section

```
% E-NTU Method Comparison-----------------------------------------------------
%ENTU relationship in perforated plate heat exchangers (G. Venkatarathnam)
%Includes axial conduction, uses average material properties with T, P
%Properties evaluated at Tavg = 165 K, P = 500 kPa, P = 2.6 MPa
c_c_avg=5194;
c_h_avg=5199;
rho_c_avg=1.442;
rho_h_avg=7.416;
mu_c_avg=0.00001335;
mu_h_avg=0.00001354;
k_c_avg=0.1038;
k_h_avg=0.1056;
k_ss_avg=10.46;
k_cu_avg=414.8;
k_p_ENTU=k_cu_avg;

%Constant properties cold low P side
V_gap_c_avg=(mdot./(rho_c_avg.*Ac_total_open_oneside))*((H_fin+H_gap)./H_gap)
;
Re_c_avg=rho_c_avg.*V_gap_c_avg.*D_H./mu_c_avg;
lnNu_c_avg=1.40181903E+00-5.73104443E-01.*log(Re_c_avg)+6.84944358E-
01.*log(Re_c_avg).^2-2.37733746E-01.*log(Re_c_avg).^3+4.14739472E-
02.*log(Re_c_avg).^4-3.59179995E-03.*log(Re_c_avg).^5+1.24664773E-
04.*log(Re_c_avg).^6;
Nusselt_c_avg=exp(lnNu_c_avg);
h_c_avg=Nusselt_c_avg.*k_c_avg./D_H;

%Constant properties hot high P side
V_gap_h_avg=(mdot./(rho_h_avg.*Ac_total_open_oneside))*((H_fin+H_gap)./H_gap)
;
Re_h_avg=rho_h_avg.*V_gap_h_avg.*D_H./mu_h_avg;
lnNu_h_avg=1.61900259E+00-1.00786470E+00.*log(Re_h_avg)+9.89242546E-
01.*log(Re_h_avg).^2-3.41092028E-01.*log(Re_h_avg).^3+5.99006080E-
02.*log(Re_h_avg).^4-5.24759039E-03.*log(Re_h_avg).^5+1.83775818E-
04.*log(Re_h_avg).^6;
```

```
Nusselt_h_avg=exp(lnNu_h_avg);
h_h_avg=Nusselt_h_avg.*k_h_avg./D_H;

%Constant properties axial conduction parameter
R_plate_avg=n_plates.*th_plate./(k_cu_avg.*Acm_cu);
R_spacer_avg=(n_plates+1)*th_spacer./(k_ss_avg.*Acm_ss);
lambda_avg=(1./(R_plate_avg+R_spacer_avg))./Cmin;

%Constant property capacitance rates
C_1_ENTU=mdot.*c_c_avg;
C_2_ENTU=mdot.*c_h_avg;
nu_ENTU=C_1_ENTU./C_2_ENTU; % Note: ~1  ----> balanced heat exchanger

% Geometry (Venkatarathnam nomenclature)
% Note: low pressure side channel = 1, high pressure side channel = 2
% In their notation, my H is their W and vice versa

% Axial conduction parameter
lambda_ENTU=lambda_avg;

% Total fluid NTU (before other resistance modulations)
n_tu_f_1_ENTU=h_c_avg.*(As_fin.*n_fins)./C_1_ENTU;
n_tu_f_2_ENTU=h_h_avg.*(As_fin.*n_fins)./C_2_ENTU;

% Dimensionless LATERAL plate conductance in each channel
n_tu_p_1_ENTU=k_p_ENTU.*Ac_fin.*n_fins./(W_channel.*C_1_ENTU);
n_tu_p_2_ENTU=k_p_ENTU.*Ac_fin.*n_fins./(W_channel.*C_2_ENTU);

% Dimensionless conductance of separating wall in LATERAL direction
lambda_p_ENTU=k_p_ENTU.*H_overall.*th_plate./(b.*C_1_ENTU);

% Overall plate conductance
n_tu_po_ENTU=1./(1./lambda_p_ENTU+1./(3.*n_tu_p_1_ENTU)+nu_ENTU./(3.*n_tu_p_2
_ENTU));

% Intermediate Parameters
alpha_1_ENTU=exp(-n_tu_f_1_ENTU);
alpha_2_ENTU=exp(-n_tu_f_2_ENTU);

% Effective NTU with axial conduction included, for balanced HX
N_tu_eff_ENTU=n_plates.*(1-alpha_1_ENTU).*(1-
alpha_2_ENTU)./(n_plates.*lambda_ENTU.*(1-alpha_1_ENTU).*(1-alpha_2_ENTU)+1-
alpha_1_ENTU.*alpha_2_ENTU+(1-alpha_1_ENTU).*(1-alpha_2_ENTU)./n_tu_po_ENTU);

% Resulting effectiveness
eff_ENTU=N_tu_eff_ENTU./(1+N_tu_eff_ENTU);
% ------------------------------------------------------------------------
```

File Creation and Combination Section

```
%Estimating remaining calculation time
ElapsedTime=toc;
TimeToCompletion_Sec=(n_dp-loopcount)*(ElapsedTime/loopcount);
TimeToCompletion_DD_HH_MM=datestr(seconds(TimeToCompletion_Sec),'DD:HH:MM');
```

```
fprintf('\n');
disp(TimeToCompletion_DD_HH_MM);

%Set unique matlab data file name based on design point values
filename=sprintf('%f_%f_%f_%f_%f.mat',mdot,H_gap,W_channel,L,Weight);
save(filename); %Save matlab data file
end

mat_file_list=dir('*.mat'); %Find all .mat files in project directory
%Initialize data structure size and fields
[filelistsizerow,filelistsizecolumn]=size(mat_file_list);
data_amalgamation=struct('DeltaPc_total',repmat({zeros(1)},filelistsizerow,1)
,'DeltaPh_total',repmat({zeros(1)},filelistsizerow,1),'H_fin',repmat({zeros(1
)},filelistsizerow,1),'H_gap',repmat({zeros(1)},filelistsizerow,1),'H_total',
repmat({zeros(1)},filelistsizerow,1),'L',repmat({zeros(1)},filelistsizerow,1)
,'W_channel',repmat({zeros(1)},filelistsizerow,1),'b',repmat({zeros(1)},filel
istsizerow,1),'effc',repmat({zeros(1)},filelistsizerow,1),'effh',repmat({zero
s(1)},filelistsizerow,1),'mdot',repmat({zeros(1)},filelistsizerow,1),'n_plate
s',repmat({zeros(1)},filelistsizerow,1),'th_plate',repmat({zeros(1)},filelist
sizerow,1),'th_spacer',repmat({zeros(1)},filelistsizerow,1),'Weight',repmat({
zeros(1)},filelistsizerow,1),'V_total',repmat({zeros(1)},filelistsizerow,1),'
eff_ENTU',repmat({zeros(1)},filelistsizerow,1),'Re_c_avg',repmat({zeros(1)},f
ilelistsizerow,1),'Re_h_avg',repmat({zeros(1)},filelistsizerow,1));

%For each file in the mat file list
for i=1:length(mat_file_list)
    fprintf('Concatenating mat file # %f',i);
    fprintf('\n');
    %combine into one structure

data_amalgamation(i)=load(mat_file_list(i).name,'DeltaPc_total','DeltaPh_tota
l','H_fin','H_gap','H_total','L','W_channel','b','effc','effh','mdot','n_plat
es','th_plate','th_spacer','Weight','V_total','eff_ENTU','Re_c_avg','Re_h_avg
'); %Read files into single structure
end

save('amalgam.mat','data_amalgamation');
```

Solution Algorithm

```
function[Qm,Qh,Qc,X,Qdh,Qdc,Qdhm,Qdmc,Qpdh,Qpdc,Qpdm,Qdmhot,Qdmcold,effh,effc
,eff_avg,UBtotal,layer,betac,betah,lambda,mu,nu,DeltaPh,DeltaPc,DeltaPh_total
,DeltaPc_total,DeltaP_total,h_c,h_h,kss,kcu,Re_c,Re_h]=HXCryogenics_II(n,wt,c
f,mhot,mcold,g,tol1,tol2)

global L

%setup empty vectors and matrices
Xm=zeros(n+2,1);
Xf=zeros(n+1,1);
DeltaX=zeros(n+1,1);
N=3*n+4;
A=spalloc(3*n+4,3*n+4,13*n+6);
b=spalloc(3*n+4,1,3*n+4);
S=spalloc(3*n+4,1,3*n+4);

%setup grid
DeltaX(1,1)=0;
DeltaX(n+2,1)=0;

for i=2:(n+1)
    DeltaX(i,1)=L/n;
end

%Normalize DeltaX
DeltaX=DeltaX/sum(DeltaX);

Xm(1,1)=0;
Xm(2,1)=DeltaX(2,1)/2;
for i=1:n
   Xm(i+1,1)=Xm(i,1)+(DeltaX(i,1)+DeltaX(i+1,1))/2;
end
Xm(n+2,1)=1;
Xf(1,1)=0;
for i=1:n
   Xf(i+1,1)=Xf(i-1+1,1)+DeltaX(i+1,1);
end

%position
x=Xm.*L;
deltax=DeltaX.*L;

layer(1,1)=0;
layer(n+2,1)=0;
for k=2:(n+1)
    if mod(k,2) == 0
        layer(k,1)=0;
    else
        layer(k,1)=1;
    end
end
```

```
%initial guesses
Qm=1-Xm;
Qh=1-Xf;
Qc=1-Xf;

done=0;

while(done==0)

   %element by element function evaluation

[betac,DeltaPc,h_c,Re_c]=arrayfun(@betacf,Qc(1:n+1),Qm(1:n+1),deltax(1:n+1));

[betah,DeltaPh,h_h,Re_h]=arrayfun(@betahf,Qh(1:n+1),Qm(1:n+1),deltax(1:n+1));
   [lambda,kss,kcu]=arrayfun(@lambdaf,Qm(1:n+2));
   mu=arrayfun(@muf,Qh(1:n+1));
   nu=arrayfun(@nuf,Qc(1:n+1));
   chih=arrayfun(@chihf,Qh(1:n+1));
   chic=arrayfun(@chicf,Qc(1:n+1));
   chim=arrayfun(@chimf,Qm(1:n+1));

   %setup matrix
   %hot fluid
   i=1:n;
   A((n+3+i-1)*N+n+3+i)=(betah(i+1,1)+betah(i-
1+1,1)).*DeltaX(i+1,1)/4+(mu(i+1,1)+mu(i-1+1,1))/2;
   A((n+3+i-1-1)*N+n+3+i)=(betah(i+1,1)+betah(i-1+1,1)).*DeltaX(i+1,1)/4-
(mu(i+1,1)+mu(i-1+1,1))/2;
   A((i+1-1)*N+n+3+i)=-(betah(i+1,1)+betah(i-1+1,1)).*DeltaX(i+1,1)/2;
   b(n+3+i,1)=(chih(i+1,1)+chih(i-1+1,1)).*DeltaX(i+1,1)/2;
   A(n+3+0,n+3+0)=1;
   b(n+3+0,1)=1;

   %cold fluid
   if(cf==1)
      i=1:n;
      A((2*n+4+i-1)*N+2*n+4+i)=(betac(i+1,1)+betac(i-1+1)).*DeltaX(i+1,1)/4-
(nu(i+1,1)+nu(i-1+1,1))/2;
      A((2*n+4+i-1-1)*N+2*n+4+i)=(betac(i+1,1)+betac(i-
1+1)).*DeltaX(i+1,1)/4+(nu(i+1,1)+nu(i-1+1,1))/2;
      A((i+1-1)*N+2*n+4+i)=-(betac(i+1,1)+betac(i-1+1,1)).*DeltaX(i+1,1)/2;
      b(2*n+4+i,1)=(chic(i+1,1)+chic(i-1+1,1)).*DeltaX(i+1,1)/2;
      A(2*n+4+0,2*n+4+n)=1;
      b(2*n+4+0,1)=0;
   else
      i=1:n;
      A((2*n+4+i-1)*N+2*n+4+i)=(betac(i+1,1)+betac(i-
1+1)).*DeltaX(i+1,1)/4+nu(i+1,1);
      A((2*n+4+i-1-1)*N+2*n+4+i)=(betac(i+1,1)+betac(i-
1+1)).*DeltaX(i+1,1)/4-nu(i-1+1,1);
      A((i+1-1)*N+2*n+4+i)=-(betac(i+1,1)+betac(i-1+1,1)).*DeltaX(i+1,1)/2;
      b(2*n+4+i,1)=(chic(i+1,1)+chic(i-1+1,1)).*DeltaX(i+1,1)/2;
      A(2*n+4+0,2*n+4+0)=1;
      b(2*n+4+0)=0;
   end
```

```
   %metal
   i=1:n;
   A((i+1-
1)*N+i+1)=(lambda(i+1,1)+lambda(i+1+1,1))./(DeltaX(i+1,1)+DeltaX(i+1+1,1))+(l
ambda(i+1,1)+lambda(i-1+1,1))./(DeltaX(i+1,1)+DeltaX(i-
1+1,1))+(betah(i+1,1)+betah(i-1+1,1)).*DeltaX(i+1,1)/2+(betac(i+1,1)+betac(i-
1+1,1)).*DeltaX(i+1,1)/2;
   A((i+1+1-1)*N+i+1)=-
(lambda(i+1,1)+lambda(i+1+1,1))./(DeltaX(i+1,1)+DeltaX(i+1+1,1));
   A((i-1+1-1)*N+i+1)=-(lambda(i+1,1)+lambda(i-
1+1,1))./(DeltaX(i+1,1)+DeltaX(i-1+1,1));
   A((n+3+i-1)*N+i+1)=-(betah(i+1,1)+betah(i-1+1,1)).*DeltaX(i+1,1)/4;
   A((n+3+i-1-1)*N+i+1)=-(betah(i+1,1)+betah(i-1+1,1)).*DeltaX(i+1,1)/4;
   A((2*n+4+i-1)*N+i+1)=-(betac(i+1,1)+betac(i-1+1,1)).*DeltaX(i+1,1)/4;
   A((2*n+4+i-1-1)*N+i+1)=-(betac(i+1,1)+betac(i-1+1,1)).*DeltaX(i+1,1)/4;
   b(i+1,1)=chim(i+1,1).*DeltaX(i+1,1);
   if(mhot=='a')
      A(0+1,0+1)=1;
      A(0+1,1+1)=-1;
   else
      A(0+1,0+1)=1;
      b(0+1,1)=mhot;
   end
   if(mcold=='a')
      A(n+1+1,n+1+1)=1;
      A(n+1+1,n+1)=-1;
   else
      A(n+1+1,n+1+1)=1;
      b(n+1+1,1)=mcold;
   end

   %decompose matrix
   S=A\b;
   i=0:n;
   Qhn(i+1,1)=S(n+3+i);
   Qcn(i+1,1)=S(2*n+4+i);
   i=0:(n+1);
   Qmn(i+1,1)=S(i+1);

   %calculate error
   err=max([max(abs(Qc-Qcn)),max(abs(Qh-Qhn)),max(abs(Qm-Qmn))]);

   %check for convergence
   if(err<tol1)
      done=1;
      Qh(0+1,1)=Qhn(0+1,1);
        Qc(0+1,1)=Qcn(0+1,1);
        i=1:n;
    Qh(i+1,1)=(Qhn(i+1,1)+Qhn(i-1+1,1))/2;
        Qc(i+1,1)=(Qcn(i+1,1)+Qcn(i-1+1,1))/2;
        Qh(n+2,1)=Qhn(n+1,1);
        Qc(n+2,1)=Qcn(n+1,1);
        Qm=Qmn;
        X=Xm;
   else
      i=0:n;
```

```
        Qc(i+1,1)=wt*Qcn(i+1,1)+(1-wt)*Qc(i+1,1);
        Qh(i+1,1)=wt*Qhn(i+1,1)+(1-wt)*Qh(i+1,1);
        i=0:(n+1);
        Qm(i+1,1)=wt*Qmn(i+1,1)+(1-wt)*Qm(i+1,1);
    end
end

Qh=full(Qh);
Qc=full(Qc);
Qm=full(Qm);

Qdh=integral(@muf,Qh(n+2),1,'AbsTol',tol2,'ArrayValued',true);
if(cf==1)
    Qdc=integral(@nuf,0,Qc(0+1),'AbsTol',tol2,'ArrayValued',true);
else
    Qdc=integral(@nuf,0,Qc(n+2),'AbsTol',tol2,'ArrayValued',true);
end
DeltaPh_total=sum(DeltaPh);
DeltaPc_total=sum(DeltaPc);
DeltaP_total=DeltaPh_total+DeltaPc_total;

%non-dim heat transfer rates from each fluid to metal
Qdhm=trapz(X,betahf(Qh,Qm,deltax).*(Qh-Qm));
Qdmc=trapz(X,betacf(Qc,Qm,deltax).*(Qm-Qc));
%max possible non-dim heat transfer rate
Qdmaxh=integral(@muf,0,1,'AbsTol',tol2,'ArrayValued',true);
Qdmaxc=integral(@nuf,0,1,'AbsTol',tol2,'ArrayValued',true);
Qdmax=min(Qdmaxh,Qdmaxc);
%effectivenesses
effh=Qdh/Qdmax;
effc=Qdc/Qdmax;
eff_avg=(effh+effc)./2;
%non-dim parasitic heat transfer rates
Qpdh=trapz(X,chihf(Qh));
Qpdc=trapz(X,chicf(Qc));
Qpdm=trapz(X,chimf(Qm));
%non-dim conduction into hot END
Qdmhot=lambdaf(Qm(1))*2*(Qm(1)-Qm(2))/DeltaX(2);
%non-dim conduction out of cold END
Qdmcold=lambdaf(Qm(n+2))*2*(Qm(n+1)-Qm(n+2))/DeltaX(n+1);
%overall energy balance. should ~ 0
UBtotal=-Qdh+Qdc-Qpdh-Qpdc-Qpdm-Qdmhot+Qdmcold;
```

Hot Side NTU Function

```
function[betah,DeltaPh,h_h,Re_h]=betahf(Qh,Qm,deltax)

global Thin Tcin Cmin W_channel Ac_total_open_oneside mdot n_fins Per_fin
Ac_fin As_fin n_plates D_H th_plate b H_overall H_gap H_fin

Th=Qh.*(Thin-Tcin)+Tcin; %Hot fluid temperature
Tm=Qm.*(Thin-Tcin)+Tcin; %metal temperature
T_film=(Th+Tm)./2;       %hot side film temperature

%helium properties @ P = 2.6 MPa, 30 K <= T <= 300 K
mu=0.00000235923+1.09566E-07.*T_film-4.69171E-10.*T_film.^2+1.32716E-
12.*T_film.^3+2.65368E-15.*T_film.^4-2.23958E-17.*T_film.^5+3.30992E-
20.*T_film.^6;
k=0.0226087+0.000598232.*T_film-4.68041E-07.*T_film.^2-2.90332E-
09.*T_film.^3+2.13475E-11.*T_film.^4-5.61647E-14.*T_film.^5+5.45558E-
17.*T_film.^6;
rho=84.9811-2.37484.*T_film+0.033441.*T_film.^2-
0.000257617.*T_film.^3+0.00000109912.*T_film.^4-2.43334E-
09.*T_film.^5+2.17837E-12.*T_film.^6;
%copper thermal conductivity, 30 K <= T <= 300 K
k_cu=6098.79-204.205.*Tm+3.01561.*Tm.^2-0.0231658.*Tm.^3+0.000097175.*Tm.^4-
2.10909E-07.*Tm.^5+1.85247E-10.*Tm.^6;%copper conductivity

V_gap=(mdot./(rho.*Ac_total_open_oneside))*((H_fin+H_gap)./H_gap);
Re_h=rho.*V_gap.*D_H./mu;

%Lmicro=0.05 to 1 mm,Htotal=0.5 m,Vinlet=0.006 to 6 m/s,D_h=2*H_gap,V=V_gap
lnNu=1.61900259E+00-1.00786470E+00.*log(Re_h)+9.89242546E-01.*log(Re_h).^2-
3.41092028E-01.*log(Re_h).^3+5.99006080E-02.*log(Re_h).^4-5.24759039E-
03.*log(Re_h).^5+1.83775818E-04.*log(Re_h).^6;
Nusselt=exp(lnNu);
%Mikulin correlation for comparison
% Re_Mikulin=Re_h./2;%Mikulin correlations built using Dh a factor of 2 lower
than fluent
% Nusselt_Mikulin=2.*0.22.*Re_Mikulin.^(0.69);%Need a factor of 2 (again) due
to correlation use of Dh in Nu
% Nusselt=Nusselt_Mikulin;

h_h=Nusselt.*k./D_H;

%Resistance of each fin
mL_onefin=sqrt(Per_fin.*h_h./(k_cu.*Ac_fin)).*(W_channel);
% eta_onefin=tanh(mL_onefin)./mL_onefin; %Conventional
eta_onefin=1./(1+mL_onefin.^2./3); %Fleming
R_onefin=1./(eta_onefin.*h_h.*(As_fin));

%Parallel resistance of all fins on a plate
R_allfins=R_onefin./n_fins;

%Resistance to conduction through separator
R_base=(b./2)./(k_cu.*H_overall.*th_plate);
```

```
%Total thermal resistance of one side of one plate
R_plate=R_allfins+R_base;

%Total UA of heat exchanger, with all plates
R_total=R_plate./n_plates;
betah=(1./(R_total.*Cmin));

%Pressure drop
%Lmicro=0.05 to 1 mm,Htotal=0.5 m,Vinlet=0.006 to 6 m/s,D_h=2*H_gap,V=V_gap
lnf=9.80180517E+00-1.24645156E+01.*log(Re_h)+8.97122754E+00.*log(Re_h).^2-
3.32708769E+00.*log(Re_h).^3+6.30120299E-01.*log(Re_h).^4-5.81647947E-
02.*log(Re_h).^5+2.07648077E-03.*log(Re_h).^6;
f=exp(lnf);
%Mikulin correlation for comparison
% por=0.5;%With shared Lmicro for all designs because Hfin = Hgap
% cd_prime=(0.707*(1-por)^0.5+(1-por))^2;
% cd=cd_prime*(1+0.18*(1)^(-1.58));%With shared Lmicro, th_spacer/H_gap =
Lmicro/Lmicro = 1
% f_Fanning=cd/4;%Because (th_plate+th_spacer)/Dh_Mikulin =
(Lmicro+Lmicro)/Lmicro = 2
% f_Mikulin_darcy=4*f_Fanning;
% f=f_Mikulin_darcy;

DeltaPh=f.*(deltax./D_H).*(1/2).*rho.*V_gap.^2;
```

Cold Side NTU Function

```
function[betac,DeltaPc,h_c,Re_c]=betacf(Qc,Qm,deltax)

global Thin Tcin Cmin W_channel Ac_total_open_oneside mdot n_fins Per_fin
Ac_fin As_fin n_plates D_H th_plate b H_overall H_gap H_fin

Tc=Qc.*(Thin-Tcin)+Tcin; %Cold fluid temperature
Tm=Qm.*(Thin-Tcin)+Tcin; %metal temperature
T_film=(Tc+Tm)./2;       %cold side film temperature

%helium properties @ P = 500 kPa, 30 K <= T <= 300 K
mu=0.00000131507+1.35207E-07.*T_film-8.37240E-10.*T_film.^2+4.22282E-
12.*T_film.^3-9.83067E-15.*T_film.^4+5.39908E-18.*T_film.^5+8.13495E-
21.*T_film.^6;
k=0.0118481+0.000850979.*T_film-0.00000378044.*T_film.^2+2.13168E-
08.*T_film.^3-7.83080E-11.*T_film.^4+1.58871E-13.*T_film.^5-1.34369E-
16.*T_film.^6;
rho=17.48-0.491194.*T_film+0.00690287.*T_film.^2-
0.0000530352.*T_film.^3+2.25756E-07.*T_film.^4-4.98883E-
10.*T_film.^5+4.45957E-13.*T_film.^6;
%copper thermal conductivity, 30 K <= T <= 300 K
k_cu=6098.79-204.205.*Tm+3.01561.*Tm.^2-0.0231658.*Tm.^3+0.000097175.*Tm.^4-
2.10909E-07.*Tm.^5+1.85247E-10.*Tm.^6;%copper conductivity

V_gap=(mdot./(rho.*Ac_total_open_oneside))*((H_fin+H_gap)./H_gap);
Re_c=rho.*V_gap.*D_H./mu;

%Lmicro=0.05 to 1 mm,Htotal=0.5 m,Vinlet=0.006 to 6 m/s,D_h=2*H_gap,V=V_gap
```

```
lnNu=1.40181903E+00-5.73104443E-01.*log(Re_c)+6.84944358E-01.*log(Re_c).^2-
2.37733746E-01.*log(Re_c).^3+4.14739472E-02.*log(Re_c).^4-3.59179995E-
03.*log(Re_c).^5+1.24664773E-04.*log(Re_c).^6;
Nusselt=exp(lnNu);
%Mikulin correlation for comparison
% Re_Mikulin=Re_c./2;%Mikulin correlations built using Dh a factor of 2 lower
than fluent
% Nusselt_Mikulin=2.*0.22.*Re_Mikulin.^(0.69);%Need a factor of 2 (again) due
to correlation use of Dh in Nu
% Nusselt=Nusselt_Mikulin;

h_c=Nusselt.*k./D_H;

%Resistance of each fin
mL_onefin=sqrt(Per_fin.*h_c./(k_cu.*Ac_fin)).*(W_channel);
% eta_onefin=tanh(mL_onefin)./mL_onefin; %Conventional
eta_onefin=1./(1+mL_onefin.^2./3); %Fleming
R_onefin=1./(eta_onefin.*h_c.*(As_fin));

%Parallel resistance of all fins on a plate
R_allfins=R_onefin./n_fins;

%Resistance to conduction through separator
R_base=(b./2)./(k_cu.*H_overall.*th_plate);

%Total thermal resistance of one side of one plate
R_plate=R_allfins+R_base;

%Total UA of heat exchanger, with all plates
R_total=R_plate./n_plates;
betac=(1./(R_total.*Cmin));

%Pressure drop
%Lmicro=0.05 to 1 mm,Htotal=0.5 m,Vinlet=0.006 to 6 m/s,D_h=2*H_gap,V=V_gap
lnf=9.87191937E+00-1.25801038E+01.*log(Re_c)+9.03581505E+00.*log(Re_c).^2-
3.34371876E+00.*log(Re_c).^3+6.32257690E-01.*log(Re_c).^4-5.82989459E-
02.*log(Re_c).^5+2.07988149E-03.*log(Re_c).^6;
f=exp(lnf);
%Mikulin correlation for comparison
% por=0.5;%With shared Lmicro for all designs because Hfin = Hgap
% cd_prime=(0.707*(1-por)^0.5+(1-por))^2;
% cd=cd_prime*(1+0.18*(1)^(-1.58));%With shared Lmicro, th_spacer/H_gap =
Lmicro/Lmicro = 1
% f_Fanning=cd/4;%Because (th_plate+th_spacer)/Dh_Mikulin =
(Lmicro+Lmicro)/Lmicro = 2
% f_Mikulin_darcy=4*f_Fanning;
% f=f_Mikulin_darcy;

DeltaPc=f.*(deltax./D_H).*(1/2).*rho.*V_gap.^2;
```

Axial Conduction Parameter Function

```
function[lambda,kss,kcu]=lambdaf(Qm)
```

```
global Cmin Thin Tcin Acm_ss Acm_cu th_spacer th_plate n_plates

Tm=Qm.*(Thin-Tcin)+Tcin; %metal temperature

%thermal conductivities, 30 K <= T <= 300 K
kss=-2.52248+0.197993.*Tm-0.000849208.*Tm.^2-0.00000433239.*Tm.^3+5.76580E-
08.*Tm.^4-2.01200E-10.*Tm.^5+2.35879E-13.*Tm.^6;%stainless conductivity
kcu=6098.79-204.205.*Tm+3.01561.*Tm.^2-0.0231658.*Tm.^3+0.000097175.*Tm.^4-
2.10909E-07.*Tm.^5+1.85247E-10.*Tm.^6;%copper conductivity

%thermal resistance of all plates in series
R_plate=n_plates.*th_plate./(kcu.*Acm_cu);
%thermal resistance of all spacers in series
R_spacer=(n_plates+1)*th_spacer./(kss.*Acm_ss);

%overall axial conduction parameter under given property conditions
lambda=(1./(R_plate+R_spacer))./Cmin;
```

Hot Side Dimensionless Capacitance Rate Function

```
function[mu]=muf(Qh)

global Cmin Thin Tcin mdot

Th=Qh.*(Thin-Tcin)+Tcin; %hot side fluid temp
%specific heat capacity of helium @ P=2.6 MPa, 30 K <= T <= 300 K
c_h=6762.2-57.8438.*Th+0.893344.*Th.^2-0.00718172.*Th.^3+0.0000313679.*Th.^4-
7.04555E-08.*Th.^5+6.36825E-11.*Th.^6;
Ch=mdot.*c_h;

%dimensionless capacitance rate on hot side
mu=Ch./Cmin;
```

Cold Side Dimensionless Capacitance Rate Function

```
function[nu]=nuf(Qc)

global Cmin Thin Tcin mdot

Tc=Qc.*(Thin-Tcin)+Tcin; %cold side fluid temp
%specific heat capacity of helium @ P=500 kPa, 30 K <= T <= 300 K
c_c=5574.4-14.4836.*Tc+0.227804.*Tc.^2-
0.00185276.*Tc.^3+0.00000815612.*Tc.^4-1.84217E-08.*Tc.^5+1.67193E-11.*Tc.^6;
Cc=mdot.*c_c;

%dimensionless capacitance rate on cold side
nu=Cc./Cmin;
```

Hot Side Parasitic Heat Leak Function

```
function[chih]=chihf(Qh)

global alpha_r phi_c_in phi_h_in

% dimensionless parasitic heat load input to hot side fluid
chih=alpha_r.*(1-(phi_c_in+Qh.*(phi_h_in-phi_c_in)).^4)./(phi_h_in-phi_c_in);
```

Cold Side Parasitic Heat Leak Function

```
function[chic]=chicf(Qc)

global alpha_r phi_c_in phi_h_in

% dimensionless parasitic heat load input to cold side fluid
chic=alpha_r.*(1-(phi_c_in+Qc.*(phi_h_in-phi_c_in)).^4)./(phi_h_in-phi_c_in);
```

Metal Parasitic Heat Leak Function

```
function[chim]=chimf(Qm)

global alpha_r phi_c_in phi_h_in

[m,n]=size(Qm);
qmp=0*ones(m,1); % metal parasitic heat transfer rate per unit length

% dimensionless parasitic heat load input to metal
chim=qmp;
% chim=alpha_r.*(1-(phi_c_in+Qm.*(phi_h_in-phi_c_in)).^4)./(phi_h_in-
phi_c_in);
```

Plot Creation and Determination of Viable Designs

```
%Postprocessing of Matlab Results
clear PData
clear par

%Create a dataset from the solution structure
SolData=struct2dataset(data_amalgamation);

%Maximum allowable pressure drop for each side
DeltaPc_max=100000;
DeltaPh_max=300000;
eff_min=0.99;

% %Determine the viable design configurations
% %Initialize ViableDesigns fields using SolData
ViableDesigns=SolData;
%Clear ViableDesigns field entries
ViableDesigns(:,:)=[];
```

```
%For each design point, find viable designs
for m=1:length(SolData)
    if (SolData.effc(m) > eff_min) && (SolData.DeltaPc_total(m) <
DeltaPc_max) && (SolData.DeltaPh_total(m) < DeltaPh_max)
        ViableDesigns = vertcat(ViableDesigns,SolData(m,:));
    end
end

% Comment and uncomment this line to include or exclude unviable designs
SolData=ViableDesigns;

%Visualization of parametric study
%String names of variables of interest
varNames = {'L_m_i_c_r_o [m]'; 'W_c_h_a_n_n_e_l [m]'; 'Weight [lb]';
'V_t_o_t_a_l [m^3]'; 'n_p_l_a_t_e_s'; 'Length [m]'; 'm_d_o_t [kg/s]'};

%Break into a seperate dataset for each class of mass flow rate
SolData_mdot_006=SolData(SolData.mdot == 0.006,:);
SolData_mdot_008=SolData(SolData.mdot == 0.008,:);
SolData_mdot_010=SolData(SolData.mdot == 0.010,:);
SolData_mdot_012=SolData(SolData.mdot == 0.012,:);

%Select data subset in mass flow and pressure to view
% SolData_plot=SolData_mdot_012;
SolData_plot=SolData;
DeltaP_plot='DeltaPc_total';
% DeltaP_plot='DeltaPh_total';

%Assign appropriate max deltaP and pressure data based on viewing choice
if strcmp(DeltaP_plot,'DeltaPc_total')==1
    DeltaP_active_max=DeltaPc_max;
    PData(:,:)=SolData_plot.DeltaPc_total;
else
    DeltaP_active_max=DeltaPh_max;
    PData(:,:)=SolData_plot.DeltaPh_total;
end

%Create matrix of data of parameters of interest
par(:,1)=SolData_plot.H_gap;
par(:,2)=SolData_plot.W_channel;
par(:,3)=SolData_plot.Weight;
par(:,4)=SolData_plot.V_total;
par(:,5)=SolData_plot.n_plates;
par(:,6)=SolData_plot.L;
par(:,7)=SolData_plot.mdot;

%For each parameter of interest
for i=1:length(varNames)
    figure
    %Plot effectiveness vs. deltaP, grouped(colored) by parameter (i)
    gscatter(PData(:,:),SolData_plot.effc,par(:,i));
    handles=gscatter(PData(:,:),SolData_plot.effc,par(:,i));

title(varNames(i),'fontname','Times','fontweight','normal','backgroundcolor',
'w')
```

```
    xlabel('Pressure Drop [Pa]','fontname','Times');
    ylabel('Effectiveness','fontname','Times');
    grid on

    %Set pressure axis scale to log
    set(gca,'xscale','log')
    %Set pressure plot axis minimum to 0
    set(gca, 'XLim', [0, get(gca, 'XLim') * [0; 1]])

    %Format gridlines
    set(gca,'GridLineStyle','-','linewidth',0.1)
    set(gca,'MinorGridLineStyle','-','linewidth',0.1)
    set(gca,'GridAlpha',1)
    set(gca,'MinorGridAlpha',1)

    %Find axes limits (most are auto)
    x1=get(gca, 'XLim');
    y1=get(gca, 'YLim');
    %Overlay lines for 0.99 effectiveness and max allowable deltaP for side
    line([1,x1(2)],[0.99,0.99],'Color','k','LineStyle','-
','HandleVisibility','off','linewidth',1.5)

line([DeltaP_active_max,DeltaP_active_max],[y1(1),1],'Color','k','LineStyle',
'-','HandleVisibility','off','linewidth',1.5)
    %Set plot window size
    set(gcf,'units','inch','position',[1,1,6.5,8])
end

%Comparing pressure drop on each side
% scatter(SolData_plot.DeltaPc_total,SolData_plot.effc,'filled','b');
% hold on
% scatter(SolData_plot.DeltaPh_total,SolData_plot.effc,'x','r');
%
%     set(gcf,'units','inch','position',[1,1,6.5,8])
%     %Format gridlines
%     set(gca,'GridLineStyle','-','linewidth',0.1)
%     set(gca,'MinorGridLineStyle','-','linewidth',0.1)
%     set(gca,'GridAlpha',1)
%     set(gca,'MinorGridAlpha',1)
%
% legend({'Low P Side','High P Side'},'fontname','Times');
% xlabel('Pressure Drop [Pa]','fontname','Times');
% ylabel('Effectiveness','fontname','Times');
% grid on
% hold off
```

Appendix B: Center for High Throughput Computing Scripts

Submit File (submit.sub)

```
universe = vanilla

arguments = $(thspacer) $(thplate) $(Hfin) $(Hgap) $(mdot) $(Temperature) $(Pressure) $(Density) $(Heatcap) $(Conductivity) $(Viscosity)

log = $(thspacer)_$(thplate)_$(Hfin)_$(Hgap)_$(mdot)_$(Temperature)_$(Pressure)_$(Cluster)_$(Process).log
output = $(thspacer)_$(thplate)_$(Hfin)_$(Hgap)_$(mdot)_$(Temperature)_$(Pressure)_$(Cluster)_$(Process).out
error = $(thspacer)_$(thplate)_$(Hfin)_$(Hgap)_$(mdot)_$(Temperature)_$(Pressure)_$(Cluster)_$(Process).err

executable = progenitus.sh

should_transfer_files = YES
when_to_transfer_output = ON_EXIT

transfer_input_files = wbscript.py, onedpforCHTC.wbpj, onedpforCHTC_files
# Transfer no output files generated by ansys. Just log, output, and error files
transfer_output_files = ""

request_cpus = 1
request_memory = 4GB
request_disk = 4GB

# Most jobs to queue at a time
#max_materialize = 5000
concurrency_limits = ANSYS

Requirements = (Target.HasGluster == true)
getenv = true

# This command tells Condor to re-submit a job if it does not return a value of 0 (successful termination) in the log file
#max_retries = 5
retry_until = 0
#If the job has been running on a machine for more than the defined number of seconds, remove the job from the queue
periodic_remove = (RemoteWallClockTime - CumulativeSuspensionTime) > 86400

queue thspacer,thplate,Hfin,Hgap,mdot,Temperature,Pressure,Density,Heatcap,Conductivity,Viscosity from joblist.txt
#queue thspacer,thplate,Hfin,Hgap,mdot,Temperature,Pressure,Density,Heatcap,Conductivity,Viscosity from failedjoblist.txt
```

Executable (progenitus.sh)

```
#!/bin/bash

# Command to enable modules
. /etc/profile.d/modules.sh

# Set the value of each parameter for each job, and give its script a corresponding unique name
# Note that $# is just the placeholder identifier for parameters in the queue list

sed "s/thspacer/$1/g;\
        s/thplate/$2/g;\
        s/Hfin/$3/g;\
        s/Hgap/$4/g;\
        s/mdot/$5/g;\
        s/Temperature/$6/g;\
        s/Pressure/$7/g;\
        s/Density/$8/g;\
        s/Heatcap/$9/g;\
        s/Conductivity/${10}/g;\
        s/Viscosity/${11}/g;" wbscript.py >> $1_$2_$3_$4_$5_$6_$7_wbscript.py

# Load ansys module version 18.2
module load ansys-19.1
#module load ansys.191

# Open ansys in batch mode. Open file onedp.wbpj. Run script with prescribed parameters
runwb2 -B -F onedpforCHTC.wbpj -R $1_$2_$3_$4_$5_$6_$7_wbscript.py
```

Ansys Workbench Script (wbscript.py)

```
# This script is run within ansys on the node computer. The name of each parameter that is changed
# is retrieved, the parameter value is set as defined by progenitus.sh and an update is attempted.
# If successful, the new parameter values and outputs are printed to the output file.
# If the update fails, the job is flagged in the output file (which is detected in the file amalgamation script)
# A dummy piece of code is included to cause a scripting error in Condor (instead of just ANSYS)
# The submit file specifies to retry the job until successful. Very few truely fail. Most succeed afer a few tries

# In ANSYS: get parameter handles. Set values for the current job's
thshandle = Parameters.GetParameter(Name="P46")
thshandle.Expression = str(thspacer) + " [mm]"
thphandle = Parameters.GetParameter(Name="P47")
thphandle.Expression = str(thplate) + " [mm]"
Hfhandle = Parameters.GetParameter(Name="P48")
Hfhandle.Expression = str(Hfin) + " [mm]"
Hghandle = Parameters.GetParameter(Name="P4")
Hghandle.Expression = str(Hgap) + " [mm]"
mdhandle = Parameters.GetParameter(Name="P62")
mdhandle.Expression = str(mdot)
Thandle = Parameters.GetParameter(Name="P23")
Thandle.Expression = str(Temperature)
#Thandle.Expression = str(Temperature) + " [K]"
Phandle = Parameters.GetParameter(Name="P24")
Phandle.Expression = str(Pressure)
#Phandle.Expression = str(Pressure) + " [Pa]"
Denhandle = Parameters.GetParameter(Name="P26")
Denhandle.Expression = str(Density) + " [kg m^-3]"
Chandle = Parameters.GetParameter(Name="P27")
Chandle.Expression = str(Heatcap) + " [J kg^-1 K^-1]"
Condhandle = Parameters.GetParameter(Name="P28")
Condhandle.Expression = str(Conductivity) + " [W m^-1 K^-1]"
Vischandle = Parameters.GetParameter(Name="P29")
Vischandle.Expression = str(Viscosity) + " [Pa s]"


# Attempt to update the project
try:
        print("Update attempting")
        Project.Update()
        # The remainder of the try statement only executes if update returns no errors
        print("Update successful. New values:")
        # Write up-to-date parameter values to output file
        for param in Parameters.GetAllParameters():
                prmString = "   " + param.Name + ": " + param.DisplayText + " = " + param.Value.ToString()
                print (prmString)
except TypeError as neg:
        print("FLAG: Update failed (TypeError)")
        print(neg)

# Except statement occurs if update returns an error
except Exception as e:
        print("FLAG: Update failed (Other)")
        #testmessage=StoredMessage.GetMessages()
        #print(testmessage)
        # FLAG is detected when using the file amalgamation script
        print(e)
        for msg in GetMessages():
                msgString = "    " + msg.DateTimeStamp.ToString() + " " + msg.Details + ": " + msg.DisplayText + "\n"
                print(msgString)

        # Geometry.Stop() does not actually perform a function. It is here to cause an error at the
        # Condor level rather than the ANSYS level to trigger a Condor resubmission. An ANSYS job can
        # run and have errors, but still be considered a successfully completed job by Condor.
        # It causes a Python scripting error: module has no attribute 'stop'
        Geometry.Stop()
```

Output File Combiner (amalgamator.py)

```
# The following code opens each individual output text file, finds the correlation parameter values,
# and writes them into a single tab delimited text file to be opened in an EES lookup table
# from which linear regression is performed to make the correlations.
# It also finds failed jobs and creates a new tab delimited text file to be used in the submit
# script to re-submit the failed jobs

# Import modules
import os
import csv

# open(file, "w").close() clears all text from the files
open("C:\Users\esheehan\Desktop\File Amalgamation/failedjoblist.txt", "w").close()
open("C:\Users\esheehan\Desktop\File Amalgamation/amalgam.txt", "w").close()

# Make column headers
with open("C:\Users\esheehan\Desktop\File Amalgamation/amalgam.txt", "a") as fileoutput:
        ParamRow = ['LnST','LnSL','LnAR','LnRe','Lnf','LnNu','LnPr','Tresidual']
        writer = csv.writer(fileoutput, delimiter='\t')
        writer.writerow(ParamRow)

# Loop through each output file. Find identifier for each parameter (or failure) and get value.
for file in os.listdir("C:\Users\esheehan\Desktop\File Amalgamation"):
        if file.endswith(".out"):
                # Initialize fail to false for each file in directory
                Fail = False
                fileinput = open(file, "r")
                for line in fileinput:
                        # Search for failure flag. If found, set fail to true (for this file) and break from for loop
                        if line.startswith("FLAG:"):
                                Fail = True
                                break


                        if line.startswith("  P67: Tresidual = "):
                                Tresidual = float(line.replace('  P67: Tresidual = ',''))
                                if Tresidual > float(1E-7):
                                        Fail = True
                                        break
```

```
        # Gets rid of everything but the parameter value and converts from string to float
        #NOTE: May need to view -> indentation -> convert indentation to tabs to get the format correct
        if line.startswith("  P39: LnST = "):
                LnST = float(line.replace('  P39: LnST = ',''))
        if line.startswith("  P40: LnSL = "):
                LnSL = float(line.replace('  P40: LnSL = ',''))
        if line.startswith("  P41: LnAR = "):
                LnAR = float(line.replace('  P41: LnAR = ',''))
        if line.startswith("  P42: LnRe = "):
                LnRe = float(line.replace('  P42: LnRe = ',''))
        if line.startswith("  P43: Lnf = "):
                Lnf = float(line.replace('  P43: Lnf = ',''))
        if line.startswith("  P44: LnNu = "):
                LnNu = float(line.replace('  P44: LnNu = ',''))
        if line.startswith("  P66: LnPr = "):
                LnPr = float(line.replace('  P66: LnPr = ',''))
        if line.startswith("  P67: Tresidual = "):
                Tresidual = float(line.replace('  P67: Tresidual = ',''))
fileinput.close()

# If a job failed, add its parameters to the tab delimited text file of jobs to re-submit
# Note: Because properties are not included in the file name, must copy resulting file into EES
# and calculate properties. Resave table with properties included as the actual resubmission file
if Fail == True:
        with open("C:\Users\esheehan\Desktop\File Amalgamation/failedjoblist.txt", "a") as failoutput:
                FileIdentifiers = file.split("_")
                writer = csv.writer(failoutput, delimiter='\t')
                writer.writerow(FileIdentifiers[0:7])
# Write the output of each successful job to a row of tab delimited file to open in EES
else:
        with open("C:\Users\esheehan\Desktop\File Amalgamation/amalgam.txt", "a") as fileoutput:
                ParamRow = [LnST,LnSL,LnAR,LnRe,Lnf,LnNu,LnPr,Tresidual]
                writer = csv.writer(fileoutput, delimiter='\t')
                writer.writerow(ParamRow)
```

Appendix C: EES Code for Correlation Comparisons

```
"NON-DIMENSIONAL----------"
"duct flow----------"
Pr=0.7 "Prandtl # largely independent but ranges from 0.6591 to 0.7444 through range of T, P"
Aspect=0.00000000000000001 "Assume infinitely wide duct, as in Fluent model"
RelRough=0

LoverD_h=1 "With shared Lmicro, and L = th_plate+th_spacer = 2*Lmicro and Dh = 2*Lmicro, LoverD_h = Lmicro/(2*Lmicro) = 0.5"

Re_duct=Re_fluent "Same Reynolds # definition as used in Fluent model"

Call ductflow_nd(Re_duct,Pr,LoverD_h, Aspect,RelRough: Nusselt_T_duct, Nusselt_H_duct, f_duct)

"fluent correlations----------"

 "cold (low P) side"
"Lmicro =0.05 to 1, Vin = 0.006 to 6 m/s, Htotal = 0.5 m, D_h = 2*H_gap, V = V_gap"
lnNu=1.40181903E+00-5.73104443E-01*ln(Re_fluent)+6.84944358E-01*ln(Re_fluent)^2-2.37733746E-01*ln(Re_fluent)^3+4.14739472E-02*ln(Re_fluent)^4-3.59179995E-03*ln(Re_fluent)^5+1.24664773E-04*ln(Re_fluent)^6
"hot (high P) side"
"Lmicro =0.05 to 1, Vin = 0.006 to 6 m/s, Htotal = 0.5 m, D_h = 2*H_gap, V = V_gap"
{lnNu=1.61900259E+00-1.00786470E+00*ln(Re_fluent)+9.89242546E-01*ln(Re_fluent)^2-3.41092028E-01*ln(Re_fluent)^3+5.99006080E-02*ln(Re_fluent)^4-5.24759039E-03*ln(Re_fluent)^5+1.83775818E-04*ln(Re_fluent)^6}

Nusselt_fluent=exp(lnNu)

 "cold (low P) side"
"Lmicro =0.05 to 1, Vin = 0.006 to 6 m/s, Htotal = 0.5 m, D_h = 2*H_gap, V = V_gap"
lnf=9.87191937E+00-1.25801038E+01*ln(Re_fluent)+9.03581505E+00*ln(Re_fluent)^2-3.34371876E+00*ln(Re_fluent)^3+6.32257690E-01*ln(Re_fluent)^4-5.82989459E-02*ln(Re_fluent)^5+2.07988149E-03*ln(Re_fluent)^6
"hot (high P) side"
"Lmicro =0.05 to 1, Vin = 0.006 to 6 m/s, Htotal = 0.5 m, D_h = 2*H_gap, V = V_gap"
{lnf=9.80180517E+00-1.24645156E+01*ln(Re_fluent)+8.97122754E+00*ln(Re_fluent)^2-3.32708769E+00*ln(Re_fluent)^3+6.30120299E-01*ln(Re_fluent)^4-5.81647947E-02*ln(Re_fluent)^5+2.07648077E-03*ln(Re_fluent)^6}

f_fluent=exp(lnf)

"Mikulin paper correlations----------"

Re_Mikulin=Re_fluent/2 "Mikulin correlations built using Dh a factor of 2 lower than fluent"

Nusselt_Mikulin=2*0.22*Re_Mikulin^(0.69) "Need a factor of 2 (again) due to correlation use of Dh in Nu"

"plate porosity"
por=0.5 "With shared Lmicro for all designs because Hfin = Hgap"

cd_prime=(0.707*(1-por)^0.5+(1-por))^2

cd=cd_prime*(1+0.18*(1)^(-1.58)) "With shared Lmicro, th_spacer/H_gap = Lmicro/Lmicro = 1"
```

```
cd=4*f_Fanning "Because (th_plate+th_spacer)/Dh_Mikulin = (Lmicro+Lmicro)/Lmicro = 2"

f_Mikulin_darcy=4*f_Fanning


 "DIMENSIONALIZATION----------------------------------------------------------------------------------------------------------"

{T=165[K]
P=500000 [Pa]

rho=density(Helium,T=T,P=P)
mu=viscosity(Helium,T=T,P=P)
Pr=prandtl(Helium,T=T,P=P)
k=conductivity(Helium,T=T,P=P)}

{H_total=0.5 [m]
W_channel=0.01 [m]
H_gap=0.00025 [m]
H_fin=H_gap
th_plate=H_gap
th_spacer=H_gap}

{m_dot_total=9*convert(g/s,kg/s)

A_c_total=W_channel*H_total

V=m_dot_total/(rho*A_c_total)*(H_gap+H_fin)/H_gap} "Velocity in gap"

"duct flow-------------------------------------------------------------------------------------------------------------------"

{D_h_duct=2*H_gap*W_channel/(H_gap+W_channel)}
{Aspect=H_gap/W_channel}

{LoverD_h=(th_plate+th_spacer)/D_h_duct}

{Re_duct=rho*V*D_h_duct/mu}

{h_duct=Nusselt_T_duct*k/D_h_duct

DELTAPh_duct=f_duct*((th_plate+th_spacer)/D_h_duct)*(1/2)*rho*V^2}

"fluent correlations----------------------------------------------------------------------------------------------------------"
{D_h_fluent=2*H_gap}
{Re_fluent=rho*V*D_h_fluent/mu}

{h_fluent=Nusselt_fluent*k/D_h_fluent}

{DELTAPh_fluent=f_fluent*((th_plate+th_spacer)/D_h_fluent)*(1/2)*rho*V^2}

"Mikulin paper correlations---------------------------------------------------------------------------------------------------"

{D_h_Mikulin=H_gap*W_channel/(H_gap+W_channel) {This paper doesn't include the factor of 2 in Dh}}

{Re_Mikulin=rho*V*D_h_Mikulin/mu}
```

{h_Mikulin=Nusselt_Mikulin*k/D_h_Mikulin}

{cd=cd_prime*(1+0.18*(th_spacer/H_gap)^(-1.58))}

{cd=2*f_Fanning*(th_plate+th_spacer)/D_h_Mikulin}

{DELTAPh_Mikulin=f_Mikulin_darcy*((th_plate+th_spacer)/D_h_Mikulin)*(1/2)*rho*V^2

N_plates=1
DELTAPh_Mikulin_test=cd*N_plates*rho*V^2}

Appendix D: Similar Heat Exchanger Corrected ΔP Predictions EES Code

***Call* ductflow_nd**(Re,Pr,LoverD_h, Aspect,RelRough: Nusselt_T, Nusselt_H, f)

"Corrected Hydraulic Diameter Similar HXer DeltaP Calculations"

"Material Properties and Flow Conditions"
T=295
P=101325
rho=**density**(***Helium***,***T***=T,***P***=P)
mu=**viscosity**(***Helium***,***T***=T,***P***=P)
Pr=**prandtl**(***Helium***,***T***=T,***P***=P)
{m_dot_g=0.069}
m_dot=m_dot_g***convert**(g/s,kg/s)

"Geometry"
H_gap=0.2***convert**(mm,m)
L_slot=3.61***convert**(mm,m)
th_plate=(0.2)***convert**(mm,m)
th_spacer=(0.3)***convert**(mm,m)
RelRough=0
N_finrows=8
N_gapsperrow=18
n_plates=100
LoverD_h=th_plate/D_h
Aspect=H_gap/L_slot
D_h=4*L_slot*H_gap/(2*(L_slot+H_gap))

"Gap Velocity"
V=m_dot/(rho*N_finrows*N_gapsperrow*H_gap*L_slot)

Re=rho*V*D_h/mu

"Plate Pressure Drop"
DELTAP_perplate=f*((th_plate)/D_h)*(1/2)*rho*V^2
DELTAP_total=DELTAP_perplate*n_plates***convert**(Pa,kPa)

"Spacer Expansion and Contraction Pressure Drops"
sigma=0.226
Kc=0.79352+0.060341*sigma-0.44822*sigma^2
Ke=1-2.35386*sigma+0.96156*sigma^2

DELTAP_i_perplate=0.5*rho*V^2*(Kc+Ke)
DELTAP_i_total=DELTAP_i_perplate*n_plates***convert**(Pa,kPa)

"Total Pressure Drop for All Plates and Spacers"
DELTAP_all_total=DELTAP_total+DELTAP_i_total

Appendix E: Slots vs. Holes Conductance Density Comparison

"Constant T_surf hAs Comparison"

"Arbitrary fluid thermal conductivity"
k=1

"Arbitrary circle diameter or lesser slot dimension"
a=1
{b=5}

"Duct aspect ratio"
AR=(a/b)

"Fully developed flow condition Nusselt numbers"
Nusselt_circle=3.66
Nusselt_duct=7.541*(1-2.610*AR+4.970*(AR)^2-5.119*(AR)^3+2.702*(AR)^4-0.548*(AR)^5)

"# Circles that can fit side-by-side in a slot"
N_circles=b/a

"Ideal"
{A_s_circle_prime=pi*a*(N_circles)}

"Manufacturing constraint of material equal to plate thickness and perforation size between perforations"
A_s_circle_prime=pi*a*(N_circles)/2

A_s_duct_prime=2*(a+b)

"Hydraulic diameters"
D_h_circle=a
D_h_duct=4*(a*b)/(2*(a+b))

"Convective heat transfer coefficients"
h_circle=Nusselt_circle*k/D_h_circle
h_duct=Nusselt_duct*k/D_h_duct

"Conductance per unit length"
hA_circle=h_circle*A_s_circle_prime
hA_duct=h_duct*A_s_duct_prime

Ratio=hA_circle/hA_duct

Appendix F: Wiedemann-Franz LM721 Alloy Thermal Conductivity Estimate

"Lucas-Milhaupt 721 Braze Alloy Thermal Conductivity Estimate"

T=295

"Published room temperature electrical conductivity, in %IACS"
LM721_Percent_IACS=87

"Standard %IACS copper electrical resistivity"
rho_e_IACS=1.72*10^(-8)

"Conversion from %IACS to Siemens/m"
sigma_LM721=(LM721_Percent_IACS/100)/rho_e_IACS

"Lorentz number"
L=2.44*10^(-8)

"Estimated room temperature thermal conductivity"
k_LM721=sigma_LM721*L*T